

The effect of red blood cell deformability on microscale blood flows

Andreas Passos

A dissertation submitted for the degree of

Doctor of Philosophy
of
University College London

Department of Mechanical Engineering
University College London

2020

‘Real generosity towards the future lies in giving all to the present.’

Albert Camus

Abstract

The non-Newtonian nature of blood arises from the presence of suspended formed elements which are the red blood cells (RBCs), white blood cells (WBCs) and platelets. Red blood cells or erythrocytes are the predominant constituent elements of blood, hence their role on haemodynamics is of great importance. Their remarkable deformability enables their flow in microvessels and is vital to oxygen delivery to tissue. Different diseases, such as malaria, sickle cell anaemia, diabetes etc. affect the mechanical properties and mainly the deformability of RBCs leading to pathological conditions and disorders in the microcirculation. However, the exact role of RBC deformability in microvascular flows has not been established hitherto. In this study, the role of red blood cell deformability on microscale haemodynamics was examined by perfusing artificially hardened RBCs in straight and bifurcating microchannels mimicking the microvasculature.

RBC microchannel flows were resolved using brightfield micro-PIV methods. Advanced image processing routines were implemented in MATLAB to simultaneously determine the velocity and haematocrit distributions for a range of flow rates and feed haematocrit conditions. At low feed haematocrits (5%) hardened RBCs were found to be more dispersed in the straight microchannel flows compared to healthy RBCs, consistent with reports of decreased migration of hardened cells. At high haematocrits (25%) hardened RBCs produced less blunted velocity profiles compared to healthy RBCs, implying a reduction in the shear thinning behaviour of the suspensions. However, the haematocrit profiles appeared to also be sharper indicating some complex interactions between

hardened cells. These findings were supported by cell tracking experiments which produced similar cell distributions for fluorescent hardened RBCs in a hardened RBC suspension, in contrast to observed margination of the same cells when suspended in healthy RBCs suspensions. Experiments with higher aspect microchannels confirmed the same trends, indicating that the latter were not due to confinement.

The extent of RBC aggregation – indicated by the bluntness of the velocity and haematocrit profiles as well as the standard deviation of the image intensity – was found to be decreased in flows of hardened RBCs, compared to healthy ones in the whole range of the measured flow rates.

RBC flows showed a higher level of heterogeneity in the bifurcating microchannels with both haematocrit and velocity profiles downstream of the T-junction bifurcation, exhibiting skewness the extent of which depended on the flow ratio between branches and RBC properties. RBC aggregation appeared to affect the non-uniformity of the haematocrit and velocity distributions downstream the bifurcation to a larger extent than RBC hardening which showed smaller variations compared to healthy non-aggregated RBC suspensions. Finally, the parent branch flow rate affected the redistribution of RBCs downstream of the bifurcation producing less skewed distributions with increasing flow rate.

The thesis elucidated the physics of RBCs flows with impaired deformability providing thus the fundamental knowledge that is required for the development of medical diagnostic tools able to capture and assess the severity of diseases associated with impaired RBC deformability.

Impact statement

Red blood cell (RBC) deformability is of great significance for tissue perfusion and a key determinant of blood rheology. Various pathologies and disorders, as well as prolonged storage, have been associated with RBC membrane stiffening. However, the exact role of RBC deformability on microscale blood flow is not fully understood.

In the present study, the role of RBC deformability was investigated in straight and bifurcating geometries in the presence and absence of aggregation. Key outcome of this work is the characterization of the velocity and haematocrit distributions of impaired hardened RBC suspensions in microchannels mimicking the microvascular flows. The results showed that the haematocrit and velocity distributions indicated distinctive differences between healthy and hardened RBC suspensions that can be utilised as biomarkers for diagnostic purposes.

In addition, the observed margination effect of hardened RBCs suspended within healthy RBC suspensions can serve as the base to develop medical tools for separation of impaired (hardened) RBCs, similarly to the techniques that are currently used for platelet and white blood cell separation from whole blood. It might be useful for conditions, such as malaria, that are known to stiffen the cells but also to screen stored blood prior to transfusion.

Finally, the experiments herein provide extended data sets that can be employed to optimize and verify numerical models and computational studies related to diseased RBCs in flow or even multi-phase particulate flows in general.

Scientific dissemination

The parts from the present thesis that have been published in journals or presented in national and international conferences are listed below:

Journal Papers

Passos A, Sherwood JM, Kaliviotis E, Agrawal R, Pavesio C, Balabani S. (2019) The effect of deformability on the microscale flow behavior of red blood cell suspensions. *Phys Fluids* 31, 091903

Conference Papers

Passos A, Sherwood JM, Agrawal R, Pavesio C, Balabani S. Effects of erythrocyte properties on microscale blood flow velocities measured by μ PIV. 9th World Conference on Experimental Heat Transfer, Fluid Mechanics and Thermodynamics, Iguazu Falls, Brazil, 12-15 June 2017.

Passos A, Sherwood JM, Kaliviotis E, Agrawal R, Pavesio C, Balabani S. Effect of RBC stiffness on microhaemodynamics. 5th Micro and Nano Flows Conference (MNF), Milan, Italy, 11-14 September 2016.

Conferences

Passos A, Sherwood JM, Kaliviotis E, Agrawal R, Pavesio C, Balabani S. Velocity, hematocrit and aggregation characteristics of stiffened erythrocytes in microflow. 6th Micro and Nano Flows Conference Atlanta, USA, 9-12 September 2018 (oral).

Passos A, Sherwood JM, Kaliviotis E, Balabani S. Microscale flow behaviour of stiffened erythrocyte suspensions. Young Researchers' Conference "Frontiers of Simulation and Experimentation for personalised Cardiovascular Management and Treatment", University College London, UK, 19-20th of July 2018 (oral).

Passos A, Sherwood JM, Kaliviotis E, Agrawal R, Pavesio C, Balabani S. Velocity, haematocrit and aggregation characteristics of stiffened RBC suspension flows.

HemPhys: 1st International School on HemoPhysics, Montpellier, France, May 15-18, 2018 (oral).

Passos A, Sherwood JM, Balabani S. Hardened red blood cells in confined flows. Blood Flow: Current State and Future Prospects, Paris, France, 9 - 11 October 2017 (poster).

Passos A, Balabani S. Red blood cells biomechanical properties and microhaemodynamics. 1st meeting of the UCL Cross-Disciplinary Network on Soft Materials, London, UK, 19th June 2017 (poster).

Passos A, Sherwood JM, Kaliviotis E, Agrawal R, Pavesio C, Balabani S. Effect of RBC stiffness on microhaemodynamics. 5th Micro and Nano Flows Conference (MNF), Milan, Italy, 11-14 September 2016. (oral)

Acknowledgements

Undertaking this thesis was a long journey of experiences which among others will shape my future perspective. In the beginning, I would like to express my gratitude to my supervisor Prof. Balabani for her support, enthusiasm and patience as well as the guidance she provided me to excel in the scientific writing.

I would also like to thank the academics and clinicians who provided input into discussions, presentations and publications: Dr. Efstathios Kaliviotis, Dr. Carlos Pavesio, Dr. Rupesh Agrawal and special thanks to Dr. Joseph Sherwood for the provided methodology and useful advices.

Moreover, I would like to thank the Institute of Biomedical Engineering (IBME) and Centre for Nature Inspired Engineering (CNIE) for the funding support. Many thanks to the people who donated blood for my research as well as the people from the Department of haematology who helped with blood collection.

I am grateful for all the friends I made at UCL, who supported me and made this long journey light as a feather: Anastasia P., Rallia V., Nikos B., Nikos K., Antonis S., Shigang Z., Thore B., Viktor K., Viktor V., Tom L. and Neil C.

Finally, I want to express my deepest appreciation to my parents who supported me in any level all these years enabling me to freely follow my interests.

Table of Contents

ABSTRACT	2
IMPACT STATEMENT	4
SCIENTIFIC DISSEMINATION	5
Journal Papers	5
Conference Papers	5
Conferences.....	5
ACKNOWLEDGEMENTS	7
TABLE OF CONTENTS.....	8
NOMENCLATURE.....	13
Roman Symbols	13
Greek symbols	15
Abbreviations.....	15
LIST OF FIGURES.....	17
LIST OF TABLES.....	24
CHAPTER 1 INTRODUCTION.....	25
1.1 Background.....	Error! Bookmark not defined.
1.2 Blood and red blood cells (RBCs)	27
1.3 Microvasculature and microcirculation	29
1.4 Dynamics of microcirculation flows.....	32
1.5 RBC deformability	43
1.6 RBC aggregation.....	46
1.7 RBC hardening	51

1.8 Microfluidic studies with hardened RBCs	57
1.9 Aims and objectives	63
1.10 Structure of the thesis	64
CHAPTER 2 EXPERIMENTAL METHODS	66
2.1 Blood sample preparation	67
2.1.1 Red blood cell separation	67
2.1.2 Artificially stiffening of RBCs.....	67
2.1.3 Aged RBCs.....	69
2.1.4 Aggregating RBC samples	70
2.1.5 Fluorescent labelling of RBCs for cell tracking.....	71
2.2 Microchannels	71
2.3 Experimental set up.....	72
2.3.1 Perfusion system and data acquisition.....	72
2.3.2 Particle Image Velocimetry (PIV) setup and processing	76
2.3.3 Image processing	80
2.4 Data analysis.....	84
2.4.1 Velocity profiles	85
2.4.2 Velocity bluntness index.....	86
2.4.3 Calibration of image intensity and haematocrit.....	88
2.4.4 Haematocrit profile bluntness.....	91
2.4.5 Velocity and haematocrit skewness	91
2.4.6 Tracking of labelled RBCs.....	92
2.5 Statistical significance of the results.....	96
2.6 Sources of uncertainty	97
2.6.1 Sample variations	97
2.6.2 Glutaraldehyde hardening.....	98
2.6.3 Errors in PIV analysis.....	99

2.6.4 Errors in flux conservation.....	101
2.7 Closure.....	104
CHAPTER 3 HARDENED RBC SUSPENSIONS IN STRAIGHT MICROCHANNEL.....	105
3.1 Introduction.....	106
3.2 Velocity profiles.....	108
3.3 Haematocrit profiles.....	114
3.4 Velocity and haematocrit relationship.....	118
3.5 Discussion.....	121
3.6 Closure.....	124
CHAPTER 4 CONFINEMENT AND MARGINATION OF HARDENED RBCS	126
4.1 Introduction.....	127
4.2 Margination of hardened RBCs.....	129
4.3 The effect of aspect ratio.....	133
4.3.1 Velocity distribution for a Newtonian fluid.....	133
4.3.2 Velocity profiles of hardened RBCs in 100 x 25 μm channels.....	137
4.3.3 Haematocrit profiles of hardened RBCs in 100 x 25 μm channels	140
4.4 Discussion.....	142
4.4.1 Margination of hardened RBCs	142
4.4.2 Effect of confinement.....	143
4.5 Closure.....	144
CHAPTER 5 EFFECT OF RBC DEFORMABILITY ON AGGREGATION.....	146
5.1 Introduction.....	147
5.2 Aggregation intensity.....	149
5.3 Velocity profiles.....	154
5.4 Haematocrit distribution	160
5.5 Discussion.....	166

5.6	Closure	171
CHAPTER 6 HARDENED RBC SUSPENSIONS IN BIFURCATING FLOWS		173
6.1	Introduction	174
6.2	The effect of flow ratio on velocity and haematocrit distributions	177
6.2.1	Local haematocrit distributions	178
6.2.2	Flow partitioning and plasma skimming	182
6.2.3	Cell depletion layer	185
6.2.4	Velocity distributions	188
6.3	The effect of parent branch flow rate on velocity and haematocrit distributions	192
6.3.1	Local haematocrit distributions	193
6.3.2	Cell depleted layer	196
6.3.3	Velocity distributions	197
6.4	The effect of aggregation	200
6.4.1	Haematocrit distributions	201
6.4.2	Cell depletion layer	203
6.4.3	The effect of aggregation on plasma skimming	205
6.4.4	Velocity distributions	206
6.5	Discussion	210
6.5.1	Velocity/haematocrit distributions and flow ratio	212
6.5.2	Velocity/haematocrit distributions and parent branch flow rate	214
6.5.3	RBC deformability and aggregation	215
6.6	Closure	217
CHAPTER 7 CONCLUSIONS AND RECOMMENDATIONS FOR FUTURE WORK		219
7.1	Main contributions	220
7.2	Summary of main findings	221
7.3	Future work	223

REFERENCES.....	225
-----------------	-----

Nomenclature

Roman Symbols

a	Intensity fitting parameter a (-)
A	Flux-flow fitting parameter A (-)
b	Intensity fitting parameter a (-)
B	Flux-flow fitting parameter B (-)
B_H^*	Haematocrit bluntness index (-)
B_I^*	Normalised image intensity bluntness index (-)
B_U	Velocity bluntness index (-)
B_U^*	Normalised velocity bluntness index (-)
d_p	Particle diameter (μm)
e	Error in mass conservation (%)
$f^\#$	Focal number (-)
F^*	Flux ratio (-)
h	Channel height (μm)
H	Haematocrit (-)
h_c	Weighing haematocrit parameter (-)
H^*	Normalised haematocrit (-)
h_0	Haematocrit at the wall (-)
H_c	Channel haematocrit (-)
H_D	Discharge haematocrit (-)
H_F	Feed haematocrit (-)
H_P	Parent branch haematocrit (-)
H_R	Relative haematocrit (-)
H_T	Tube haematocrit (-)
I	Image intensity (-)
I^*	Normalised image intensity (-)

I_{\max}	Maximum image intensity (-)
I_{raw}	Raw image intensity (-)
K	Degree of blunting (-)
L	Channel length (mm)
m	Bluntness parameter (-)
M_t	Magnification (-)
p	statistical p-value (-)
Q	Flow rate ($\mu\text{l}/\text{min}$)
Q^*	Flow ratio (-)
Q_P	Flow rate in the parent branch ($\mu\text{l}/\text{min}$)
r	Pearson rank coefficient (-)
R	Radius (μm)
Re	Reynolds number (-)
S_H	Haematocrit skewness index (-)
S_U	Velocity skewness index (-)
U	Velocity (mm/s)
u	Velocity weighing parameter (mm/s)
\bar{U}	Average velocity (mm/s)
U^*	Normalised velocity (s^{-1})
u_0	Wall slip velocity (mm/s)
u_a	Analytical velocity (mm/s)
\bar{u}_a	Average analytical velocity (mm/s)
U_{blood}	Whole blood velocity (mm/s)
u_e	Experimental velocity (mm/s)
\bar{u}_e	Average experimental velocity (mm/s)
U_{\max}	Maximum velocity (mm/s)
U_{RBC}	Red blood cell velocity (mm/s)
W	Channel width (μm)
x^*	x coordinate normalised by channel width (-)

y^*	y coordinate normalised by channel width (-)
z^*	z coordinate normalised by channel width (-)
z_{corr}	Correlation depth (μm)

Greek symbols

$\dot{\gamma}^*$	Normalised shear rate (-)
δ	Cell depleted layer width (μm)
δ^*	Normalised cell depleted layer width (-)
Δp	Pressure drop (mPa)
Δt	Time interval (ms)
Δx	Displacement (μm)
ε	Distance of influence along optical axis in derivation of z_{corr} (m)
λ	Wavelength (nm)
μ	viscosity (mPas)
ρ	Density in the parent branch (g/mm^3)
σ	Standard deviation (-)
σ^*	Normalised standard deviation (-)

Abbreviations

AR	Aspect ratio
BSA	Bovine serum albumin
CCD	Charge-coupled device
CDL	Cell depleted layer
CFL	Cell free layer
DI	Deformability index
EDTA	Ethylenediaminetetraacetic acid
EI	Elongation index
GA	Glutaraldehyde

IW	Interrogation window
LED	Light-emitting diode
NA	Numerical aperture
PBS	Phosphate buffer saline
PCC	Pearson correlation coefficient
PDF	Probability density function
PDMS	Polydimethylsiloxane
PIV	Particle image velocimetry
RBC	Red blood cells
ROI	Region of interest
SCA	Sickle cell anaemia
WBC	White blood cells

List of Figures

Figure 1.1: Schematic of human circulatory system. Image was reproduced from urgo.co.uk .	26
Figure 1.2: Schematic of red blood cell shape and average dimensions (diameter and thickness).	28
Figure 1.3: (a) Pressure drop as a function of vessel diameter measured in cat mesentery (Pries et al. 1990). (b) Velocity profile of blood platelets flowing in a 32 μm arteriole during systolic phase obtained with a μPIV technique. Two fittings were applied according to equation (1.1) with $K = 2$ (parabola) and $K = 4.02$ (Tangelder et al. 1986).	30
Figure 1.4: Representation of migration of rigid particles and deformable drops in dilute suspensions. On the left in Stokes flows (negligible inertial effects - $\text{Re} \ll 1$) and on the right in flows with inertial effects (Goldsmith, 1971).	34
Figure 1.5: (a) Plasma skimming at an arteriolar bifurcation. The majority of RBCs continue to the large diameter vessel of the bifurcation and a disproportional number of RBCs perfuse the smaller vessel. (b) Corresponding schematic showing the flow trajectories of the RBCs which are directed towards the larger vessel of the bifurcation (Namgung et al., 2016).	35
Figure 1.6: Compilation of studies showing: (a) the Fåhræus–Lindqvist effect; the relative viscosity versus tube (vessel) diameter at 45% feeding haematocrit (Pries et al., (1992) modified by Cokelet (1999)). (b) Fåhræus effect; the ratio of the average haematocrit of blood in a tube (H_c) divided by the discharge haematocrit (H_D), versus tube diameter (Gaehtgens 1980 modified by Cokelet (1999)).	37
Figure 1.7: Schematic of an RBC following the branch with higher flow rate. The figures on the right show that the distribution of the pressure forces (top) and shear stress (bottom) both point to the faster stream (Fung, 1973).	39
Figure 1.8: A schematic illustration of the dynamics and multiple effects present in the microcirculation (Secomb, 2017).	40
Figure 1.9: (a) <i>In vitro</i> RBC flow in 10 μm microchannels at different velocities (Tomaiuolo et al., 2016). (b) Phase diagram of red blood cell shape as a function of the surrounding flow velocity and their reduced volume (τ). τ is described as ratio of RBC area to the area of a circle with a circumference equal to the perimeter of the cell; τ is equal to 1 when the RBC has a circular size. Image by Kaoui et al., (2009).	41
Figure 1.10: A schematic view of (a) tumbling (b) tank-treading and (c) swinging motions (Viallat and Abkarian, 2014).	42
Figure 1.11: (a) Transmission electron micrograph of RBC rouleaux formation (b) Schematic of RBC aggregation by macromolecular bridging (Chien and Jan, 1973).	47
Figure 1.12: (a) Viscoelastic behaviour of 45% RBC suspensions hardened and with and without aggregation (Chien 1970). (b) Correlation between aggregation parameter (zeta-sedimentation technique) and normalised rigidity (ratio of relaxation times). $H_t = 0.40$ and 0-4 g/dl concentrations of Dextran 70 (Jovtchev et al. 2000). (c) Normalised velocity profiles at normal and low flow rates of aggregated (Dextran 500) and non-aggregated blood suspensions perfused into a rat muscle vessel of $\sim 55 \mu\text{m}$ diameter (Bishop et al. 2001).	49
Figure 1.13: (a) Time lapse of cells entering the tooth-shaped microfluidic channel measuring the deformation index (Amirouche et al. 2020). (b) Typical blood flow patterns within the microfluidic	

network. Smallest microchannels shown are 6 μm wide; s: silent capillary (receiving only plasma in the case of untreated RBCs), p: plugged capillary (Shevkoplyas *et al.* 2006). (c) Top view of the microfluidic setup for the flow of red blood cells through a constriction. Height of the microchannel is 75 μm , $L = 200 \mu\text{m}$ and $w = 25 \mu\text{m}$ (Faivre *et al.* 2006). (d) Trains of red blood cells (highlighted in red) in the RBC flow. Scale bars: 20 μm (Iss *et al.*, 2019). 61

Figure 2.1: Reduction of RBC deformability obtained with glutaraldehyde and diamide treatment (a) Deformability measurement of glutaraldehyde fixed RBCs with different techniques (ektacytometry 3 Pa and 17 Pa, micropore filtration and artificial microvascular network) (Sosa *et al.* 2014) (b) Deformation index of healthy and fixed RBCs with diamide and glutaraldehyde (microfluidic hyperbolic contraction) (Rodrigues *et al.* 2013). 69

Figure 2.2: Sample images of 10% haematocrit samples in flow at 45 s^{-1} . (a) Healthy sample, (b) GA 0.04% fixed sample, (c) healthy aged sample, (d) GA 0.08% fixed sample. The scale bars correspond to 10 μm length. 70

Figure 2.3: Schematic of the μ -PIV experimental set up for microscale blood flow imaging. Two sources of illumination are shown, the LED microstrobe was used for brightfield imaging and the laser illumination was used only for the cell tracking experiments in Chapter 4. 75

Figure 2.4: Sample vector plot obtained by PIV processing to pre-processed images. Multi-pass correlation methods were used with a vector spacing of 2.4 μm (4 pixels). The first vector is positioned 7.2 μm from the wall. Scale bar is 10 μm 78

Figure 2.5: (a) The velocity profiles calculated upstream and downstream of the ROI taken in the middle of the microchannel (8 mm from inlet). (b) The velocity field extracted from PIV processing indicating the regions upstream and downstream of the ROI. 80

Figure 2.6: (a) Original image of RBC flow in a T-junction microchannel and (b) the intensity distribution along the x-axis (across the daughter branch). (c) Image after correction of the uneven illumination and (d) the new intensity distribution along the x-axis. The red areas in (a) and (c) indicate the region that the intensity distribution was calculated. Flow is from left to right. 82

Figure 2.7: Time averaged image, obtained after correction for uneven illumination. The walls of the channel were identified from the peaks of the intensity profile (inverse intensity $1-I^*$, eq 2.5) shown with the red line. The inset shows the corresponding cropped ROI in the RBC image. . 83

Figure 2.8: (a) Instantaneous sample image showing the cropped, corrected and rescaled section (ROI) used for PIV processing. (b) Time averaged image obtained from 120 instantaneous images indicating the cropped section that was used to determine the haematocrit distribution. The ROI is located in the middle of a 16 mm long channel i.e. 160 widths downstream the inlet. 83

Figure 2.9: Instantaneous sample image of the T-junction showing the selected ROIs in the parent, daughter and outlet branches. The inset shows the time averaged image obtained from 120 instantaneous images that was used to determine the haematocrit distribution in ROIs at the respective locations. Flow is from left to right. 84

Figure 2.10: A typical velocity profile extracted from PIV data (GA 0.08% RBC sample of 25% haematocrit); each point represents the average velocity along the length of the region of interest of the channel. The blue curve is the fitted velocity profile using equation (2.2). The error bars correspond to one standard deviation and the red lines are confidence intervals of 95%. 86

Figure 2.11: Time averaged sample images at various haematocrits for the (a) healthy RBC sample (5%, 10%, 25%, 35% haematocrits) and (b) GA 0.08% RBC sample (2%, 5%, 10%, 15%, 20%, 30% haematocrits). (c) Calibration curves correlating haematocrit to image intensity. 90

Figure 2.12: A typical haematocrit distribution for a 25% haematocrit sample obtained from time averaged image intensity using the calibration curve in Figure 2.11c.	91
Figure 2.13: Typical skewed (a) velocity and (b) haematocrit profiles in the daughter branch of the T-junction microchannel. The profiles are normalised against the average velocity and haematocrit respectively. The profiles are smoothed using spline interpolation.	92
Figure 2.14: (a) Sample image of the suspension acquired with the LED illumination (b) Sample images of fluorescently labelled stiffened RBCs acquired with the laser illumination (c) Image after background subtraction (d) Image intensity and area-based thresholding to identify in-plane single cells. (e) Centroid estimation of the labelled cells.	95
Figure 2.15: Distributions of RBC cortical tension used as an indication of RBC deformability between six healthy donors (Guo <i>et al.</i> , 2014).	98
Figure 2.16: Flow rate in each branch as a function of flow ratio, Q^* : (a) Healthy RBCs in PBS, (b) Healthy RBCs in Dextran, (c) GA 0.08% RBCs in PBS and (d) GA 0.08% RBCs in Dextran.	103
Figure 3.1: (a) Sample images of RBC samples of 25% haematocrit perfused at 45 s^{-1} (b) Time averaged image intensity of the samples at 25% haematocrit (c) Normalised time averaged image intensity with maximum image intensity.	108
Figure 3.2: Typical velocity profiles of healthy-unfixed hardened (0.04%, 0.08% GA) and aged RBC samples obtained in the square microchannel at around 40 s^{-1} and haematocrit (a) 5% and (b) 25%. The grey area indicates the analytical velocity profile for a Newtonian fluid in a square channel.	109
Figure 3.3: Velocity bluntness index as a function of normalised velocity U^* for samples with the same stiffness and different haematocrit levels: (a) unfixed – healthy samples at 5%, 10% and 25% Hct (b) GA 0.04% hardened RBC samples at 10% and 25% Hct, (c) GA 0.08% hardened RBC samples at 5%, 10% and 25% Hct and (d) aged RBC samples at 10% and 25% Hct. The error bars $\text{d}B_{U^*}$ were calculated from eq. 2.4 and $\text{d}U^*$ show one standard deviation.	111
Figure 3.4: Comparison of bluntness indices of measured velocity profiles as a function of normalised velocity U^* for each of the samples at (a) Hct = 5% (b) Hct = 10% and (c) Hct = 25%. Velocity profile bluntness indices were calculated from equation (2.3). The error bars, $\text{d}B_{U^*}$, were calculated from eq. 2.4 and $\text{d}U^*$ show one standard deviation.	112
Figure 3.5: Boxplots summarising the data: bluntness index of the measured velocity profiles within the range of $1 - 230 \text{ s}^{-1}$ for each of the samples at (a) Hct = 5%, (b) Hct = 10%, c) Hct = 25%. The central red lines indicate the median of the measurements and the bottom and top sides of the box indicate the 25th and 75th percentiles, respectively.	114
Figure 3.6: (a) Typical measured haematocrit profiles normalized by the average haematocrit; (b) Fitted haematocrit profiles (25% feed haematocrit and $U^* = 58 \text{ s}^{-1}$).	115
Figure 3.7: Haematocrit bluntness index as a function of normalised velocity U^* for each of the measured samples at (a) Ht = 5% (b) Ht = 10% and (c) Ht = 25%.	116
Figure 3.8: Boxplots summarising the data: bluntness index of measured haematocrit profiles at (a) Hct = 5%, b) 10% and (c) Hct = 25%. The central red lines, indicate the median and the bottom and top edges of the box indicate the 25th and 75th percentiles, respectively.	117
Figure 3.9: Velocity bluntness vs haematocrit bluntness index for the measured samples at (a) Ht = 5%, (b) Ht = 10% and (c) Ht = 25%.	119

Figure 3.10: Shear rate distribution of normalised velocity profiles around 40 s^{-1} of 25% haematocrit samples, compared to analytical. The shear rate was calculated using central differencing.....	123
Figure 4.1: Distribution of labelled hardened RBCs in dense suspensions of healthy and hardened RBCs near the inlet and outlet of the square microchannel. The velocity per unit width was 60 s^{-1} and the distributions were produced by 1253 cells on average.	131
Figure 4.2: Probability density function (PDF) of 1% labelled hardened RBCs flowing within a 25% suspension of (a) hardened RBCs and (b) within healthy RBCs. (c) and (d) Normalised image intensity distribution for the (a) and (b) suspensions respectively. Measurements were acquired at a distance of $10W$ near the outlet of the $50 \times 50 \mu\text{m}^2$ microchannel and $U^* \approx 60 \text{ s}^{-1}$. A total of (a) 1154 and (b) 1353 RBCs were tracked to produce the distributions.	132
Figure 4.3: Probability density function of hardened RBCs, suspended in healthy RBCs. Comparison of the experimental results of the present study with data from literature. Data were reproduced from Chen et. (2017).....	133
Figure 4.4: Cross-sectional velocity distribution of a Newtonian fluid described by the analytical form (Equation (2.1)) of (a) $50 \mu\text{m}$ square channel and (b) $100 \mu\text{m} \times 25 \mu\text{m}^2$ channel.	134
Figure 4.5: (a) Analytical velocity profiles for a Newtonian fluid (2.1), normalised with maximum velocity for 25, 50 and $100 \mu\text{m}$ channel widths. (b) Shear rate distribution of the normalised analytical velocity profiles distributed for channel widths of 25, 50 and $100 \mu\text{m}$. The red profile corresponds to the $50 \times 50 \mu\text{m}^2$ channel: $U_{xyz} = 25 = U_{xzy} = 0$. The blue and black profiles correspond the $100 \times 25 \mu\text{m}^2$ channel for $U_{xyz} = 12.5$ and $U_{xzy} = 0$ respectively.	135
Figure 4.6: Healthy RBC suspensions in flow in (a) $50 \times 50 \mu\text{m}^2$ channel and (b) $100 \times 25 \mu\text{m}^2$ channel. Haematocrit 25%. Scale bars correspond to $10 \mu\text{m}$	136
Figure 4.7: (a) Comparison of normalised velocity profiles for 25% haematocrit flows of healthy, and hardened (0.04% and 0.08% GA) RBCs at 29 s^{-1} . The grey area indicates the analytical solution for the laminar flow of a Newtonian fluid in the rectangular channel. Comparison of normalised RBC velocity profiles at $U^* = 29 \text{ s}^{-1}$ in 100×25 and $50 \times 50 \mu\text{m}^2$ channels for the three samples (b) Healthy, (c) GA 0.04%, (d) GA 0.08%.	138
Figure 4.8: (a) Velocity bluntness index as a function of normalised velocity U^* for RBC samples with different membrane stiffness at different flow rates. (b) Boxplots of B_U for the three samples. The central red lines indicate the median of the measurements and the bottom and top sides of the box indicate the 25th and 75th percentiles, respectively.	139
Figure 4.9: Typical image intensity profiles, normalised with the average image intensity, measured in the high aspect ratio microchannel for the healthy and hardened RBCs suspensions of 25% haematocrit at $U^* = 29 \text{ s}^{-1}$	140
Figure 4.10: (a) Image intensity (equivalent to haematocrit) bluntness index, B_I^* , as a function of normalised velocity U^* for RBC samples with different membrane stiffness at different flow rates. The error bars show one standard deviation. (b) Boxplots of B_I^* for the three samples. The central red lines indicate the median of the measurements and the bottom and top sides of the box indicate the 25th and 75th percentiles, respectively.	141
Figure 5.1: Images of washed RBCs under static conditions suspended in (a) PBS and (b) PBS and Dextran 2000 solution showing the formation of the rouleaux.....	149
Figure 5.2: Probability density functions of image intensity and corresponding RBC images for flows of healthy RBCs suspended in (a) PBS and (b) Dextran and GA 0.08% RBCs in (c) PBS	

and (d) Dextran at low flow rates; $U^* = 6, 8, 9, 8 \text{ s}^{-1}$ respectively for the a,b,c and d. Image intensity is normalised with maximum intensity. Scale bars correspond to $10 \mu\text{m}$	151
Figure 5.3: Normalised standard deviation of image intensity (σ^*) as a function of normalised velocity (U^*) for healthy, GA 0.04% and GA 0.08% samples suspended in (a) PBS and (b) Dextran solutions.	152
Figure 5.4: Uncertainty of image contrast standard deviation estimated from 60 pairs of images. RBC samples suspended in (a) PBS and (b) Dextran. The uncertainty was calculated as the standard deviation of σ^*	154
Figure 5.5: (a) Typical velocity profiles of Dextran samples: healthy-unfixed, hardened with GA 0.04%, GA 0.08% and healthy sample suspended in PBS, obtained in the square microchannel at 18 s^{-1} and 25% haematocrit. (b) A close up of the profiles. The profiles are normalised by the average velocity. The grey area indicates the analytical velocity profile for a Newtonian fluid in a square channel (Bruus 2008).	156
Figure 5.6: Normalised velocity profiles suspended in PBS and Dextran of healthy RBC and GA 0.08% hardened RBCs samples. Healthy samples at normalised velocities: (a) 15 s^{-1} (c) 54 s^{-1} (e) 120 s^{-1} and GA 0.08% hardened samples at (b) 16 s^{-1} (d) 62 s^{-1} and (f) 135 s^{-1}	157
Figure 5.7: Bluntness index of measured velocity profiles as a function of normalised velocity U^* for (a) PBS and (b) Dextran samples of 25% haematocrit.	158
Figure 5.8: Bluntness index of the measured velocity profiles within the range of $1 - 230 \text{ s}^{-1}$ for each of the 25% haematocrit samples suspended in (a) PBS solution and (b) Dextran solution. The central red lines indicate the median of the measurements and the bottom and top sides of the box indicate the 25th and 75th percentiles, respectively. Outliers are plotted individually with '+' and correspond to the outer 0.7% of the data.	159
Figure 5.9: Sample RBC images and time averaged sample images respectively with image intensity distribution profiles at 25% haematocrit for (a,b) healthy-Dextran sample at 15 s^{-1} (c,d) healthy-Dextran sample at 120 s^{-1} (e,f) GA 0.08% - Dextran sample at 16 s^{-1} , (g,h) GA 0.08% - Dextran sample at 132 s^{-1}	161
Figure 5.10: Haematocrit profiles of healthy and GA 0.08% hardened RBCs samples suspended in PBS and Dextran. Healthy samples at normalised velocities: (a) 15 s^{-1} (c) 54 s^{-1} (e) 120 s^{-1} and GA 0.08% hardened samples at (b) 16 s^{-1} (d) 62 s^{-1} and (f) 135 s^{-1}	163
Figure 5.11: Haematocrit profile bluntness index as a function of normalised velocities of 25% haematocrit samples suspended in (a) PBS (non-aggregating) and (b) Dextran (aggregating).	164
Figure 5.12: Box plots of the bluntness index of haematocrit profiles of 25% suspensions of healthy, GA 0.04% and GA 0.08% RBCs in (a) PBS and (b) Dextran. The central red lines indicate the median and the bottom and top edges of the box indicate the 25th and 75th percentiles, respectively and outliers are plotted individually with "+" and correspond to the outer 0.7% of the data.	164
Figure 5.13: Haematocrit bluntness comparison for samples with the same membrane stiffness samples suspended in PBS and Dextran. (a) Healthy samples (b) GA = 0.04% and (c) GA = 0.08%.	165
Figure 5.14: Velocity vs haematocrit bluntness index of healthy, GA 0.04% and GA 0.08% samples suspended in a Dextran solution at 25% haematocrit.	168

- Figure 6.1: Sample instantaneous image of flow of aggregating healthy RBCs in the T-junction microchannel. Shaded areas indicate the regions of interest (ROI) where profiles are calculated from. RBC suspensions enter through the parent branch (left of figure) and exit through the daughter and outlet branches. The flow ratio Q^* between outlet and daughter branch is 0.94. 177
- Figure 6.2: Haematocrit bluntness index comparison in the parent branch between samples suspended in PBS healthy against hardened (GA 0.08%). 179
- Figure 6.3: Haematocrit profiles of healthy and GA 0.08% RBC samples at low medium and high flow ratios with the time averaged images from which the profiles were extracted from; outlet branch on the left side (a,c) and daughter branch on the right side (b,d). (a,b) Healthy sample suspended in PBS (c,d) GA 0.08% hardened sample suspended in PBS. The contrast of the time averaged images was enhanced for clarity. 180
- Figure 6.4: Haematocrit profile skewness, against flow ratio; comparison of healthy samples against GA 0.08% hardened sample both suspended in PBS, (a) outlet branch and (b) daughter branch. 182
- Figure 6.5: Haematocrit ratio H/H_P against flow ratio; comparison of healthy against GA 0.08% hardened RBC samples in PBS in (a) outlet branch and (b) daughter branch. 183
- Figure 6.6: Flux-flow ratio curves; Comparison of healthy samples against GA 0.08% hardened sample both suspended in PBS in the (a) outlet branch and in (b) daughter branch. Fitting curves according to Equation (6.4), dotted line corresponds to $F^* = Q^*$ 185
- Figure 6.7: (a) Sample image of healthy RBCs in the daughter branch, $Q^* = 0.09$. (b) Time averaged image out of 60 pairs of images; the red line shows the image intensity distribution and blue line the derivative of image intensity across the channel width. (c) Binarised time averaged image. 186
- Figure 6.8: Normalised cell depleted layer with channel width, δ^* , as a function of flow ratio, Q^* . Comparison between healthy and hardened (GA 0.08%) RBC samples in PBS (a) in the outlet branch and (b) in the daughter branch. 188
- Figure 6.9: Velocity profile bluntness index against normalised velocity, U^* , in the parent branch. Comparison between healthy samples and hardened RBCs (GA 0.08%) suspended in PBS. 189
- Figure 6.10: Normalised velocity profiles of the samples at different flow ratios. The velocity skewness index, S_U , is also indicated. Healthy RBC sample suspended in PBS in the (a) outlet and (b) in the daughter branch. GA 0.08% hardened RBC samples suspended in PBS (c) in the outlet and (d) in the daughter branch. The grey area indicates the analytical velocity profile for a Newtonian fluid in a square channel. 190
- Figure 6.11: Velocity profile skewness plotted against flow ratio. Comparison between healthy sample against GA 0.08% hardened sample suspended in PBS in the (a) outlet and (b) daughter branches respectively. 191
- Figure 6.12: Velocity profile skewness S_U , against haematocrit skewness S_H ; comparison of healthy sample against GA 0.08% hardened sample suspended in PBS in the (a) outlet and (b) daughter branch. 192
- Figure 6.13: Haematocrit bluntness index comparison in the parent branch of (a) healthy and hardened (GA 0.08%) RBC suspensions in PBS. 193
- Figure 6.14: Haematocrit profiles in the outlet and daughter branches at low, medium and high normalised parent branch velocities for $Q^* \approx 0.5$; Healthy sample suspended in PBS (a) outlet

and (b) daughter branches. GA 0.08% hardened sample suspended in PBS (c) outlet and (d) daughter branches.	194
Figure 6.15: Haematocrit profile skewness against parent branch normalised velocity; comparison of healthy against GA 0.08% hardened RBC samples both suspended in PBS: (a) outlet and (b) daughter branch.	196
Figure 6.16: Normalised cell depleted layer width as a function of parent branch flow rate; comparison of healthy against GA 0.08% hardened RBC samples both suspended in PBS in (a) the outlet and (b) daughter branches.	197
Figure 6.17: Velocity bluntness index against normalised velocity in the parent branch. Comparison between healthy and GA 0.08% hardened RBC samples suspended in PBS.	198
Figure 6.18: Normalised velocity profiles for different parent branch flow rates, U_P^* . Comparison of healthy RBC samples suspended in PBS in the (a) outlet and (b) daughter branches. GA 0.08% hardened RBC samples in PBS in the (c) outlet and (d) daughter branches.	199
Figure 6.19: Velocity profile skewness, against parent branch U^* . Comparison of healthy and GA 0.08% hardened RBC samples in the (a) outlet and (b) daughter branches.	200
Figure 6.20: Haematocrit profile skewness S_H as a function of flow ratio Q^* . Comparison between healthy and GA 0.08% hardened RBC samples suspended in PBS-Dextran solution in the (a) outlet and (b) daughter branches respectively of a T-junction bifurcation.	201
Figure 6.21: Haematocrit profile skewness S_H as a function of parent branch normalised velocity U^* . Comparison between healthy and GA 0.08% hardened RBC samples suspended in PBS-Dextran solution in (a) the outlet and (b) daughter branches respectively of a T-junction bifurcation.	203
Figure 6.22: Normalised cell depleted layer width, δ^* , as a function of flow ratio Q^* . Comparison of healthy and GA 0.08% hardened RBC samples suspended Dextran in the (a) outlet and (b) daughter branches.	204
Figure 6.23: Normalised cell depleted layer width, δ^* , as a function of parent branch U^* . Comparison of healthy and GA 0.08% hardened RBC samples suspended Dextran in the (a) outlet and (b) daughter branches.	205
Figure 6.24: Flux-flow ratio curves; outlet branch on the left side (a,c), daughter branch on the right side (b,d). Fitting curves according to equation (6.9). (a,b) Comparison of healthy samples suspended in PBS against Dextran ones (c,d) Comparison of GA 0.08% hardened sample suspended in PBS against Dextran. Dotted line corresponds to $F^* = Q^*$	206
Figure 6.25: Normalised velocity profiles of aggregated RBC samples at different flow ratios. The velocity skewness index, S_U , is also indicated. Healthy RBC sample suspended in Dextran in the (a) outlet and (b) in the daughter branch. GA 0.08% hardened RBC samples suspended in Dextran (c) in the outlet and (d) in the daughter branch. The grey area indicates the analytical velocity profile for a Newtonian fluid in a square channel.	207
Figure 6.26: Velocity profile skewness S_U , as a function of flow ratio Q^* . Comparison of healthy and GA 0.08% hardened RBC samples suspended in Dextran in the (a) outlet and (b) daughter branches.	208
Figure 6.27: Velocity profile skewness S_U , against haematocrit skewness S_H ; Comparison of healthy sample against GA 0.08% hardened sample suspended in Dextran in the (a) outlet and (b) daughter branch.	209

Figure 6.28: Velocity profile skewness S_U , as a function of parent branch flow rate U^* . Comparison of healthy and GA 0.08% hardened RBC samples suspended in Dextran in the (a) outlet and (b) daughter branches. 210

List of Tables

Table 1.1: Red blood cell morphological parameters (reproduced from Linderkamp <i>et al.</i> , 1986)	28
Table 1.2: Typical microcirculatory parameters as measured <i>in vivo</i> in cat sartorius muscle (Popel & Johnson 2005). <i>In vitro</i> viscosity was estimated by (Pries <i>et al.</i> 1996).	31
Table 1.3: Protocols of red blood cell hardening using Glutaraldehyde.	54
Table 1.4: Summary of recent <i>in vitro</i> microfluidic studies investigating the effect of RBC deformability on haemodynamics and blood properties.	62
Table 2.1: Summary of the cases investigated in this thesis in terms of RBC samples, feeding haematocrit and used geometry. GA samples are the hardened samples with glutaraldehyde, the aggregating RBC samples are expressed as Dextran and non-aggregating as PBS.	76
Table 2.2: Average parent flow rate and mean percentage errors in flow conservation during the perfusion of each sample.	104
Table 3.1: Pearson correlation coefficients for velocity and haematocrits bluntness indices. ...	120
Table 3.2: T-test coefficients comparing the data sets of each sample against the healthy sample.	121
Table 5.1: Pearson correlation coefficients for velocity and haematocrits bluntness indices. ...	169
Table 6.1: The range of perfused flow rates, expressed in U^* , for the four samples. The flow rate was measured in the parent branch.	178
Table 6.2: Fitting coefficients A and B for the fitting for the samples in outlet and daughter branches of Figure 6.6 with 95% confidence intervals.	185
Table 6.3: Pearson correlation coefficients for haematocrit skewness as a function of parent branch flow rate in outlet and daughter branches. RBCs suspended in PBS (no aggregation).	195
Table 6.4: Pearson correlation coefficients for haematocrit skewness in the outlet and daughter branches as a function of parent branch flow rate.	203
Table 6.5: Fitting coefficients A and B for the fitting for the samples in outlet and daughter branches of Figure 6.24 with 95% confidence intervals.	206

Chapter 1

Introduction

1.1 Background

The human circulatory system comprises a network of blood vessels and the heart. It supplies tissues with blood which has three main functions: transportation (oxygen, nutrients, waste products etc.), regulation (pH, temperature) and protection (clotting, immune responses) (Tortora and Grabowski, 2001). The vascular circulation is a closed loop fluid system, pressure driven by the heart consisting of around 10^{11} vessels in humans (Schmid-Schönbein, 1999). Deoxygenated blood is pumped from the right side of the heart to the lungs, where it absorbs oxygen, returns to the left side of the heart and is pumped around the body (Figure 1.1). The oxygenated blood is carried towards the body and away from the heart by the arteries and deoxygenated blood returns towards the heart from the body through the veins. In between the arteries and veins lies

the microvasculature where the delivery of oxygen to the tissues and organs is carried out (Popel and Johnson, 2005).

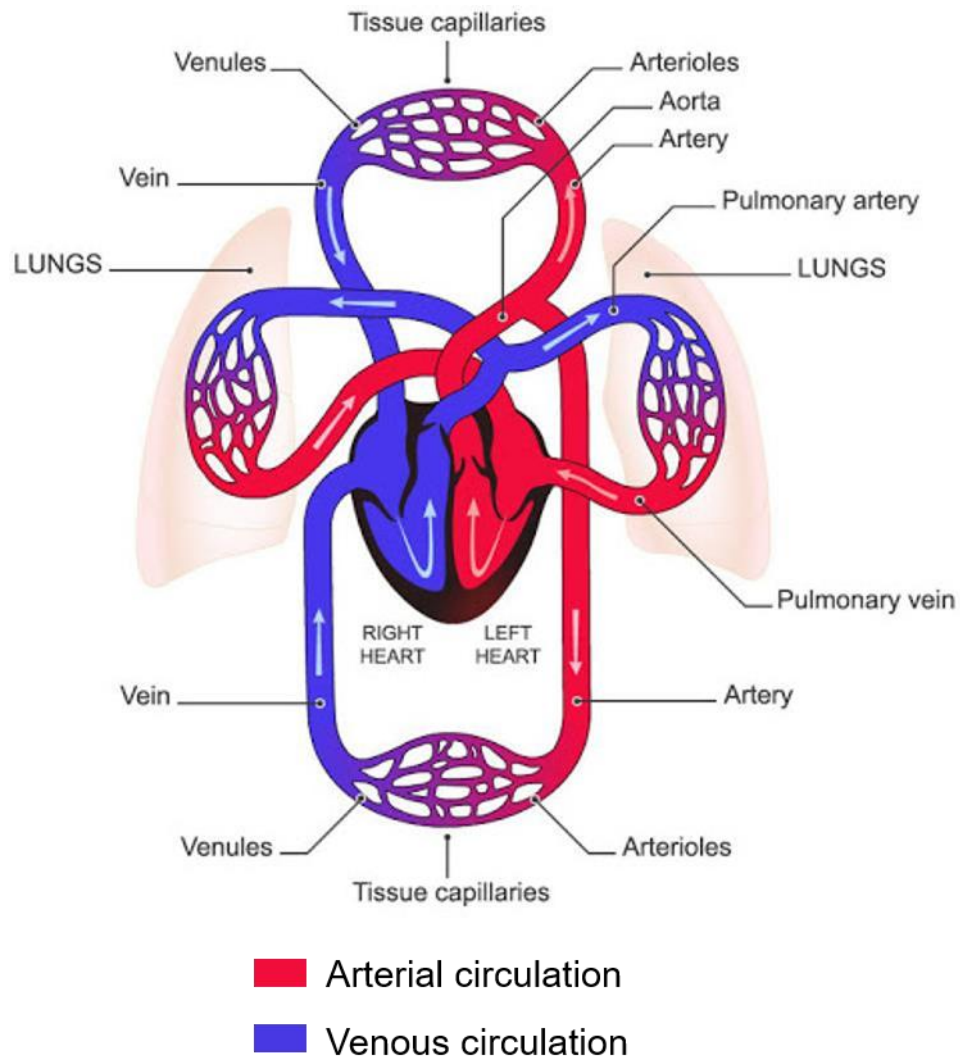


Figure 1.1: Schematic of human circulatory system. Image was reproduced from urgo.co.uk.

1.2 Blood and red blood cells (RBCs)

Blood can be described as a two-phase fluid, consisting of plasma, which is an aqueous solution, and formed elements: the red blood cells (RBCs), white blood cells (WBCs) and platelets. By volume, plasma occupies about 54.3% and red blood cells 45%; the remaining 0.7% comprises mostly white blood cells or leukocytes and a very small amount of platelets (<0.002%).

The plasma consists mainly of water (~93% (Caro, 2012)) and solutes, mainly proteins such as fibrinogen which is responsible for haemostasis (blood clotting) and aggregation. From a fluid dynamics point of view, plasma viscosity has been considered for decades as a Newtonian fluid and its viscosity has been measured to be between 1.15 mPas and 1.35 mPas at a physiological temperature of 37 degrees (Lowe, 1988), however, more recent studies have revealed a viscoelastic behaviour (Brust *et al.*, 2013; Varchanis *et al.*, 2018).

Red blood cells, or erythrocytes, are the most abundant cells in blood and their structure is relatively simple as they have no nucleus and are essentially a flexible membrane surrounding cytosol and haemoglobin. In terms of shape they are biconcave discs with a thick rim and thin sunken centre (so called discocytes) (Figure 1.2). Their diameter and thickness are approximately 8 μm and 2 μm respectively. Their average volume is around 89 μm^3 and their surface area 132 μm^2 (Table 1.1, Linderkamp *et al.*, 1986). They are mainly responsible for delivering oxygen (O_2) and carbon dioxide (CO_2) to and from the body tissues respectively. Their shape combined with their elastic membrane result in a highly deformable cell. Their ability to deform under different flow conditions or due to

geometrical constrictions allows them to pass through the microvasculature of the human body whose capillary vessels have diameters significantly smaller than RBC dimensions: as low as $2.8\ \mu\text{m}$ (Halpern and Secomb, 1992). During this passage, they fold and squeeze in such a way as to maximize the cell area in contact with the endothelial wall and optimize the gas exchange function (Yoon *et al.*, 2009).

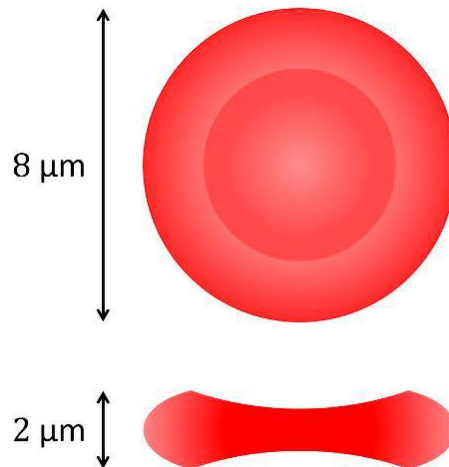


Figure 1.2: Schematic of red blood cell shape and average dimensions (diameter and thickness).

Table 1.1: Red blood cell morphological parameters (reproduced from Linderkamp *et al.*, 1986)

RBC properties	Sample size	Adult RBCs
Diameter (μm)	25	7.8 ± 0.3
Thickness (μm)	10	1.92 ± 0.13
Area (μm^2)	5	132.1 ± 6.7
Volume (fl)	35	89.4 ± 4.9
Weight (pg)	35	29.5 ± 2.0

1.3 Microvasculature and microcirculation

The macrovasculature consists of arteries and veins which are responsible for the rapid transport of blood from the heart towards the organs and back. Microvasculature includes all the vessels that have diameters below 100 μm . The term microcirculation refers to the blood flow in microvascular vessels. The microvascular system is composed of complex bifurcating geometries of three types of microvessels: arterioles, venules and capillaries which are responsible for regulating the blood in the individual organs. At any given moment, about 30% of the blood in the systemic circulation will be found in the arteries, 5% in the capillaries and 65% in the veins (Woods, 1995). Almost 80% of the total pressure drop between the main arteries and veins, aorta and vena cava respectively, occurs in microvasculature (Pries *et al.*, 1990; Popel and Johnson, 2005) (Figure 1.3(a)).

The arteries branch and narrow into arterioles leading to capillaries. Blood returns from the capillary bed through venules that drain out to the veins before reaching the heart in order to be recirculated. Arterioles range in diameter from 10 μm to 100 μm and they are surrounded by muscular walls which control the perfusion via dilation and contraction. As they sequentially bifurcate they decrease in size and lead into capillaries. *In vivo* velocity measurements in arterioles have shown blunted velocity profiles which deviate from the parabolic-like distribution (Ellsworth and Pittman, 1986; Tangelder *et al.*, 1986; Nakano *et al.*, 2003). In general, the blood velocity profile $U(r,t)$ in a microvessel of radius R can be described by the empirical equation:

$$U(r,t) = U_{\max} \left(1 - \left(\frac{r}{R} \right)^K \right) f(t) \quad (1.1)$$

Where $f(t)$ is a periodic function of time with respect to the cardiac cycle and K the degree of blunting, with $K=2$ indicating a parabolic profile. Tangelder *et al.* (1986) obtained the velocity profiles in small arterioles ($17 \mu\text{m} - 32 \mu\text{m}$) by tracking the platelets. The bluntness of the profiles was increased and K was measured to vary from 2.4 to 4 (Figure 1.3 (b)).

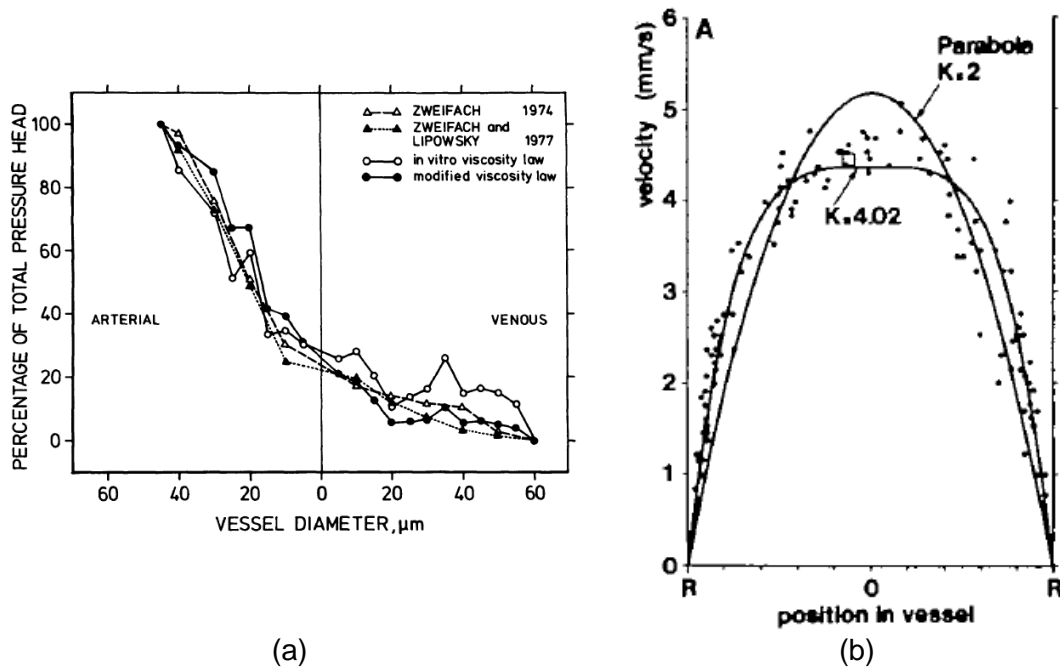


Figure 1.3: (a) Pressure drop as a function of vessel diameter measured in cat mesentery (Pries *et al.* 1990). (b) Velocity profile of blood platelets flowing in a $32 \mu\text{m}$ arteriole during systolic phase obtained with a μPIV technique. Two fittings were applied according to equation (1.1) with $K = 2$ (parabola) and $K = 4.02$ (Tangelder *et al.* 1986).

Venules have similar diameters with arterioles but their dimensions increase with blood direction, i.e. away from the capillary bed. The flow in venules larger than $\sim 25 \mu\text{m}$ can be described as two-phase and continuous like in arterial flow

(Cokelet, 1999) or as described by Long *et al.* (2004) a flow with a continuous variation of local haematocrit and shear-thinning behaviour in the core of the flow. Furthermore, due to the local haematocrit variations, different local viscosities exhibit across the flow leading to non-axisymmetric velocity profiles (Das *et al.*, 1997; Das *et al.*, 1998).

Table 1 shows some typical microcirculatory parameters both in *in vitro* and *in vivo* conditions as reported by Popel and Johnson (2005). The flow rates occurring in venules are lower compared to arterioles with similar diameters. Furthermore, the blood viscosity has been measured *in vivo* and *in vitro*. In both venules and arterioles, the measured *in vitro* viscosity has been found to be lower than the *in vivo* one even for a whole blood haematocrit slightly lower than that, 40% against 45% respectively. Lipowsky and Zweifach (1974) found that the apparent viscosity exhibits great increase in capillaries where the diameter reaches the size of the cell, as will be discussed later.

Table 1.2: Typical microcirculatory parameters as measured *in vivo* in cat sartorius muscle (Popel & Johnson 2005). *In vitro* viscosity was estimated by (Pries *et al.* 1996).

	Diameter (μm)	Mean velocity (mm/s)	Re	Pseudo- shear rate (s^{-1})	Wall shear stress (Dyn/cm^2)	<i>In vitro</i> viscosity at H=0.45 (cP)	<i>In vivo</i> viscosity at H=0.4 (cP)
Arterioles	15 60	7 12	0.03 0.2	200 470	60 140	1.8 2.6	2.8 4.9
Capillaries	5	0.2	$3 \cdot 10^{-4}$	40	12	1.8	15
Venules	18 72	0.2 2.4	0.001 0.05	10 30	3 10	1.9 2.7	4.2 2.9

1.4 Dynamics of microcirculation flows

In the microcirculation the Reynolds number hardly ever exceeds unity and most of the time it is much less than 0.1. The inertial effects in comparison to the effects of viscosity are considered negligible and the flow is laminar and in particular termed as creeping or Stokes flow. Stokes flow is described by the Stokes equation (1.2) and the continuity equation (1.3):

$$\rho \frac{\partial \mathbf{u}}{\partial t} + \rho \mathbf{u} \cdot \nabla \mathbf{u} = -\nabla p + \mu \nabla^2 \mathbf{u} \xrightarrow{\text{Re} \ll 1} \nabla p = \mu \nabla^2 \mathbf{u} \quad (1.2)$$

$$\frac{\partial \rho}{\partial t} + \nabla \cdot (\rho \mathbf{u}) = 0 \xrightarrow{\rho = \text{ct}} \nabla \cdot \mathbf{u} = 0 \quad (1.3)$$

where \mathbf{u} is the fluid velocity, p the fluid pressure, ρ the fluid density, and μ the fluid dynamic viscosity. The Stokes equation, is thus an approximation of the Navier-Stokes equations, representing the conservation of momentum, considering that inertial terms are neglected ($\text{Re} \ll 1$), while the continuity equation represents the conservation of mass. The flow assumed to be incompressible, with ρ , constant and for steady-state ($\frac{\partial}{\partial t} = 0$), i.e. the flow properties (velocity, pressure, cross-section) may differ spatially but not temporally.

A single rigid sphere in Stokes flow is expected to rotate and move along the streamlines without migrating across them. On the other hand, a liquid drop, a flexible sphere, or the RBC in this case, deform under the influence of the shear stresses acting on it and experience an inward migration acquiring a velocity

transverse to the flow away from the walls. This is known as shear induced migration and in the case of RBCs in microscale flows is the result of both deformability, flow curvature and wall effects. More specifically, the deformability of RBCs induces a migration away from solid boundaries as the pressure between the cell and the wall increases when the cell approaches the wall, pushing the cell away from it inducing a wall-lift force. In addition, the parabolic-like shape of the velocity profile produces a shear gradient that decreases towards the centreline. This results in a rotation of the cell with the side closer to the centreline to rotate in the direction of the flow. The radial migration velocity is higher near the wall and decreases as the deformable particle or RBC moves towards the centre of the tube (Figure 1.4) (Goldsmith, 1971; Leighton and Acrivos, 1987; Grandchamp *et al.*, 2013; Geislinger and Franke, 2014).

In dense suspensions, the effect of inward migration is counterbalanced by another phenomenon that occurs due to the cell-cell or particle-particle interactions. In blood flow, RBCs interact with each other and interactions become more frequent and intense with the increase of haematocrit. The interactions and collisions result in a net diffusion-like motion directed away from the cell concentration gradient, i.e. towards the wall. This cell-cell interaction effect, is termed shear-induced diffusion or dispersion, and opposes to the mechanisms that drive the migration towards the centre of the flow (Leighton and Acrivos, 1987; Secomb, 2017).

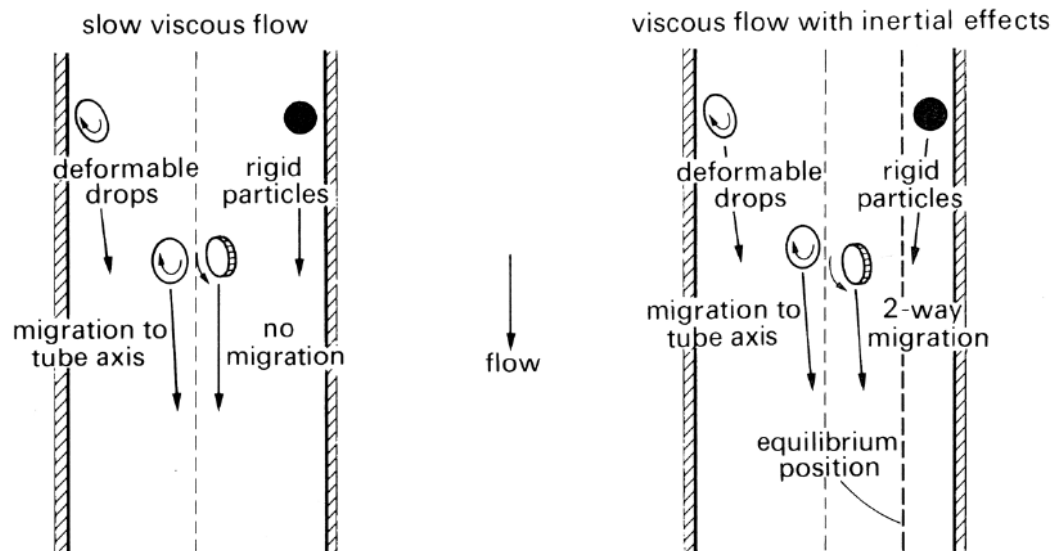


Figure 1.4: Representation of migration of rigid particles and deformable drops in dilute suspensions. On the left in Stokes flows (negligible inertial effects - $Re \ll 1$) and on the right in flows with inertial effects (Goldsmith, 1971).

The combined influence of wall effects, curvature of velocity profile and cell interactions during flow result in a non-uniform RBC distribution across the channel and the formation of a cell-free layer (CFL) or cell-depleted layer (CDL) near the vessel or channel walls. The concentration of RBCs is higher in the centre of the channel while gradually reduces towards the walls, meaning that the haematocrit of the RBC core is not constant and uniform. The width of the cell-depleted layer depends on the haematocrit, RBC deformability, vessel diameter, presence of aggregation and endothelial layer thickness (Alonso *et al.*, 1993; Pries *et al.*, 1994; Kim *et al.*, 2007).

The presence of the cell-depleted layer leads to uneven partition of RBC distributions in diverging bifurcations as the plasma, which is the main constituent of the CDL, skims on the bifurcated vessels (Figure 1.4). This effect is known as

plasma skimming and is mainly responsible for the large haematocrit variations throughout the microvasculature. When RBCs reach a bifurcation, they have the tendency to flow through the vessel with the higher flow ratio resulting in a disproportional distribution of haematocrit between the vessels.

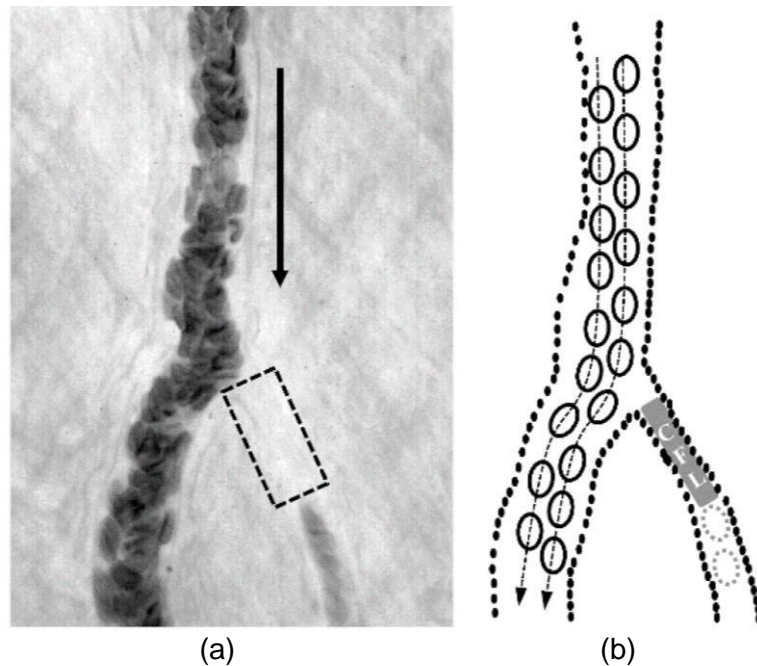


Figure 1.5: (a) Plasma skimming at an arteriolar bifurcation. The majority of RBCs continue to the large diameter vessel of the bifurcation and a disproportional number of RBCs perfuse the smaller vessel. (b) Corresponding schematic showing the flow trajectories of the RBCs which are directed towards the larger vessel of the bifurcation (Namgung *et al.*, 2016).

Fåhræous and Fåhræous – Lindqvist effects are phenomena related to the haematocrit non-uniform distribution. Fåhræous showed that the haematocrit decreases as blood flows through vessels with diameter less than $300\ \mu\text{m}$ (Fåhræus, 1929) and this phenomenon is known as Fåhræous effect. The migration of RBCs in the centre of flow produce higher average RBC velocities, U_{RBC} , compared to the average velocity of the whole blood, U_{blood} . Thus, the

amount of RBCs that will flow through a microvessel in a certain time would be higher than expected and in order for the discharge haematocrit, H_D , to remain equal with the feed haematocrit, H_F , the channel (or tube) haematocrit, H_C (or H_T) is reduced. The haematocrit ratio or relative haematocrit, H_R is defined as:

$$H_R = \frac{H_C}{H_F} = \frac{H_C}{H_D} = \frac{U_{\text{blood}}}{U_{\text{RBC}}} \quad (1.4)$$

A consequence of the haematocrit reduction in microvessels, is the reduction in the apparent viscosity. The decreased concentration of RBCs results in less viscous dissipation of the fluid and less frequent cell-cell and cell-wall interactions. In addition, RBCs achieve higher velocities which deform them to a greater extent leading them to align with flow and causing a further reduction of viscosity. The reduction of apparent viscosity with decreasing the channel diameter is known as Fahraeus-Lindqvist effect (Fåhræus and Lindqvist, 1931). The effect continues down to about 7 μm while in even smaller diameters a steep increase of viscosity occurs (Figure 1.6a) as the single file flow of the RBCs in microcapillaries produce narrow cell depleted layers and reduced plasma concentration. On the other hand, due to Fåhræus effect the haematocrit decreases for vessel diameters down to about 15 μm before starting to increase again (Figure 1.6b). Therefore, the critical vessel diameters for the Fåhræus–Lindqvist and the Fåhræus effect are different (7 μm versus 15 μm).

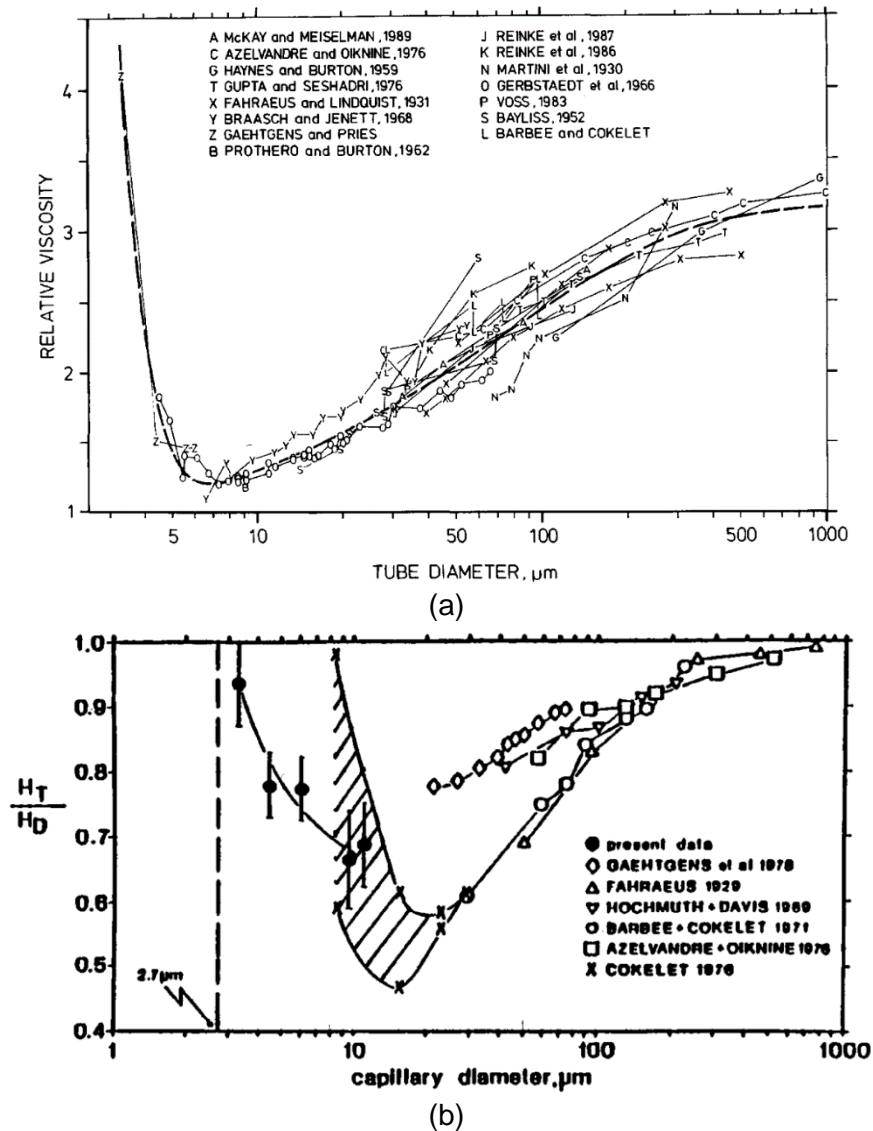


Figure 1.6: Compilation of studies showing: (a) the Fåhræus–Lindqvist effect; the relative viscosity versus tube (vessel) diameter at 45% feeding haematocrit (Pries et al., (1992) modified by Cokelet (1999)). (b) Fåhræus effect; the ratio of the average haematocrit of blood in a tube (H_T) divided by the discharge haematocrit (H_D), versus tube diameter (Gaehtgens 1980 modified by Cokelet (1999)).

Fåhræus and Fåhræus–Lindqvist effects describe the haematocrit and viscosity reduction respectively with decreasing diameter; for the general case of a parent branch bifurcating into two daughter branches there is a disproportional distribution of RBC volume fraction between the daughter branches with higher

and lower flow rate. This phenomenon is called Fåhræus for networks or bifurcation law or most commonly as Zweifach-Fung effect (Svanes and Zweifach, 1968; Fung, 1973). According to Fung (1973) an RBC in a flow bifurcation experiences an attraction towards the high flow rate branch due to the gradients of pressure and shear acting on it. As illustrated in Figure 1.7, the gradient of pressure is not axisymmetric (top right figure), pulling the RBC towards the left branch with the higher flow rate (larger pressure gradient). In addition, the shear force produced by the flowing plasma surrounding the RBC is higher towards the higher flow rate branch, dragging the cell towards the faster stream. However, in the more recent studies of Barber *et al.* (2008) and Doyeux *et al.* (2011) an opposing argument has been provided, suggesting that RBCs are attracted towards the branch with the lower flow rate. This has also been investigated *in silico* by Li *et al.*, (2012) showing that malaria-infected stiff RBCs have a tendency to travel into the low flowrate daughter branch because of their different initial distribution in the parent channel.

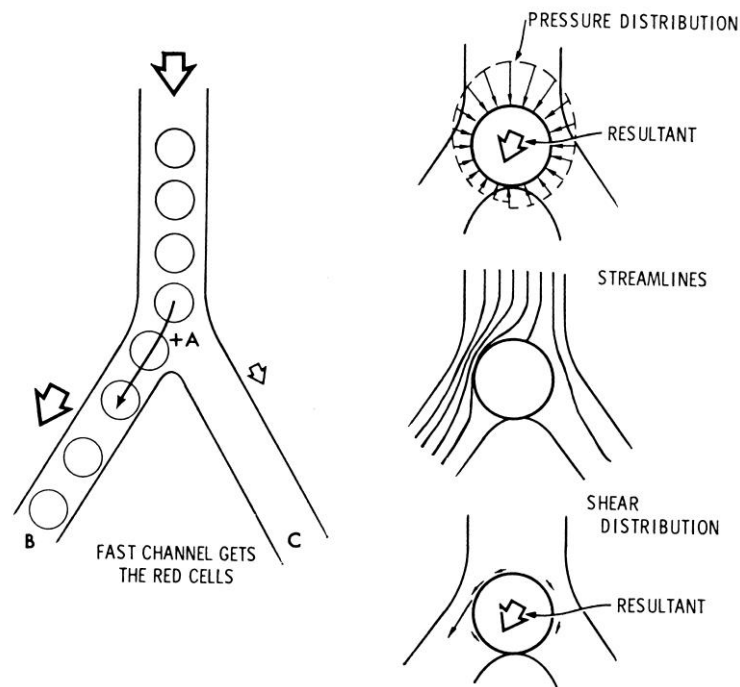


Figure 1.7: Schematic of an RBC following the branch with higher flow rate. The figures on the right show that the distribution of the pressure forces (top) and shear stress (bottom) both point to the faster stream (Fung, 1973).

The mechanical phenomena and dynamics associated with red blood cells flowing in the microcirculation are illustrated by Secomb (2017) in the schematic of Figure 1.8.

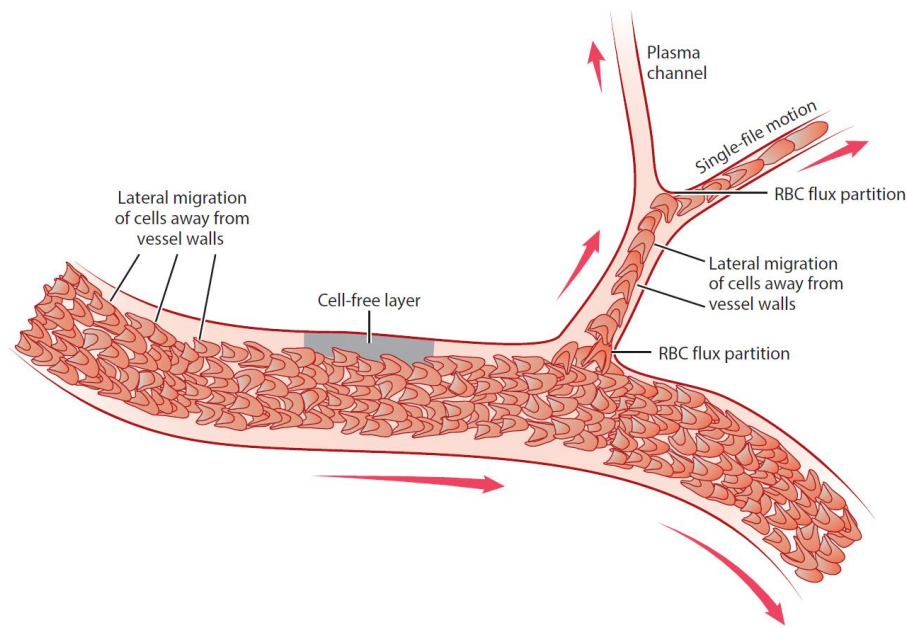


Figure 1.8: A schematic illustration of the dynamics and multiple effects present in the microcirculation (Secomb, 2017).

RBCs exhibit strong deformation in the microcirculation due to flow and geometrical constraints. Due to their high membrane deformability and in microvessels with diameters less than $20\text{ }\mu\text{m}$ (Skalak and Branemark, 1969), RBCs attain different shapes with the most common being the ‘parachute’ and ‘slipper’ shapes (Gaehtgens *et al.*, 1980; Abkarian *et al.*, 2008; Stone *et al.*, 2009) (Figure 1.9a). The transition from the discocyte shape to parachute-like or slipper-like shapes occurs in low velocity regimes (speeds in mm/s) and it is dependent on both the velocity (Noguchi and Gompper, 2005; Kaoui *et al.*, 2009) (Figure 1.9b) and the position of the centre of mass of the cell relative to the centerline of the flow (Pozrikidis, 2005). Kaoui *et al.*, (2009) also pointed out that the shape transition causes a decrease in the velocity difference between the cell and the flow, which could potentially enhance the efficiency of blood flow.

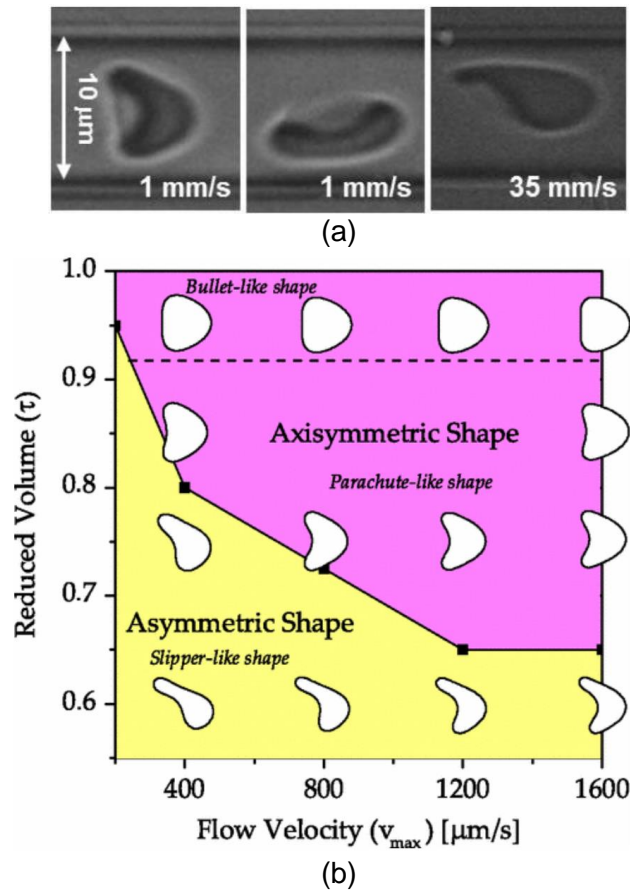


Figure 1.9: (a) *In vitro* RBC flow in 10 μm microchannels at different velocities (Tomaiuolo *et al.*, 2016). (b) Phase diagram of red blood cell shape as a function of the surrounding flow velocity and their reduced volume (τ). τ is described as ratio of RBC area to the area of a circle with a circumference equal to the perimeter of the cell; τ is equal to 1 when the RBC has a circular size. Image by Kaoui *et al.*, (2009).

In microvessels with diameters larger than 20 μm , RBCs retain their stress-free shape at low flow rates and exhibit different motion patterns. The three main motions that single RBCs exhibit are the (i) tumbling (TB), (ii) the tank-treading (TT) and (iii) the swinging motion which are described by the schematics in Figure 1.10. These motions are dependent on the shear rate, viscosity contrast between internal and external fluid viscosities, membrane viscoelasticity, confinement and

other parameters (Schmid-Schönbein and Wells, 1969; Abkarian et al., 2007; Skotheim and Secomb, 2007; Dupire et al., 2012; Kaoui et al., 2012). At low shear rates, RBCs perform the tumbling motion while at higher shear rates they switch to tank-treading and swinging motion. It has also been reported that the shear thinning nature of blood is caused mainly by the tumbling-to-tank-treading transition (TB-TT transition) rather than the cellular deformability as was previously believed (Forsyth *et al.*, 2011; Fischer and Korzeniewski, 2013). Moreover, Krüger *et al.* (2013) showed that the TB-TT transition can also occur at quite high volume fractions (up to 65% haematocrit), and is accompanied by orientational ordering of the cells. Skotheim and Secomb (2007) predicted that the TB-TT transition occurs at a shear rate of 1.3 s^{-1} . The shear thinning behaviour of blood has also been attributed to the presence of aggregation that is explained in the next section.

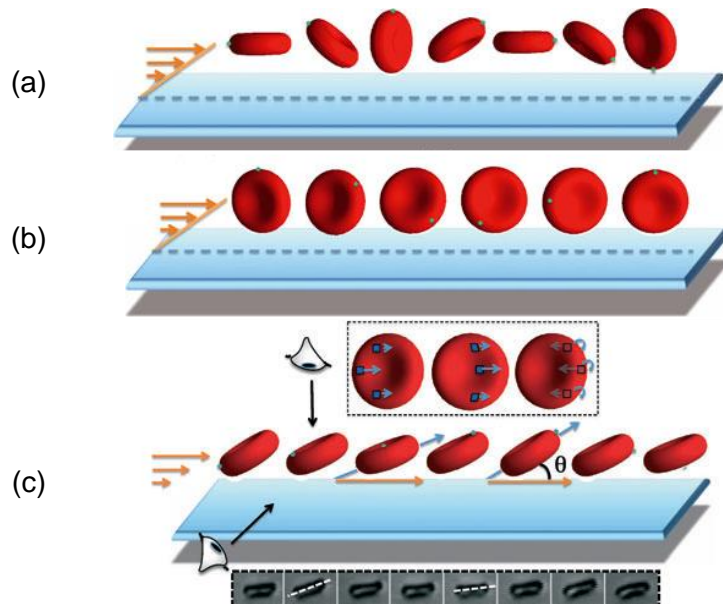


Figure 1.10: A schematic view of (a) tumbling (b) tank-treading and (c) swinging motions (Viallat and Abkarian, 2014).

1.5 RBC deformability

As mentioned earlier, the ability of RBCs to deform is key to their function of nutrient and waste transport as it allows them to flow through microvessels with dimensions comparable to or smaller than their size. Pathologies such as sickle cell anaemia, malaria, or diabetes are associated with both less deformable RBCs and microangiopathies, such as ischemia and vaso-occlusion (Kaul and Nagel, 1993). Decreased RBC deformability has been reported in malaria (Mohandas and Gallagher, 2008), sickle cell anaemia (Li *et al.*, 2016), and other metabolic inflammatory or vascular diseases such as diabetes, Alzheimer, and stroke (Tsukada *et al.*, 2001; Fornal *et al.*, 2006; Shin *et al.*, 2007; Agrawal *et al.*, 2016). In particular, studies of malaria diseased blood have a reported reduction of membrane deformability of red blood cells up to ten times (Mohandas & Gallagher 2008) while diabetes and sickle cell anaemia produce reduction in membrane deformability by a factor of three (Tsukada *et al.*, 2001; Brown *et al.*, 2005; Agrawal *et al.*, 2016; Moon *et al.*, 2016).

Various techniques have been used to measure RBC deformability, employing different RBC parameters. One of the first and most common method of measuring RBC deformability is micropipette aspiration. Red blood cells are aspirated with a micropipette, with smaller inner diameter (1-3 μm), while their viscoelastic and geometrical properties are monitored. The measured parameters vary, e.g. volume and surface area, (Linderkamp and Meiselman, 1982), shear elastic modulus (Evans, 1973), and surface viscosity (Meiselman,

Evans and Hochmuth, 1978; Hochmuth, Worthy and Evans, 1979). The size and shape of the pipette play an important role in the measurements and reliable comparisons can be made only by samples that have been measured with equal-sized pipette.

Optical tweezers is a commonly employed technique to characterise RBC deformability. Two tightly focused laser beams attached to diametrically opposite ends of the cell, work like optical traps that elongate and manipulate the cells obtaining a deformability index (DI) which is a correlation between the long and short axes of the stretched cell ($DI = L-W / L+W$, where L and W are the major and minor axes of the deformed cell). The maximum stretching is obtained exactly when the cell “escapes” from the trap and the main measurements are related to bending and elastic moduli (Hénon *et al.*, 1999; Lenormand *et al.*, 2001; Agrawal *et al.*, 2016). However, the applied force cannot be measured directly and the laser increases the temperature of the sample which may affect the measured cell membrane properties.

Atomic force microscopy (AFM) is a high resolution imaging technique that is widely used for the characterization of the mechanical, electrical and magnetic properties of cells (Bremmell, *et al.*, 2006; Wu *et al.*, 2009), the determination of the Young’s modulus (26 ± 7 KPa) of the cell membrane (Dulińska *et al.*, 2006) and the surface roughness (Girasole *et al.*, 2007; Buys *et al.*, 2013). A microscopic tip contacts or penetrates the cell’s membrane and relatively to the deflection of the cantilever, which is attached to the tip, the local value of the

Young's modulus can be determined through the force-distance curves and Hooke's law.

Several microfluidic techniques that characterize RBC deformability have been developed which can be classified according to the stimulus that is used to deform the cells. A classic approach of measuring and quantifying RBC deformability is perfusion of the cell through a geometrical constriction. This structure-induced deformation or flow can be performed either with a stenosis in a microchannel (Guo *et al.*, 2014; Tsai, Kaneko and Arai, 2014) or a filtration technique (Moia *et al.*, 1985; Tsukada *et al.*, 2001) or even perfusion through artificial microvascular networks (Shevkoplyas *et al.*, 2006; Sosa, Nielsen, Vignes, Chen and Shevkoplyas, 2014). Usually, the range of dimensions of the microchannels are comparable to RBC dimensions or even smaller in order for the cells to deform (2 μm - 50 μm). Moreover, the flow-induced deformation techniques are also popular and are based on the high deformability that RBCs exhibit under flow shear stresses. The most common geometries are converging microchannels (Lee *et al.* 2009; Forsyth *et al.* 2010; Yaginuma *et al.* 2013) or cross-slot junctions (Gossett *et al.* 2012) which generate extensional flows. The dimensions of the microchannels range between 15 μm and 200 μm and regions with increased shear stress are generated that deform the cells. In microfluidic deformability studies the most common parameters that determine RBC deformability are the transit time through the constriction, the elongation index ($EI = L/W$, where L and W are the length and width of the deformed cell respectively), the deformability index of the cell, as it was defined earlier, and the pressure drop variations. The elongation index is also employed by commercial devices such

as ektacytometers which measure the deformability of RBCs subject to either increasing shear stress or an osmotic gradient at a constant value of applied shear stress (Parrow *et al.*, 2018).

In studies examining the effect of RBC deformability on haemodynamics, artificially stiffened RBCs are often used in order to provide a controlled and safe environment to validate the sensitivity of the techniques and extract important conclusions about the effects of membrane stiffening on RBC functionality before studying diseased blood. A detailed description of the methods that are used to artificially harden the RBCs follows in section 1.7 and reported *in vitro* studies utilising such cells in section 1.8.

1.6 RBC aggregation

Aggregation of red blood cells is a physiological phenomenon where the cells stack into denser structures by clumping their wide surface with each other forming rouleaux or as they often called ‘coin-like’ structures. The mechanism of aggregation is mostly associated with the plasma protein, fibrinogen, as when it is in high concentration aggregation is enhanced (Ben-Ami *et al.*, 2003; Falcó *et al.*, 2005; Brust *et al.*, 2015). In *in vitro* experiments, the most common way to induce aggregation is with the use of a high molecular weight Dextran (a polysaccharide). The mechanism of aggregation is described by two different models: the bridging model and the depletion model. The bridging model was the first approach to describe the aggregation mechanism and suggests that macromolecules that act as a bridge, accumulate on the RBCs surface binding them together (Chien and Jan, 1973; Maeda and Shiga, 1985) (Figure 1.11). On

the contrary, the depletion model suggests that low concentration of macromolecules on the RBCs surface, generates an osmotic pressure gradient forcing the fluid within the cells to skim away, generating an attractive force between the cells (Neu and Meiselman, 2002; Meiselman, 2009). These theories seem to have contradictory principles but Bronkhorst et al. (1997) suggested that both mechanisms might be active in a way that depletion mechanism brings the cells close enough for the macromolecules to be linked according to the bridging model. It has also been suggested that the mechanism of aggregation is a result of a three-way interaction among fibrinogen, albumin and immunoglobulin (Ig) that synergistically induce RBC aggregation (Ben-Ami *et al.*, 2003).

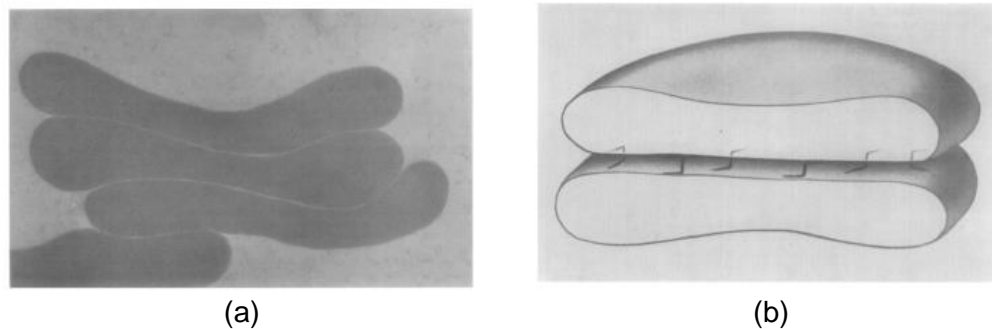


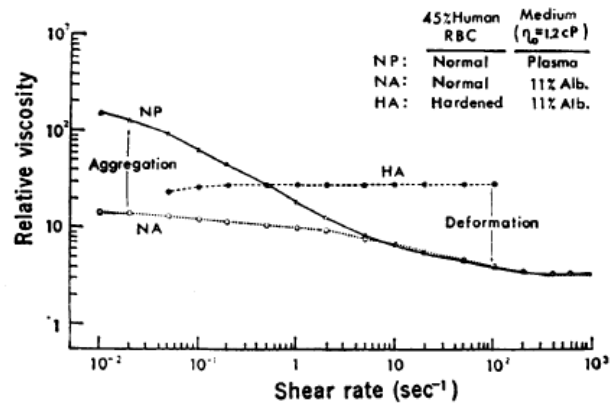
Figure 1.11: (a) Transmission electron micrograph of RBC rouleaux formation (b) Schematic of RBC aggregation by macromolecular bridging (Chien and Jan, 1973).

The effect of aggregation on haemodynamics has been extensively studied both *in vivo* and *in vitro*. Chien (1970) reported with viscometer experiments the effect of aggregation on the shear-thinning behaviour of blood as in low shear rates aggregated RBC suspensions showed a 75% increase of relative viscosity and hardened RBCs a 25% increased viscosity at higher shear rates (Figure 1.12a); it was also noticed that the viscosity of hardened RBCs exhibited no shear dependent behaviour. In a more recent study, Lanotte *et al.* (2016) confirmed the

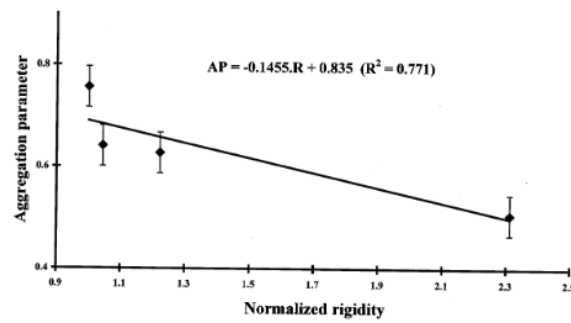
Newtonian behaviour of hardened RBCs and provided further evidence that RBC deformability as well as changes in RBC dynamic morphologies and motion during shearing, account for the shear thinning blood behaviour in microcirculation. The extent of aggregation was also found to be decreasing with RBC hardening (Maeda *et al.*, 1983; Jovtchev *et al.*, 2000). This was attributed to the physical difficulty of adhesion between the hardened RBCs (Figure 1.12b). Kaliviotis *et al.* (2017) investigated the relationship between aggregate size and flow partitioning in a bifurcation showing that larger aggregates follow the higher flow branch and small ones have the tendency to follow the branches with lower flow ratio which is counterintuitive on the basis of the low shear occurrence of aggregation. Sherwood *et al.* (2014) quantified the flow and haematocrit distributions of aggregated RBCs in straight and bifurcating geometries, correlating the bluntness of the velocity and haematocrit profiles and demonstrating the heterogeneity of the flow therein. Cokelet and Goldsmith (1991) also found that flow resistance, which is associated with relative viscosity, increases with decreased shear rates and the presence of aggregation. *In vivo* experiments by Bishop *et al.* (2001) examined the effect of aggregation on the velocity distribution and showed that in low flow rates, when aggregation is present, the velocity profiles become blunter than the non-aggregated cases as seen in Figure 1.12c.

The extent of aggregation or ‘aggregability’ is attributed to intrinsic and extrinsic factors. The intrinsic factors include the cell type, age, membrane deformability (Kim *et al.*, 2009). The extrinsic factors are considered the shear, haematocrit level (Schmid-Schönbein, Volger and Klose, 1972), temperature (Schmid-

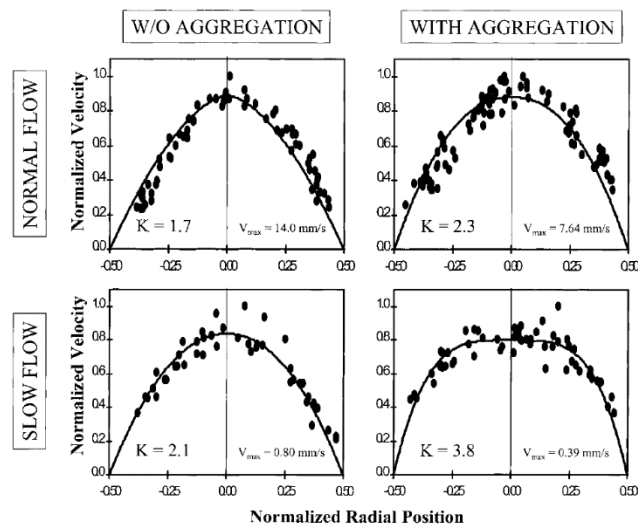
Schönbein, Volger and Klose, 1972), fibrinogen concentration (Falcó *et al.*, 2005) and aggregating agents concentration, like Dextran (Chien & Jan 1973).



(a)



(b)



(c)

Figure 1.12: (a) Viscoelastic behaviour of 45% RBC suspensions hardened and with and without aggregation (Chien 1970). (b) Correlation between aggregation parameter (zeta-sedimentation technique) and normalised rigidity (ratio of relaxation times). $H_t = 0.40$ and

0-4 g/dl concentrations of Dextran 70 (Jovtchev et al. 2000). (c) Normalised velocity profiles at normal and low flow rates of aggregated (Dextran 500) and non-aggregated blood suspensions perfused into a rat muscle vessel of $\sim 55\ \mu\text{m}$ diameter (Bishop et al. 2001).

However, *in vivo* studies have shown contradictory results regarding the impact of aggregation on the viscosity and flow resistance; although several studies agree with Bishop *et al.* (2001) i.e. that aggregation increases flow resistance, a number of studies has shown that flow resistance decreased with aggregation (Charansonney *et al.*, 1993; Baskurt *et al.*, 1999) or even no viscosity dependence with aggregation and flow rate (Gustafsson et al. 1981).

Although, aggregation is considered a physiological phenomenon, under pathological conditions enhanced aggregation has been reported. In sickle cell anaemia (SCA) the plasma protein, fibrinogen, associated with aggregation is increased leading to non-physiological aggregation levels (Barabino *et al.*, 2010). It has also been shown that the force required to disrupt aggregates of sickled RBCs is around four times greater than that in the healthy RBCs (Lemonne *et al.*, 2012). Additionally, in diabetic blood, Babu and Singh (2004) found increased RBC aggregation and decreased cell deformability. It is not clear how aggregation is associated with various pathologies and disorders. Both aggregation and reduced RBC deformability, increase apparent viscosity of blood which can have implications to physiological blood flow. Further study is needed to develop a more evidenced knowledge about the effect of aggregation and deformability in blood flow.

1.7 RBC hardening

Different ways are used to harden the membrane of the cells which can be classified in stiffening with the use of chemical compounds or stiffening with more natural procedures like heating or ageing. The most common chemical compounds that are used in literature for membrane stiffening are glutaraldehyde and diamide. Glutaraldehyde is an organic compound used mainly in medical and dental equipment sterilisation. As a strong sterilant, it is toxic and irritant which impacts on the RBCs by changing their membrane stiffness by crosslinking the membrane proteins of the cell (Kawahara *et al.*, 1997). Additional effects on RBCs have also been reported such as a suspension viscosity increase (Chien, 1970) , increase of the surface negative charge (Vassar *et al.*, 1972), density increase (Tong and Caldwell, 1995) and diameter decrease (Goldsmith and Marlow, 1972). The amount of glutaraldehyde that is needed depends on the haematocrit level but in general small doses are used, less than 0.1%, to the final solution (Fujiwara *et al.*, 2009; Forsyth *et al.*, 2010; Rodrigues R *et al.*, 2013; Guo *et al.*, 2014; Sosa *et al.*, 2014; Abay, Simionato, *et al.*, 2019).

Diamide is also used often in the literature for RBC membrane stiffening. Diamide treatment results in dose-dependent decreases of elongation and relaxation time. As with glutaraldehyde, diamide is also used in very small doses to the final solution that do not exceed 0.1% (Artmann, 1995; Forsyth *et al.*, 2010; Sosa *et al.*, 2014). However, there is contradictory evidence in the literature regarding the ability of diamide to reduce deformation of the RBC membrane (Forsyth *et al.* 2010).

More natural procedures of membrane stiffening without the use of chemical substances are also used like for example thermal treatment of the cells. Heating of the RBCs in order to change their properties is a method that was developed over a century ago (Schultze, 1865). In elevated temperatures (above 37 °C) the RBCs change their morphological characteristics and their oval biconcave disc shape changes to a spherical one with small spicules (echinocytes). Also, it has been found that membrane rigidity occurs due to a partial denaturation of the membrane proteins. Other changes can also be induced like increased osmotic and mechanical fragility, increased resistance to packing and increased viscosity (Baar and Arrowsmith, 1970; Tong and Caldwell, 1995). Aging-storing RBCs is also reported to affect deformability (Celle, 1969) and morphological changes as they progressively change their shape to a sphere-like shape due to osmotic effects, is related to the decreased deformability characteristics (Park *et al.*, 2016).

An alternative method to change the deformability of the RBCs is to tune the viscosity contrast between the haemoglobin and the suspending medium. Shen *et al.* (2015) used suspending media with different viscosities (1.94 mPas and 23.4 mPas at 20 °C) compared to the viscosity of the internal haemoglobin of healthy RBCs which is around 20 mPas, producing viscosity ratios of 10.3 and 0.85. Moreover, *in silico* studies showed that changing the internal-external viscosity ratio can trigger the transition from tank-treading to tumbling motion (Kaoui *et al.*, 2012)

In the present study, glutaraldehyde (GA) was employed to artificially harden the RBCs. In literature, many different protocols have been followed for hardening the cells using glutaraldehyde. The variations between the protocols lie in the blood sample preparation (e.g. RBC separation techniques, suspending media etc.), the GA introduction to the blood samples, the incubation time, the concentration of GA, and the measuring time after GA treatment. Table 1.3 summarises the different methods and protocols from literature on GA induced RBC hardening. In most of the studies, RBCs were separated from whole blood by centrifugation and then washed using phosphate buffer saline (PBS). The samples are treated with GA by incubation with GA concentration was typically ranging from 0.0005% to 8% depending on the application and the amount of hardening to be induced. After the incubation, in most cases RBCs are washed using PBS and resuspended in PBS before used for the experiments. In some cases, after washing and before resuspending in PBS, RBCs are incubated in PBS-BSA solution to prevent adhesion (Zheng et al., 2013). Measurements are conducted immediately after GA treatment but in many studies the samples have been used 3 hours later than fixation.

Table 1.3: Protocols of red blood cell hardening using Glutaraldehyde.

#	Article	Blood sample preparation (medium)	GA treated samples preparation (medium)	GA concentration	Incubation time	Measuring time after GA treatment
1	(Chien, 1970)	Normal RBCs in 11 per cent albumin-Ringer solution	Hardened RBC washed in 11 per cent albumin-Ringer solution	0.5%	-	-
2	(Morel et al., 1971)	75cc acid citrate dextrose (anticoagulant) in 500cc of blood. 3000g for 10min. No further washing	10 cc of aqueous glutaraldehyde solution to 10 cc of 600 mEq/L buffered saline	1% - 8%	-	Within 3 days from withdrawal, after shape assessment
3	(Vassar et al., 1972)	Washing, 1200g, 15min in saline, 3 times (21°C).	Fixation was performed in stoppered glass tubes rotated on a Fisher Roto-Rack at 21°C	1.65 g% and 3.3 g%	-	-
4	(Squier et al., 1976)	(Saline) and (PBS)	(PBS)	0.5% - 5%	2min to 2hours	2min to 2hours
5	(Bellelli et al., 1988)	Washed in physiological saline and resuspended in (PBS).	At room temperature the reaction was stopped by dilution with isotonic Tris-HCl buffer, followed by repeated washing of cells in PBS	2.5 to 5 mM	20 min	-
6	(Walter and Krob, 1989)	Washed 4 times with at least 10 times the cell volume of isotonic aqueous salt solution (saline)	RBCs were pipetted into 10 times their volume of a 280 mosM sodium phosphate buffer with GA%. The cells were again agitated at 30 min intervals for 3 hours (Sodium phosphate buffer)	0.1, 0.25 or 1.85% (w/v)	3 hours	-
7	(Tong and Caldwell, 1995)	RBCs were sedimented and washed three times in (PBS)	The supernatant of the red cell suspension was replaced by an equal volume of glutaraldehyde solution	0.001%, to 1%	2 hours	-

			buffered by PBS. After fixation the cells were washed with PBS			
8	(Szwarcrock et al., 2001)	600×g for 10 min. Three times in (PBS)	Room temperature (PBS)	0.0005 to 0.035%	20 min	-
9	(Baskurt et al., 2004)	In vivo measurements	-	0.0005–0.002%		-
10	(Faivre et al., 2006)	RBCs washed twice in PBS	The cells were treated with a solution of glutaraldehyde 1% v/v while being agitated for ten minutes. Washed in PBS and dispersed in dextran solution	1% v/v	10 min	-
11	(Cabrales, 2007)	Hamster blood: washed 3 times by centrifugation in PBS	Incubated in room temperature in 0.01 M (PBS). Washed 3 times in PBS and re-suspended in PBS with human serum albumin	0.02%	30 min	-
12	(Mohandas and Gallagher, 2008)	PBS containing 0.1% bovine serum albumin	by infusing glutaraldehyde in PBS into the observation chamber in four steps of increasing concentration up to 1% at intervals of 1 min. After a further 10 min, excess reagent flushed out with PBS.	Up to 1%	10 min	-
13	(Forsyth et al., 2010)	3000 RPM for 3 min - room temperature - washed three times (PSS)	-	0.05% v/v	20 min	used immediately in experiments
14	(Katsumoto et al., 2010)	Blood was suspended in PBS, centrifuged for 10 min at 2000g. then suspended in PBS with 8 wt.% (PVP)	RBCs were suspended in PBS-GA solution at room temperature. then RBCs were washed twice. Then suspended in PBS solution with 8%wt (PVP)	0.025% wt	30 min	within 3h after the preparation

15	(Rodriguez R <i>et al.</i> , 2013)	2000 RPM - 15min - room temperature – then washed twice in (PSS) 0.9%	After incubation were washed with (PSS) 0.9% and re-suspended in Dextran 40	0.04% or 0.08%	10 min	used immediately in experiments
16	(Zheng <i>et al.</i> , 2013)	Whole blood samples were anticoagulated with EDTA anticoagulant and washed twice with (PBS) before further treatment	Incubated into PBS-GA at room temperature. then washed three times with (PBS) and suspended in PBS with 1% BSA and incubated for 30 min to prevent adhesion	0.005%	30 min	-
17	(Sosa <i>et al.</i> , 2014)	800xg for 5 minutes - 22°C (PBS)	Incubated in GA-PBS – reaction quenched with (GASP) and washed in GASP 800x2, 2min	0.02% - 0.08% w/v	10 min	-
18	(Guo <i>et al.</i> , 2014)	washed in PBS by centrifugation 700g for 5 min	RBCs were incubated (25 °C) in 0–0.003% glutaraldehyde. After incubation, the RBC suspension was washed three times in PBS and resuspended in 0.2% Pluronic F-127 in PBS	0–0.003%	30 min	Microfluidic analysis was performed immediately
19	(Lanotte <i>et al.</i> , 2016)	1,000 × g for 20 min twice (PBS) and resuspended in PBS-BSA solution (1mg/1ml)	GA added during shearing. Then washed and suspended in (PBS) solution	3%	2 min	-
20	(Abay <i>et al.</i> , 2019)	EDTA (1.6 mg/ml), centrifugation, 1500g for 5 min, 3 times (PBS)	The solutions were incubated in GA and washed with (PBS) three times	0.1%	1 hour	-
21	(Iss <i>et al.</i> , 2019)	Pinprick (30µL). Washed three times in (DPBS-G) 500xg for 3 min.	RBCs were diluted in (DPBS-G) supplemented with 0.1% GA. Incubated for at least 15 min in 4 °C. Washed 3 times before resuspension	0.1%	15 min	Immediate use

1.8 Microfluidic studies with hardened RBCs

Various *in vitro* studies have examined the effect of RBC reduced deformability on haemodynamics mostly by investigating dilute RBC suspensions or single RBCs. The deformability of impaired RBCs has been measured with microfluidics by Guo *et al.* (2014) who quantified the cortical tension of RBC membrane by perfusing healthy and GA hardened single RBCs through a microscale funnel constriction measuring the transit critical pressure. Significant differences were observed between healthy and hardened RBCs as well as, inter-donor and intra-donor variations in RBC deformability. Amirouche *et al.* (2020) correlated RBC deformability with shape recovery time and deformation index as biomarkers to distinguish malaria infected RBCs (*Plasmodium falciparum*) from healthy ones. The shape recovery time of diseased RBCs was estimated to exhibit a significant decrease (less than the half) while the measured deformation index (DI) revealed that the hardened RBCs elongate roughly 1.6 times less than the healthy RBCs (Figure 1.13a). Shevkoplyas *et al.* (2006) fabricated an artificial microfluidic network as a tool for evaluating the impact of impaired deformability of RBCs on blood flow. They observed the perfusion of that network with hardened RBCs produced intermittent flow as the capillary microchannels were occasionally blocked by the non-deformable RBCs. It was shown, by perfusing RBCs with a different range of membrane deformability, that the artificial network exhibited higher sensitivity to changes of RBC deformability than conventional filtration assays (Figure 1.13b). In addition a few studies investigated the margination of hardened RBCs; Chen *et al.* (2017) investigated the margination of dilute GA

hardened RBC suspension while flowing within healthy RBC. This study consisted of both *in vitro* and *in vivo* experiments and elucidated the role of vessel geometry on margination by determining the hardened RBC distributions. Czaja *et al.* (2020) investigated the influence of RBC deformability on platelet margination. Mixed suspensions of healthy and hardened RBCs showed that the heterogeneous RBC collisions increase the margination of the hardened RBCs, resulting in reduced platelet margination. In the same study, the simulations showed that healthy RBC pairs exhibit higher displacement after a collision compared to hardened ones. Other group of studies investigated the shear induce migration of hardened RBCs and their distribution in flow. Tatsumi *et al.*, (2019) investigated the concentration distribution of GA hardened RBCs in straight microchannels analysing the effect of deformability on RBC migration and cell-cell collisions, showing that the hardened RBCs were concentrated at the near-wall region. Losserand *et al.*, (2019) examined the role of RBC deformability to the shear induced migration by comparing the lateral displacement of dilute suspensions of healthy and GA hardened RBCs; the GA hardened cells showed a decreased lateral displacement indicating that deformability is an important parameter in migration dynamics. Faivre *et al.* (2006) observed that dilute GA rigidified RBCs suspensions ($H < 3\%$) when perfused through a constriction, produced an enhanced cell-free layer width downstream of the constriction compared to the cell-free layer upstream of the constriction. Moreover this effect was less pronounced for healthy RBCs (Figure 1.13c). Iss *et al.* (2019) investigated the structural differences between healthy and hardened RBCs during flow by quantifying the self-organization phenomenon of the RBCs. The

dynamic structures of healthy and hardened RBCs were compared showing that the lack of deformability prevented the organization of RBCs in long structures (train-structures) in contrast to healthy ones (Figure 1.13d). Table 1.4 summarises the *in vitro* studies examining RBC deformability in microflow, providing further details on haematocrit concentrations, channel dimensions and geometries, hardening methods and the type of measurements performed.

Additionally, a number of *in silico* studies have investigated the role of deformability on microscale blood flow. For example, Fedosov *et al.* (2010) showed a reduction of the cell depletion layer and an up to 50% increase in blood flow resistance with increasing levels of parasitemia (percentage of malaria infected cells) in 45% haematocrit suspensions flowing in 10 μm vessels, attributed to impaired packing of stiffer RBCs. 2D simulations of RBC flows in a rectangular microchannel by Zhang *et al.* (2009) showed that less deformable RBCs were more dispersed resulting in thinner cell depletion layer (almost no cell depletion layer was evident) and higher relative viscosity. Increased dispersion resulting from the tumbling motion and random alignment of less deformable RBCs was also demonstrated by Bagchi *et al.* (2007) through 2D simulations. A reduction in the centreline velocity and the cell depletion layer with loss of deformability was also shown. Haan *et al.* (2018) found no change in haematocrit distribution for RBC suspensions with a change in viscosity contrast – typically used to tune deformability and RBC dynamics – between cells and suspending medium.

Despite the various *in vitro* studies in the literature dealing with impaired RBC deformability the impact of impaired RBC suspensions on microhemodynamics, and in particular velocity and haematocrit distributions, has not been systematically investigated. The present thesis aims to elucidate the role of RBC impaired deformability on microscale haemodynamics by providing extensive experimental results on velocity and haematocrit distributions for dense RBC suspensions with different deformability, at various flow rates, in the presence and absence of aggregation, in straight and bifurcating flows.

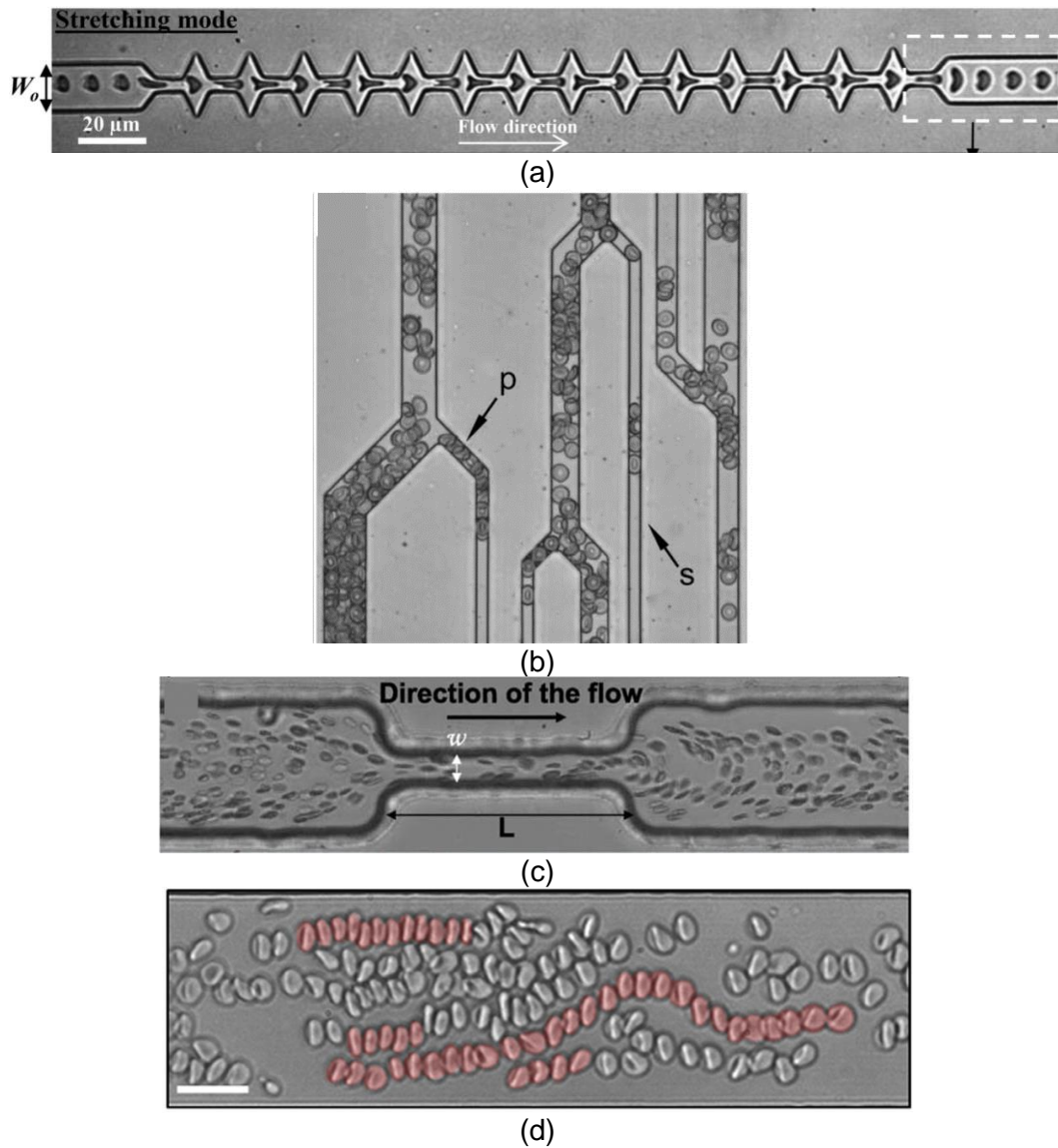


Figure 1.13: (a) Time lapse of cells entering the tooth-shaped microfluidic channel measuring the deformation index (Amirouche *et al.* 2020). (b) Typical blood flow patterns within the microfluidic network. Smallest microchannels shown are 6 μm wide; s: silent capillary (receiving only plasma in the case of untreated RBCs), p: plugged capillary (Shevkoplyas *et al.* 2006). (c) Top view of the microfluidic setup for the flow of red blood cells through a constriction. Height of the microchannel is 75 μm , $L = 200 \mu\text{m}$ and $w = 25 \mu\text{m}$ (Faivre *et al.* 2006). (d) Trains of red blood cells (highlighted in red) in the RBC flow. Scale bars: 20 μm (Iss *et al.*, 2019).

Table 1.4: Summary of recent *in vitro* microfluidic studies investigating the effect of RBC deformability on haemodynamics and blood properties.

	Hct	Channel Dimensions (wxh) μm^2	Method of hardening	Measurement	Geometry	Type
Faivre et al. 2006	<3%	(25-200) x 75	GA (1%)	CFL after a constriction	constriction	<i>In vitro</i>
Shevkoplyas 2006	40%/1%	(6-70) x 6, 5x5	GA (0-0.1%/0-1%)	RBC velocity/ filtration time	Microfluidic network/ 2D filter	<i>In vitro</i>
Guo et al. 2014	Single RBCs	(2-200) x (2.5 - 3.5)	GA (0-0.003%)	RBC membrane cortical tension	Micro funnel	<i>In vitro</i>
Chen et al. 2017	0.3% of hardened in healthy RBCs (v/v)	100 x 40	Diamide (200 μM)	Cell tracking, hardened RBC distribution	Rectangular, triangular, circular	<i>In vitro</i> , <i>In vivo</i> , <i>In silico</i>
Tatsumi et al. 2019	9-16%	(28 x 27)	GA (0.025%)	Haematocrit distribution	Straight channel	<i>In vitro</i> , <i>In silico</i>
Iss et al. 2019	1-18%	(30,60) x 9	GA (0.1%)	Length of train structures, Lateral position of RBCs	Straight channel	<i>In vitro</i> , <i>In silico</i>
Losserand et al. 2019	0.1%	(8-54) x (10-20)	GA (>0.1%)	Lateral displacement	Straight long channel	<i>In vitro</i>
Czaja et al. 2020	30%	5000 x 100	TBHP (0.5-1.0 mM)	CFL width, platelet margination, cell displacement after collision	Straight channel	<i>In vitro</i> , <i>In silico</i>
Amirouche et al. 2020	Single RBCs	(5-25) x 5	Malaria diseased RBCs	Deformation index, recovery time	Tooth-like shaped channel	<i>In vitro</i>

1.9 Aims and objectives

RBC deformability is key to their physiological function and membrane stiffening has been associated with various pathologies and disorders. The aim of the present study is to improve the understanding of the role of RBC deformability on microscale haemodynamics by employing microfluidics and artificially hardened RBCs. In order to achieve the aforementioned aims the following objectives were defined:

1. Quantify microscale blood flows by determining the velocity field and haematocrit distribution in straight microchannels at physiological feed haematocrits and flow rates.
2. Investigate the impact of RBC deformability and haematocrit on the velocity and haematocrit distributions.
3. Explore the impact of microchannel aspect ratio on the flow properties for healthy and hardened RBCs.
4. Analyse the behaviour of hardened RBCs suspended within healthy RBC suspensions (margination effect).
5. Examine the effect of aggregation on hardened RBCs for a range of flow rates.
6. Study the impact of RBC deformability on velocity and haematocrit distributions as well as the plasma skimming effect downstream of a T-junction bifurcation.

The work investigates and evaluates the flow properties of impaired hardened RBCs, compared to healthy ones, that can be used as biomarkers for diagnostic

purposes. Moreover, this work provides experimental data and results that improve our fundamental understanding on cell hydrodynamic interactions, an area of considerable interest in the soft matter community.

1.10 Structure of the thesis

The remaining thesis is structured as follows:

In Chapter 2 the methodologies that were utilised are described. In particular, the experimental set up and procedures are detailed including blood collection and treatment, the fabrication of microchannels and the acquisition methods. A detailed description of the processing of the acquired data is given: image processing, PIV processing, extraction of the velocity and haematocrit profiles, statistical analysis of the results and a discussion on the experimental systematic errors.

Chapter 3 reports experimental RBC velocity and haematocrit distributions for four different RBC suspensions varying in deformability perfused through straight microchannels and for various flow rates and feed haematocrits.

In Chapter 4, two independent sets of experiments are presented examining (i) the distribution of a small concentration of hardened RBCs flowing within a dense suspension of healthy RBCs and (ii) the effect of channel aspect ratio on the measured velocity and haematocrit distributions. The first experiment investigated the exclusion effect of RBCs depending on deformability and the second experiment the effect of shear rate gradient on RBCs with different deformability.

Chapter 5 extends the study of Chapter 3, to examine the impact of RBC deformability on aggregation. In particular, aggregating and non-aggregating RBC samples with different deformability are compared in terms of velocity and haematocrit distribution across the flow and the extent of aggregation intensity is evaluated in each case.

Chapter 6 extends the study to more complex, bifurcating flows of RBC suspensions. Results for healthy and hardened RBCs perfused through a T-junction in the presence or absence of aggregation are presented investigating (i) the effect of flow ratio and (ii) the effect of parent branch flow rate on velocity and haematocrit distributions upstream and downstream of the bifurcation. The effect of deformability on the plasma skimming effect is examined for different flow ratios.

Chapter 2

Experimental Methods

The experimental procedures described in this chapter were conducted in a class 9 clean room providing a 'dust free' environment that was required for certain microfluidic experiments. The protocols that were followed regarding blood collection, treatment, hardening and labelling, and the fabrication methods of the microchannels employed are described. Moreover, a detailed explanation of the experimental set up is given, consisting of the pneumatic perfusion system, the data acquisition and the PIV processing. The image processing methodology that was applied to enhance the quality of acquired data is given. The methods employed for analysing the data, such as the calibration of image intensity to haematocrit method and the definitions of bluntness and skewness indices for both velocity and haematocrit profiles, are explained. Finally, the experimental systematic errors are discussed, such as the interdonor uncertainty in RBC deformability and PIV processing errors.

2.1 Blood sample preparation

Human blood was collected from healthy donors with ethical approval from South East London NHS Research Ethics Committee (Ref:10/H0804/21). The blood was collected into vacutainers (Beckton Dickinson, UK) preloaded with 1.8 mg/ml ethylenediaminetetraacetic acid (EDTA) to prevent coagulation. All RBC treatments and experiments took place in room temperature and were carried out within 5 hours from venepuncture.

2.1.1 Red blood cell separation

Fresh blood was drawn from four healthy donors by venepuncture and red blood cells were separated from whole blood via centrifugation at 500 G (3400 rpm) for 6 min in which plasma and buffy coat were aspirated. Then the RBCs were washed 3 more times with phosphate buffer saline (PBS – Gibco, pH 7.4) by centrifugation at 500 G for 9 min in order to ensure that plasma and the rest blood constituents were fully removed.

2.1.2 Artificially stiffening of RBCs

As mentioned in chapter 1, various methods can be employed to harden cells. Various levels of membrane stiffening were artificially introduced in the present study using Glutaraldehyde (GA) which has been extensively used in the literature and its effects on RBC deformability have been quantified in various studies. Two concentrations of GA were used, 0.04% and 0.08% v/v, which were selected based on the literature in order to obtain up to three times reduction of

RBC normalised deformability, which is reported to occur for example in type 2 diabetes (Brown *et al.*, 2005; Agrawal *et al.*, 2016; Moon *et al.*, 2016; Chang *et al.*, 2017). Figure 2.1a, shows the decrease of RBC deformability with GA treatment measured with 4 different techniques (ektacytometry 3 Pa and 17 Pa, micropore filtration and artificial microvascular network) (Sosa *et al.*, 2014) and Figure 2.1b by RBC perfusion through a microchannel with a hyperbolic contraction (Rodrigues *et al.*, 2013). In both cases a GA concentration of 0.08% is shown to result a threefold reduction in RBC deformability.

The fixation protocol that was used in this study was a combination from three different studies (Rodrigues *et al.*, 2013; Zheng *et al.*, 2013; Sosa, *et al.*, 2014) RBC suspensions with a concentration of 25% by volume (haematocrit) were incubated with selected GA concentrations for 12 min. The cross-linking reaction of glutaraldehyde was quenched by adding 1% v/v bovine serum albumin (BSA) in PBS, in a volume ratio of 5:1 to the initial RBC solution. After washing the RBCs twice with 1% v/v BSA-PBS and PBS respectively, the hardened RBCs samples were suspended in 1% v/v BSA-PBS solution for 30 minutes to prevent adhesion between RBCs following the fixation protocol by Zheng *et al.* (2013). The GA hardened RBCs were inspected under the microscope for any changes and found to retain their discoid shape. Moreover, the GA hardened RBCs, seem to retain their morphology during flow, compared to the more deformable healthy RBCs which tend to exhibit higher deformation during flow as seen in Figure 2.2a,b and d.

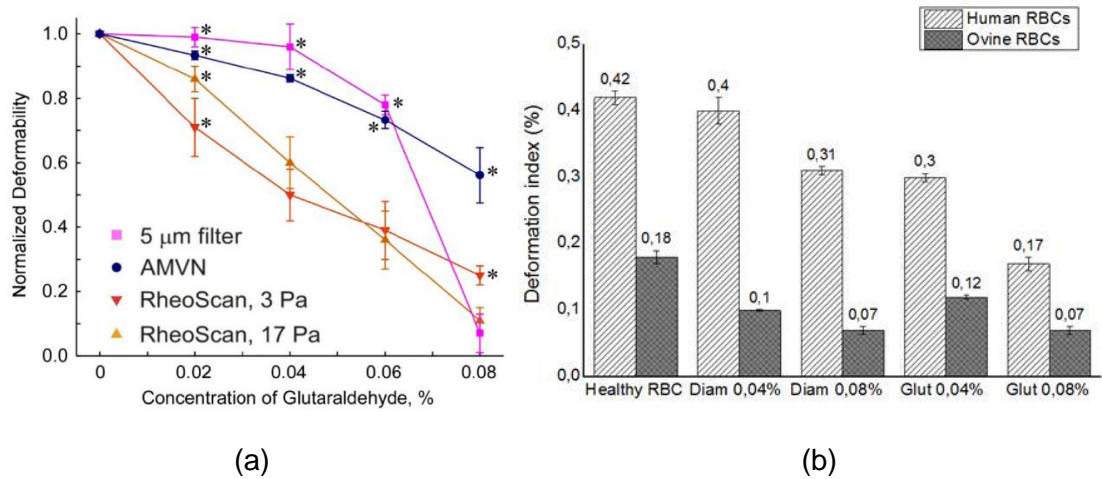


Figure 2.1: Reduction of RBC deformability obtained with glutaraldehyde and diamide treatment (a) Deformability measurement of glutaraldehyde fixed RBCs with different techniques (ektacytometry 3 Pa and 17 Pa, micropore filtration and artificial microvascular network) (Sosa et al. 2014) (b) Deformation index of healthy and fixed RBCs with diamide and glutaraldehyde (microfluidic hyperbolic contraction) (Rodrigues et al. 2013).

2.1.3 Aged RBCs

In addition to the artificially stiffened RBCs a sample of 7-days aged RBCs was prepared since aging is known to decrease RBC deformability (Celle, 1969). A healthy RBC sample was stored for one week in the fridge at 4 °prior to flow measurements. The size of the aged RBCs seems to be reduced and their morphology has changed to a rounder shape compared to the typical biconcave shape of normal RBCs (Figure 2.2d). Park *et al.* (2016) also observed notable alterations in morphology and deformability of stored RBCs. In particular, RBCs after day 5 of storage were shown to transform from discocytes to a spherical shape, possibly as a result of water efflux through their membrane.

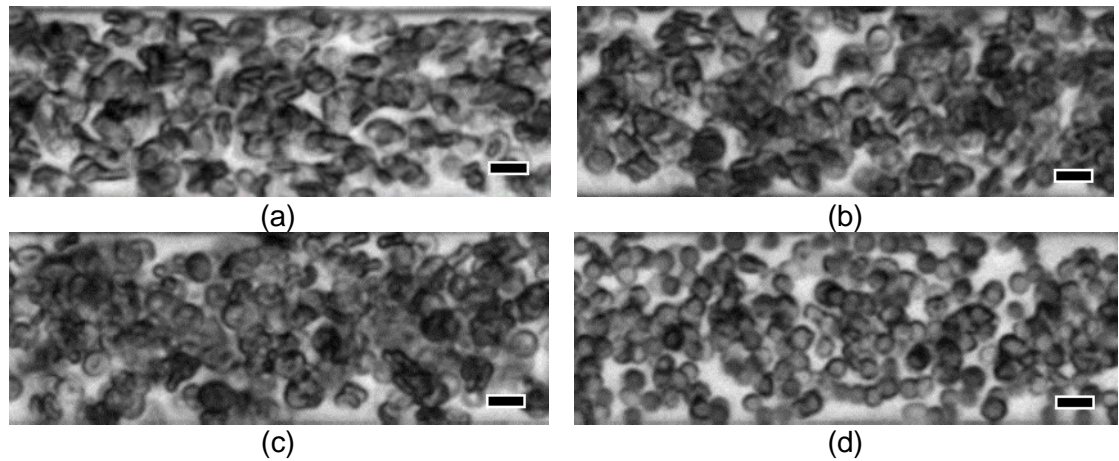


Figure 2.2: Sample images of 10% haematocrit samples in flow at 45 s^{-1} . (a) Healthy sample, (b) GA 0.04% fixed sample, (c) healthy aged sample, (d) GA 0.08% fixed sample. The scale bars correspond to $10 \mu\text{m}$ length.

2.1.4 Aggregating RBC samples

RBC aggregation was induced using a small quantity of Dextran 1500-2800 kDa (Sigma Aldrich, UK) for the test cases examining the effects of aggregation; this was done to ensure repeatability and minimise variation in aggregability of different donor samples. RBC samples were suspended in a PBS-Dextran solution with a Dextran concentration of 8 g/L . The concentration of Dextran was selected in order to change the viscosity of the suspending medium as little as possible while inducing an apparent level of aggregation (Sherwood *et al.*, 2014). The viscosity of PBS-Dextran solution (8 g/L) was measured at 1.49 mPas while the viscosity of PBS measured at 1.01 mPas in room temperature using a parallel plate rheometer (ARES).

2.1.5 Fluorescent labelling of RBCs for cell tracking

For the cell tracking experiments (described in Chapter 4), a small quantity of hardened RBCs were labelled using a PKH-26 Red Fluorescent Cell Linker (Sigma-Aldrich, UK) and following the manufacturer's instructions. In brief, 85 μ l of hardened RBCs were centrifuged and separated from the supernatant before suspended in 1 ml of Diluent C: an aqueous solution designed to maintain cell viability, while maximizing dye solubility and staining efficiency (Tario *et al.*, 2012). Then the suspension was added in 1ml of Diluent C mixed with 4 μ l of PKH-26 ethanolic dye solution (Van Amersfoort and Van Strijp, 1994). The cells were incubated for 5 min with periodic mixing, before terminating the staining process by adding an equal volume of 1% v/v BSA-PBS solution. Finally, the labelled RBCs were washed three more times with PBS to ensure the removal of unbound dye and re-suspended in the RBC samples under investigation at 1% concentration. The labelling was conducted after the hardening of RBCs.

2.2 Microchannels

Straight and T-shaped junction microchannels were fabricated for the current experiments. The microchannels were made of PDMS (Polydimethylsiloxane) polymer and fabricated using the soft lithography technique. A silicon wafer containing the negative microscale features of the microchannel geometries was used as the master mould (FlowJEM, US). The straight microchannels had a length of 16 mm and square and rectangular cross sectional areas of 50 x 50 μ m² and 100 x 25 μ m² respectively; the corresponding aspect ratios were 1:1 and 4:1

respectively. The T-shaped microchannels had a $50 \times 50 \mu\text{m}^2$ cross sectional area and were 16 mm in length.

Sylgard 184 (Sigma-Aldrich, UK) was used as prepolymer and mixed with a curing agent at 10:1 ratio. The polymer was degassed in a vacuum chamber to remove air bubbles before pouring it onto the silicon mould. The mould was baked at 65 °C overnight and then the PDMS was peeled off the silicon wafer. Inlet and outlet holes were created using a biopsy punch, before sealing the polymer chips by bonding them on glass slides using oxygen plasma treatment to both surfaces using a handheld corona (Electro-Technic Products Inc., BD20-AC). The PDMS-glass bonding process protocol that was followed is described in detail in Haubert *et al.*, (2006).

2.3 Experimental set up

2.3.1 Perfusion system and data acquisition

In the current study flow rates similar to the physiological flow rates in the microvasculature were used – expressed in terms of a normalised velocity ($U^* = \bar{U}/W$) similar to a nominal shear rate – 1 to 200 s^{-1} (Bishop *et al.*, 2001). The most common method to deliver microfluidic flows in literature is using a syringe pump; however, in the present experiments this was not a suitable option as the range of the flow rates employed was relatively low for most commercial syringe pumps. Syringe pumps induce flow oscillations generated by their stepper motor and these could reach up to 50% of the mean flow rate for the range of flow rates used in the present study. Thus, a custom made pneumatic pressure control

system was used to deliver the flow into the microchannels as described in detail by Sherwood (2013). The system is controlled by a LabVIEW interface (National Instruments, UK); it makes use of a nitrogen cylinder (BOC, UK) as the pressure source and a series of pressure valves and regulators to provide accurate pressure control. The pressure is monitored with a pressure transducer (Omega, UK: PX243A, Range ± 20 kPa) which is used as an input to the system control. The pressure range of the measurements was between 5 and 20 kPa and the system provided a stable pressure with a resolution of 10 Pa.

The controlled pressure was applied in the sealed inlet reservoir in which the RBC samples were placed. A magnetic stirrer was used to mix the sample in order to prevent sedimentation in the reservoir and keep the feeding haematocrit constant. Polyethylene tubing (SLS, UK) with 0.205 mm internal diameter was used to perfuse the RBC samples from the inlet reservoir to the microchannels. The length of the tubing was kept to a minimum of around 30 cm. The microchannel was placed on the stage of an inverted microscope (Leica: DM ILM, Germany) for imaging. A 10x air objective (NA = 0.25) was used, focusing in the midplane of the microchannel. Figure 2.3 shows a schematic of the experimental set up. In between the acquisition of data, a high pressure was applied, i.e. high flow rate, in order to redistribute and disaggregate the RBCs, and minimize any accumulated sedimentation effects in the microchannel. In order to acquire the data, the pressure was dropped to the target value and the data acquisition time was set to 10 sec. Within this time frame and the employed flow rate in the measurements, sedimentation can be considered negligible. Alonso *et al.* (1995) found negligible sedimentation over a period of 5 min in a 59 μ m deep

microchannel for the flow rates used in these experiments. The flow was illuminated using a green Light Emitting Diode (LED) microstrobe for the bright field imaging and a Nd:YAG laser (ESI: New Wave Solo, Germany) at 532 nm, for the cell tracking experiments of Chapter 4. The PKH-26 labelled RBCs (see 2.1.5) are excited at 551 nm and emit light at 567 nm. The emitted light passes through the microscope objective and through a dichroic mirror which filters the light at 610nm with a 75nm bandwidth allowing the fluorescent signal to pass through and collected by the camera. A high sensitivity CCD (charge-couple device) camera (Hamamatsu: C8484-05C, Japan) was used for imaging the flow in the microchannels. For the cell tracking of experiments of chapter 4 the images were acquired using both illumination modes in an alternate fashion: each round of acquisition included two pairs of images, with the same Δt , acquired with alternating the LED and laser light sources respectively. The acquisition timing was synchronised and controlled using an inhouse LabVIEW configuration.

The used pressure based perfusion system allows an accurate control of the pressure provided in the inlet reservoir; however, the flow rate value cannot be directly estimated during the experiments; instead they were calculated from the velocity flow fields measured using Particle Image Velocimetry (PIV) as described in the next section. Table 2.1 summarised all the cases studied in terms of RBC samples, feeding haematocrit and microchannel geometries used per chapter.

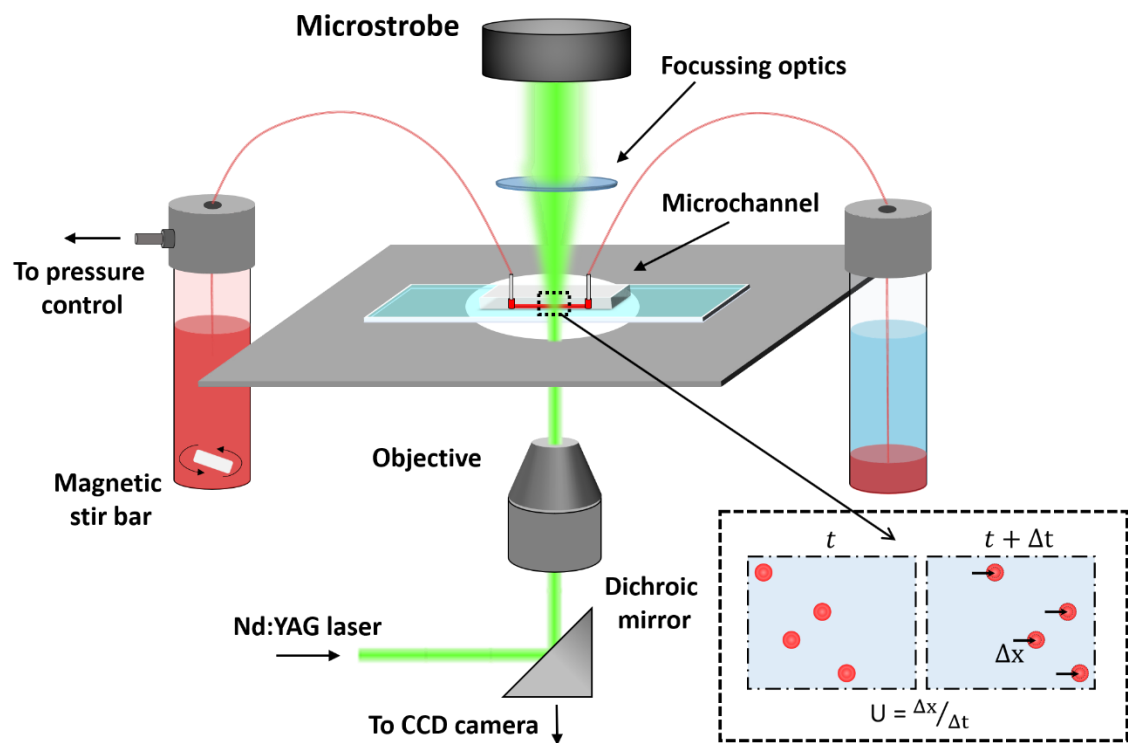


Figure 2.3: Schematic of the μ -PIV experimental set up for microscale blood flow imaging. Two sources of illumination are shown, the LED microstrobe was used for brightfield imaging and the laser illumination was used only for the cell tracking experiments in Chapter 4.

Table 2.1: Summary of the cases investigated in this thesis in terms of RBC samples, feeding haematocrit and used geometry. GA samples are the hardened samples with glutaraldehyde, the aggregating RBC samples are expressed as Dextran and non-aggregating as PBS.

Chapter	RBC samples	Feeding haematocrit	Geometry
3	Healthy-PBS GA 0.04%-PBS GA 0.08%-PBS Aged-PBS	5% 10% 25%	Straight 50 x 50 μm^2 (AR 1:1)
4	Healthy-PBS GA 0.08%-PBS Labelled RBCs	25%	Straight 50 x 50 μm^2 (AR 1:1) Straight 100 x 25 μm^2 (AR 4:1)
5	Healthy-PBS GA 0.04%-PBS GA 0.08%-PBS Healthy-Dextran GA 0.04%-Dextran GA 0.08%-Dextran	10% 25%	Straight 50 x 50 μm^2 (AR 1:1)
6	Healthy-PBS GA 0.08%-PBS Healthy-Dextran GA 0.08%-Dextran	25%	T-junction, 50 x 50 μm^2 (AR 1:1)

2.3.2 Particle Image Velocimetry (PIV) setup and processing

PIV is a common technique used in fluid dynamics for providing the velocity field of a flow. The basic principle entails capturing the displacement (Δx) of neutrally buoyant particles seeded in the flow within a predetermined time interval (Δt) and calculating their velocity (U) along the flow ($U = \Delta x / \Delta t$). The seeding-tracer particles are small enough to follow the streamlines and not affect the flow significantly. The standard method is to acquire consecutive images of the flow within equal time intervals and apply a space-time cross-correlation of the tracer particles in order to identify the most probable distance that the particles travelled

within each time interval. The images are separated into smaller regions called interrogation windows (IW) providing more accurate results and higher spatial resolution of the velocity field.

In the current experiments an alternative approach was applied that is often used in blood flows. The red blood cells were used as the tracer particles, considering that the aim of these experiments was to resolve the velocity field of the RBCs rather than that of the suspending medium. In this case the cross-correlation is based not on discrete images but rather in intensity changes of the images. In particular, 60 pairs of images ($1344 \times 1024 \text{ px}^2$ resolution) were acquired and the sampling rate was 6Hz meaning that the acquisition time was 10 sec. The time interval Δt between the image pairs was varied between 0.5 ms and 4 ms depending on the perfused flow rate. The images were acquired in the middle of the channel length, 8 mm downstream of the inlet and the focusing plane was at the middle region of the channel height, i.e. $25 \mu\text{m} \pm 2 \mu\text{m}$ and $12.5 \mu\text{m} \pm 2 \mu\text{m}$ away from the bottom of the channel for the $50 \mu\text{m}$ and $25 \mu\text{m}$ deep microchannels respectively.

The velocity field was obtained using multi-pass ensemble PIV cross-correlation algorithms (ensemble correlation) implemented in the open source JPIV platform (<https://eguvep.github.io/jpiv/>). Ensemble correlation was shown to increase the accuracy of the processing for a stack of 50 or more images by greatly reducing the number of invalid vectors (Vennemann *et al.*, 2006). Three passes with 50% overlap were utilised with interrogation windows of starting size of 32×16 pixel and 16×8 pixels (width x height) in the final pass. The IWs were chosen to be

rectangular with the larger dimension following the flow direction, hence the interrogation window width was approximately 80% larger than the largest diameter of a single RBC. For the 10x magnification used lens the image resolution corresponds to $0.60\ \mu\text{m}/\text{pixel}$ the spatial resolution of the velocity measurements was $2.4\ \mu\text{m}$ (4 pixels vector spacing based on IW height and 50% overlap). Due to diffraction, the pixels near the wall were omitted from the PIV processing as they generate erroneous vectors; hence, the first vector was located 10 pixels from the wall, i.e. $6\ \mu\text{m}$. For the more dilute RBC sample (5%), the first vectors considered were located $7.2\ \mu\text{m}$ away from the wall, in order to avoid PIV errors due to reduced RBC concentration near the wall. Figure 2.4 shows a typical vector field superimposed on a sample image. The coordinate system is also shown on the same figure. Normalised coordinates were used in the description of the acquired profiles with the width of the channel ranging from -0.5 to 0.5, $y^*=y/W$. For all data sets reported in the following chapters, the invalid vectors were less than 0.1% and were replaced by the median of the neighbouring vectors (Westerweel and Scarano, 2005).

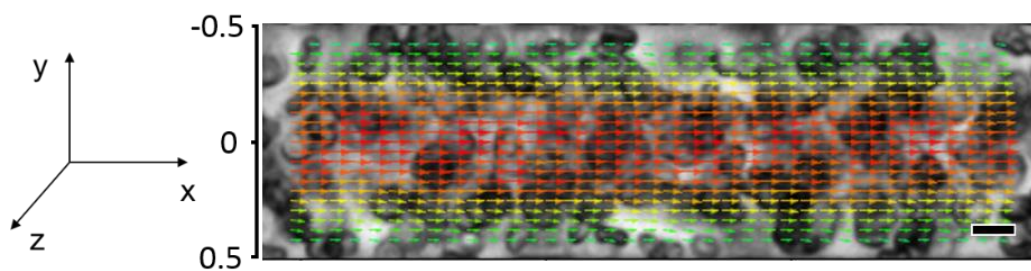


Figure 2.4: Sample vector plot obtained by PIV processing to pre-processed images. Multi-pass correlation methods were used with a vector spacing of $2.4\ \mu\text{m}$ (4 pixels). The first vector is positioned $7.2\ \mu\text{m}$ from the wall. Scale bar is $10\ \mu\text{m}$.

The PIV processing was first validated by conducting experiments with water as working fluid and 1 μm diameter rhodamine dyed polystyrene microspheres (Invitrogen, UK) as tracers. The measured velocity profiles were compared against the analytical solution for flow of a Newtonian fluid in a rectangular channel, given by equation (2.1) (Bruus, 2008).

$$U(y, z) = \frac{4h^2\Delta p}{\pi^3\mu L} \sum_{n,\text{odd}} \frac{1}{n^3} \left[1 - \frac{\cosh\left(n\pi\frac{y}{h}\right)}{\cosh\left(n\pi\frac{w}{2h}\right)} \right] \sin\left(n\pi\frac{z}{h}\right) \quad (2.1)$$

where y, z are the channel width and height ranging from 0 to h and $\pm 0.5W$ respectively, Δp is the pressure drop, μ the viscosity and L the length of the channel. The differences between the analytical and experimental velocity profiles were less than 1%.

Subsequently, in order to increase the time efficiency of the processing and minimise the size of the processed data, shorter ROIs were tested using healthy RBC suspensions. In particular, ROIs of two ($2W$) and three ($3W$) channel widths length were tested and compared against a ROI with a length equal to $5W$ showing differences below 0.03% and 0.04%, respectively. Thus, a ROI length of two channel widths was deemed suitable for the processing of the acquired RBC images. Moreover, the selected location of ROI, in the middle of the channel, i.e. 8 mm away from the inlet (160 channel widths) was further validated by comparing the velocity profiles measured upstream and downstream of the ROI. The flow rates determined from these profiles were found to be consistent within

2%, providing also an indication of the error in the velocity measurements (Figure 2.5a,b).

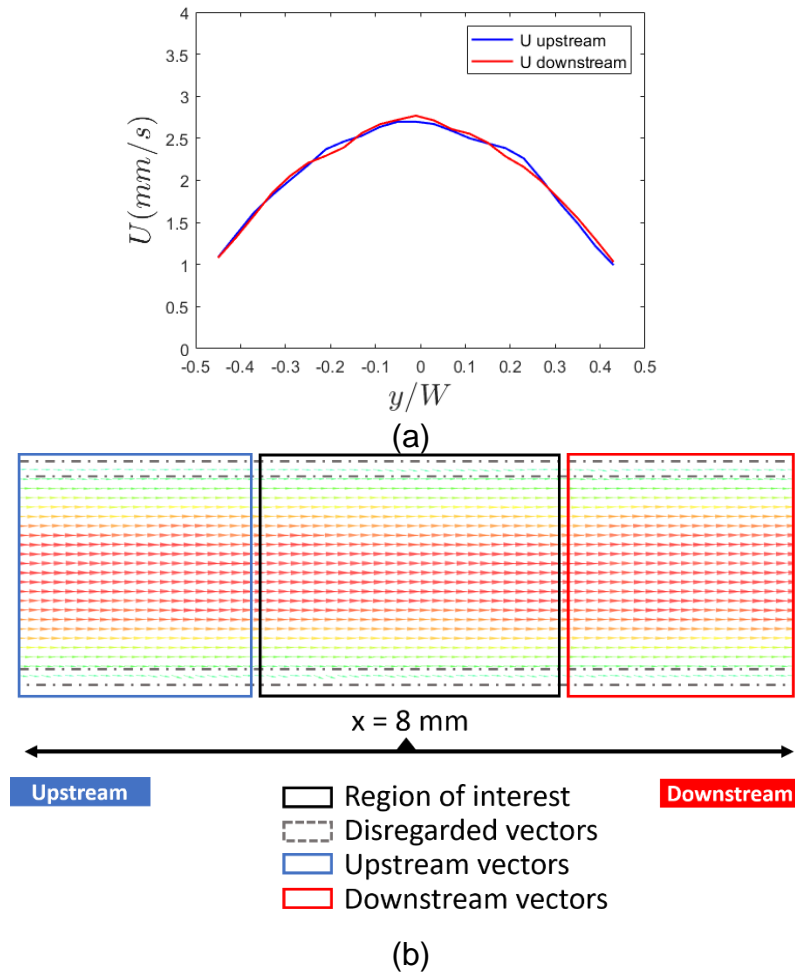


Figure 2.5: (a) The velocity profiles calculated upstream and downstream of the ROI taken in the middle of the microchannel (8 mm from inlet). (b) The velocity field extracted from PIV processing indicating the regions upstream and downstream of the ROI.

2.3.3 Image processing

Image pre-processing was applied in the acquired images for two main purposes: (i) to correct the images for uneven illumination and (ii) to extract the exact region of interest (ROI) for PIV processing. All image processing algorithms and processes were implemented in MATLAB (Mathworks).

Firstly, the acquired images were corrected for uneven illumination. The LED microstrobe illumination was focused in the centre of the image resulting in Gaussian light distribution across the imaging plane. Figure 2.6a shows an original image of RBC flow in the bifurcating microchannel where the uneven illumination is evident. The intensity distribution along the x-axis in the indicated area (shown in red) is presented in the graph of Figure 2.6b. It can be seen that the image intensity outside the microchannel is uneven which might result in biased intensity profiles especially when comparing the parent with the outlet intensity distributions. Figure 2.6c, shows the corrected image in terms of uneven illumination and the intensity graph of Figure 2.6d shows the resultant uniform distribution along the x-axis. This correction step is significant for the precise correlation between haematocrit and image intensity which will be described later in this chapter. Following the illumination correction step, the channel walls were located by making use of the image intensity profile across the channel estimated from the time averaged images, as seen in Figure 2.7. The channel walls produce a sharp peak in the intensity profiles which can be used to detect them precisely and in an automated fashion. Once the walls were located, the acquired images were cropped so that the ROI containing only flow information, i.e. flowing RBCs, can be selected for analysis; this spanned the width of the channel and a length equal to two channel widths. Figure 2.8a shows the ROI that was used for PIV processing selected from the straight $50 \times 50 \mu\text{m}^2$ channel. Figure 2.8b shows the ROI that was selected from the time averaged image for estimating the haematocrit distribution using the method that will be described later in the chapter. The ROI of the images was aligned horizontally and rescaled according

to the PIV interrogation windows; the width of the processed images was modified to be a multiple of the larger interrogation window size used in PIV processing giving a final image resolution of $0.60 \mu\text{m}$ per pixel. The same process was followed for the T-junction microchannels used in Chapter 6. The ROIs were selected to be two channel widths away from the centre of the bifurcation as seen in Figure 2.9.

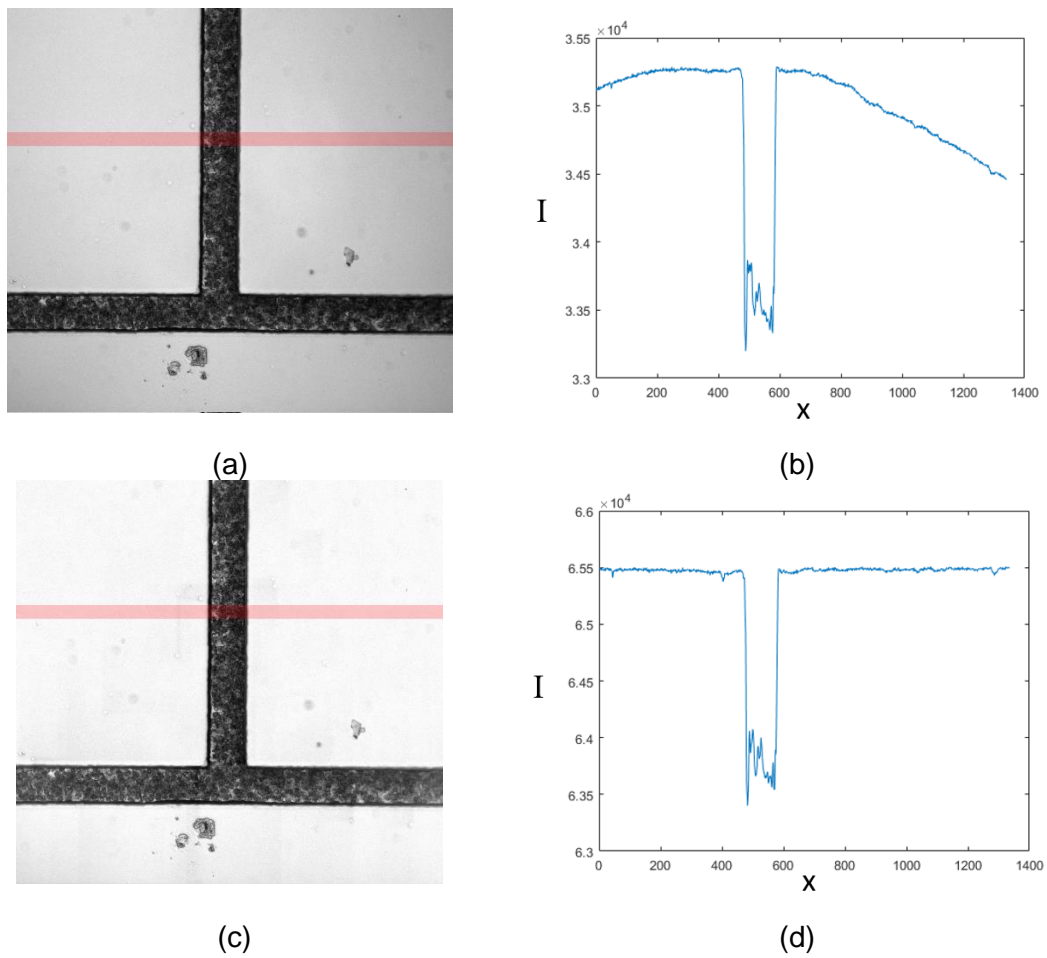


Figure 2.6: (a) Original image of RBC flow in a T-junction microchannel and (b) the intensity distribution along the x-axis (across the daughter branch). (c) Image after correction of the uneven illumination and (d) the new intensity distribution along the x-axis. The red areas in (a) and (c) indicate the region that the intensity distribution was calculated. Flow is from left to right.

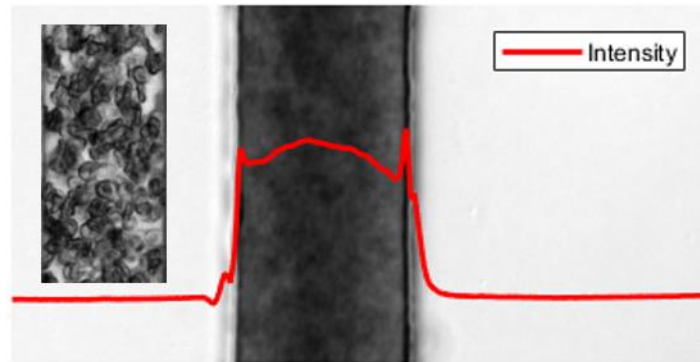


Figure 2.7: Time averaged image, obtained after correction for uneven illumination. The walls of the channel were identified from the peaks of the intensity profile (inverse intensity $1-I^*$, eq 2.5) shown with the red line. The inset shows the corresponding cropped ROI in the RBC image.

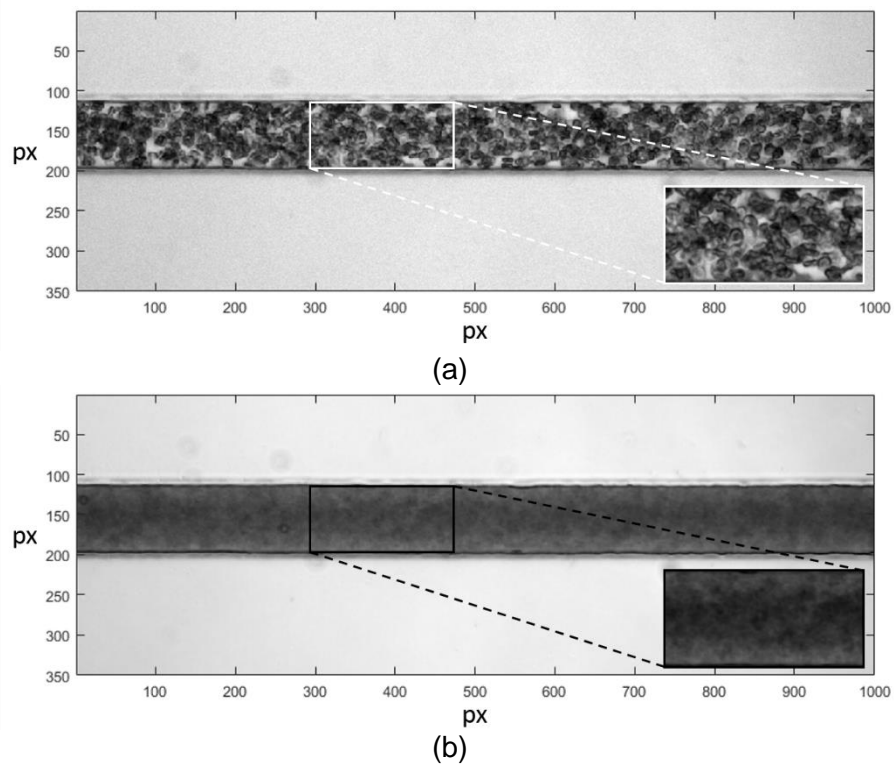


Figure 2.8: (a) Instantaneous sample image showing the cropped, corrected and rescaled section (ROI) used for PIV processing. (b) Time averaged image obtained from 120 instantaneous images indicating the cropped section that was used to determine the haematocrit distribution. The ROI is located in the middle of a 16 mm long channel i.e. 160 widths downstream the inlet.

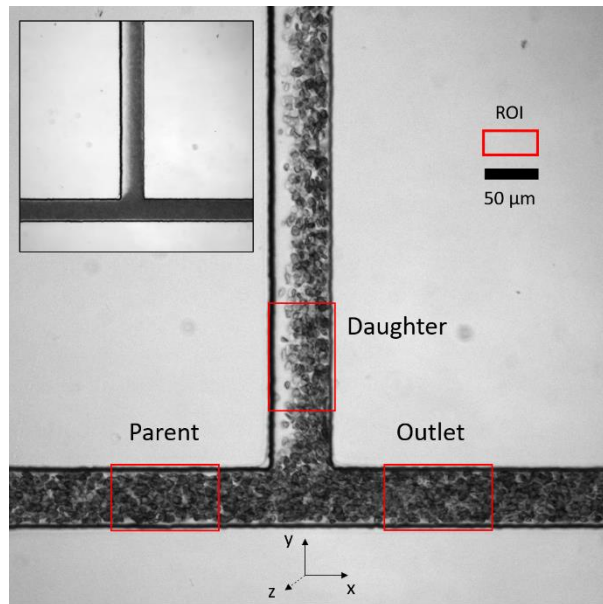


Figure 2.9: Instantaneous sample image of the T-junction showing the selected ROIs in the parent, daughter and outlet branches. The inset shows the time averaged image obtained from 120 instantaneous images that was used to determine the haematocrit distribution in ROIs at the respective locations. Flow is from left to right.

2.4 Data analysis

Following the PIV and image processing steps described above, the data were further analysed as follows. The velocity flow fields obtained from the PIV processing were used to extract the velocity profile across the ROI. The velocity profiles were further characterised in terms of bluntness for the straight channels and the parent branch of the T-junction channels and in terms of skewness for the daughter and outlet branches of the T-junction. The haematocrit distribution was determined from the time averaged images by correlating the intensity of the images to haematocrit. This analysis is a well-tested protocol developed in our lab (Sherwood *et al.*, 2014a,b) and will be used in order to examine the changes

in the shape of velocity and haematocrit distributions with RBC deformability, with a view to develop physical biomarkers for disease.

2.4.1 Velocity profiles

RBC velocity profiles were extracted by averaging the vector field within the ROI in the direction of the flow. The error at each radial position was defined as the standard deviation of the vectors. A slip wall condition was considered since RBCs have finite size, comparable to the dimensions of the channel, and the ones that flow in the cell depleted layer or come in contact with the wall tend to slip or roll along it. Due to the omitted vectors near the walls an extrapolation was used to estimate the slip velocity, using the following empirical fitting on the experimental data:

$$U = u \left(\frac{\cosh(0.5^m) - \cosh(|y_i|^m)}{\cosh(0.5^m) - 1} \right) + u_0 \quad (2.2)$$

U corresponds to the fitted velocity profile at the central plane of the flow where velocity is maximum, u is a weighing parameter related to the average velocity, m parametrises the bluntness of the profile and u_0 is the wall slip velocity. Equation (2.2) is an empirical fitting approach with u , m , and u_0 as free parameters, used to smooth the data and remove noise for the calculation of the flow rate; it is a simplified form of the analytical solution for Newtonian flow in rectangular channels (Equation (2.1)), which accounts for the non-zero wall velocity at the wall and varying profile bluntness. Figure 2.10 shows a typical velocity profile produced by fitting the experimental velocity data with 95%

confidence intervals and error bars corresponding to one standard deviation. The flow rate was expressed in terms of a normalized velocity, U^* , or nominal shear rate defined as $U^* = \bar{U}/W$, where \bar{U} is the average flow velocity and W the width of the channel. U^* varied from 1 to 250 s^{-1} .

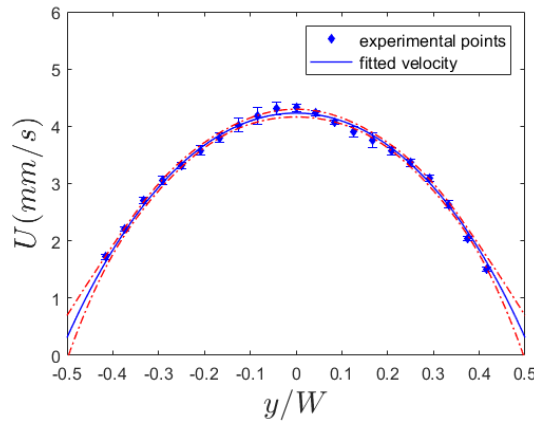


Figure 2.10: A typical velocity profile extracted from PIV data (GA 0.08% RBC sample of 25% haematocrit); each point represents the average velocity along the length of the region of interest of the channel. The blue curve is the fitted velocity profile using equation (2.2). The error bars correspond to one standard deviation and the red lines are confidence intervals of 95%.

2.4.2 Velocity bluntness index

The shape of the velocity profiles is a measure of the non-Newtonian/Newtonian character of the flow with shear thinning fluids like blood known to exhibit blunter velocity profiles. In this study a velocity bluntness index, expressed as the difference of the measured profile from the analytical one for a Newtonian fluid, was employed to facilitate a comparison of the velocity profiles at different levels of membrane stiffening. The velocity bluntness index (B_U) is defined as follows (Sherwood *et al.*, 2014).

$$B_U = \int_{-0.5}^{0.5} \left| \frac{u_a(y^*)}{\bar{u}_a} - \frac{u_e(y^*)}{\bar{u}_e} \right| dy^* \quad (2.3)$$

Where u_e is the experimental velocity and \bar{u}_e the average experimental velocity calculated as the average of the three-dimensional velocity profile (Sherwood *et al.*, 2014). In the $50 \times 50 \mu\text{m}^2$ microchannels the flow is axisymmetric and fully developed – in the straight microchannels and the parent branch of the bifurcating ones – hence the average velocity, both analytical and experimental was calculated as the average of the three-dimensional distribution in the yz plane. On the contrary, in the $100 \times 25 \mu\text{m}^2$ microchannels it was calculated from the two-dimensional profile across the channel. The analytical velocity u_a is calculated using equation (2.1). If u_e matches u_a the bluntness index will be equal to zero. On the other hand, a uniform distribution of velocity, like in plug flow, would yield $B_U = 0.363$. Thus, $B_U^* = B_U/0.363$ is the normalised velocity bluntness index which is equal to 0 for a Newtonian fluid and 1 for a uniform velocity distribution. The error of the velocity bluntness index estimation is given by the average value of the standard deviation, normalised by the average experimental velocity (Sherwood *et al.* 2014):

$$dB_U = \int_{-0.5}^{0.5} \left| \frac{du_e(y^*)}{\bar{u}_e} \right| dy^* \quad (2.4)$$

2.4.3 Calibration of image intensity and haematocrit

The haematocrit distribution was estimated by correlating the time averaged image intensity of the acquired images to haematocrit values. The intensity of 120 images (60 pairs) was averaged and the pixel intensity values were converted to haematocrit level using a calibration curve. The calibration process was performed by perfusing RBC samples, through the straight microchannel at feeding haematocrits ranging from 2% to 35%. The calibration was conducted for both healthy and GA fixed cells since GA might alter slightly the optical properties of the RBCs (Abay *et al.*, 2019).

Typical calibration images are shown in Figure 2.11 a and b. The average intensity was normalised by the maximum image intensity, $I^* = I_{\text{raw}}/I_{\text{max}}$, estimated from a region outside of the channel. The normalised intensity was then expressed as, $1-I^*$, in order for the low values of intensity to correspond to low haematocrit and plotted against the haematocrit as shown in Figure 2.11c. The calibration data were subsequently fitted with an equation of the form (Sherwood *et al.*, 2014):

$$1 - I^* = a(1 - e^{bH_F}) \quad (2.5)$$

The fitting parameters for the healthy sample were $a = 0.72 \pm 0.12$ and $b = -9.1 \pm 0.78$ and for the GA sample were $a = 0.77 \pm 0.09$ and $b = -9.7 \pm 0.77$. The R^2 value for both fitting lines is 0.99. The fitting parameters that were calculated for

the healthy RBC samples were used for correlating the image intensity to haematocrit for the healthy and aged RBC samples while the fitting parameters that were calculated for the GA 0.08% samples were used for the GA samples. Figure 2.12 shows a typical haematocrit profile estimated by converting the intensity to haematocrit using equation (2.6). The haematocrit distribution was fitted using equation (2.7) which is the equivalent of the velocity fitting equation (Equation (2.2)) but with haematocrit values, where h_c is a weighting parameter related to the average haematocrit, h_0 is the haematocrit at the wall (Sherwood et al., 2014).

$$H = \frac{1}{b} \ln \left(1 - \frac{1 - I^*}{a} \right) \quad (2.6)$$

$$H = h_c \left(\frac{\cosh(0.5^m) - \cosh(|y_i^*|^m)}{\cosh(0.5^m) - 1} \right) + h_0 \quad (2.7)$$

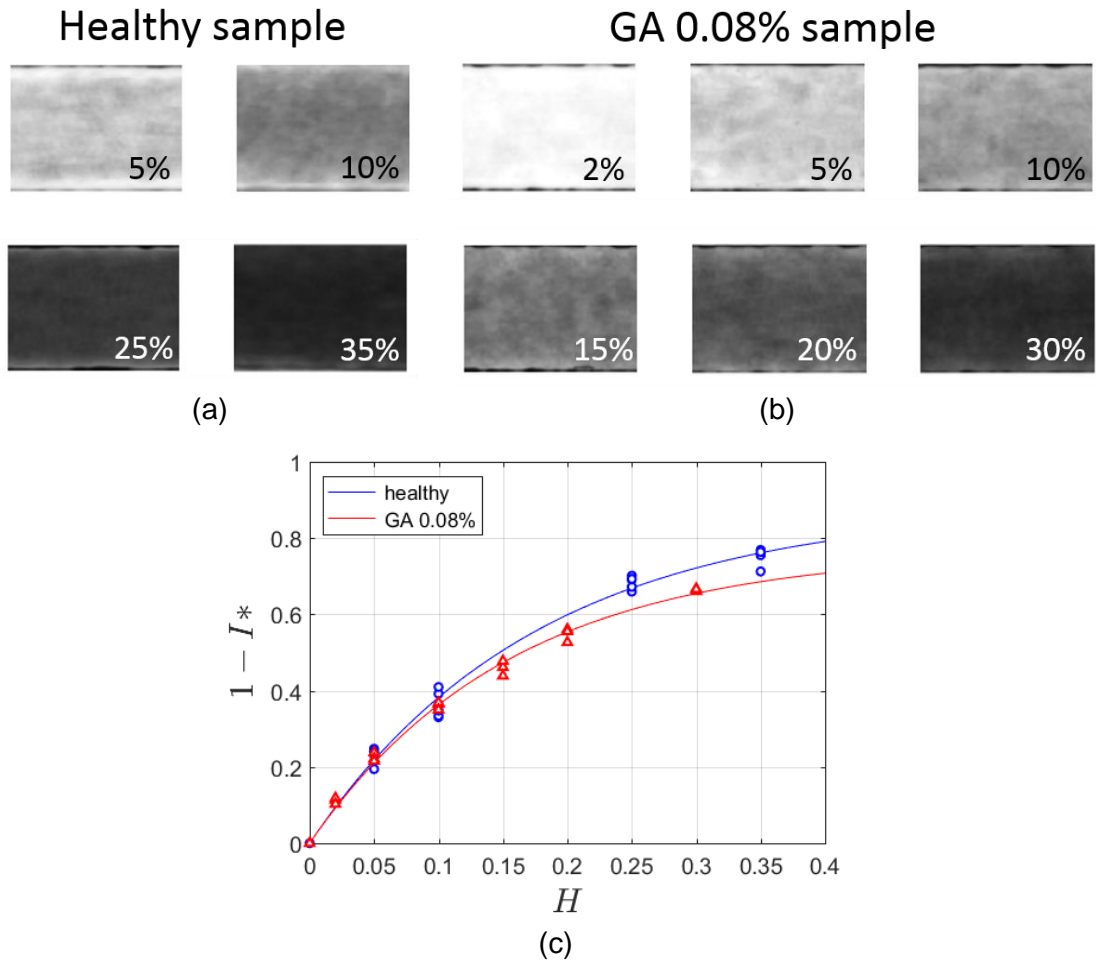


Figure 2.11: Time averaged sample images at various haematocrits for the (a) healthy RBC sample (5%, 10%, 25%, 35% haematocrits) and (b) GA 0.08% RBC sample (2%, 5%, 10%, 15%, 20%, 30% haematocrits). (c) Calibration curves correlating haematocrit to image intensity.

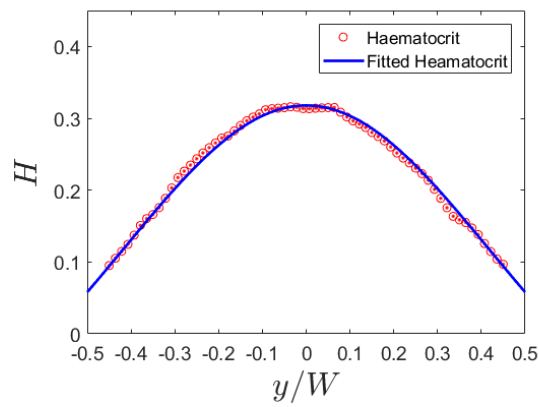


Figure 2.12: A typical haematocrit distribution for a 25% haematocrit sample obtained from time averaged image intensity using the calibration curve in Figure 2.11c.

2.4.4 Haematocrit profile bluntness

In order to characterise the distribution of haematocrit across the channels for the various samples examined the haematocrit bluntness index, B_H^* , as described by Sherwood *et al.* (2014) was employed. The haematocrit bluntness index is defined in Equation (2.8) and is based on the proportion of RBC flow in the central third of the flow ($-0.166 < y^* < 0.166$). In the case that all RBCs flow within the central third, B_H^* would be zero while in a uniform distribution across the channel B_H^* would be equal to 1.

$$B_H^* = \frac{3}{2} \left\{ \frac{\int_{-0.5}^{0.5} H(y^*) dy^* - \int_{-0.166}^{0.166} H(y^*) dy^*}{\int_{-0.5}^{0.5} H(y^*) dy^*} \right\} \quad (2.8)$$

2.4.5 Velocity and haematocrit skewness

Non-symmetrical velocity and haematocrit profiles are expected in the daughter branches of the bifurcating flows examined in chapter 5 for certain flow ratios. In order to fully characterise the shape of these profiles and the degree of asymmetry a skewness index was defined for both the velocity and haematocrit profiles (Sherwood *et al.* 2014) as follows:

$$S_U = \left| \frac{\int_0^{0.5} U(y^*) dy^*}{\int_{-0.5}^{0.5} U(y^*) dy^*} - 0.5 \right| \quad (2.9)$$

$$S_H = \left| \frac{\int_0^{0.5} H(y^*) dy^*}{\int_{-0.5}^{0.5} H(y^*) dy^*} - 0.5 \right| \quad (2.10)$$

The equations above are based on the idea of dividing the profiles in half and comparing the area under the profiles on one half against the total. If the profile is symmetric, according to the above equations, the skewness will be equal to zero. Figure 2.13 shows typical skewed velocity and haematocrit profiles in the daughter branches of the T-shaped bifurcation in which the velocity and haematocrit skewness index equations (2.9) and (2.10) were applied. The profiles were firstly smoothed with spline interpolation.

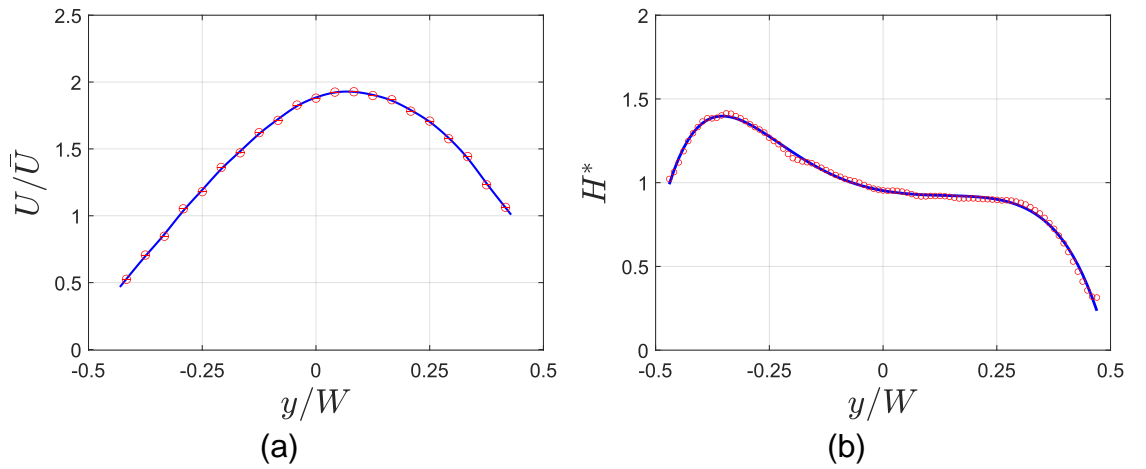


Figure 2.13: Typical skewed (a) velocity and (b) haematocrit profiles in the daughter branch of the T-junction microchannel. The profiles are normalised against the average velocity and haematocrit respectively. The profiles are smoothed using spline interpolation.

2.4.6 Tracking of labelled RBCs

Cell tracking experiments were conducted using fluorescently labelled RBCs in order to study the spatial distribution of a dilute concentration of hardened RBCs

within suspensions of both healthy and hardened RBCs. Since fluorescent labelling might affect the properties of RBCs only hardened cells were labelled using a PKH-26 Red Fluorescent Cell Linker (Sigma-Aldrich) as described earlier in the chapter.

RBC solutions were perfused into square microchannels of $50 \times 50 \mu\text{m}^2$ with constant flow rates of 60 s^{-1} . Measurements were obtained in two sections of the microchannel, ten channel widths downstream of the flow inlet and upstream of the outlet respectively, leaving 15 mm, i.e. 300 channel widths, distance between the two sections of measurement. As discussed earlier, alternate illumination was employed to capture images of both the labelled RBCs separately from the whole suspension (Figure 2.3). 300 pairs of images were acquired in each measurement.

Figure 2.14 shows the various processing steps followed to track the distribution of the fluorescent RBCs across the channel. The boundaries of the channel were detected from the brightfield RBC images (Figure 2.14a) and the images were cropped accordingly. Figure 2.14b shows a sample original image acquired with laser illumination of flowing fluorescently labelled RBCs. The background was subtracted (Figure 2.14c) and subsequently two thresholding operations were implemented. Intensity based thresholding was applied to locate the labelled RBCs flowing on the focusing plane (Figure 2.14d) as cells with higher intensity are more likely to flow within that plane (Fitzgibbon *et al.*, 2015; Namgung *et al.*, 2017). An area-based thresholding was applied in order to ensure that single cells were detected. Finally, the centroid of the detected RBCs was estimated. The

location of this centroid was taken as the cell's lateral position across the channel (Figure 2.14e). The lateral positions of more than a 1000 labelled RBCs per measurement were estimated producing a 'continuous' distribution across the channel width which was considered as the probability density function of the RBC distribution across the channel. These will be discussed in chapter 4.

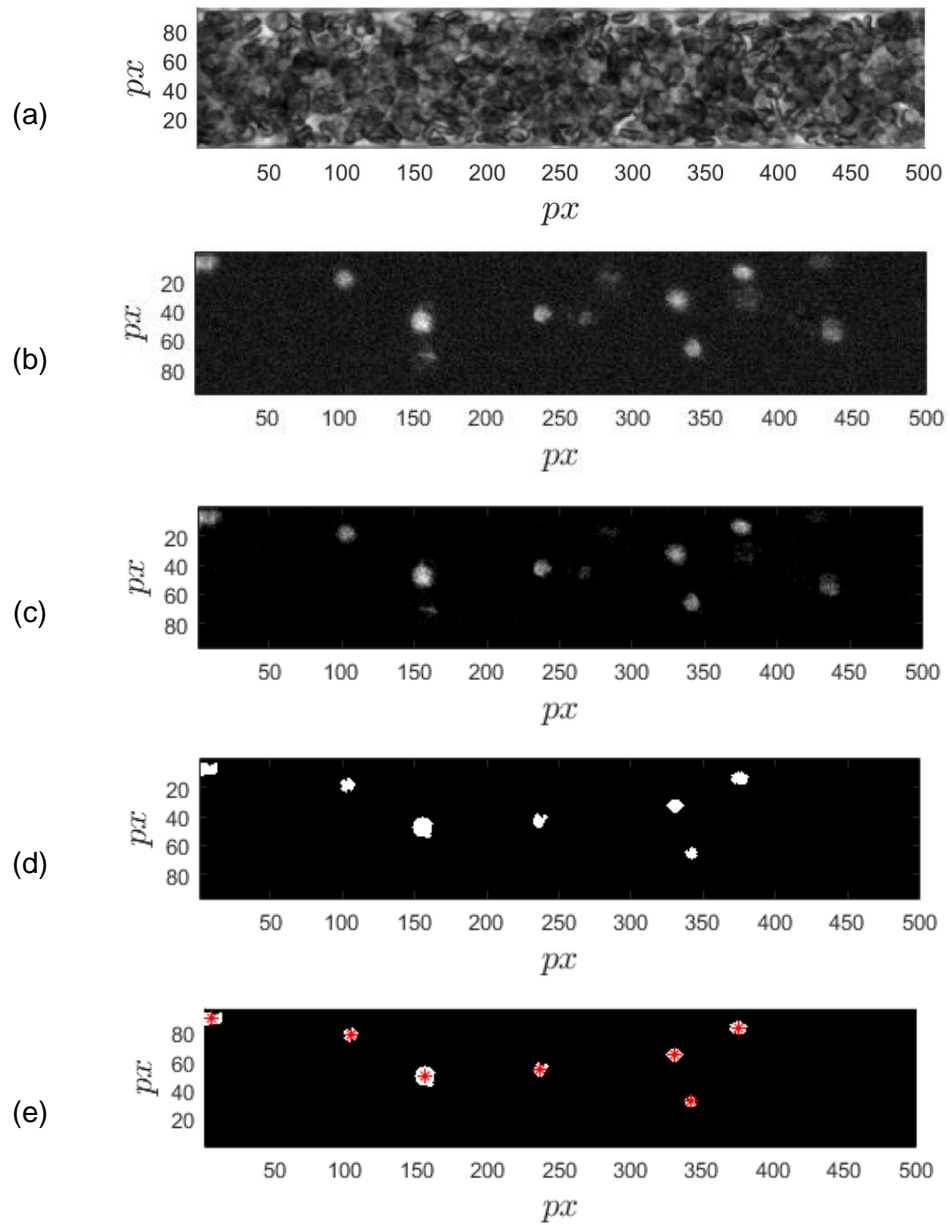


Figure 2.14: (a) Sample image of the suspension acquired with the LED illumination (b) Sample images of fluorescently labelled stiffened RBCs acquired with the laser illumination (c) Image after background subtraction (d) Image intensity and area-based thresholding to identify in-plane single cells. (e) Centroid estimation of the labelled cells.

2.5 Statistical significance of the results

Statistical analysis of the parametric investigation presented in Chapters 3, 4, 5, 6 was necessary in order to confirm whether the observed trends were statistically significant. Two main statistical methods were used to quantify the correlation of the results; the student's t-test hypothesis test and Pearson correlation coefficient (PCC). The threshold of p-value that was used as benchmark to verify significance was set to 5%, i.e. $p < 0.05$.

The student's t-test is a common statistical method used to determine if there is a significant difference between the means of two groups of data. For example, in order to determine if the means of the velocity bluntness indices of healthy ($B_{U,h}$) and glutaraldehyde fixed (0.08%) RBCs ($B_{U,GA}$) exhibit a statistically significant difference, the t-test hypothesis testing was used (Figure 3.5). These two data sets have different means ($\bar{B}_{U,h} \neq \bar{B}_{U,GA}$) and the t-test determined that these two populations have statistically significant difference with p-value, $p < 10^{-7}$, meaning that there is a low probability (10^{-7}) that the difference between these data sets is by chance.

The Pearson rank correlation coefficient or Pearson's r-value (r) was used to examine trends of single data sets against a parameter which exhibits or is expected to exhibit a linear correlation. For example, in chapter 6, healthy RBC samples in the outlet branch showed a decrease of haematocrit profile skewness with the normalised velocity of the parent branch (Figure 6.15a). This trend was tested using the Pearson test in order to examine if this decrease is statistically

significant. The Pearson test showed that there is a statistically significant negative correlation between the haematocrit skewness and normalised velocity of the parent branch with $p < 10^{-4}$.

2.6 Sources of uncertainty

2.6.1 Sample variations

Blood was collected from 4 different donors in the work described in this study. The intrasample and interdonor variation in RBC deformability have been reported to be approximately 20% (Guo *et al.*, 2014) (Figure 2.15). However, these variations are expected to have negligible effects in the distribution of RBCs in the channel, for example due to margination of the less deformable cells (Kumar and Graham, 2012b; Chen *et al.*, 2017; Namgung *et al.*, 2017). It should be also noted that the measured differences between healthy and hardened RBCs, as well as the reported trends were consistent between the different donors.

Apart from the deformability variations between the same samples the non-uniform feeding haematocrit due to RBC sedimentation had to be addressed as mentioned earlier. In order to maintain the feeding haematocrit of the RBC samples at a constant level, extra care was taken during the experiments to minimise RBC sedimentation. The RBC samples in the inlet reservoir were under a constant non-periodic stirring to maintain uniform haematocrit. Moreover, the suspensions were perfused first at a high flowrate ($> 1200 \text{ s}^{-1}$) that allowed the

redistribution of the cells before each measurement and data were acquired within a short time interval (10 s) that also ensured that haematocrit remained constant during acquisition.

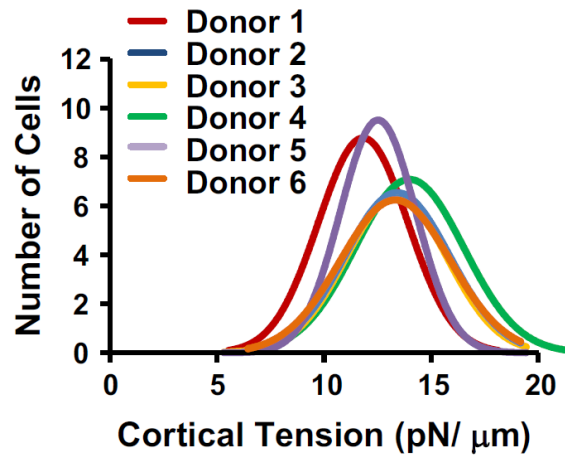


Figure 2.15: Distributions of RBC cortical tension used as an indication of RBC deformability between six healthy donors (Guo *et al.*, 2014).

2.6.2 Glutaraldehyde hardening

This study relies on the use of glutaraldehyde (GA) which is commonly employed to artificially harden RBCs. This has been found to perform with more consistency than other agents such as diamide (Schmid-Schönbein and Gaehtgens, 1981; Forsyth *et al.*, 2010; Abay *et al.* 2019). Although it is an artificial treatment that does not entirely replicate RBC changes in disease, it provides a good starting point to appreciate the role of such changes in a systematic manner. In addition to altering RBC deformability, GA also induces changes to other cell properties, such as cell volume (Squier, *et al.*, 1976), osmolarity (Morel *et al.*, 1971), charge (Vassar *et al.*, 1972), which could potentially affect the observed cell dynamics and interactions. However, the differences between healthy and hardened

samples found in the present study are expected to be primarily due to RBC deformability differences as the GA concentration used is well above the critical value of 0.003% (Baskurt *et al.*, 2009) that is required to produce statistically significant changes in the latter.

Incubation with glutaraldehyde, might potentially induce cell clustering which could give rise to increased migration, which is particle size dependent, and hence increased concentration of RBCs towards the centreline, as found in flows of aggregated RBC suspensions (Sherwood *et al.*, 2014a,b). In order to rule out the possibility of GA induced RBC clustering, the intensity distribution of images of hardened and healthy RBCs was examined, a technique demonstrated by Kaliviotis *et al.* (2016) which enables to discern suspensions of aggregating RBCs from those suspended in PBS. The two distributions were found to be statistically similar ($p = 0.99$) ruling out the GA induced RBC clustering as discussed in chapter 5. Moreover, the effect of GA on optical properties of RBCs was also accounted for through the haematocrit calibration procedure as mentioned earlier.

2.6.3 Errors in PIV analysis

PIV processing methods often produce a number of invalid or spurious vectors, usually as an outcome of the size of the interrogation windows, the particle density (tracers) within the IW, the displacement of the tracers within the Δt , the correlation of out of plane tracers and others.

In the current experiments a validation procedure was applied to reduce the amount of erroneous vectors. Considering that the IW sizes were maintained throughout the experiments for consistency, the Δt of the measurements was chosen so that the maximum particle displacement follows the quarter rule, i.e. the displacement of the RBCs to be no more than a quarter of the initial pass IW size (Smith and Neal, 2016). Moreover, multi-pass ensemble correlation was conducted using smaller IW in later passes in order to refine and improve the spatial resolution and accuracy of results. The laminar nature of the flow in straight channels does not produce complex velocity fields resulting in PIV processing with a reduced amount of errors. However, two main sources of uncertainty had to be considered in the current experiments. Firstly, the PIV processing near the channel walls produced vectors with high uncertainty as a result of light diffraction which formed a low image intensity area (≈ 4 pixels) near the channel walls. Thus, the vectors near the walls could not be used and were omitted as mentioned earlier in the chapter. Secondly, the use of RBCs with 8 μm diameter as tracers increases the correlation depth of the measurements compared to 1 μm particles, meaning that out of plane RBCs, with lower velocities, contribute to the velocities measured, resulting in an underestimation of velocity. The correlation depth was estimated using equation (2.11) (Olsen and Adrian, 2000) and was found to be larger than 50 μm which is the channel height, meaning that the flow was ‘depth-saturated’.

$$z_{\text{corr}} = \left[\frac{(1-\sqrt{\epsilon})}{\sqrt{\epsilon}} \left(f^{\#2} d_p^2 + \frac{5.95(M_t+1)^2 \lambda^2 f^{\#4}}{M_t^2} \right) \right]^{1/2} \quad (2.11)$$

where M_t is the total magnification of the system, d_p is the particle diameter, λ is the wavelength of the light emitted by the particle and $f^\#$ is the focal number of the lens ($NA = 1/2f^\#$). ε is a parameter which defines the distance of influence along the optical axis, beyond which a particle will not contribute to the correlation function and is generally chosen to be 0.1. Poelma *et al.* (2012) suggested a correction factor of 1.5, when using RBCs as tracers for μ PIV, in order to scale up the underestimated velocities. This factor was applied in the current experiments in order to calculate the absolute velocity values and hence the flow rate, expressed through the normalised velocity U^* . Considering the above the invalid vectors in all the measurements were less than 0.1% and were replaced by the median of the neighbouring vectors (Westerweel and Scarano, 2005).

2.6.4 Errors in flux conservation

In the bifurcating flows of chapter 6 the errors in flux conservation were estimated. Conservation of mass requires that the RBC flux upstream and downstream of the bifurcation is equal, i.e. the RBC flux in the parent branch should be equal to the sum of RBC fluxes in daughter and outlet branches as described by (2.12).

$$\rho_p Q_p = \rho_d Q_d + \rho_o Q_o \quad (2.12)$$

where the subscripts, p, d and o correspond to the parent, daughter and outlet branches respectively. The density in each branch was assumed constant since the density of whole blood is expected to vary between 1.032 and 1.044 g/ml for haematocrits of 0 to 30% (Burstain *et al.*, 1994), a difference less than 1.2%.

Thus, equation (2.12) can be simplified containing only volumetric flow rates (equation 2.13). The difference between the flow entering and leaving the bifurcating channel, given by (2.14), provides an indication of the errors in flow conservation incurred in the measurements.

$$Q_p = Q_d + Q_o \quad (2.13)$$

$$e = \frac{Q_p - (Q_d + Q_o)}{Q_p} \quad (2.14)$$

The RBC suspensions flow rate, Q , was estimated using the $Q = \bar{U}/A$, where \bar{U} is the average experimental velocity of each measurement determined by PIV processing and A the cross-sectional area of the microchannel, here $50 \times 50 \mu\text{m}^2$. Figure 2.16 shows the flow rate variation in the first set of experiments where the flow rate in the parent branch was maintained within a narrow range. The flow rate in the outlet branch was gradually increased by elevating the hydrostatic pressure in the daughter branch. It can be seen that the parent branch flow rate was better controlled in the perfusion of healthy samples in PBS where the variation of total flow rate was 6.1% and the error in flow conservation, e , was 3.9% (Figure 2.16a). The error in flow conservation of the other samples was between 5.1% and 5.8% while the flow rate variation of GA 0.08% RBC suspensions in PBS was 20.7% (Figure 2.16c). Healthy and GA 0.08% RBCs in Dextran had flow variation of 12.9% and 10.9% respectively (Figure 2.16b, d). On the contrary, the error in flux conservation is of importance as it affects the

estimation of the flow ratio. In the experiments the errors of flux conservation were relatively low (less than 5.8%) implying a good accuracy in the estimation of flow ratio. The cases in which flow conservation error was larger than 10% were omitted from the analysis; in total less than 3% of the measurements. Table 2.2 summarises the average flow rate and variation in perfusion for each of the samples as well as the mean percentage errors in flow conservation.

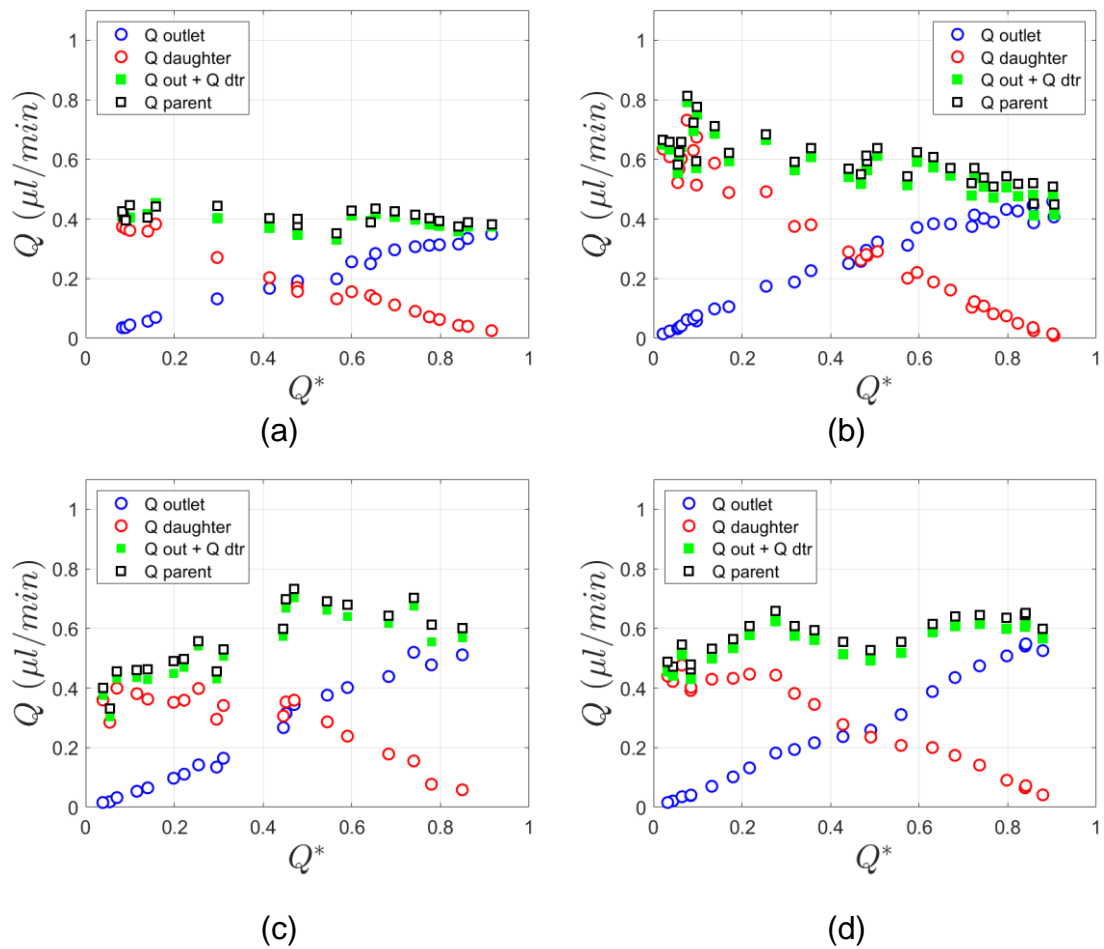


Figure 2.16: Flow rate in each branch as a function of flow ratio, Q^* : (a) Healthy RBCs in PBS, (b) Healthy RBCs in Dextran, (c) GA 0.08% RBCs in PBS and (d) GA 0.08% RBCs in Dextran.

Table 2.2: Average parent flow rate and mean percentage errors in flow conservation during the perfusion of each sample.

Sample	Avg Q_p ($\mu\text{l}/\text{min}$)	e	Std Q_p
Healthy in PBS	0.41	3.9%	0.03 (6.1%)
Healthy in Dextran	0.65	5.1%	0.08 (12.9%)
GA 0.08% in PBS	0.56	5.6%	0.12 (20.7%)
GA 0.08% in Dextran	0.58	5.8%	0.06 (10.9%)

2.7 Closure

In this chapter the protocols of blood collection and treatment during hardening and labelling were described. A detailed description of the experimental design was given, consisting of the pneumatic perfusion system, the image acquisition set up and PIV techniques that were used. The image processing methods that were applied on the acquired data (images) were explained as well as the methods that were used for analysing and investigating the flow and haematocrit of the RBC samples, such as the bluntness and skewness indices of the velocity and haematocrit profiles. Finally, a discussion regarding the systematic errors of the experiments was given.

The next chapter presents the effect of red blood cell deformability on velocity and haematocrit distribution across the flow in a straight microchannel. Velocity and haematocrit profiles of RBC samples with different haematocrit and deformability will be compared and characterised in terms of bluntness.

Chapter 3

Hardened RBC suspensions in straight microchannel

In this chapter, the effect of red blood cell membrane hardening on the velocity and haematocrit distributions of RBC suspensions flowing in a straight microchannel are examined. In particular, the velocity and haematocrit profiles of RBC samples with different degrees of cell deformability are determined experimentally and characterised in terms of bluntness for various flow rates and feed haematocrits.¹

¹ The data presented in this chapter have been published in 'Passos A, Sherwood JM, Kaliviotis E, Agrawal R, Pavesio C, Balabani S. (2019) The effect of deformability on the microscale flow behavior of red blood cell suspensions. *Phys Fluids* 31, 091903. The work was also presented at '5th Micro and Nano Flows Conference (MNF)', Milan, Italy, 11-14 September 2016

3.1 Introduction

Red blood cell membrane deformability is of clinical significance as has been highlighted in many diseases. Decreased deformability has been reported in sickle cell anemia (Li *et al.*, 2016), malaria (Dondorp *et al.*, 2000, 2002; Mohandas and Gallagher, 2008), sepsis (Condon *et al.*, 2003), prolonged storage of blood (Haradin *et al.*, 1969; Stuart and Nash, 1990) and many metabolic and inflammatory diseases such as diabetes, Alzheimer and stroke (Tsukada *et al.*, 2001; Fornal *et al.*, 2006; Shin *et al.*, 2007). Despite the clinical significance of RBC deformability, limited information exists on the flow properties of stiffer RBCs and their potential effects in the microcirculation. Chien *et al.* (1970) reported increased viscosity of hardened RBCs compared to healthy RBCs but most importantly a significant reduction of the shear thinning behaviour of hardened RBC suspensions. The velocity distribution across the flow is an important indication of shear thinning behaviour. Laminar flows of Newtonian fluids produce parabolic velocity profiles in circular tubes described by the Poiseuille law while in rectangular channels described by equation (2.1). Shear thinning fluids, such as blood, produce blunter velocity distributions than the analytical parabolic profile of the Newtonian fluids. Hardened RBC solutions are expected to have more Newtonian like behaviour than healthy RBCs (Chien, 1970; Lanotte *et al.*, 2016) and as a result exhibit different velocity distributions across the flow. Other properties such as RBC radial migration and cell-cell interactions (Hou *et al.*, 2010; Kumar and Graham, 2012b) are expected to be affected with RBC

hardening. This, in turn will result in different haematocrit distributions across the flow between hardened and healthy RBC suspensions.

In this chapter, the role of deformability on the microscale flow behaviour of red blood cells is examined. Velocity and haematocrit distributions were determined experimentally by perfusing RBC samples with different membrane deformability through straight microchannels with square cross-sectional area of $50 \times 50 \mu\text{m}^2$. Four RBC samples were tested: a healthy RBC sample which was used as the control sample, two GA hardened RBC samples with 0.04% v/v and 0.08% v/v concentrations and a 7 days aged sample stored at 4°C . In the following analysis, the parameters considered apart from membrane deformability were the RBC concentration (haematocrit) and flow rate. The samples were perfused at various flow rates, expressed using a normalised velocity ($U^* = \bar{U}/W$) similar to a nominal shear rate; a range between $1 - 150 \text{ s}^{-1}$ and three RBC concentrations (feed haematocrit), 5%, 10% and 25% were examined. The shape of the measured velocity and haematocrit profiles were characterised in terms of their bluntness; alterations due to membrane deformability, normalised flow velocity and haematocrit levels were determined. Figure 3.1a shows some typical RBC images of flows of different RBC samples at 10% haematocrit. The time averaged image intensity (Figure 3.1b) was normalised with the maximum image intensity measured outside of the channel (Figure 3.1c) and used to determine the haematocrit profiles.

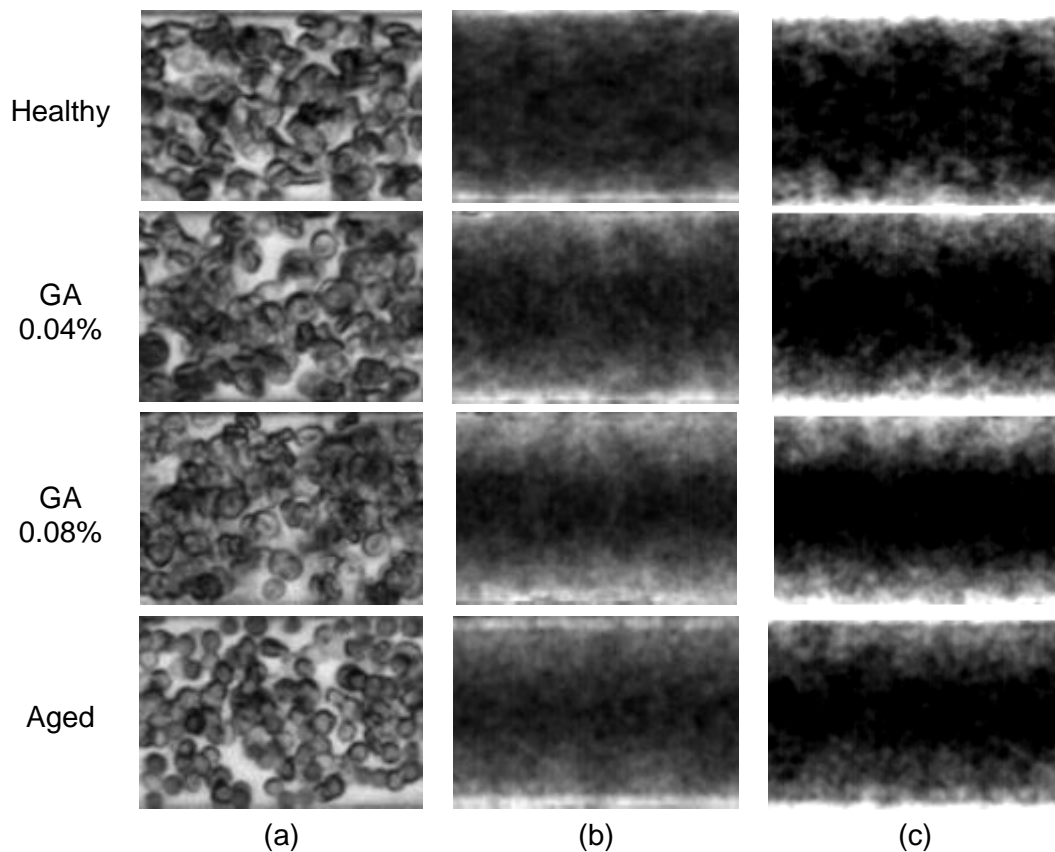


Figure 3.1: (a) Sample images of RBC samples of 25% haematocrit perfused at 45 s^{-1} (b) Time averaged image intensity of the samples at 25% haematocrit (c) Normalised time averaged image intensity with maximum image intensity.

3.2 Velocity profiles

In Figure 3.2, typical velocity profiles for healthy, aged and hardened RBC suspensions at 5% and 25% haematocrit are shown. The profiles are compared with the analytical solution for a Newtonian flow in the square microchannel (Bruus, 2008), indicated by the grey area.

In Figure 3.2a low concentration (5%) velocity profiles of healthy and hardened (GA 0.08%) are compared. The profiles match and are close to the analytical

profile as expected given the low haematocrit. On the contrary, at higher haematocrit (25%) healthy RBCs exhibit blunter velocity profiles compared to the hardened ones which show a progressively reduced bluntness with membrane hardening, exhibiting a more Newtonian-like behaviour.

The velocity profile bluntness is a well-documented aspect of shear thinning fluids including those of healthy RBC suspensions (Goldsmith, 1968; Bishop *et al.*, 2001; Sherwood *et al.*, 2014). The decrease in bluntness observed with hardened or aged cells agree with the viscosity-flow curves for hardened RBCs which show a noticeable decrease in shear thinning behaviour with the loss of deformability (Chien, 1970; Lanotte *et al.*, 2016).

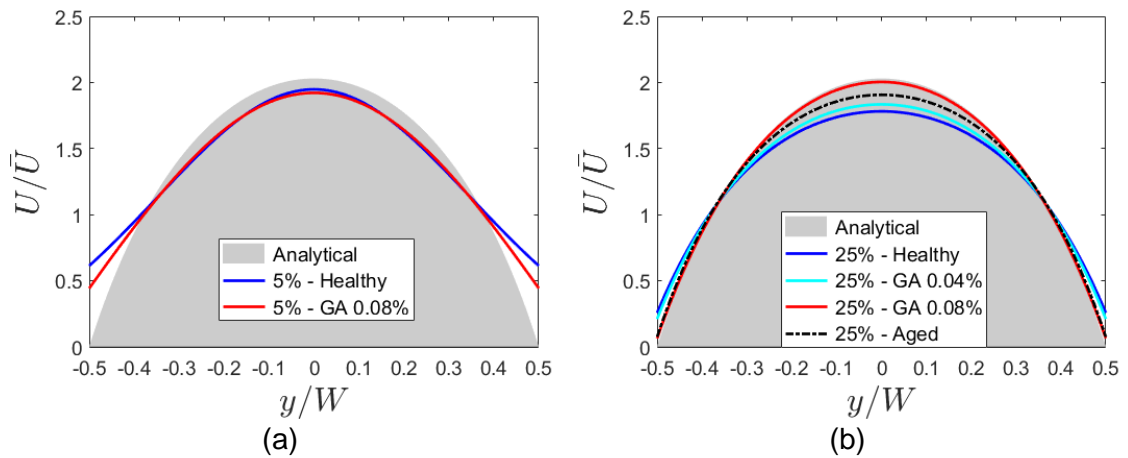


Figure 3.2: Typical velocity profiles of healthy-unfixed hardened (0.04%, 0.08% GA) and aged RBC samples obtained in the square microchannel at around 40 s^{-1} and haematocrit (a) 5% and (b) 25%. The grey area indicates the analytical velocity profile for a Newtonian fluid in a square channel.

Similar trends were observed at different flow rates and haematocrits. In order to quantify the impact of impaired RBC deformability on the velocity distribution, the velocity bluntness index was utilised expressed by equation (2.3).

Figure 3.3 compares the velocity bluntness index of healthy, hardened and aged RBC suspensions at concentrations of 5%, 10% and 25% as a function of normalised velocity. The more deformable RBC samples, healthy and GA 0.04%, show a gradual reduction in velocity bluntness with haematocrit decrease as illustrated in Figures 3.2a,b, whereas less deformable RBC samples, aged and GA 0.08%, show no significant difference in velocity bluntness with haematocrit decrease (Figure 3.2c,d). Moreover, velocity bluntness does not exhibit a strong dependency on the flow rate in the range investigated. The dilute case of 5% haematocrit was studied for the two extreme cases in this study: healthy and GA 0.08% fixed RBCs, in order to appreciate the role of cell migration and cell-cell interactions in the measured profiles.

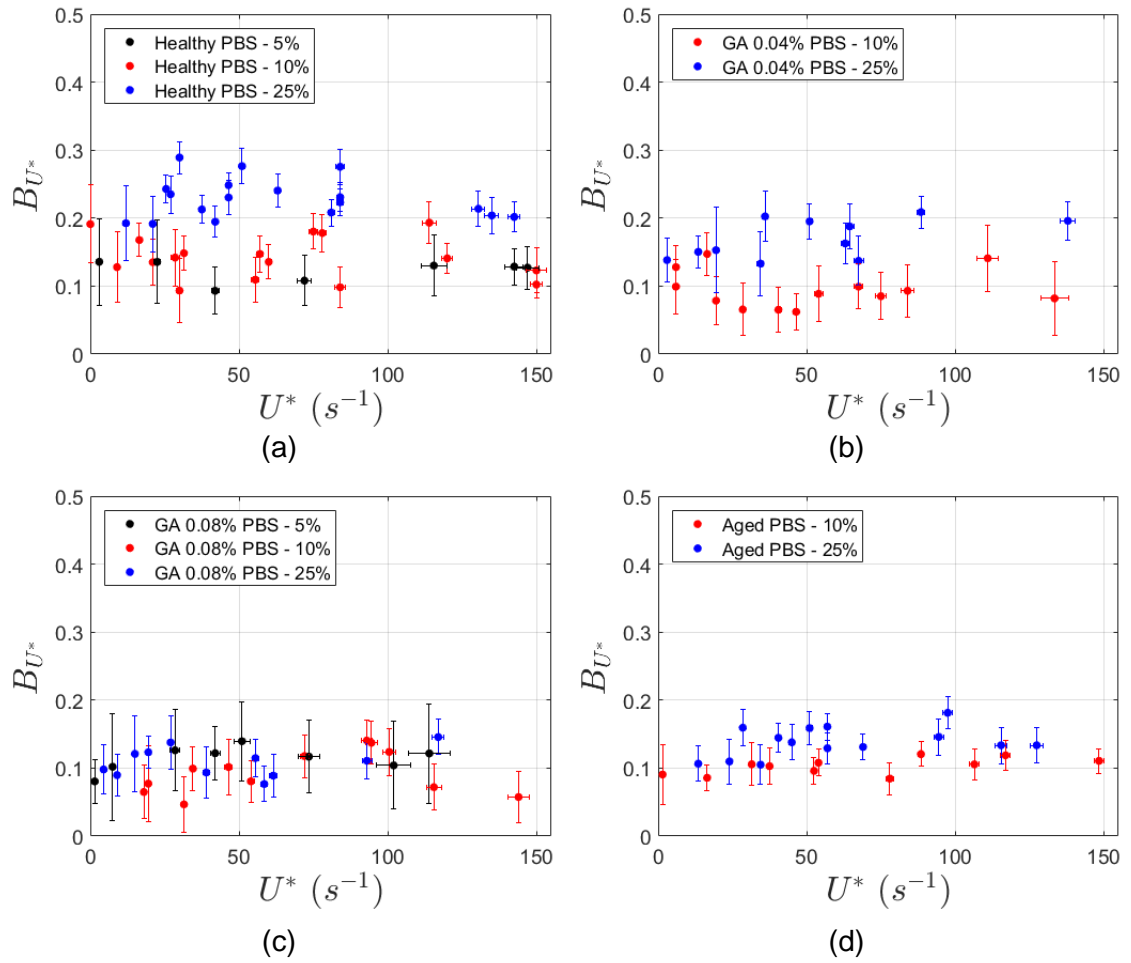


Figure 3.3: Velocity bluntness index as a function of normalised velocity U^* for samples with the same stiffness and different haematocrit levels: (a) unfixed – healthy samples at 5%, 10% and 25% Hct (b) GA 0.04% hardened RBC samples at 10% and 25% Hct, (c) GA 0.08% hardened RBC samples at 5%, 10% and 25% Hct and (d) aged RBC samples at 10% and 25% Hct. The error bars δB_{U^*} were calculated from eq. 2.4 and δU^* show one standard deviation.

RBC samples with the same haematocrit and different membrane stiffness were compared in order to demonstrate the relationship of velocity distribution to RBC hardening. Figure 3.4 shows a comparison between healthy, GA 0.04%, GA 0.08% and aged samples at 5%, 10% and 25% haematocrits. Velocity bluntness gradually decreases with membrane stiffening as haematocrit increases. Figure 3.4c shows a significant difference of B_{U^*} between healthy and GA 0.08% while

in 10% the relative difference decreases (Figure 3.4b) and at 5% Ht there are no significant differences (Figure 3.4a). The statistical significance of the velocity bluntness index differences between healthy and GA 0.08% hardened samples was examined using the t-test. T-test provided p-values of $p_{5\%} = 0.09$, $p_{10\%} < 0.003$, $p_{25\%} < 10^{-7}$ for haematocrits 5%, 10% and 25% respectively, showing statistically significant differences of B_{U^*} between healthy and hardened RBC samples for the 10% and 25% haematocrit levels while for the 5% the differences are insignificant.

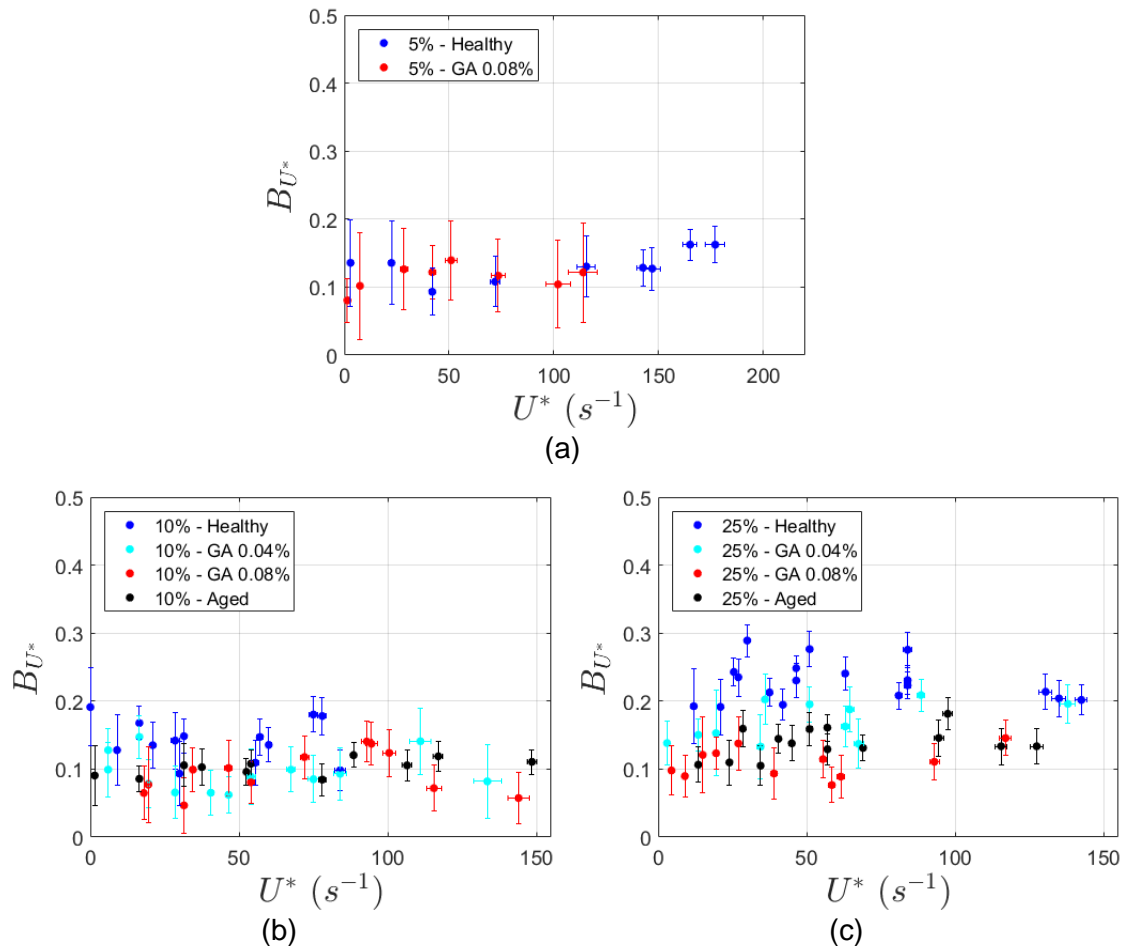


Figure 3.4: Comparison of bluntness indices of measured velocity profiles as a function of normalised velocity U^* for each of the samples at (a) Hct = 5% (b) Hct = 10% and (c) Hct = 25%.

Hct = 25%. Velocity profile bluntness indices were calculated from equation (2.3). The error bars, dB_{U^*} , were calculated from eq. 2.4 and dU^* show one standard deviation.

The box plots in Figure 3.5 summarise all data sets providing a non-parametric comparison of B_{U^*} variation between the RBC samples with different deformability. A progressive reduction in bluntness can be clearly seen in all the data plotted. This becomes more apparent at the higher haematocrit case (25%) (Figure 3.5c). It can be seen that the effect of haematocrit on bluntness is more pronounced in healthy and lightly hardened (GA 0.04%) RBC samples; the median velocity bluntness increases when the haematocrit increases from 10% to 25%. On the other hand, the GA 0.08% hardened samples exhibit the same bluntness index regardless of the haematocrit level. In even lower haematocrits (5%) the velocity bluntness of healthy and GA 0.08% do not show any significant difference (Figure 3.5a).

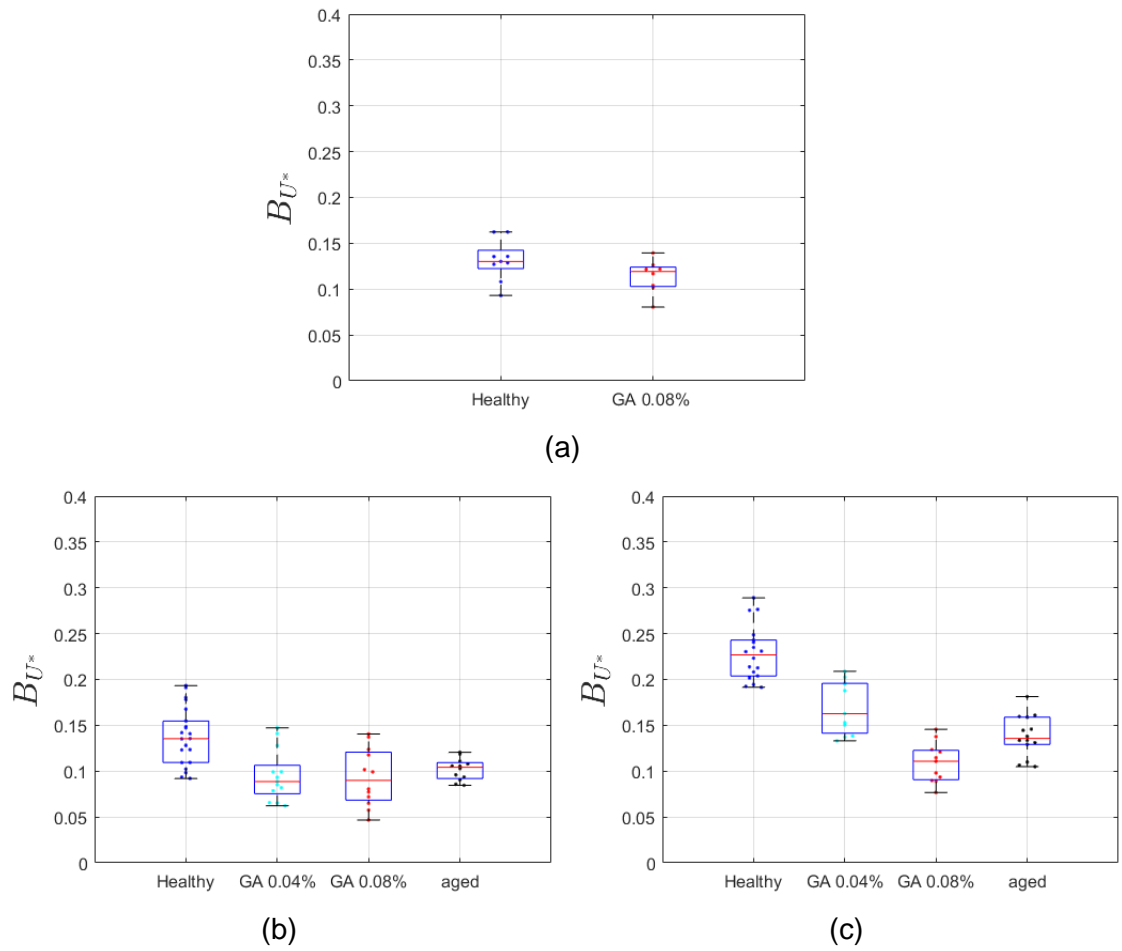


Figure 3.5: Boxplots summarising the data: bluntness index of the measured velocity profiles within the range of $1 - 230 \text{ s}^{-1}$ for each of the samples at (a) Hct = 5%, (b) Hct = 10%, c) Hct = 25%. The central red lines indicate the median of the measurements and the bottom and top sides of the box indicate the 25th and 75th percentiles, respectively.

3.3 Haematocrit profiles

Figure 3.6a shows typical haematocrit (H^*) profiles determined from flows of healthy, aged and hardened RBCs at a feeding haematocrit of 25%. The haematocrit values are normalised by the average haematocrit obtained by integrating the haematocrit profiles across the channel). Figure 3.6b shows

smoothed profiles obtained by fitting the data as described in Chapter 2. Healthy RBC profiles appear uniform in the central part of the channel for the particular flowrate in agreement with Sherwood *et al.*, (2012, 2014). However, less deformable RBCs seem to concentrate in the centre of the channel producing sharper haematocrit profiles. This trend is more pronounced for the most hardened RBCs fixed with GA 0.08%.

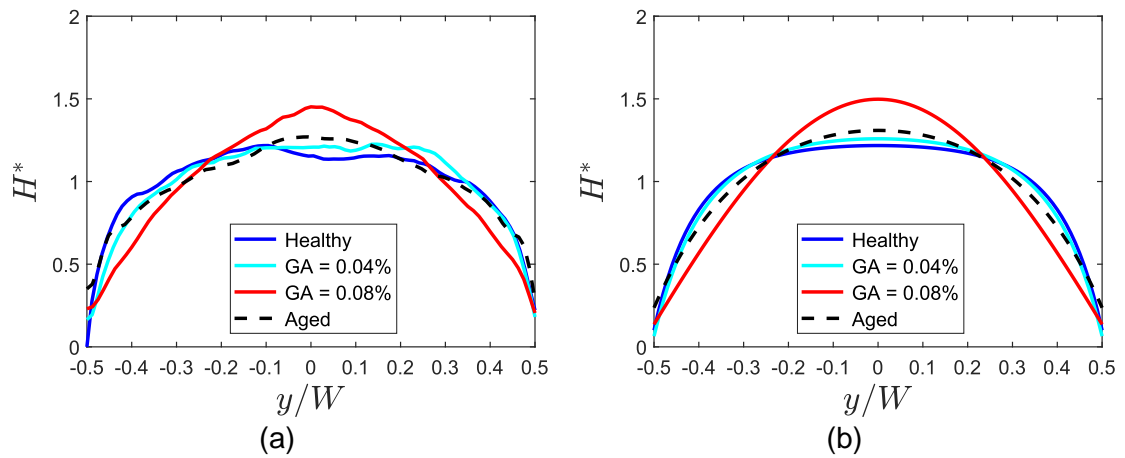


Figure 3.6: (a) Typical measured haematocrit profiles normalized by the average haematocrit; (b) Fitted haematocrit profiles (25% feed haematocrit and $U^* = 58 \text{ s}^{-1}$).

To further analyse the observed trends for all flowrates and haematocrits studied, the bluntness index of the measured profiles is plotted in Figure 3.7. It can be seen that at low haematocrits the bluntness index of the hardened RBCs appears slightly higher than that of healthy ones.

On the contrary, the bluntness index of denser suspensions shows the opposite trend: a reduction in deformability is associated with a progressive decrease in haematocrit bluntness. Figure 3.7 also shows that the flowrate has an effect at the low cell concentrations studied (5%, 10%) - as indicated by the spread of the boxes in Figure 3.8a,b - but this effect diminishes when the haematocrit is

increased to 25%. At 10% haematocrit (Figure 3.7b) B_H^* was found to increase with the flow rate for healthy, aged and fixed samples with Pearson test: $r_{unf} = 0.83$, $p_{unf} < 10^{-5}$, $r_{g04} = 0.95$, $p_{g04} < 10^{-7}$, $r_{g08} = 0.91$, $p_{g08} < 10^{-3}$, $r_{age} = 0.98$, $p_{age} < 10^{-4}$.

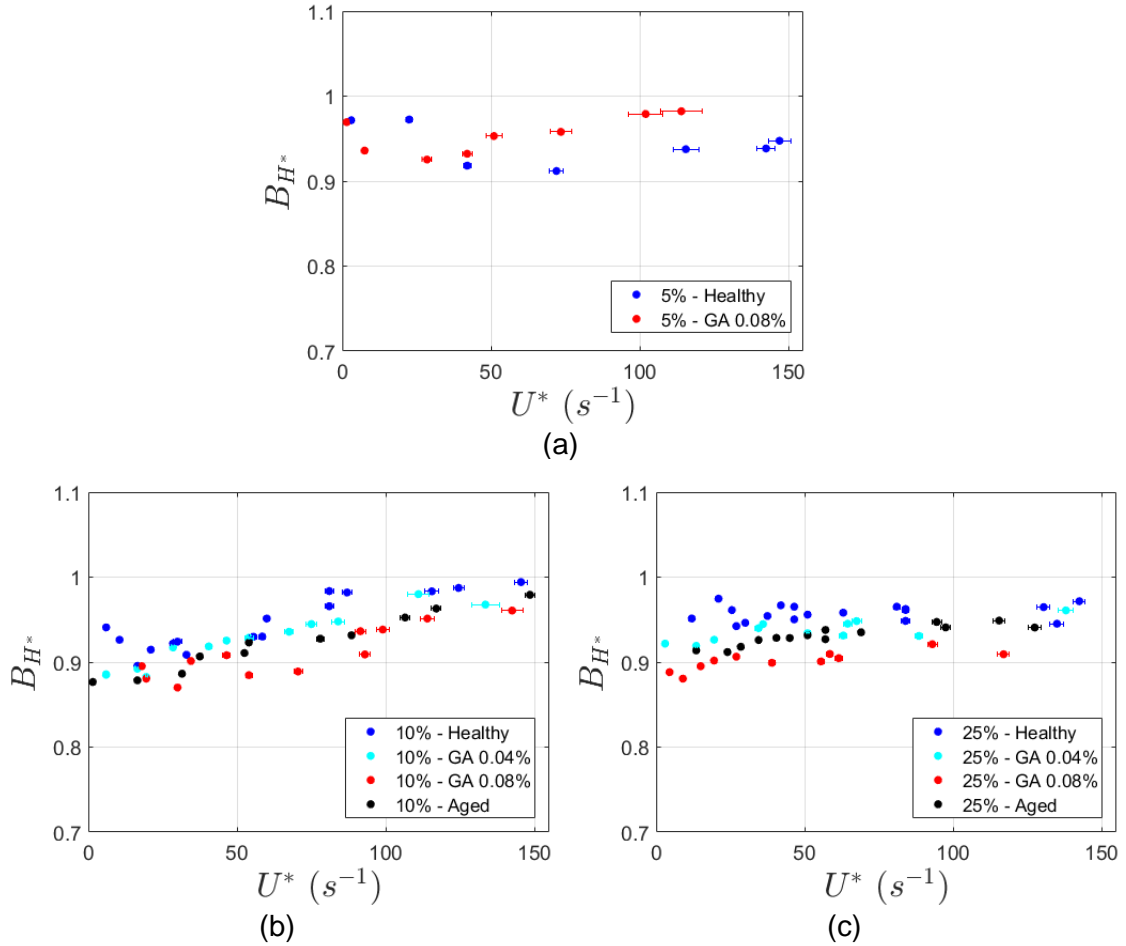


Figure 3.7: Haematocrit bluntness index as a function of normalised velocity U^* for each of the measured samples at (a) $H_t = 5\%$ (b) $H_t = 10\%$ and (c) $H_t = 25\%$.

The boxplots in Figure 3.8 summarise the above data, illustrating the trends more clearly. Hardened RBCs tend to concentrate towards the centre of flow. This indicates sharper haematocrit distributions, i.e. decreased haematocrit bluntness index, in comparison with healthy RBCs. The trend is pronounced at 25% haematocrit (Figure 3.8c) while in 10% the effect is present but less apparent

(Figure 3.8b). At 5% haematocrit, the most dilute sample, the haematocrit bluntness indices between healthy and GA 0.08% hardened RBCs seem to be similar and in particular, the hardened RBCs seem to have slightly higher bluntness index which indicates more uniform distributions than the healthy RBCs. The more uniform haematocrit distributions of hardened RBCs measured in this dilute case, are consistent with reports of stiffer cells exhibiting decreased migration properties.

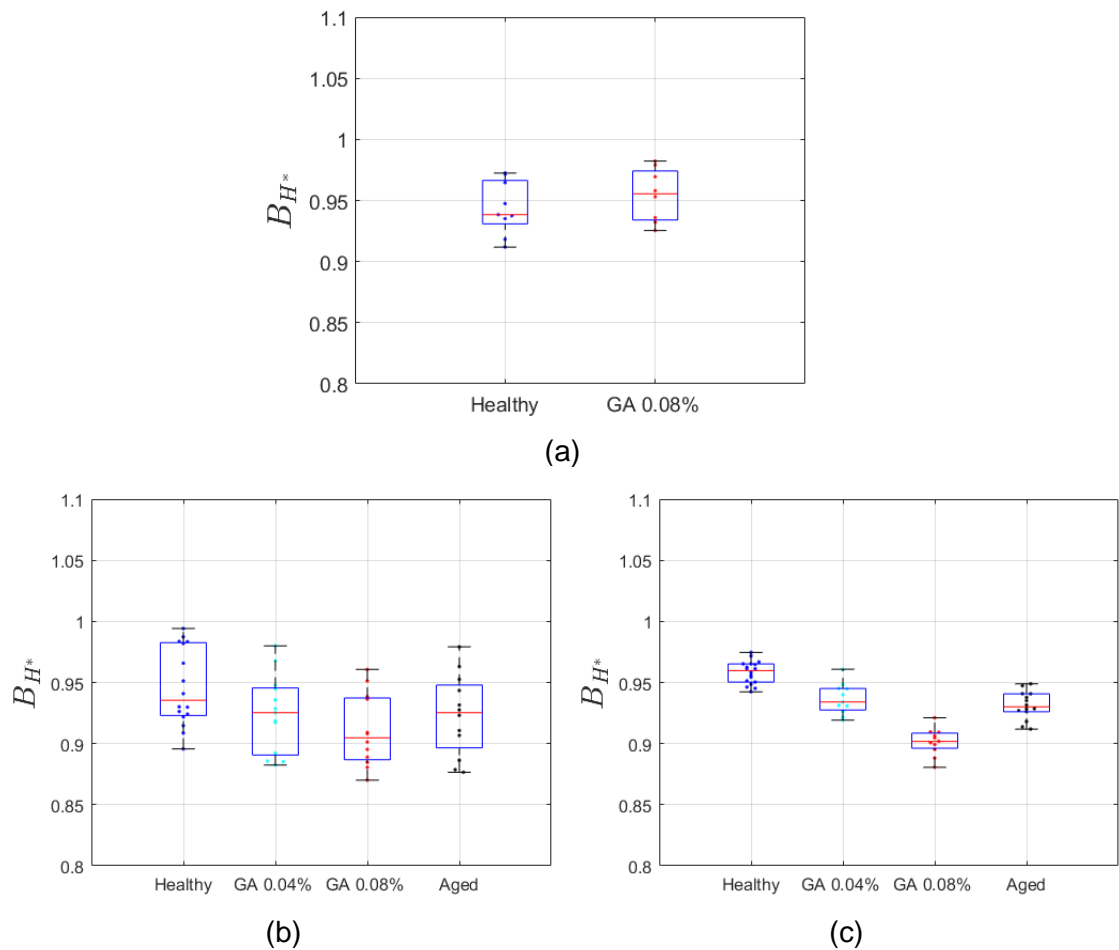


Figure 3.8: Boxplots summarising the data: bluntness index of measured haematocrit profiles at (a) Hct = 5%, b) 10% and (c) Hct = 25%. The central red lines, indicate the median and the bottom and top edges of the box indicate the 25th and 75th percentiles, respectively.

3.4 Velocity and haematocrit relationship

In order to better illustrate the effect of RBC deformability on the relationship between the velocity and haematocrit distributions correlation maps between the estimated corresponding bluntness indices were produced. Figure 3.9 compares these correlations for healthy, GA 0.04%, GA 0.08% and aged samples at haematocrits, 5%, 10% and 25% respectively. Pearson's correlation was used to measure linear correlations between the velocity and haematocrit indices of each sample and at each level of haematocrit (Table 3.1). In addition, due to the fact the population of each sample was not large enough to indicate certain statistical results, all the 'non-healthy' RBC samples (GA 0.04%, GA 0.08% and Aged samples) were grouped and examined statistically at each haematocrit level. Moreover, the populations of the samples were tested using the t-test hypothesis to examine statistical differences between the populations (Table 3.2).

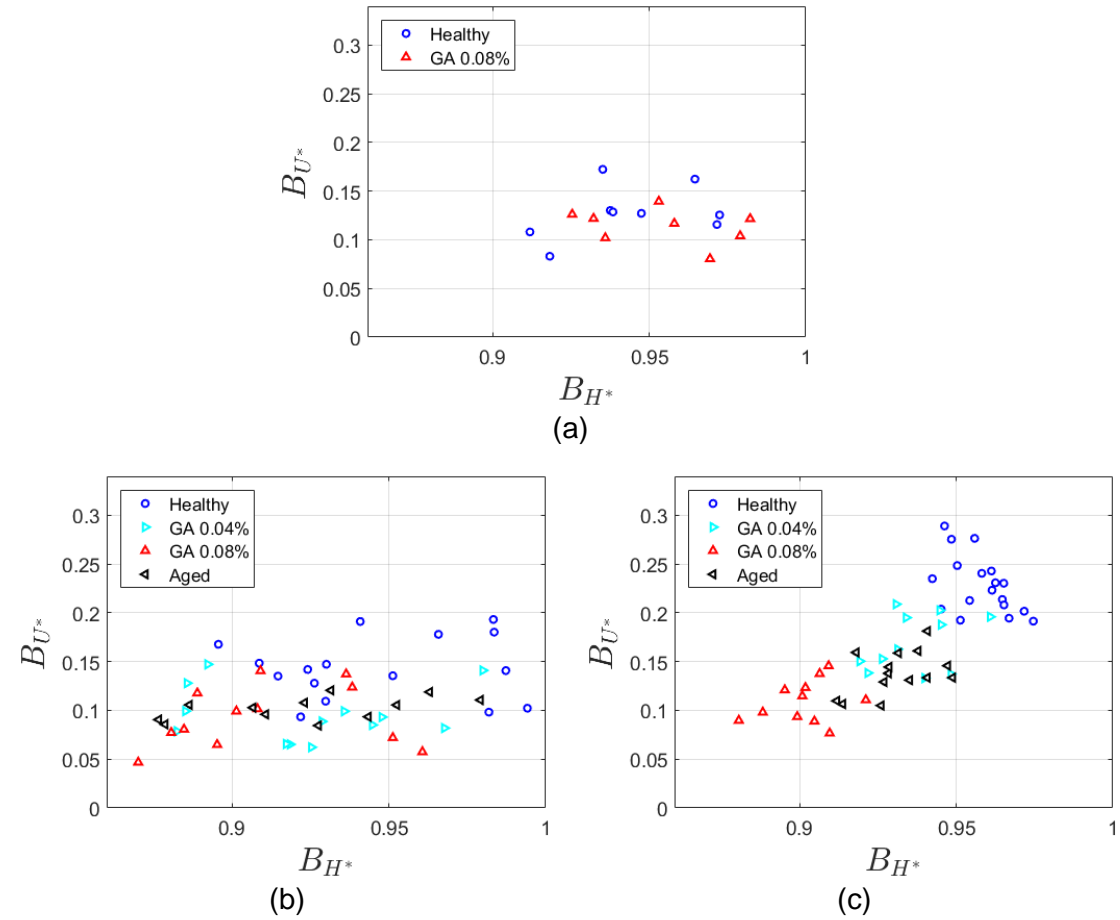


Figure 3.9: Velocity bluntness vs haematocrit bluntness index for the measured samples at (a) Ht = 5%, (b) Ht = 10% and (c) Ht = 25%.

The samples at lower haematocrits 5% and 10% (Figure 3.9 a, b) show no significant correlation between haematocrit and velocity bluntness. However, the t-test statistical hypothesis, between the hardened and aged samples in comparison to the healthy sample, show statistically significant differences at 10% haematocrit level with p-values: $p_{\text{healthy-GA0.04\%}} < 10^{-3}$, $p_{\text{healthy-GA0.08\%}} < 10^{-4}$, $p_{\text{healthy-Aged}} < 0.05$ (Table 3.2). At 5% haematocrit the GA 0.08% sample in comparison to the healthy sample show no significant differences in B_{U^*} - B_{H^*} values ($p > 0.05$).

On the contrary, at 25% haematocrit the healthy RBC samples show a significant negative correlation ($r_{\text{healthy}} = -0.50$, $p = 0.03$) between the velocity and haematocrit profile bluntness in agreement with previous studies (Sherwood *et al.* 2014b). On the other hand, the hardened and aged samples show positive correlation between velocity and haematocrit indices, but the trends are not statistically significant ($r_{\text{GA } 0.04\%} = 0.32$, $r_{\text{GA } 0.08\%} = 0.42$, $r_{\text{aged}} = 0.47$ with $p > 0.05$). However, the grouped analysis of the non-healthy RBC samples shows significant positive correlation of B_U-B_H with $r_{\text{group}} = 0.67$ and $p_{\text{group}} < 10^{-5}$.

Table 3.1: Pearson correlation coefficients for velocity and haematocrits bluntness indices.

Ht	sample	Pearson r	p-value
5%	Healthy	0.16	0.67
	GA 0.08%	-0.43	0.30
10%	Healthy	-0.28	0.21
	GA 0.04%	0.03	0.78
	GA 0.08%	0.17	0.58
	Aged	0.53	0.07
	Grouped	0.15	0.36
25%	Healthy	-0.50	0.03
	GA 0.04%	0.32	0.27
	GA 0.08%	0.42	0.33
	Aged	0.47	0.09
	Grouped	0.67	$<10^{-5}$

Table 3.2: T-test coefficients comparing the data sets of each sample against the healthy sample.

Ht	sample	t-test	p-value
5%	Healthy - GA 0.08%	0	0.28
10%	Healthy - GA 0.04%	1	$<10^{-3}$
	Healthy - GA 0.08%	1	$<10^{-4}$
	Healthy - Aged	1	0.05
25%	Healthy - GA 0.04%	1	$<10^{-5}$
	Healthy - GA 0.08%	1	$<10^{-5}$
	Healthy - Aged	1	$<10^{-9}$

3.5 Discussion

The measured velocity profiles (Figure 3.2b) and corresponding bluntness indices (Figure 3.4c) of denser RBC suspensions, indicate that loss of deformability results in sharper more Newtonian like velocity profiles. This implies a reduction in the shear thinning nature of RBC suspensions with hardening which is well documented in the literature. It has been clearly demonstrated that the loss of RBC deformability results in blood to be less shear thinning exhibiting lower viscosity values at the low shear region and elevated values at high shear rates compared to the healthy RBC suspensions (Chien, 1987; Lanotte *et al.*, 2016). Hardened RBCs are able to preserve their hydrodynamic - stress-free shape during shear deformation resulting in constant viscosity values with increasing shear rate. In contrast, healthy RBCs tend to adopt 'croissant' or

'sliper' like shapes depending on velocity (Kihm *et al.*, 2018), within the studied range of normalised velocities. The shape alteration of healthy RBCs, results in symmetry breaking inducing an additional deformability induced lift force which increases RBC lateral migration, while RBC hardening decreases the deformability induced lift forces and hence hardened cells are expected to migrate less laterally (Goldsmith, 1968; Losserand, Couplier and Podgorski, 2019). The increased lateral activity that healthy RBCs exhibit, correspond to increased energy dissipation; hardened RBCs are apt to accumulate in the axial region of the channel where minimum shear applies, resulting in decreased energy dissipation compared to healthy RBCs (Jeffery, 1922; Fahraeus, 1958). This can be seen at the measured velocity profiles of denser suspensions (25% haematocrit) which indicate that hardened RBCs exhibit less blunt velocity profiles (more Newtonian like behaviour) compared to healthy RBCs. In the more dilute samples - 10% haematocrit - the effect is less pronounced (Figure 3.4b) and it is not apparent at 5% haematocrit (Figure 3.4a) where healthy and hardened RBCs produce velocity profiles with similar bluntness.

The decreased lateral migration properties of hardened RBCs compared to healthy suspensions are expected to result to more dispersed distribution of cells across the flow. The measured haematocrit profiles of dilute suspensions - 5% haematocrit - show a slight increase in the haematocrit profile bluntness for hardened RBCs compared to normal RBCs implying more uniform cell distributions (Figure 3.8a). On the contrary, the measured haematocrit profiles of denser RBCs suspensions show a sharper distribution for hardened RBCs

compared to healthy ones (Figure 3.6, Figure 3.7c), implying that hardened RBCs concentrate more towards the centre of the channel.

Sharp concentration distributions have been reported for dense rigid particle suspensions in rectangular channel flows by Lyon and Leal (1998) and have been attributed to shear induced migration effects. RBC hardening affects the individual motion of the cells and in addition the collision dynamics. These effects in combination with the altered local shear gradients might give rise to the observed haematocrit distributions at the denser RBC suspensions. In Figure 3.10 a comparison of shear rate distribution is exhibited between the RBC samples. Hardened RBCs samples exhibit higher shear rates than the healthy samples near the walls indicating stronger shear induced migration of the RBCs towards the centre of the flow where the shear rate is lower.

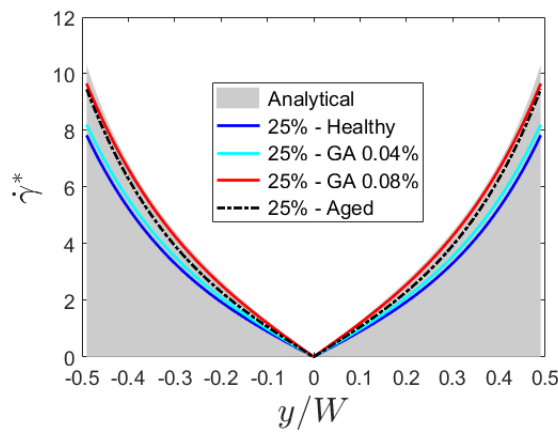


Figure 3.10: Shear rate distribution of normalised velocity profiles around 40 s^{-1} of 25% haematocrit samples, compared to analytical. The shear rate was calculated using central differencing.

The inversely proportional relationship of velocity and haematocrit bluntness between healthy and hardened RBCs (Figure 3.9c) might seem as counter

intuitive according to the dependency of suspension viscosity on particle concentration. It would be expected that the increase of local viscosity with haematocrit concentration in the centreline, would decrease the local velocity therein, producing a blunter velocity profile. However, that was not the case in this study; this might imply that for the range of haematocrits examined there is no significant effect of cell concentration on viscosity. Indeed, it a very moderate increase in viscosity for hardened cells has been reported (Chien *et al.*, 1967) for haematocrits varied up to 30%.

Moreover, hardened RBCs show a substantial increase in tumbling behaviour within these flow rates (Forsyth *et al.*, 2010) leading to higher effective viscosity (Chien, 1987) and corresponding to the least dissipation of energy (Dupire, Socol and Viallat, 2012). Low haematocrits promote the tumbling motion of hardened RBCs since there is more space for the cells to rotate freely. At higher concentrations though, simulations of plate like particles have shown that as the volume fraction increases the particles tend to align in ordered layers forming stacks as there is not sufficient volume around the particles to perform tumbling motion (Meng and Higdon, 2008). In this way, due to this flow alignment and RBC ordering there is no elevated viscosity in the centreline which can further explain the observed trends.

3.6 Closure

In this chapter the effect of deformability on the microscale flow behaviour of red blood cell suspensions was examined. RBC samples with different deformability were perfused in a straight microchannel at different flow rates and feed

haematocrits. Velocity and haematocrit profiles were determined experimentally and compared. Hardened RBCs exhibited sharper haematocrit profiles than the healthy RBCs meaning that their distribution was more focused in the centre of the channel. In addition, the velocity profiles of the hardened RBCs were sharper than the healthy ones. This trend was haematocrit dependent as it was mostly apparent in the denser RBC suspensions, i.e. 25%, while for the most dilute suspensions (5%) the differences were negligible. Furthermore, the flowrates that were examined seemed to not have any statistically significant effect on the haematocrit and velocity profiles of the perfused samples. In the next chapter, the margination of hardened RBCs while flowing within healthy RBCs will be examined, as well as, the effect of confinement by perfusing healthy and hardened samples in $100 \times 25 \mu\text{m}^2$ channels.

Chapter 4

Confinement and margination of hardened RBCs

In this chapter, the margination of hardened RBCs within healthy and hardened RBC suspensions are examined. A small amount of hardened RBCs were fluorescently labelled and suspended in both healthy and hardened RBC suspensions. The lateral position of the labelled cells was tracked and determined near the inlet and outlet of the channel respectively, obtaining the probability density function of their distribution.

Moreover, the effect of confinement on velocity and haematocrit distributions of healthy and hardened RBC samples was examined. The samples were perfused through a straight microchannel with higher aspect ratio ($AR = 4$) in order to compare the velocity and haematocrit profiles between channels of different aspect ratios.

4.1 Introduction

In blood vessels, RBCs migrate towards the centre resulting in the formation of a cell depletion layer near the wall. The mechanism of the inward migration is a combined effect of the curvature of the velocity profile and the boundary interactions with vessel walls. The membrane deformability of red blood cells is an important migration parameter as the rate of migration increases with deformability (Goldsmith, 1971; Kumar and Graham, 2012a, 2012b; Namgung *et al.*, 2017a). White blood cells and platelets have been found to flow within the RBC depleted layer, i.e. near the vessel walls, a process called 'margination'. The mechanism of this flow induced margination is attributed to cell-cell collisions which eventually segregate cells with different shape, size and deformability (D'Apolito *et al.*, 2015). Decreased membrane deformability has been shown to be the main reason of margination of WBCs and platelets compared to RBCs (Tangelder *et al.*, 1985; Fiebig *et al.*, 1991). Similarly, RBCs with decreased deformability, due to various pathologies (malaria, diabetes, sickle cell anemia), tend to marginate near the walls (Chen *et al.*, 2017). Hou *et al.*, (2010) developed a microfluidic device that segregated malaria infected RBCs by marginating them toward the wall of straight PDMS channels. The design consisted of a 3cm long $15 \times 10 \mu\text{m}^2$ (width x height) microchannel with an expanded 3-outlet ending that separated the stiffer malaria infected RBCs by their margination.

The margination of hardened RBCs has been also investigated *in vivo* showing that hardened RBCs preferentially accumulate near the vessel walls (Chen *et al.*, 2017; Namgung *et al.*, 2017), in particular within the range 0.7 – 0.9 of the vessel

radius. Kumar and Graham (2011,2012) through numerical simulations reported margination of the leukocytes due to their stiffer membrane. However, Freund (2007) suggested that leukocyte margination is much less correlated with their stiffer membrane but it is associated with the blunting of the velocity profile.

RBC dynamics vary from a single-cellular level to dense suspensions where collective hydrodynamic interactions are at play. Especially, in spatially confined geometries the collective haemodynamics of semi-dilute and dense suspensions play an important role to effects such as cell migration (Raj *et al.*, 2018). In addition, it has been reported that the aspect ratio of the channel affects the distribution of RBCs in microchannels with comparable dimensions to the size of an RBC (Grandchamp *et al.*, 2013). The $50 \times 50 \mu\text{m}^2$ microchannels that were used in Chapter 3 with aspect ratio 1:1, provided an axisymmetric distribution of velocity and shear along the y and z direction. Hence, under the assumption of negligible RBC sedimentation, the distributions of velocity and haematocrit were assumed to be the same in horizontal and vertical axes. Microchannels with higher aspect ratio would be expected to affect the velocity and haematocrit distributions of RBCs since the shear induced diffusion, wall lift force and cell-wall and cell-cell interactions are not symmetric in the directions perpendicular to the flow.

In this chapter, two types of experiments were conducted in order to examine firstly the margination of hardened RBCs with healthy RBCs in flow and secondly the role of aspect ratio on the haematocrit and velocity distributions respectively.

A small amount of hardened RBCs was perfused within a suspension of healthy RBCs in order to investigate the potential exclusion of hardened RBCs from healthy ones, due to deformability differences. In particular, RBC samples with 25% haematocrit were perfused through $50 \times 50 \mu\text{m}^2$ straight PDMS polymer microchannels and the ratio between healthy and hardened RBC was 25 to 1 respectively. Hardened RBCs were labelled with fluorescent dye and their lateral position in flow was tracked in order to determine their distribution across the flow.

The effect of aspect ratio was examined by perfusing healthy and hardened (GA 0.08%) RBC samples of 25% haematocrit through straight microchannels with a cross sectional area of $100 \times 25 \mu\text{m}^2$ (width = $100 \mu\text{m}$ and height = $25 \mu\text{m}$) at flow rates ranging between 1 and 200 s^{-1} and comparing the results with those of Chapter 3 where $50 \times 50 \mu\text{m}^2$ microchannels were used. In $50 \times 50 \mu\text{m}^2$ microchannels the ratio between channel height and RBC diameter is around 6.25 considering a channel height of $50 \mu\text{m}$ and an RBC diameter of $8 \mu\text{m}$, while in $100 \times 25 \mu\text{m}^2$ channel the cell-channel size ratio is 12.5 and 3.13 for the $100 \mu\text{m}$ and $25 \mu\text{m}$ widths respectively.

4.2 Margination of hardened RBCs

The findings in Chapter 3 have demonstrated a negative correlation between the bluntness of the velocity and haematocrit profiles of hardened RBCs in dilute suspensions (5% Ht). On the other hand, dense suspensions (25% Ht) of hardened RBCs showed a contradictory trend with the haematocrit profile of hardened cells appearing sharper. The contradictory trends between dense and dilute hardened RBC suspensions might be attributed to collective

hydrodynamics effects. In some diseases, for example malaria, the majority of RBCs become stiffer, while in other diseases, a lower amount of RBCs is affected. In this work, the flow of a low concentration hardened RBCs within dense suspension of healthy RBCs was studied. Two cases were analysed: labelled-hardened RBCs flowing within hardened RBCs (as the control case) and labelled-hardened RBCs flowing among healthy RBC suspensions. In both cases the total haematocrit was 25% out of which 1% was the labelled-hardened RBCs. Fluorescent dye was utilised for labelling the cells and the distribution of labelled RBCs was determined by tracking their lateral position as described in Chapter 2. The flow was monitored 10 channel widths (i.e. 500 μm) downstream the inlet and upstream the outlet at flow rate of 60 s^{-1} . The total length of the microchannel was 16 mm.

Figure 4.1 shows a comparison between the distributions of labelled-hardened cells near the inlet and outlet for each of the samples. In Figure 4.1a the hardened labelled RBCs were suspended in dense suspensions of healthy RBCs and their distribution near the inlet seems to follow the overall haematocrit distribution, determined by the mean image intensity, while near the outlet of the channel the distribution of labelled-hardened cells shows evidence of margination. On the contrary, in Figure 4.1b the labelled-hardened RBCs flowing in hardened RBC suspensions, exhibit distributions that follow the overall haematocrit profile, as shown in Figure 4.2c through image intensity, both near the inlet and the outlet.

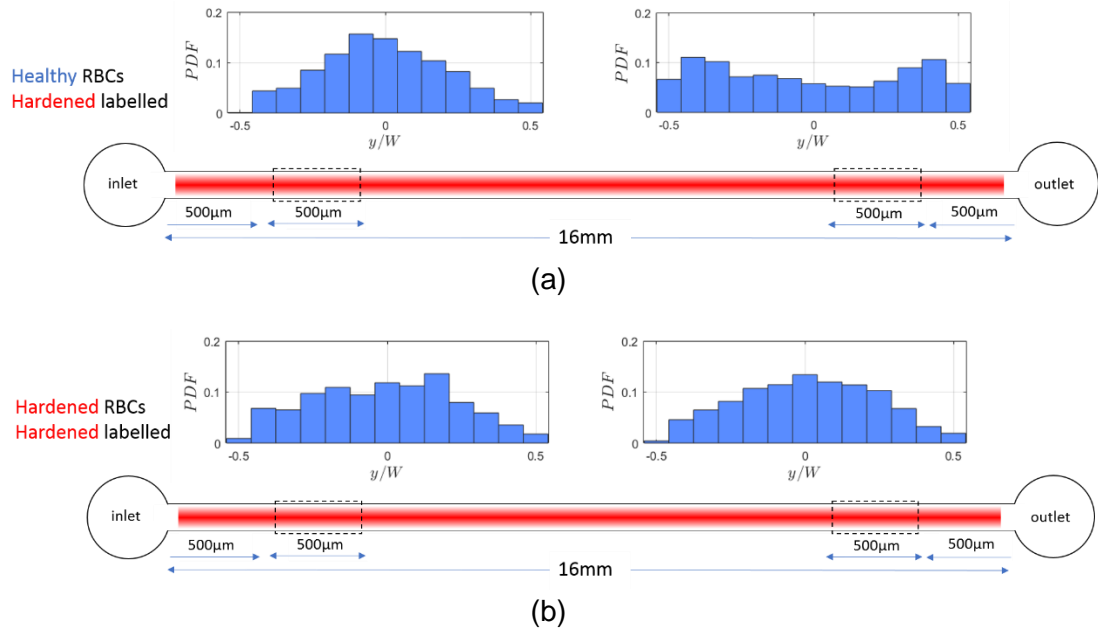


Figure 4.1: Distribution of labelled hardened RBCs in dense suspensions of healthy and hardened RBCs near the inlet and outlet of the square microchannel. The velocity per unit width was 60 s^{-1} and the distributions were produced by 1253 cells on average.

The distribution profiles of labelled RBCs near the outlet are more interesting to analyse since the migration phenomena through hydrodynamic forces or due to cell-cell interactions could be assumed to have reached an equilibrium (Noso et al., 2015). Figure 4.2a and b compare the probability density function (PDF) of the hardened labelled RBCs (1%) within the flow of a dense (25%) suspension of hardened and healthy RBCs near the outlet. Figure 4.2c,d show the corresponding time averaged image intensity distribution of the whole suspensions, illustrating the haematocrit distribution across the channel. The probability density function of the labelled RBCs follows the intensity distribution (and hence haematocrit) of the suspension of hardened cells (Figure 4.2a,c). In contrast, hardened labelled RBCs when suspended within healthy and fully deformable RBCs (Figure 4.2b) tend to migrate towards the wall in agreement with literature reporting margination of stiffer cells or particles (e.g. hardened

RBCs, white blood cells, platelets) (Kumar and Graham, 2012a, 2012b; Carboni *et al.*, 2016; Chen *et al.*, 2017; Namgung *et al.*, 2017).

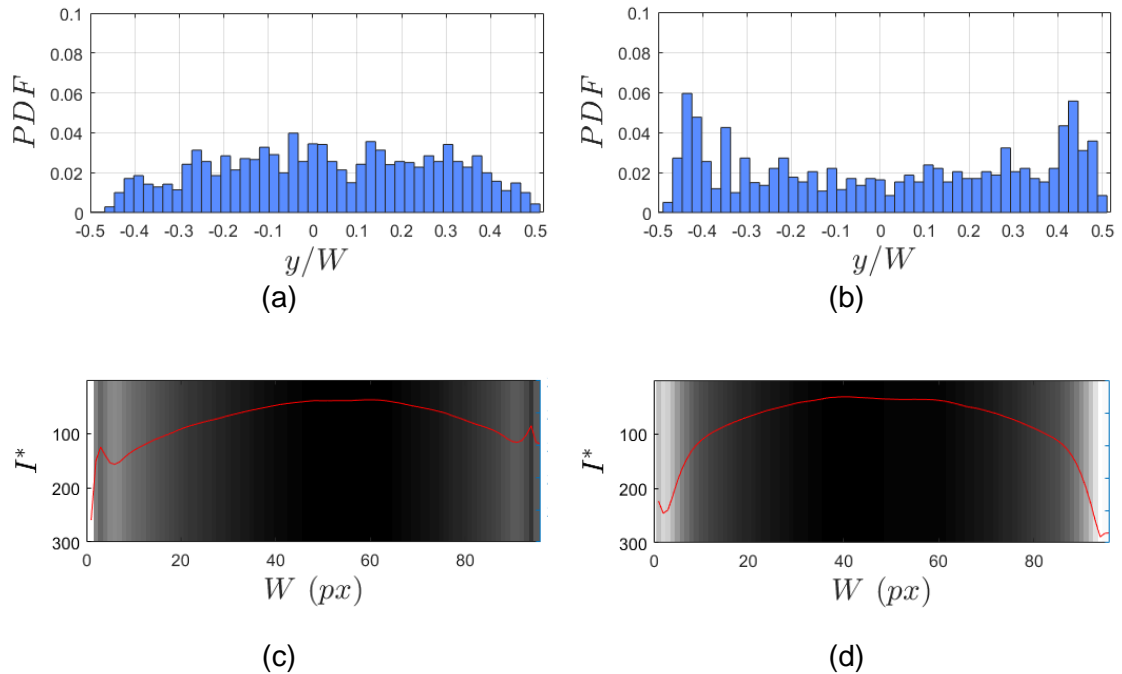


Figure 4.2: Probability density function (PDF) of 1% labelled hardened RBCs flowing within a 25% suspension of (a) hardened RBCs and (b) within healthy RBCs. (c) and (d) Normalised image intensity distribution for the (a) and (b) suspensions respectively. Measurements were acquired at a distance of $10W$ near the outlet of the $50 \times 50 \mu\text{m}^2$ microchannel and $U^* \approx 60 \text{s}^{-1}$. A total of (a) 1154 and (b) 1353 RBCs were tracked to produce the distributions.

Chen *et al.* (2017) investigated the margination of hardened RBCs through *in vivo* and *in vitro* experiments. In that study, *in vitro* experiments were conducted in rectangular microchannels ($100 \times 40 \mu\text{m}^2$) using 30% haematocrit and RBCs were artificially stiffened using diamide. Figure 4.3 shows a comparison of the present experiments with that study. The margination of hardened cells is apparent in both cases, however, in Chen *et al.* margination is more pronounced. This can be attributed mainly to the different aspect ratio of the channels, as non-

symmetrical hydrodynamic interactions were produced along the y and z directions. The effect of channel aspect ratio on haematocrit distribution will be further examined in the next section.

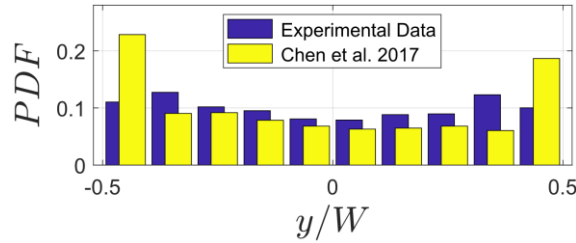


Figure 4.3: Probability density function of hardened RBCs, suspended in healthy RBCs. Comparison of the experimental results of the present study with data from literature. Data were reproduced from Chen et. (2017).

4.3 The effect of aspect ratio

4.3.1 Velocity distribution for a Newtonian fluid.

In Chapter 3, microchannels with $50 \times 50 \mu\text{m}^2$ cross - sectional area were studied i.e. aspect ratio 1:1 ($AR = 1$). The velocity and hence shear rate distribution in this channel is symmetric with respect to the centreline, i.e. the xy distribution is same as xz one. This allowed quasi-steady assumptions to be made as explained in Sherwood et al. (2014). In order to investigate the effect of confinement and the consistency of the results in channels with different aspect ratios, additional experiments were conducted using $100 \times 25 \mu\text{m}^2$ microchannels with an aspect ratio 4:1 ($AR = 4$).

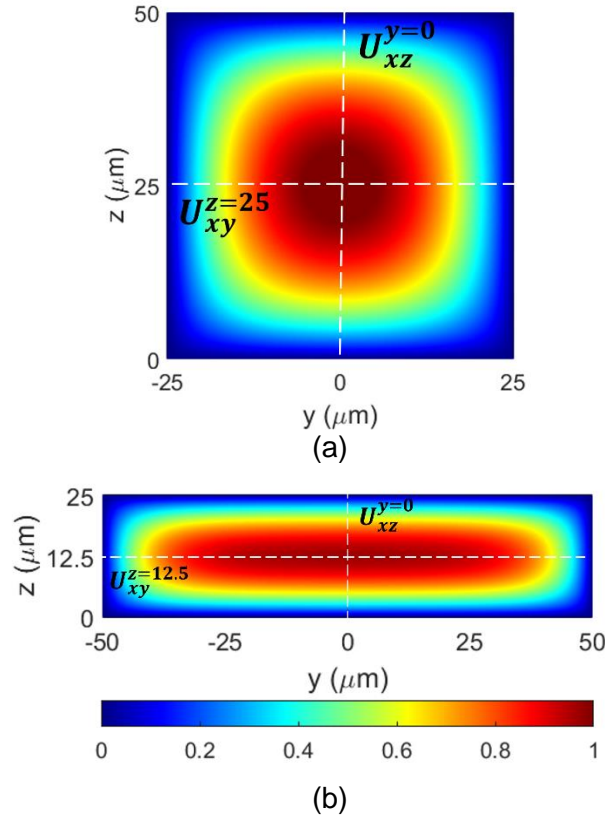


Figure 4.4: Cross-sectional velocity distribution of a Newtonian fluid described by the analytical form (Equation (2.1)) of (a) 50 μm square channel and (b) 100 μm x 25 μm² channel.

Figure 4.4 shows the cross-sectional velocity distribution in 50 x 50 μm² and 100 x 25 μm² channels as described by the analytical solution for rectangular microchannels (Equation (2.1)). The xy-plane, $z = 25$ μm and $z = 12.5$ μm for the 50 x 50 μm² and 100 x 25 μm² respectively, correspond to the planes of observation i.e. the measurement planes. Considering that sedimentation effects are negligible within the duration of each measurements – 60 images and 6 Hz acquisition frequency (10 sec) – it can be safely assumed that for the 50 x 50 μm² channels, the velocity distribution is similar between the measuring plane (xy-plane) and the perpendicular plane (xz-plane) i.e. $U_{xy}^{z=\text{middle}} = U_{xz}^{y=\text{middle}}$. However, in higher aspect ratio channels the velocity and shear rate distribution

along the two planes is not equivalent. In the $100 \times 25 \mu\text{m}^2$ channel, the velocity and shear rate curvature is expected to be higher perpendicularly to the measuring plane, i.e. along the z-direction.

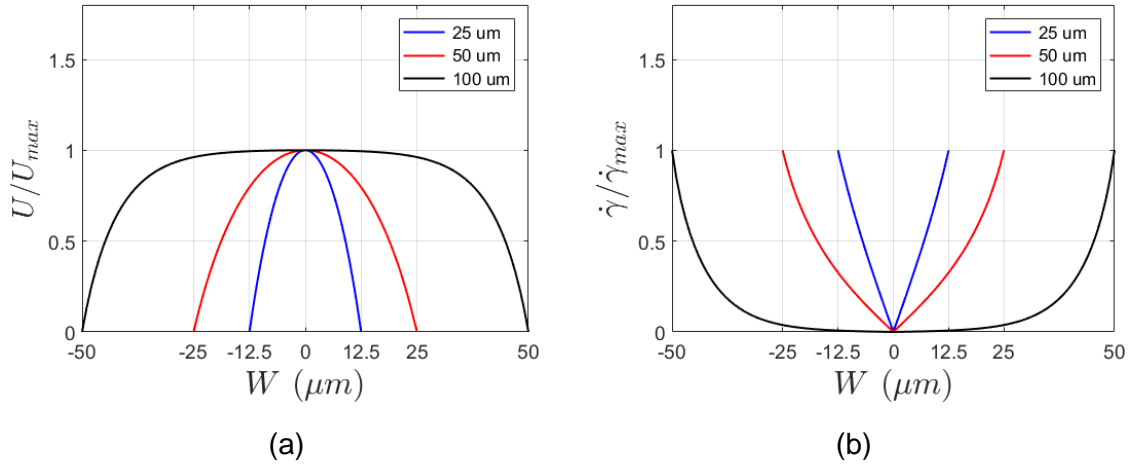


Figure 4.5: (a) Analytical velocity profiles for a Newtonian fluid (2.1), normalised with maximum velocity for 25, 50 and 100 μm channel widths. (b) Shear rate distribution of the normalised analytical velocity profiles distributed for channel widths of 25, 50 and 100 μm . The red profile corresponds to the $50 \times 50 \mu\text{m}^2$ channel: $U_{xy}^{z=25} = U_{xz}^{y=0}$. The blue and black profiles correspond the $100 \times 25 \mu\text{m}^2$ channel for $U_{xy}^{z=12.5}$ and $U_{xz}^{y=0}$ respectively.

Figure 4.5a shows the analytical velocity profiles for flow of Newtonian fluids in rectangular channels. The analytical solution is described by equation (2.1) and the profiles are normalised by the maximum velocity. The black velocity profile corresponds to the mid xy-plane ($z = 12.5 \mu\text{m}$) of the $100 \times 25 \mu\text{m}^2$ channel with while the blue corresponds to the velocity profile in the mid xz-plane ($y = 0 \mu\text{m}$), the widths for each case are 100 μm and 25 μm respectively. The velocity profile of the wider side (black profile – Figure 4.5a) is more uniform in the centre of the channel along the measuring plane (xy-plane), corresponding to a fairly wide region of negligible shear rate (black profile – Figure 4.5b) in the centre of the

channel. The cross-streamline migration of RBCs is proportional to the curvature of the velocity profile, hence shear rate, (Kaoui *et al.*, 2008; Kumar and Graham, 2011; Grandchamp *et al.*, 2013), leading to pronounced shear induced migration along the z-direction (perpendicularly to the measurement plane) compared to the y-direction. Moreover, the ratio of RBC size to channel dimensions, changes within channels with different aspect ratio ($50 \times 50 \mu\text{m}^2$ and $100 \times 25 \mu\text{m}^2$ channels) affecting the wall effects on the RBCs. The wall-lift force increases as the ratio of channel dimensions to RBC size decreases (Chu and Ng, 1989). The typical RBC diameter is considered around $r_{\text{RBC}} = 8 \mu\text{m}$, hence the RBC to channel width ratio in $50 \times 50 \mu\text{m}^2$ channels was $H_{50}/r_{\text{RBC}} = 6.25$ for both xy and xz planes, while in $100 \times 25 \mu\text{m}^2$ was $W_{100}/r_{\text{RBC}} = 12.50$ and $H_{25}/r_{\text{RBC}} = 3.13$ for the measuring xy and xz-planes respectively. Figure 4.6 shows sample images of healthy RBC suspensions of 25% haematocrit in $50 \times 50 \mu\text{m}^2$ and $100 \times 25 \mu\text{m}^2$ microchannels and it can be seen that the impact of the high aspect ratio on the images is evident. In the next section, the velocity profiles of RBCs flowing in $100 \times 25 \mu\text{m}^2$ channels are investigated and compared to the $50 \times 50 \mu\text{m}^2$.

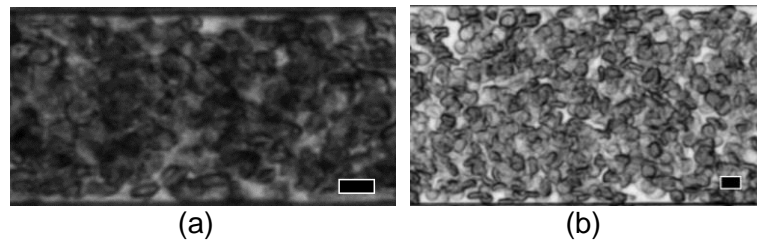


Figure 4.6: Healthy RBC suspensions in flow in (a) $50 \times 50 \mu\text{m}^2$ channel and (b) $100 \times 25 \mu\text{m}^2$ channel. Haematocrit 25%. Scale bars correspond to $10 \mu\text{m}$.

4.3.2 Velocity profiles of hardened RBCs in 100 x 25 μm channels

Figure 4.7a shows a comparison of typical velocity profiles between RBC samples with different membrane deformability for a 25% haematocrit. The velocity profiles were compared to the analytical velocity profile for a Newtonian fluid in a rectangular channel (Bruus, 2008). Similarly to Chapter 3, hardened RBCs samples produce velocity profiles closer to the analytical solution compared to the healthy RBCs samples which produce blunter velocity profiles. Due to the higher aspect ratio of the 100 x 25 μm^2 channels, the velocity profiles are expected to be more uniform than the profiles that were examined in Chapter 3 for 50 x 50 μm^2 microchannels. Figure 4.7 (b,c,d) compares the velocity profiles between the channels with different aspect ratios for the three samples the same flow rate ($U^* = 29 \text{ s}^{-1}$). The 100 x 25 μm^2 velocity profiles appear to be blunter than the 50 x 50 μm^2 channels in all cases as expected.

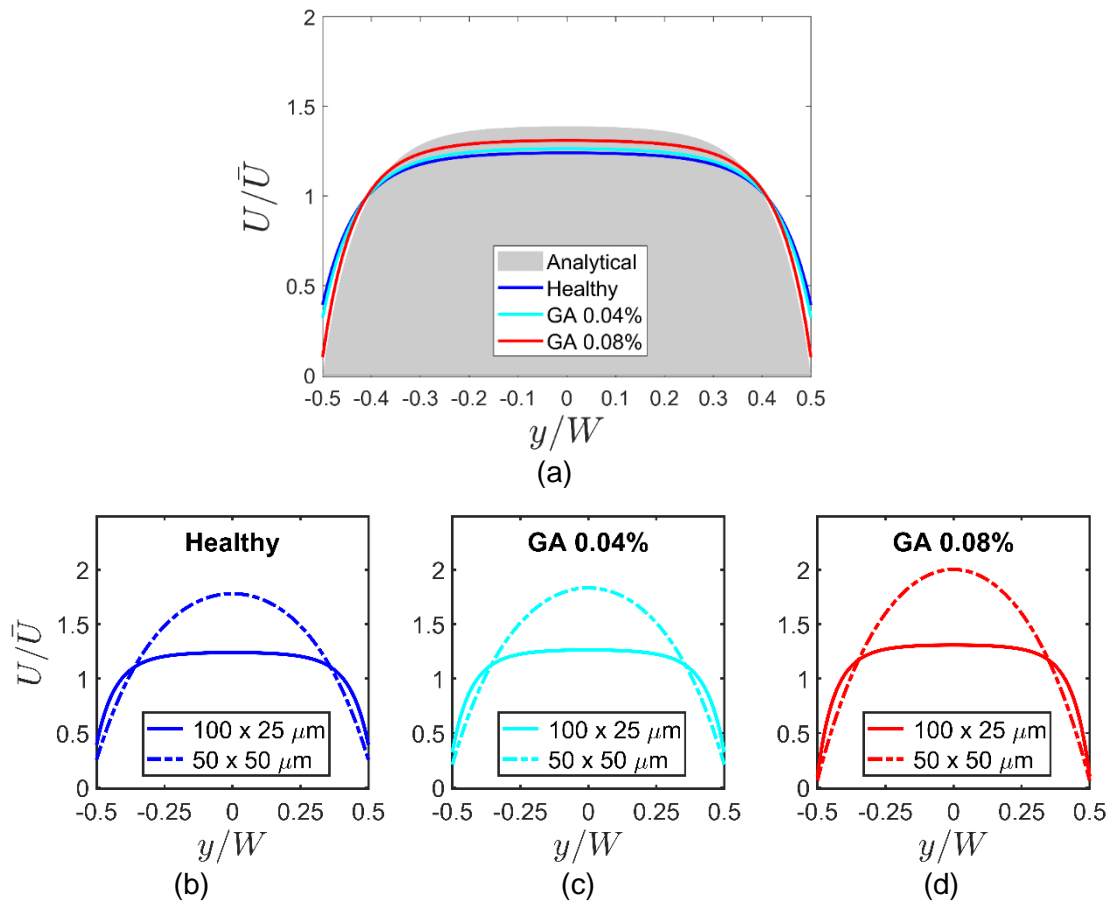


Figure 4.7: (a) Comparison of normalised velocity profiles for 25% haematocrit flows of healthy, and hardened (0.04% and 0.08% GA) RBCs at 29 s^{-1} . The grey area indicates the analytical solution for the laminar flow of a Newtonian fluid in the rectangular channel. Comparison of normalised RBC velocity profiles at $U^* = 29 \text{ s}^{-1}$ in $100 \times 25 \mu\text{m}^2$ and $50 \times 50 \mu\text{m}^2$ channels for the three samples (b) Healthy, (c) GA 0.04%, (d) GA 0.08%.

In order to investigate the effect of flow rate on the velocity profiles, the RBC suspensions were perfused in the microchannels with flow rates ranging from 1 to 200 s^{-1} . The velocity profile bluntness indices were plotted as a function of flow rate in Figure 4.8a. The healthy samples produce blunter velocity profiles in the whole range of measurements and the bluntness of the velocity profiles is not affected by the flow rate. The hardened RBC samples exhibit the same trend i.e. their velocity bluntness is flow rate independent in the measured range of flow

rates. Pearson correlation test was utilised showing non-significant correlation between B_U^* and U^* .

The boxplots in Figure 4.8b indicate that the GA 0.08% RBC samples exhibit reduced velocity bluntness index meaning that the velocity profiles exhibit sharper distribution than the healthy ones. The difference between healthy and GA 0.08% samples is statistically significant ($P < 10^{-7}$) using the t-test. The difference between healthy and GA 0.04% is less statistically significant with $p < 0.07$, indicating that the effect of decreased deformability on velocity bluntness is less pronounced in channels with higher aspect ratio.

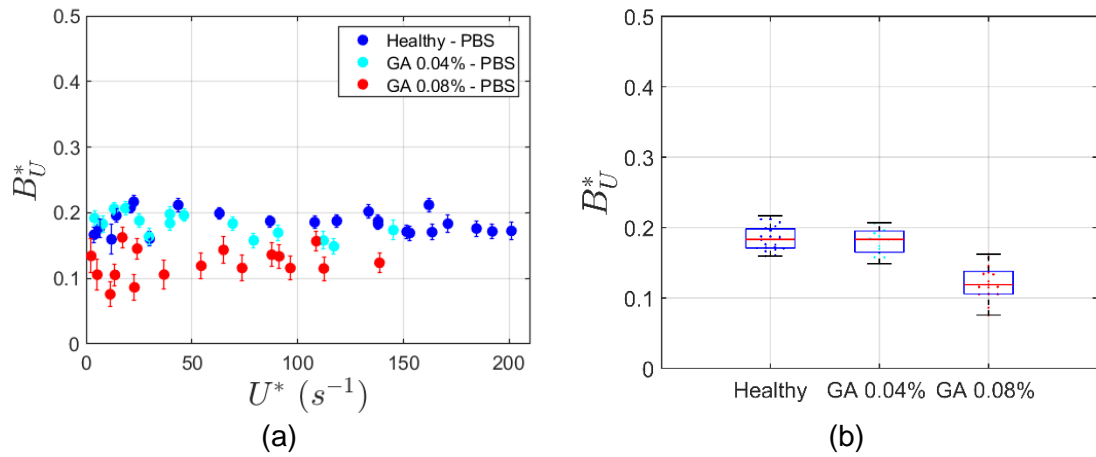


Figure 4.8: (a) Velocity bluntness index as a function of normalised velocity U^* for RBC samples with different membrane stiffness at different flow rates. (b) Boxplots of B_U for the three samples. The central red lines indicate the median of the measurements and the bottom and top sides of the box indicate the 25th and 75th percentiles, respectively.

4.3.3 Haematocrit profiles of hardened RBCs in 100 x 25 μm channels

The haematocrit distribution was expressed by utilising the image intensity distribution across the channel. For the 50 x 50 μm^2 channels the image intensity was correlated to haematocrit through a calibration procedure as explained in chapter 2. For the 100 x 25 μm^2 channels, in the absence of such calibration data, the haematocrit profiles were expressed in terms of image intensity profiles.

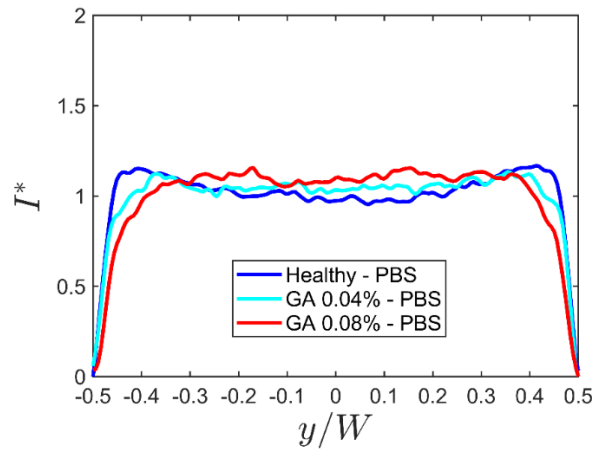


Figure 4.9: Typical image intensity profiles, normalised with the average image intensity, measured in the high aspect ratio microchannel for the healthy and hardened RBCs suspensions of 25% haematocrit at $U^* = 29 \text{ s}^{-1}$.

Figure 4.9 shows some typical normalised image intensity profiles of healthy, GA 0.04% and GA 0.08% RBC samples for 25% haematocrit at $U^* = 29 \text{ s}^{-1}$. As expected, the distribution of intensity and hence haematocrit appears flatter than the haematocrit distribution in square channels, due to the higher aspect ratio of 100 x 25 μm^2 channels. The hardened samples exhibit a sharper haematocrit (intensity) distribution than the healthy samples in agreement with the findings in Chapter 3 for 50 x 50 μm^2 microchannels. Moreover, the intensity distributions in Figure 4.9 show that the haematocrit of the healthy sample is slightly decreased

near the centre compared to the haematocrit near the walls. This can be attributed to the increased shear towards the z-direction as it will be discussed later in the chapter. A similar distribution has also been observed by Iss *et al.* (2019) in microchannels of $60 \times 9 \mu\text{m}^2$ ($\text{AR} \approx 6.5$) and 26% haematocrit.

In Figure 4.10a the effect of flow rate on the haematocrit distribution (image intensity) was examined. The RBC samples showed no significant variations with flow rate increase; the correlation between B_I and U^* was found to be insignificant using Pearson correlation test for the three samples. However, the B_I of GA 0.04% and GA 0.08% samples were significantly lower than the healthy ones in the whole range of flow rates with $p < 10^{-10}$ and $p < 10^{-3}$ respectively (Figure 4.10b); similar to the findings of Chapter 3 for the $50 \times 50 \mu\text{m}^2$ channels.

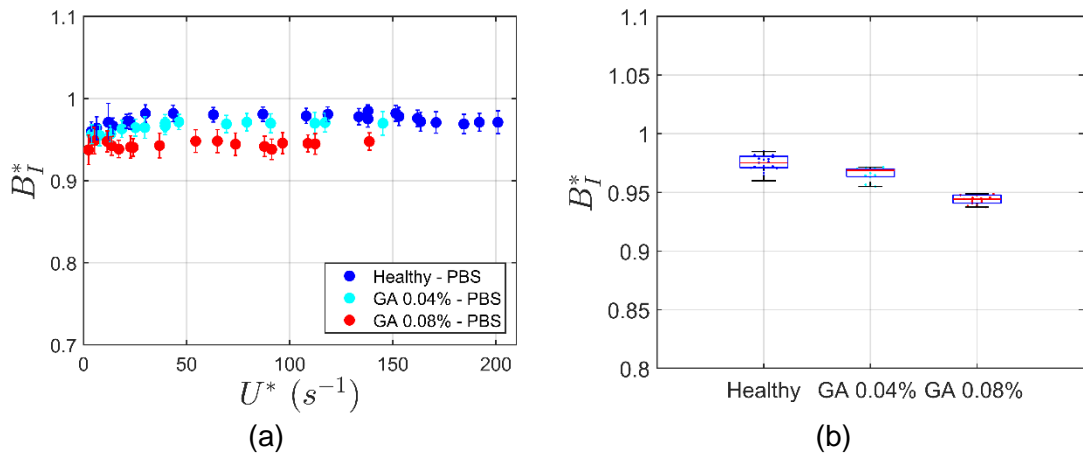


Figure 4.10: (a) Image intensity (equivalent to haematocrit) bluntness index, B_I^* , as a function of normalised velocity U^* for RBC samples with different membrane stiffness at different flow rates. The error bars show one standard deviation. (b) Boxplots of B_I^* for the three samples. The central red lines indicate the median of the measurements and the bottom and top sides of the box indicate the 25th and 75th percentiles, respectively.

4.4 Discussion

4.4.1 Margination of hardened RBCs

The distribution of labelled-hardened RBCs near the inlet followed the overall distribution of haematocrit in both RBC suspensions, healthy and hardened. This was expected since near the inlet the length was not sufficient enough for the cells with different deformability to interact in order for segregation to occur. This result agrees with the experiments of Hou *et al.* (2010) who observed that near the inlet of their device the malaria infected RBCs did not marginate while near the outlet the malaria RBCs were found to be displaced to the sidewalls.

Munn and Dupin (2008) explained the margination of stiffer particles towards the walls based on single particle arguments, namely that the more deformable particles tend to migrate toward the centreline due to the wall lift force and consequently displace hard particles to the sides. The wall induced lift force arises from the asymmetric pressure field that develops as cells deform near the wall, which consequently pushes the cells towards the flow centreline (Carboni *et al.*, 2016). The magnitude of the lift force depends on cell deformability; more deformable cells experience higher lift force magnitude than hardened ones. This approach agrees with the results of the present experiments, however, single particle arguments are not sufficient to provide full explanation of the phenomenon in dense suspensions in which the interaction between particles or cells is expected to play a dominant role to the mechanism of flow induced segregation. Kumar and Graham, (2011, 2012b) have revealed through particle dynamics simulations that collisions of ‘stiff’ particles in a ‘floppy’ particle

suspension resulted in margination of stiff particles toward the wall in agreement with the results of the current experiments.

The cases that were analysed in the present experiments were dense suspensions of (a) labelled-hardened within hardened and (b) labelled-hardened within healthy RBCs. In case (a) the distribution of labelled RBCs was expected to follow the overall distribution of hardened RBCs since the labelled cells have the same deformability with the rest of the suspension. In case (b) the collisions of labelled-hardened RBCs with the healthy-deformable RBCs push the first towards the walls. Therefore, it appears that the mean effect of these heterogeneous collisions was the margination of labelled-hardened RBCs to side of the flow in agreement with literature (Czaja *et al.*, 2020).

4.4.2 Effect of confinement

The opposing mechanisms that act on RBCs during flow in microvasculature have as a result the non-homogeneous RBC distribution. These mechanisms are mainly the wall-lift force and shear induced migration, which push the cells towards the centre of the flow, opposing to the shear induced dispersion of the RBCs, which is a result of cell-cell collisions, driving a diffusion like motion of the cells away from the areas of high concentration (Goldsmith, 1971; Leighton and Acrivos, 1987; Grandchamp *et al.*, 2013; Geislinger and Franke, 2014; Secomb, 2017).

In the current experiments, the $100 \times 25 \mu\text{m}^2$ channels were found to exhibit different velocity and haematocrit distribution compared to the $50 \times 50 \mu\text{m}^2$ as

expected. The wall-lift force, the shear induced migration and cell interactions in xy and xz planes are affected as the aspect ratio is different. In particular, the hydrodynamic interactions in the $100 \times 25 \mu\text{m}^2$ channel are dominant in the z-direction due to the increased confinement ratio (h/W). Grandchamp *et al.* (2013) performed experiments with healthy RBCs in PDMS channels with high aspect ratios ($491 \times 53 \mu\text{m}$ and $497 \times 101 \mu\text{m}$) and physiological flow rates (10 to 340 s^{-1}) and found that the strong shear in z-direction leads to a cell diffusion in y-direction causing a widening of the cell distribution. These results agree with the current findings as healthy RBCs have a wide distribution as it was shown in the individual distributions of Figure 4.9a and B₁ boxplots in Figure 4.9b. On the other hand, the hardened RBCs, exhibit less uniform distributions compared to the healthy ones. The decreased membrane deformability of hardened RBCs results in a less pronounced RBC diffusion in y-direction. This can be attributed to the different type of collisions between the hardened and healthy RBCs (Czaja *et al.*, 2020) in combination with the different effect of shear and wall lift force on the RBCs based on their deformability (Losserand *et al.*, 2019).

4.5 Closure

In this chapter, the margination of hardened RBCs within healthy RBC suspensions was examined, as well as, the effect of confinement on the haematocrit and velocity distributions of healthy and hardened RBC suspensions.

Hardened RBCs were labelled and diluted in healthy RBC suspensions in 1:25 ratio of a total 25% haematocrit. It was found that the hardened RBCs get pushed towards the walls by the healthy RBCs. The margination of hardened RBCs was

found to occur near the outlet of the channel, 300 channel widths downstream the inlet. In contrast, margination was not apparent near the inlet (10 channel widths downstream the inlet). However, when labelled-hardened RBCs were diluted within hardened RBC suspensions they did not exhibit margination as expected due to the absence of heterogeneous collisions.

In microchannels with higher aspect ratio ($100 \times 25 \mu\text{m}^2$, $\text{AR} = 4$) the haematocrit and velocity distributions of the samples were wider than the profiles in Chapter 3, with microchannels of aspect ratio equal to one. The hardened samples in the $100 \times 25 \mu\text{m}^2$ channels exhibited less uniform haematocrit distributions than the healthy ones. Moreover, the velocity profiles of hardened RBCs were closer to the analytical velocity profile of Newtonian fluids as expected from the findings of Chapter 3.

In the next chapter, the effect of deformability on aggregation properties will be examined in straight microchannels $50 \times 50 \mu\text{m}^2$.

Chapter 5

Effect of RBC deformability on aggregation

In this chapter the impact of RBC hardening on aggregation during flow in straight microchannels is examined. As in previous chapters individual velocity and haematocrit profiles were compared, and velocity and haematocrit profile bluntness indices were utilised to quantify changes in the measured distributions. The extent of aggregation was also quantified by estimating the standard deviation of the image intensity of the acquired RBC images.²

² The data presented in this chapter have been published in 'Passos A, Sherwood JM, Agrawal R, Pavesio C, Balabani S. Effects of erythrocyte properties on microscale blood flow velocities measured by μ PIV. 9th World Conference on Experimental Heat Transfer, Fluid Mechanics and Thermodynamics, Iguazu Falls, Brazil, 12-15 June 2017'. The work was also presented at '6th Micro and Nano Flows Conference Atlanta, USA, 9-12 September 2018.

5.1 Introduction

RBC aggregation is a physiological phenomenon that occurs mostly in the post capillary part of microcirculation, i.e. the venules, characterised by low shear rates. The process of aggregation is reversible and it is shear and haematocrit dependent. RBC aggregates or rouleaux increase blood viscosity at the lower flow rates (Chien *et al.*, 1967) and affect microstructural parameters like the cell depleted layer (Reinke *et al.*, 1987; Li *et al.*, 2012; Sherwood *et al.*, 2014a) and RBC migration properties (Bishop *et al.*, 2001). Aggregation can be enhanced in the presence of ongoing inflammation due to the increased levels of plasma proteins, especially fibrinogen (Demiroğlu *et al.*, 1998; Adar *et al.*, 2008). Under healthy conditions, RBC aggregates disaggregate by flow induced shear forces before they reach the microcirculation. However, in pathological conditions (e.g. bacterial sepsis) RBCs aggregate in larger clusters (Ben-Ami *et al.*, 2003) which may hinder tissue perfusion and oxygenation (Mchedlishvili, 2007). The propensity of RBCs to aggregate can be affected by altered mechanical properties of RBCs, e.g. deformability. In many pathological conditions such as in heart disease, hypertension, diabetes, malaria, and sickle cell anemia, RBCs may exhibit reduced deformability which might affect aggregation properties (Popel and Johnson, 2005).

In this chapter, the effect of RBC hardening on aggregation during flow was examined. RBCs with different membrane stiffness were perfused through straight microchannels with square cross-sectional area of $50 \times 50 \mu\text{m}^2$. The experimental protocol described in Chapter 2 was followed. Healthy and

hardened RBC samples in the presence and absence of aggregation were perfused through straight $50 \times 50 \mu\text{m}^2$ channels. The flow was monitored in the middle of the 16 mm long channels and RBC velocity profiles at the central plane were determined with ensemble PIV processing (JPIV). The haematocrit distributions were estimated from the image intensity distributions as described previously. Dextran 2000 with 8 g/L concentration was added in the PBS solution to induce aggregation (Figure 5.1b) and the viscosity of the PBS-Dextran solution increased to 1.41 mPas as mentioned in Chapter 2. The samples suspended in PBS only, did not exhibit aggregation while the ones suspended in PBS and Dextran solution were expected to aggregate at low flow rates. From now on the samples with the propensity to aggregate will be mentioned as 'Dextran samples' while the ones that exhibit no aggregation will be mentioned as 'PBS samples'.

The healthy RBC sample was considered as control sample and two additional samples with decreased membrane deformability were studied. The deformability of the samples was decreased by fixing the red blood cells with GA at different concentrations 0.04% and 0.08% which are considered as lightly and moderately fixed samples respectively as in Chapter 3. A feed haematocrit of 25% was utilised and a total of 73 data sets were acquired at various inflow velocities U^* ; ranging from 1 to 230 s^{-1} . The contrast of the acquired images was quantified using the standard deviation of the image intensity providing a measure of the extent of aggregation (Kaliviotis *et al.*, 2016). The measured velocity and haematocrit profiles were compared, and velocity and haematocrit profile bluntness indices were utilised in order to characterise the shape of the profiles and correlate with deformability.

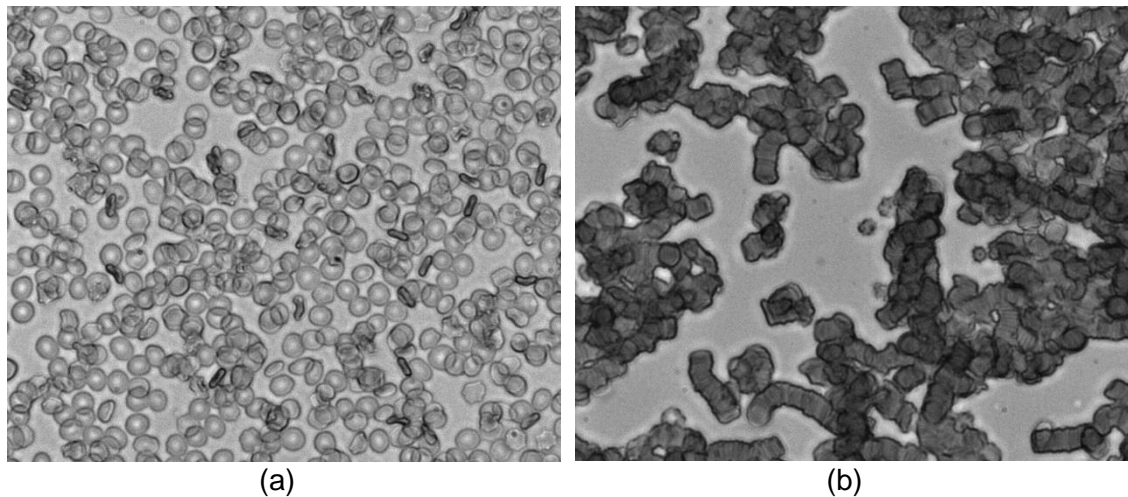


Figure 5.1: Images of washed RBCs under static conditions suspended in (a) PBS and (b) PBS and Dextran 2000 solution showing the formation of the rouleaux.

5.2 Aggregation intensity

Various methods have been used to describe the extent of aggregation. Kaliviotis and Yianneskis (2008) quantified aggregation intensity based on the inter-cellular spacing in images of aggregating RBC suspensions acquired by optical shearing microscopy. The cell-free areas in the image were identified by thresholding and used to calculate an aggregation index. Whole blood was used in that study and a narrow gap of 30 μm was utilised yielding images amenable to this type of analysis. In the present study such analysis is not possible and the amount of cell free areas in the acquired RBCs images were indirectly utilised through the mean standard deviation of image intensity, similar to Kaliviotis *et al.* (2016). The RBC clusters that form when aggregation occurs, locally enhance light absorption while the plasma gaps that are created have greater light transmission. This correspond to images with less uniform intensity distribution compared to those acquired with dispersed RBCs. These distributions have higher standard deviation in comparison with the distributions obtained from images of non-

aggregated samples where RBCs are distributed in a more uniform way producing a smaller amount of plasma gaps.

The image intensity probability density functions (PDF) of Figure 5.2 describe the variation of contrast in the image of healthy and GA 0.08% hardened RBC samples suspended in PBS and Dextran solutions. The intensity distribution of the non-aggregated RBCs (Figure 5.2a) is more concentrated towards the lower values of intensity which correspond to the darker regions i.e. regions that are occupied by RBCs. However, in Figure 5.2b, RBCs form aggregates and the image intensity of the aggregated RBCs shows a bimodal distribution, with a second peak at high intensity values corresponding to the cell-free areas. On the contrary the distribution in Figure 5.2c and d for hardened RBCs show the same distribution for PBS and Dextran samples.

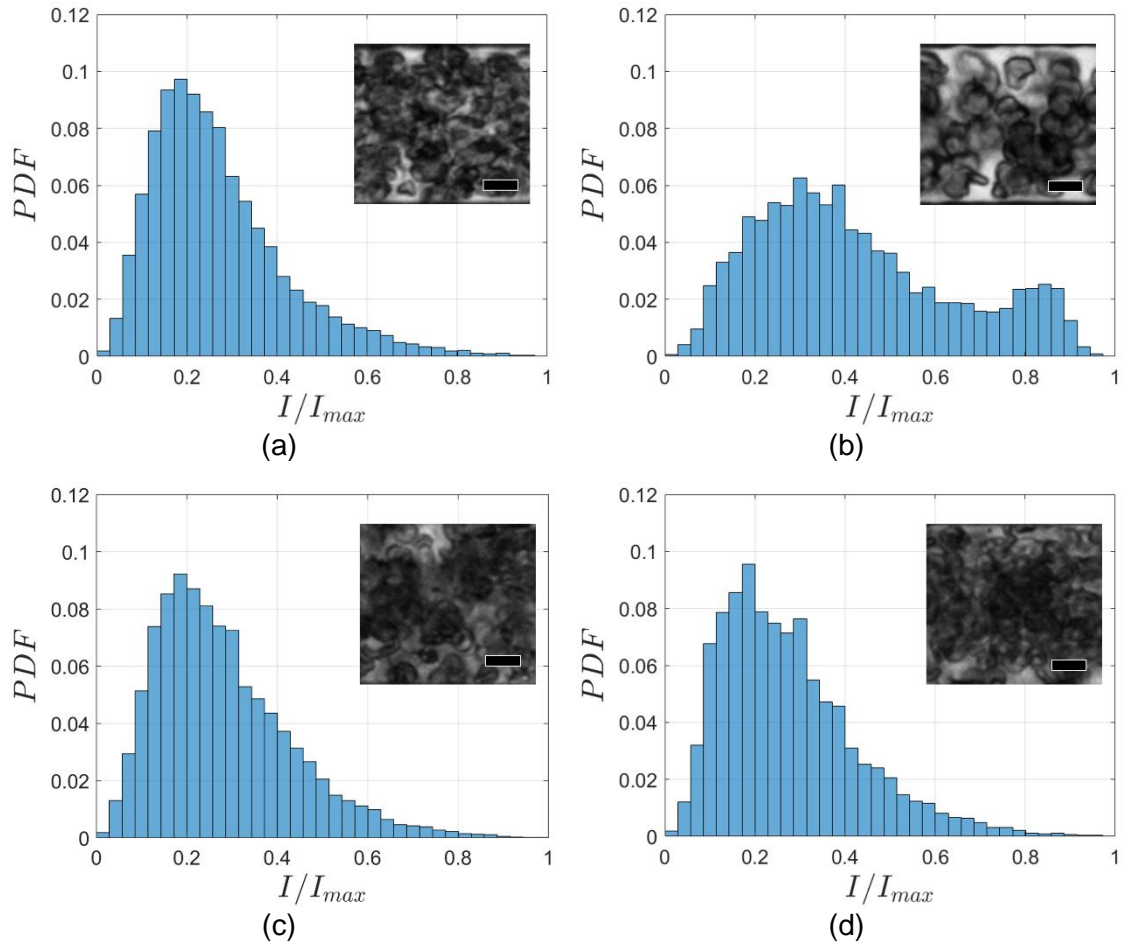


Figure 5.2: Probability density functions of image intensity and corresponding RBC images for flows of healthy RBCs suspended in (a) PBS and (b) Dextran and GA 0.08% RBCs in (c) PBS and (d) Dextran at low flow rates; $U^* = 6, 8, 9, 8 \text{ s}^{-1}$ respectively for the a,b,c and d. Image intensity is normalised with maximum intensity. Scale bars correspond to 10 μm .

The standard deviation (σ) of the image intensity was calculated for 60 pairs of images acquired at each flow rate and the resulting values were averaged. The standard deviation was normalised (σ^*) against the average value of standard deviation of healthy samples suspended in PBS ($\bar{\sigma}_{\text{healthy-PBS}}$), where aggregation was absent (Eq. (5.1)).

$$\sigma^* = \frac{\sigma}{\bar{\sigma}_{\text{healthy-PBS}}} \quad (5.1)$$

Figure 5.3a shows the standard deviation of RBC samples suspended in PBS and Figure 5.3b those suspended in Dextran solution.

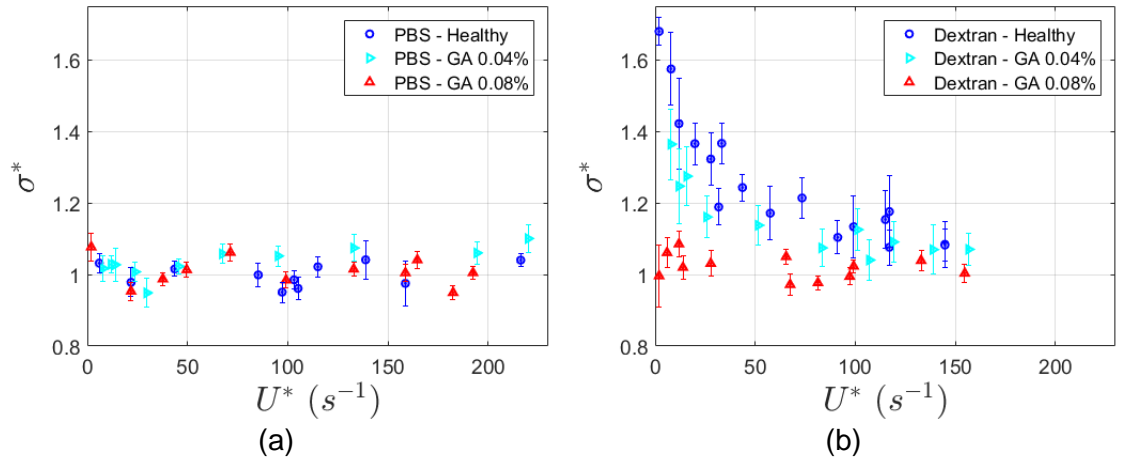


Figure 5.3: Normalised standard deviation of image intensity (σ^*) as a function of normalised velocity (U^*) for healthy, GA 0.04% and GA 0.08% samples suspended in (a) PBS and (b) Dextran solutions.

Figure 5.3a compares the standard deviation of samples with different membrane stiffness in the range of studied normalised velocities; it can be seen that the hardened samples, GA 0.04% and GA 0.08%, have similar standard deviation values to healthy ones (i.e. σ^* is around 1). This indicates that no aggregation is present within the range of measured normalised velocities for any of the samples. In contrast, Figure 5.3b shows that the standard deviation of the healthy Dextran sample is increased at low normalised velocities and gradually decreases as normalised velocities increase, approaching the σ^* of the PBS samples. The Dextran-GA 0.04% sample shows similar behaviour to Dextran-

healthy sample; on the other hand, the GA 0.08% sample shows constant σ^* values indicating the absence of RBC aggregation. Hardened RBCs are expected to exhibit weak aggregation characteristics as their stiffened membrane opposes to the flexible contacts among the RBCs in order to adhere with each other (Maeda *et al.*, 1983; Jovtchev *et al.*, 2000). The reduced aggregation characteristics of hardened RBCs can also be inferred from their rheological behaviour. The seminal work of Chien *et al.* (1970) has shown that the viscosity of hardened RBCs exhibits no shear dependent behaviour in contrast to the healthy aggregated RBCs which show 75% increase of relative viscosity at low shear rates. The Newtonian-like behaviour of hardened RBCs combined with elevated viscosity has also been reported recently by Lanotte *et al.* (2016).

The uncertainty in the estimation of the standard deviation of image intensity is shown in Figure 5.4. It can be seen that the error is smaller in samples suspended in PBS (Figure 5.4a) compared to those in Dextran (Figure 5.4b). This indicates that the image contrast variation of RBC samples in PBS is lower than the variation in Dextran samples. This might be attributed to the aggregate formation in Dextran cases which have the tendency to rearrange RBC distributions during flow to greater extent than dispersed RBCs. Having established the extent of aggregation in the microfluidic channels, the impact on measured velocities is examined in the following section.

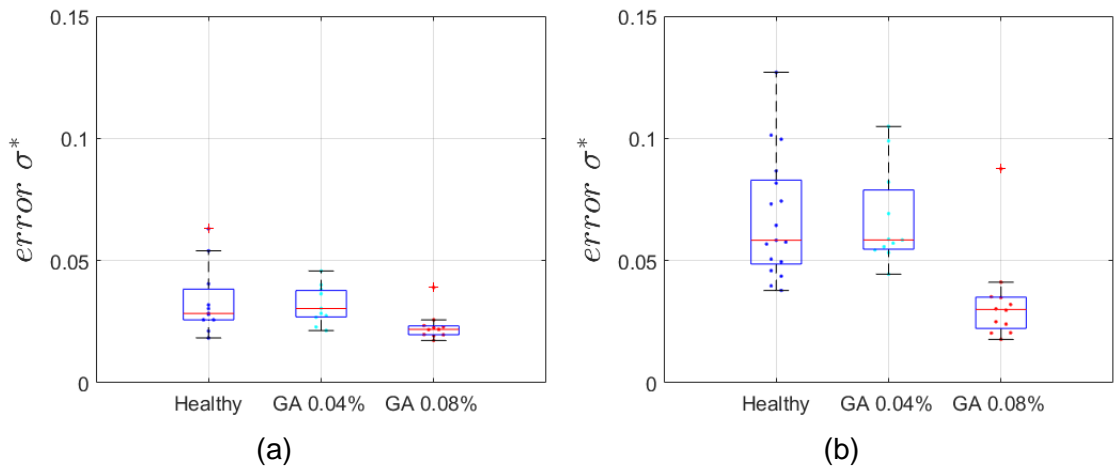


Figure 5.4: Uncertainty of image contrast standard deviation estimated from 60 pairs of images. RBC samples suspended in (a) PBS and (b) Dextran. The uncertainty was calculated as the standard deviation of σ^* .

5.3 Velocity profiles

Aggregation is an inherent property of RBCs and a key determinant of blood viscosity. It occurs in low shear rate, resulting in a viscosity increase at these rates as shown by Chien *et al.* (1970). Apart from viscosity, aggregation is known to affect other properties of blood flow such as velocity and haematocrit distribution. When aggregation takes place, RBC velocity profiles become blunter as has been illustrated by *in vivo* (Bishop *et al.*, 2001) and *in vitro* studies (Reinke *et al.*, 1987; Sherwood *et al.*, 2012). Moreover, aggregation has been shown to enhance RBC radial migration towards the centre of flow (Bishop *et al.*, 2001; Kim *et al.*, 2009) and hence the width of the cell depletion layer (Sherwood *et al.*, 2014).

In the present study, an effect of aggregation is expected at flow rates lower than 100 s^{-1} mostly for the more deformable Dextran samples. Aggregation changes the microstructure of the RBC suspension during flow affecting thus the velocity distribution across the flow. Figure 5.5 shows typical velocity profiles of samples with different membrane stiffness (healthy, GA 0.04% and GA 0.08%) of the same feed haematocrit (25%) and in low normalised velocities where aggregation is expected to be present. The velocity profiles are compared with the analytical velocity profile for a Newtonian fluid in a square channel, as well as the velocity profile of a healthy non-aggregating RBC sample at similar conditions. The healthy-Dextran samples, shown with the blue line in Figure 5.5, produce a blunter velocity profile in agreement with the *in vivo* experiments of Bishop (2001) and the *in vitro* experiments of Sherwood *et al.*, (2014b). However, the hardened aggregated RBC samples do not exhibit such bluntness. In particular, the slightly hardened samples (GA 0.04%), shown with the light blue line in Figure 5.5, produce a less blunt velocity profile compared to healthy-Dextran samples and their profile shape is similar to that for the non-aggregated healthy samples (dashed line). The most hardened RBC samples (GA 0.08%), shown with the red line, exhibit a sharper velocity distribution compared to the healthy, more deformable samples, and similar to the analytical velocity profile for Newtonian fluids in a square channel (grey area).

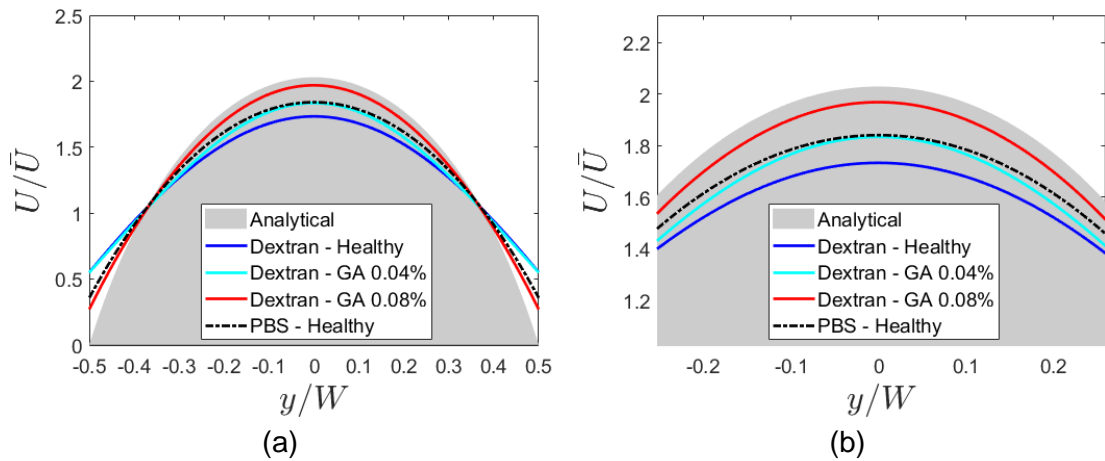


Figure 5.5: (a) Typical velocity profiles of Dextrans samples: healthy-unfixed, hardened with GA 0.04%, GA 0.08% and healthy sample suspended in PBS, obtained in the square microchannel at 18 s^{-1} and 25% haematocrit. (b) A close up of the profiles. The profiles are normalised by the average velocity. The grey area indicates the analytical velocity profile for a Newtonian fluid in a square channel (Bruus 2008).

In order, to examine further how aggregation impacts on the velocity profiles in different flow rates, Figure 5.6 shows a comparison between the velocity profiles of healthy and GA 0.08% hardened samples with and without Dextran, at different values of normalised velocities.

Figure 5.6a compares the velocity profiles of healthy samples suspended in PBS and Dextran at low normalised velocities ($U^* = 15 \text{ s}^{-1}$); the healthy-Dextran sample produces a blunter velocity profile than the healthy-PBS one as expected. This trend diminishes when the flow rate increases and at medium ($U^* = 54 \text{ s}^{-1}$) and high ($U^* = 120 \text{ s}^{-1}$) normalised velocities (Figure 5.6c,e) the velocity profiles of healthy samples are similar for both PBS and Dextran solutions. This is to be expected as the effect of aggregation was pronounced in $U^* < 100 \text{ s}^{-1}$. On the contrary, the comparison of the velocity profiles of hardened RBCs suspended in PBS and Dextran, show similar distributions in the whole range of normalised

velocities, low ($U^* = 16 \text{ s}^{-1}$), medium ($U^* = 62 \text{ s}^{-1}$) and high ($U^* = 135 \text{ s}^{-1}$), indicating the decreased effect of aggregation on the hardened RBC samples.

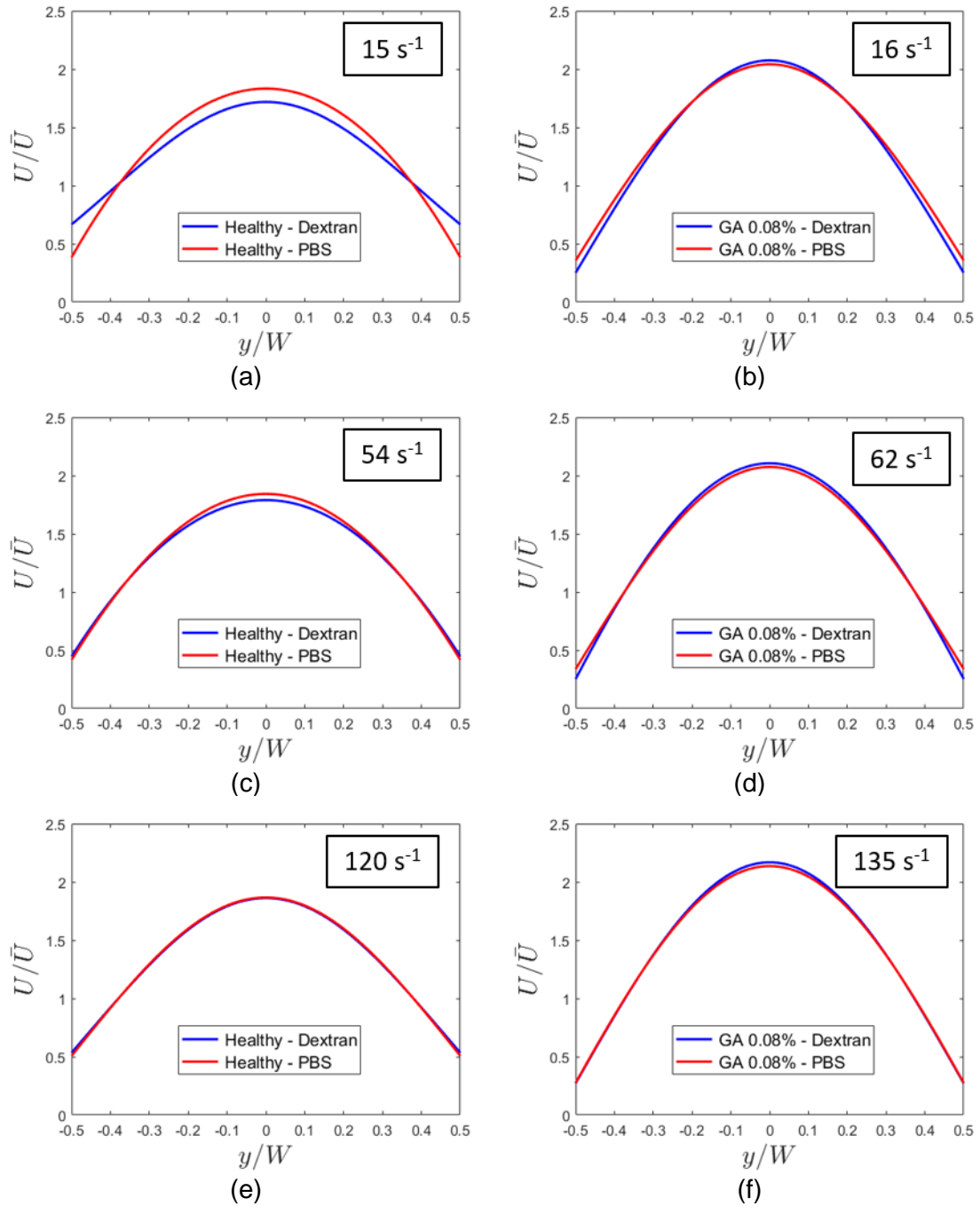


Figure 5.6: Normalised velocity profiles suspended in PBS and Dextran of healthy RBC and GA 0.08% hardened RBCs samples. Healthy samples at normalised velocities: (a) 15 s^{-1} (c) 54 s^{-1} (e) 120 s^{-1} and GA 0.08% hardened samples at (b) 16 s^{-1} (d) 62 s^{-1} and (f) 135 s^{-1} .

The above trends are better illustrated in Figure 5.7 where the velocity profile bluntness indices are compared. The bluntness of the velocity profiles is calculated using equation (2.3); it is a measure of the deviation of the experimental velocity profile from the analytical. Thus, the B_{U^*} of the analytical solution would be equal to zero.

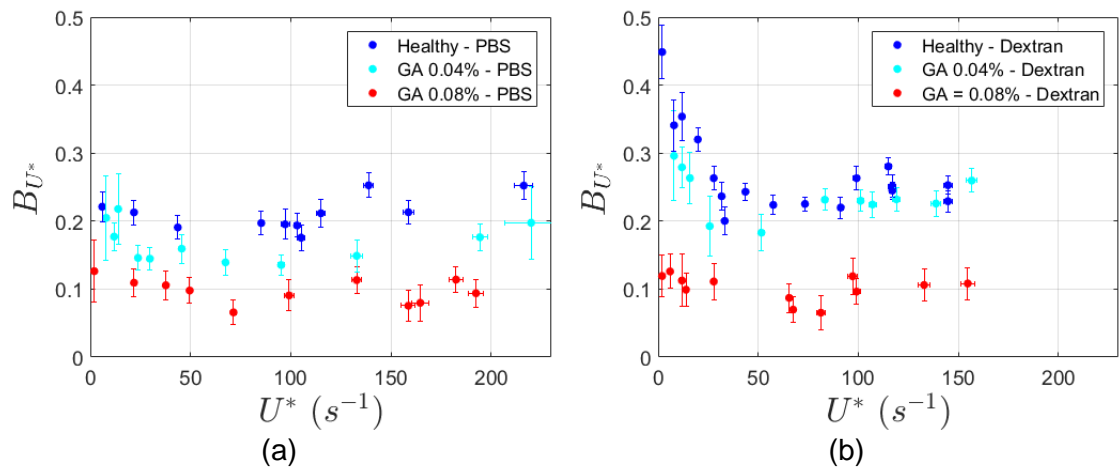


Figure 5.7: Bluntness index of measured velocity profiles as a function of normalised velocity U^* for (a) PBS and (b) Dextran samples of 25% haematocrit.

The velocity bluntness indices of the PBS samples exhibit the same trend as reported in Chapter 3. Hardened RBC samples exhibit lower B_{U^*} values than the healthy ones, indicating that hardened RBCs produce sharper velocity profiles (Figure 5.7a). In both PBS and Dextran cases the moderately fixed sample (GA 0.08%) produces sharper velocity profiles (i.e. lower B_{U^*}) than the healthy and lightly fixed (GA 0.04%) ones. Figure 5.7b shows the velocity bluntness of Dextran RBC suspensions with different membrane stiffness showing that hardened RBCs exhibit lower velocity bluntness. Moreover, the bluntness of healthy samples, i.e. the healthy and GA 0.04%, increases inversely proportionally to flow rate, when U^* is less than 50 s^{-1} in agreement with the

observed trend by Sherwood *et al.* (2014). This trend is less pronounced at the lightly fixed RBC sample (GA 0.04%) and negligible for moderately fixed sample (GA 0.08%) showing the effect of membrane stiffness on aggregation properties.

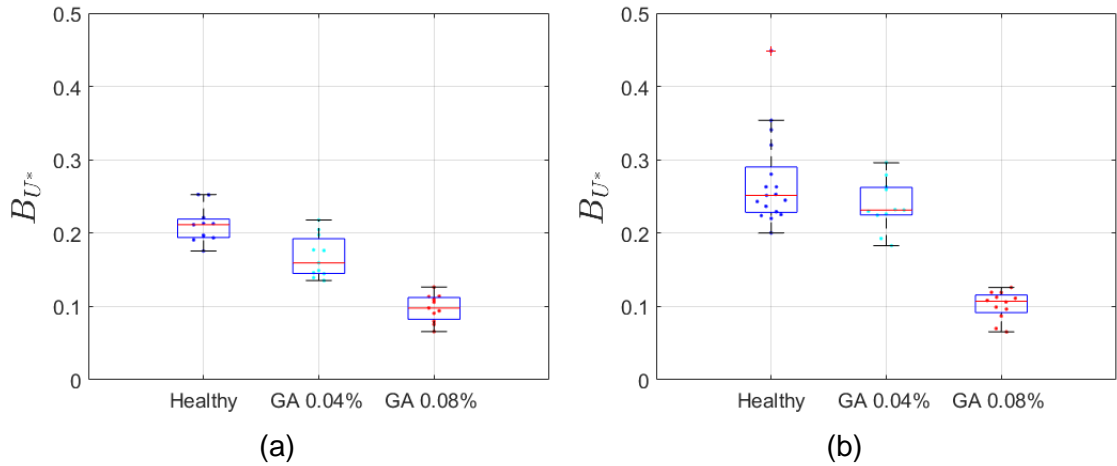


Figure 5.8: Bluntness index of the measured velocity profiles within the range of $1 - 230 \text{ s}^{-1}$ for each of the 25% haematocrit samples suspended in (a) PBS solution and (b) Dextran solution. The central red lines indicate the median of the measurements and the bottom and top sides of the box indicate the 25th and 75th percentiles, respectively. Outliers are plotted individually with '+' and correspond to the outer 0.7% of the data.

The overall trends of membrane stiffness and aggregation on bluntness index are better illustrated in the box plots of Figure 5.8a and b. It can be clearly seen that RBC hardening progressively weakens the aggregation mechanism and its effect on velocity distribution. Additionally, the healthy and GA 0.04% samples seem to have higher velocity bluntness indices while suspended in Dextran compared to PBS, in contrast with the GA 0.08% samples which exhibit similar range of velocity bluntness in both suspending media. In the next section, the corresponding haematocrit distributions are discussed.

5.4 Haematocrit distribution

As mentioned in the previous section, aggregation tends to blunt RBC velocity profiles (Reinke *et al.*, 1987; Bishop *et al.*, 2001) of healthy red blood cells. Due to the larger size of RBC aggregates compared to single cells, shear induced migration is more pronounced, leading to sharper haematocrit profiles of aggregated RBC suspensions compared to non-aggregated. This increases the local viscosity in the centre of flow which is translated to blunter RBC velocity profiles.

According to Figure 5.3, healthy RBCs suspended in Dextran solution exhibit aggregation at low flow rates in contrast to hardened RBCs. This implies that the aggregated healthy RBC samples, should concentrate more towards the centreline at low flow rates leading to sharper haematocrit profiles at low flow rates and blunter ones at high flow rates where the effects of aggregation are not evident, i.e. the haematocrit profiles are expected to exhibit the opposite trend to the velocity profiles. The sample images in Figure 5.9 show healthy and GA 0.08% RBC samples in Dextran at high ($U^* > 120 \text{ s}^{-1}$) and low flow rates ($U^* \approx 15 \text{ s}^{-1}$) respectively. It can be seen that the distribution of healthy samples changes as the flow rate increases with the intensity profiles becoming sharper indicating the presence of aggregation. On the contrary, the GA 0.08% samples show fairly similar intensity distribution in both low and high flow rates.

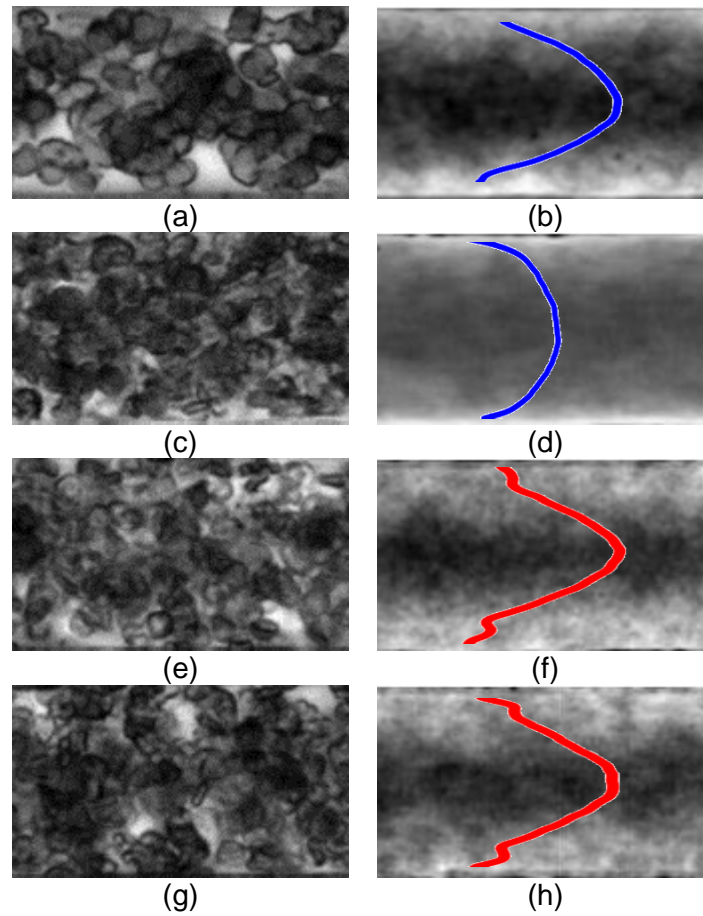
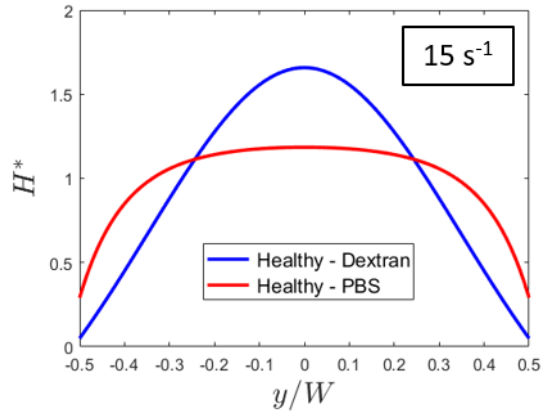


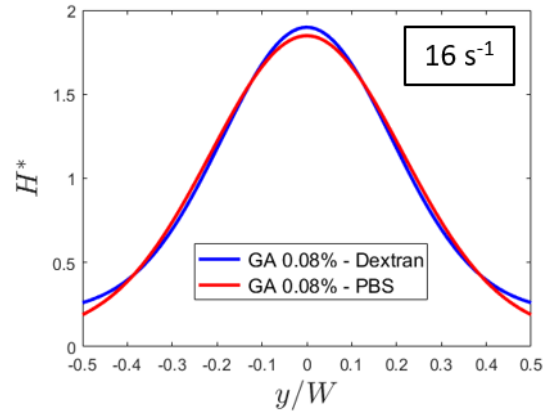
Figure 5.9: Sample RBC images and time averaged sample images respectively with image intensity distribution profiles at 25% haematocrit for (a,b) healthy-Dextran sample at 15 s^{-1} (c,d) healthy-Dextran sample at 120 s^{-1} (e,f) GA 0.08% - Dextran sample at 16 s^{-1} , (g,h) GA 0.08% - Dextran sample at 132 s^{-1} .

Figure 5.10 compares the haematocrit profiles of healthy and GA 0.08% RBCs suspended in PBS and Dextran at different flow rates. Figure 5.10a shows that in low flow rates ($U^* = 15 \text{ s}^{-1}$) the healthy-Dextran RBC samples produce a sharper haematocrit distribution compared to the healthy-PBS ones due to the presence of aggregation at this rate. Figure 5.10c and e show that as the flow rate increases and aggregates break down the haematocrit profiles become more uniform and eventually no difference between PBS and Dextran samples can be seen ($U^* = 120 \text{ s}^{-1}$). On the contrary, the haematocrit profiles of the hardened samples,

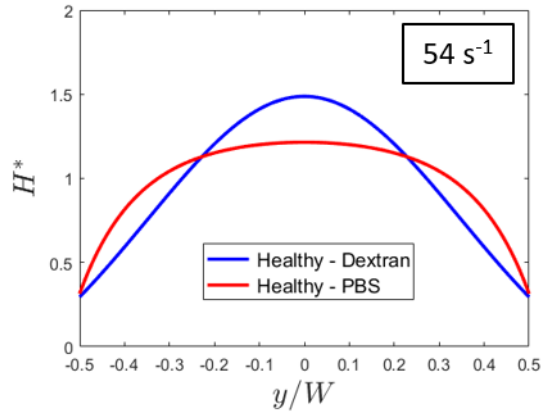
displayed in Figure 5.10 b,d,f, show that both PBS and Dextran samples produce similar haematocrit distributions within the range of measured flow rates ($U^* = 1$ - 230 s^{-1}) indicating the absence of aggregation and no effect of flow rate.



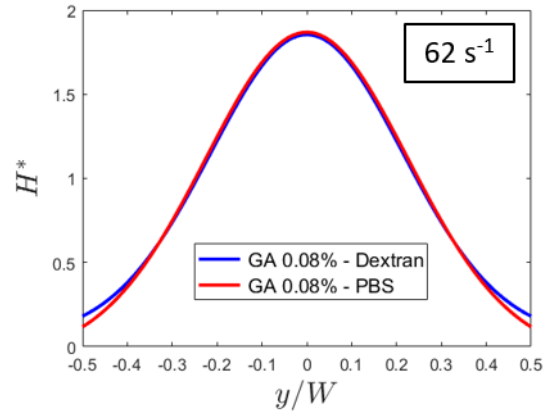
(a)



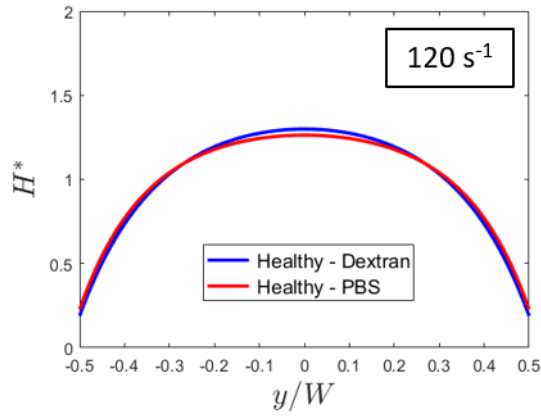
(b)



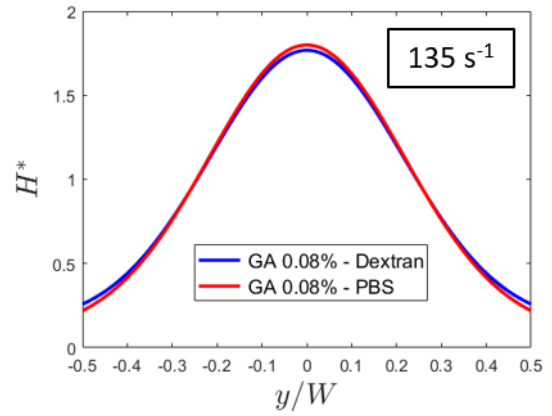
(c)



(d)



(e)



(f)

Figure 5.10: Haematocrit profiles of healthy and GA 0.08% hardened RBCs samples suspended in PBS and Dextran. Healthy samples at normalised velocities: (a) 15 s^{-1} (c) 54 s^{-1} (e) 120 s^{-1} and GA 0.08% hardened samples at (b) 16 s^{-1} (d) 62 s^{-1} and (f) 135 s^{-1} .

The shape of the haematocrit profiles was further characterised by utilizing the haematocrit profile index calculated using equation (2.8). The estimated values are plotted in Figure 5.11 for a range of flow velocities. Figure 5.11a shows that the haematocrit profile bluntness of RBC samples suspended in PBS are flow rate independent within the range of flow rates ($1 - 230 \text{ s}^{-1}$). Moreover, the hardened RBC samples exhibit lower haematocrit bluntness, as was shown in Chapter 3, indicating sharper haematocrit distributions.

On the contrary, Figure 5.11b, shows that the haematocrit profile bluntness index of healthy RBCs suspended in Dextran (blue colour), gradually decreases when the normalised velocity is lower than 50 s^{-1} due to the presence of aggregation. At higher normalised velocities ($U^* > 50 \text{ s}^{-1}$), the haematocrit bluntness index increases and remains constant with flow rate. The lightly fixed sample (GA 0.04% - light blue colour) exhibits similar trends to the healthy one but the effect of aggregation seems less pronounced. In contrast, the B_H^* values of GA 0.08% sample (red colour) are lower compared to the more deformable samples (healthy and GA 0.04%) in agreement with the findings of the experiments of Chapter 3. GA 0.08% also seem unaffected by the flow rate indicating that aggregation is absent or it has no effect on the distribution. The wide range of haematocrit bluntness for the healthy and GA 0.04% samples in Figure 5.12b indicates the variation of B_H^* with flow rate.

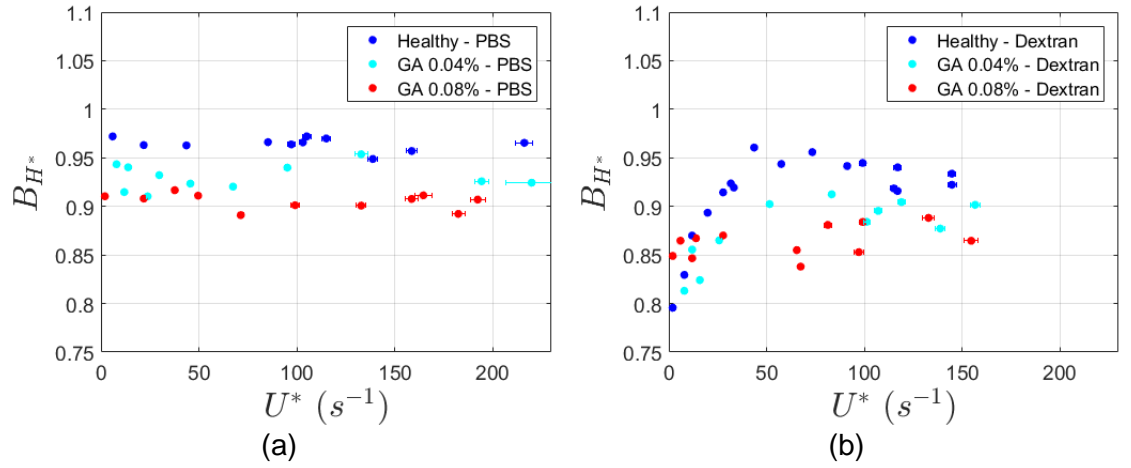


Figure 5.11: Haematocrit profile bluntness index as a function of normalised velocities of 25% haematocrit samples suspended in (a) PBS (non-aggregating) and (b) Dextran (aggregating).

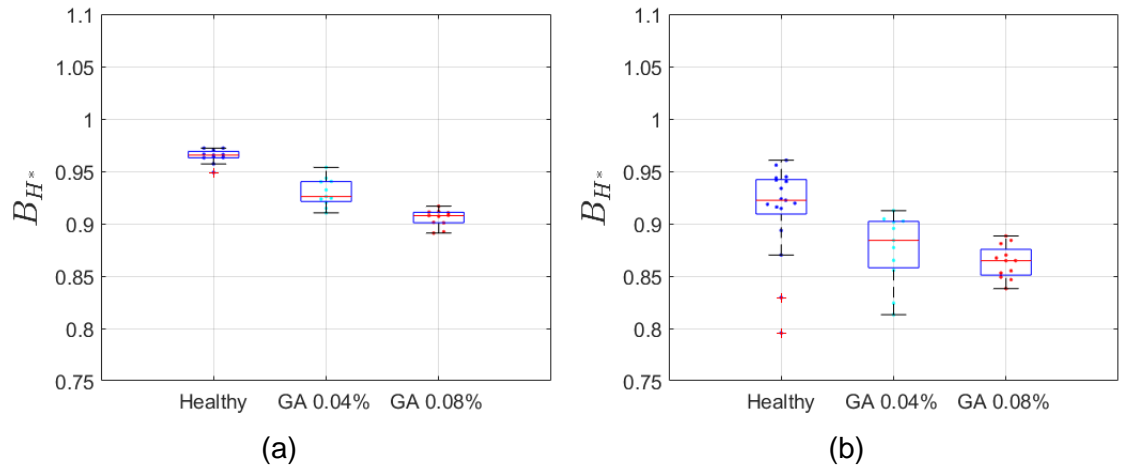


Figure 5.12: Box plots of the bluntness index of haematocrit profiles of 25% suspensions of healthy, GA 0.04% and GA 0.08% RBCs in (a) PBS and (b) Dextran. The central red lines indicate the median and the bottom and top edges of the box indicate the 25th and 75th percentiles, respectively and outliers are plotted individually with “+” and correspond to the outer 0.7% of the data.

Here, it is important to investigate if the presence of Dextran itself affects the haematocrit bluntness of the samples. It is known, that viscoelasticity of the medium tends to concentrate the flowing particles towards the centre of flow (Go *et al.*, 2017). In Figure 5.13, samples with the same membrane stiffness

suspended in PBS and Dextran are compared. It can be observed that the haematocrit bluntness indices of the samples do not show significant changes due to the suspended medium, apart from the lower region of normalised velocities (less than 50 s^{-1}) where the presence of aggregation is pronounced. Thus, it can be inferred that in low flow rates the reduction of B_H^* is a result of RBC structuring during flow and not due to a viscoelasticity effect of the medium.

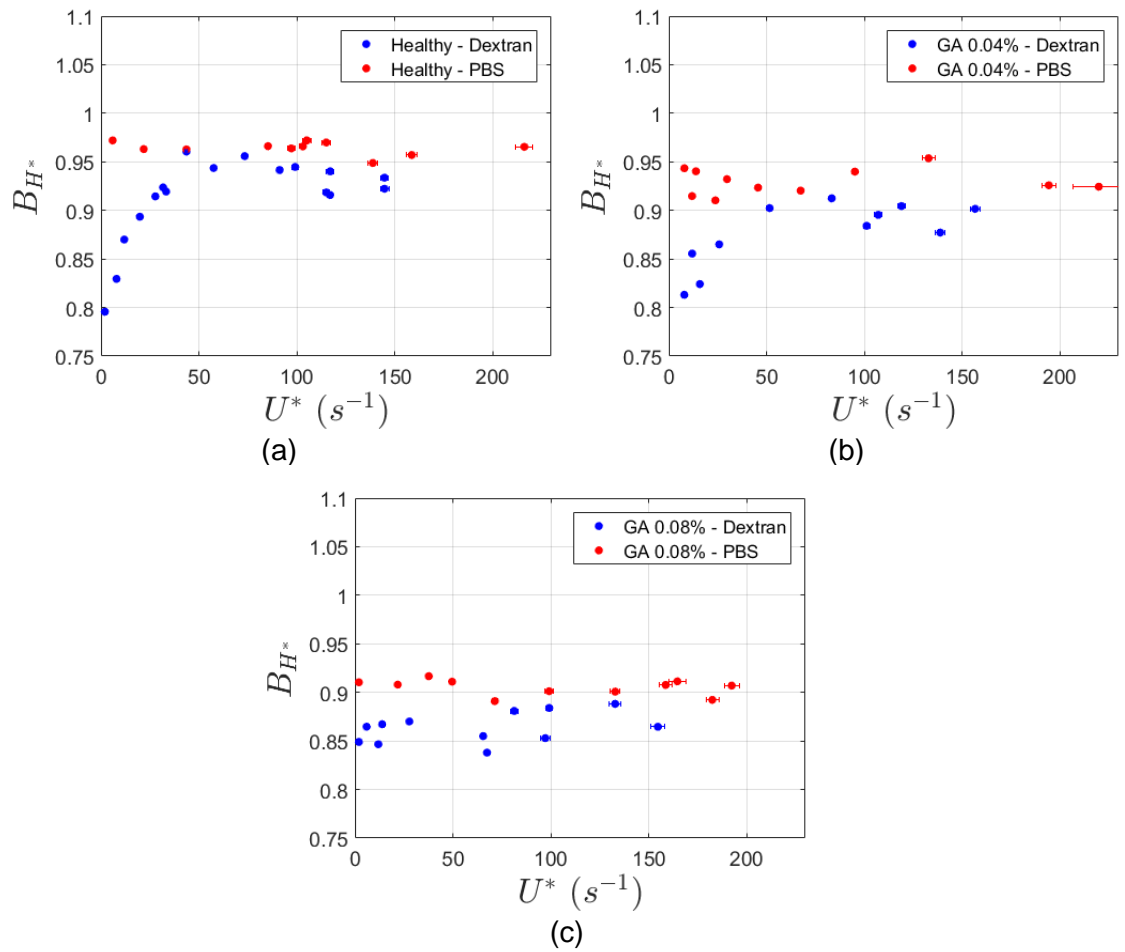


Figure 5.13: Haematocrit bluntness comparison for samples with the same membrane stiffness samples suspended in PBS and Dextran. (a) Healthy samples (b) GA = 0.04% and (c) GA = 0.08%.

5.5 Discussion

The migration of RBC aggregates towards the centre of flow is a shear dependent phenomenon that is related to the different size of single RBCs and RBC aggregates. Shear induced migration is size depended the larger aggregates tend to occupy the areas near the centre of the flow due to the lower shearing forces therein. In particular, it has been shown, that RBC aggregates migrate to the centre of the channel at higher rate than the single cells increasing the local viscosity (Goldsmith, 1968). Moreover, Kaliviotis et al. (2016) showed this size exclusion phenomenon applies on aggregates with different size as larger aggregates displace smaller aggregates in the middle of the channel.

The standard deviation of image intensity in Figure 5.3b showed that aggregation was present in the low shear rate range ($U^* < 100 \text{ s}^{-1}$) for the healthy RBC samples. The velocity and haematocrit profile bluntness were also affected by the presence of aggregation as was indicated in Figure 5.7b and Figure 5.11b. However, the presence of aggregation, as indicated by B_U^* and B_H^* , was estimated at a lower range of nominal shear rates, i.e. $U^* < 50 \text{ s}^{-1}$, compared to the image intensity method ($U^* < 100 \text{ s}^{-1}$), meaning that the image intensity method was more sensitive and the velocity and haematocrit profiles were affected by the presence of aggregation at the lower flow rate range.

In the presence of aggregation, the healthy RBCs were found to be concentrated towards the centre of the channel producing sharper haematocrit profiles. This trend is in agreement with a number of studies (Cokelet and Goldsmith, 1991; Alonso *et al.*, 1995) which found that the axial migration of red blood cells

increased by the presence of aggregation leading to higher values of local viscosity near the centre of the flow. The increased viscosity in the centre was found to produce blunter velocity profiles in agreement with studies that examined the effect of aggregation on velocity profiles (Reinke *et al.*, 1987; Bishop *et al.*, 2001; Sherwood *et al.*, 2014b).

The RBC samples fixed with GA 0.04% in which the cells are still deformable, were found to exhibit similar trends with the healthy RBC samples. However, the extent of aggregation was found to be less pronounced as illustrated in the velocity and haematocrit profiles of Figure 5.7b and Figure 5.11b respectively, as well as in the standard deviation of image intensity (Figure 5.3b). On the contrary, the GA 0.08% RBC samples which are considered as the most hardened samples, did not show evidence of aggregation. In particular, the σ^* of image intensity (Figure 5.3b) remained constant and unaffected by the flow rate while exhibiting lower values than those for the more deformable healthy and GA 0.04%, especially at low flow rates where the presence of aggregation was evident. Gradually, as the flow rate increased, the three samples with different membrane deformability approached equal levels of σ^* implying the weakening of aggregation. Moreover, the shape of velocity and haematocrit profiles of GA 0.08% RBC samples in PBS and Dextran, did not show significant differences as indicated by the B_U^* and B_H^* comparison illustrated in Figure 5.7a,b and Figure 5.11a,b respectively. This indicates a negligible effect of Dextran on the hardened RBCs (GA 0.08% RBC samples), i.e. aggregation is not induced. The decrease of aggregation intensity with hardening agrees with the findings of Jovtchev *et al.* (2009) who also investigated the effect of glutaraldehyde hardening on RBC

aggregation applying the Zeta sedimentation technique. Aggregation forces require a deformation of the cell membrane in order to form a stable contact between two cells, hence in the case of GA fixation, the membrane deformability of RBCs is decreased and the aggregation mechanism is weakened.

The observed behaviour of velocity and haematocrit bluntness for the healthy-PBS RBC sample implies a negative correlation between B_U^* and B_H^* as mentioned in Chapter 3. Figure 5.14 shows the B_U^* - B_H^* correlation of healthy, GA 0.04% and GA 0.08% RBCs in Dextran. The healthy-Dextran RBC samples, exhibit a significant negative B_U^* - B_H^* correlation using Pearson statistical test ($r_{\text{healthy}} = -0.90$, $p < 10^{-5}$). The GA 0.04% - Dextran RBC samples also exhibit a significant negative correlation ($r_{\text{GA0.04}} = -0.61$, $p = 0.045$). In contrast the GA 0.08% - Dextran RBC samples show no statistically significant correlation between B_U^* and B_H^* .

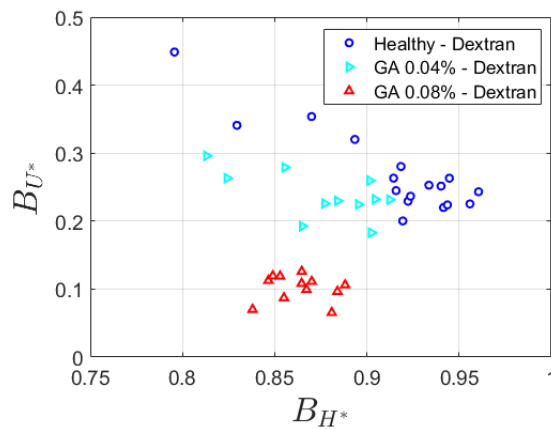


Figure 5.14: Velocity vs haematocrit bluntness index of healthy, GA 0.04% and GA 0.08% samples suspended in a Dextran solution at 25% haematocrit.

Table 5.1: Pearson correlation coefficients for velocity and haematocrits bluntness indices.

Ht	sample	Pearson r	p-value
25%	Healthy	-0.90	$< 10^{-5}$
	GA 0.04%	-0.61	0.047
	GA 0.08%	-0.07	0.56

The decreasing haematocrit profile bluntness with aggregation implies that healthy aggregated RBCs tend to concentrate more towards the centre of flow increasing the local viscosity therein; hence a decreased velocity in the central region of channel is exhibited, leading to a blunter velocity profile and indicating the shear thinning nature of blood. When flow rate increases the RBC aggregates become less stable and break due to greater shear forces, leading to a more uniform RBC distribution and less blunt velocity profiles. This negative correlation of velocity and haematocrit bluntness of healthy RBCs was observed in the current experiments (Figure 5.14), in agreement with literature (Bishop *et al.*, 2001; Sherwood *et al.*, 2014; Yeom *et al.*, 2014). However, in the present study this was not the case for the hardened RBCs as the velocity and haematocrit distributions seemed unaffected by the presence of aggregating agents (Dextran). In particular, the velocity profiles of hardened RBCs showed a more Newtonian-like behaviour for the whole range of flow rates indicating the independency of viscosity with shear increase (Simchon, Jan and Chien, 1987; Lanotte *et al.*, 2016).

The Dextran-induced RBC aggregation has been attributed to depletion (Neu and Meiselman, 2002) or bridging (Pribush *et al.*, 2007) mechanisms. The depletion model combines electrostatic repulsion due to RBC surface charge with osmotic

attractive forces due to polymer depletion near the RBC surface. The fixation of RBCs with GA could impede the aggregation mechanisms. The osmolarity of GA fixed RBCs is altered (Abay *et al.*, 2019a) and the negative charge of RBC surface (glycocalyx) (Seaman, 1975) increases due to GA fixation (Vassar *et al.*, 1972) producing stronger repulsive forces between RBCs and resulting in a weaker aggregation mechanism. The experiments of Pribush *et al.* (2007) were found to be consistent with the bridging model. Their results provided evidence that RBC aggregation was caused by the formation of Dextran bridges between the cells showing high affinity with the polysaccharides adsorption onto RBC surface. Fixing RBCs with GA decreases the membrane deformability and increases the surface negative charge among altering other properties affecting thus the strength of the aggregation mechanism.

In *in vitro* experiments using diamide treatment – another common hardening agent which crosslinks the membrane proteins reducing RBCs deformability – a decreased interaction with plasma proteins or aggregating agents (Chien, 1975; Maeda *et al.*, 1983) has also been also observed. The effect of decreased RBC deformability on aggregation has also been investigated in pathologies. Studies on aggregation of sickled cells which exhibit reduced deformability and altered morphology have reported contradictory results; in particular RBC aggregation is reported to be decreased (Usami *et al.*, 1975; Bucherer *et al.*, 1992; Connes *et al.*, 2018), enhanced (Schmid-Schönbein and Heidtmann, 1982), inhibited (Jan *et al.*, 1981) or prevented (Boynard *et al.*, 1988). In malaria disease despite the significant decrease of RBC deformability an important increase of aggregation, in particular hyper-aggregation, has been reported. The malaria diseased RBCs

(parasitized RBCs) have the tendency to attract and attach the healthy RBCs around them forming more stable aggregates than the aggregates formed among healthy RBCs; these formations are described as 'rosettes' (Jayavanth *et al.*, 2004).

Finally, in many studies, aggregation has been found to decrease the flow resistance of blood (Cokelet and Goldsmith, 1991; Charansonney *et al.*, 1993; Baskurt *et al.*, 1999). One reason for the decreased flow resistance with aggregation, has been attributed to the increase of the cell depleted layer thickness that acts as a lubricant to the flow (lubrication effect). It has also been reported that an amount of 15% reduction of RBC deformability raises the vascular resistance by 75% (Baskurt *et al.*, 2004). This has been attributed to the mechanical obstruction of hardened RBCs at the entry of capillaries leading to impaired tissue perfusion. However, based on the findings of this chapter, the weakening of aggregation mechanism due to RBC hardening might be an additional reason that vascular resistance increases.

5.6 Closure

In the present chapter the impact of red blood cell hardening on aggregation properties during flow was examined. Aggregation was induced by adding a small quantity of Dextran in the suspending medium. The extent of aggregation was quantified by measuring the standard deviation of the image intensity in the acquired images of flowing RBC suspensions. Healthy-Dextran RBC samples exhibited higher values of standard deviation at low flow rates indicating the presence of aggregation, while aggregation was less evident in hardened

samples; the extent of aggregation was reduced in GA 0.04% RBC samples while in GA 0.08% samples aggregation was negligible. The velocity and haematocrit profiles of aggregated RBC samples were compared. Aggregation showed an impact on the velocity and haematocrit profiles of the deformable cells namely the healthy and GA 0.04% RBC samples, by inducing a blunter velocity profile shape and a sharper haematocrit profile shape in aggregated samples, but no significant changes were noted in the profiles of the GA 0.08%-Dextran RBC samples.

In the next chapter, the flow aggregated and non-aggregated RBC samples with different membrane stiffness in a T-junction bifurcation will be examined. The velocity and haematocrit profiles will be analysed in both the parent and daughter branches.

Chapter 6

Hardened RBC suspensions in bifurcating flows

In this chapter the effect of RBC hardening on the velocity and haematocrit distributions of suspensions flowing past a T-junction bifurcation are examined. Four different cases were investigated: healthy and hardened RBC suspensions in the presence and absence of aggregation. Two sets of experiments were conducted; in the first set of experiments the flow ratio between the branches was varied while the flow rate in the parent branch was kept constant and in the second one the flow ratio between the branches was kept constant while the flow rate in the parent branch varied. The skewness of the velocity and haematocrit profiles downstream of the bifurcation was quantified as well as the thickness of the cell depletion layer. Finally, the effect of RBC hardening on plasma skimming was examined by calculating the flux-flow ratio between the branches, in order to identify the impact of RBC hardening.

6.1 Introduction

The extended network of bifurcations in the microcirculation results in non-uniform haematocrit distributions in microvessels and phenomena such as, plasma skimming: at diverging bifurcations, the haematocrit is distributed unevenly, with a higher haematocrit normally entering the branch with higher flow. This leads to a high degree of haematocrit heterogeneity in the microvasculature and in some cases the occurrence of vessels perfused only by plasma and no RBCs. Several important parameters that influence the disproportional distribution of red blood cells in bifurcating flows have been studied in the literature such as parent vessel haematocrit, flow rate ratio between branches (distribution of volume flow), diameter ratio between parent and daughter vessels (Chien *et al.*, 1985; Fenton *et al.*, 1985), the vessel to particle diameter ratio, the haematocrit profile in the feeding vessel (Pries *et al.*, 1989) as well as, the effect of RBC aggregation (Gaehtgens *et al.*, 1978). However, the influence of RBC deformability on the cell distribution in bifurcations has not received much attention.

In this chapter the experiments on straight micro-channels are extended to a T-shaped bifurcation microfluidic geometry. In the previous chapters it was shown that RBCs tend to concentrate towards the centre of the flow more than healthy ones resulting in sharper haematocrit distributions. In this chapter, the influence of these sharper distributions of hardened RBCs on bifurcating flows is examined and compared to those obtained with healthy RBCs samples with and without aggregation, i.e. suspended in PBS and Dextran respectively. A T-junction

geometry with channel dimensions of $50 \times 50 \mu\text{m}^2$ was employed. A region of interest of two channel widths was selected in each branch, named parent, daughter and outlet, for the analysis as shown in Figure 6.1. The coordinate system employed is also shown in the same figure. Its origin is taken in the middle of the bifurcation. Normalised coordinates are used to plot the measured profiles, $x^* = x/W$ and $y^* = y/W$ ranging from -0.5 to 0.5, with x^* and y^* corresponding to the width of the daughter and outlet branch respectively. The T-junction microchannel was perfused through the parent branch (left side in Figure 6.1). The outlet reservoirs connected to the daughter and parent branches were mounted on a micrometer stage allowing the height control of each reservoir separately, and hence the hydrostatic pressure, controlling thus the flow entering in each of the branches. This was expressed in terms of flow ratio, Q^* , defined as the ratio of flow entering to each branch, $Q^* = Q_{o,d}/Q_p$, with Q_o , Q_p and Q_p the flow in the outlet, daughter and parent branches respectively.

Two sets of experiments were conducted: in the first set experiments the effect of flow ratio between the daughter and outlet branches of the bifurcation on haematocrit and velocity distributions was investigated. The flow ratio, Q^* between the daughter and outlet branch, was adjusted through hydrostatic pressure as described above and ranged from 0.05 to 0.95 of the total flow, equal to the flow rate of the parent branch ($Q_p = Q_{\text{tot}}$). The flow rate in the parent branch was maintained within a small range of U^* values of around 100 s^{-1} so no aggregation was present upstream of the bifurcation for the Dextran cases. Healthy and GA 0.08% fixed RBCs suspensions in both PBS and Dextran were perfused through the channel at a feed haematocrit of 25%.

In the second set of experiments the flow rate in the parent branch was varied from $U^* = 1$ and 235 s^{-1} and the flow ratio between the branches was adjusted to be equal and close to one ($Q_o/Q_d \approx 1$ or $Q_{o,d}/Q_p \approx 0.5$). In this set of experiments the effect of parent branch flow rate on haematocrit and velocity distributions downstream of the bifurcation was investigated. The range of flow rates in the parent branch ($1 - 235 \text{ s}^{-1}$) was selected to include the lower shear rates where aggregation is typically present. RBC suspensions were perfused with feed haematocrit of 25% as in the first set of experiments. It should be noted that the two experiments were conducted with blood drawn from different donors.

The primary aim of these experiments was to elucidate the effect of RBC deformability on haematocrit and velocity distributions in more complex bifurcating microfluidic geometries. Both aggregating and non-aggregating samples of hardened (GA 0.08%) and healthy RBCs were examined. Although aggregation was found to be less pronounced in hardened cells, suspensions of hardened RBCs were found to exhibit a similar haematocrit distribution with aggregated RBC suspensions when aggregation is apparent, i.e. a pronounced haematocrit concentration near the centreline. A comparison between the hardened and aggregated sample distributions downstream of the bifurcation was thus deemed important.

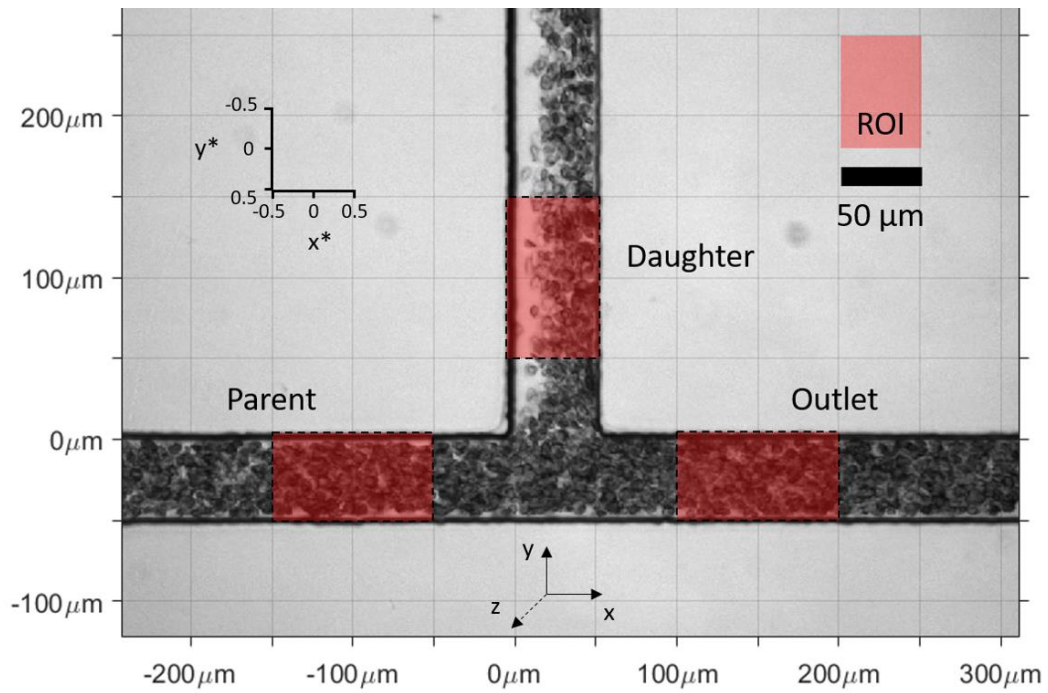


Figure 6.1: Sample instantaneous image of flow of aggregating healthy RBCs in the T-junction microchannel. Shaded areas indicate the regions of interest (ROI) where profiles are calculated from. RBC suspensions enter through the parent branch (left of figure) and exit through the daughter and outlet branches. The flow ratio Q^* between outlet and daughter branch is 0.94.

6.2 The effect of flow ratio on velocity and haematocrit distributions

In the following section, velocity and haematocrit profiles are presented for the parent, daughter and outlet branches. In the parent branch, the profiles are characterised based on their bluntness utilizing haematocrit and velocity bluntness indices, B_H^* and B_U^* respectively. For the daughter and outlet branches, the profiles are not expected to be symmetric with respect to the

centreline, hence the velocity and haematocrit profiles are characterised in terms of skewness. The skewness of velocity and haematocrit distributions, S_U and S_H , were determined by equations (2.9) and (2.10) respectively and the extent of skewness is quantified as a function of flow ratio.

6.2.1 Local haematocrit distributions

The difference in haematocrit distributions upstream of the bifurcation is expected to have an effect on the haematocrit distribution in the daughter and outlet branches downstream. Figure 6.2 shows haematocrit bluntness index comparisons between hardened and healthy RBC samples in the parent branch, i.e. upstream of the bifurcation. The flow rate, expressed as normalised velocity U^* , was maintained within a narrow range, as seen in Table 6.1, in contrast to the previous chapters in which flow rates in the range 1 to $\sim 200 \text{ s}^{-1}$ were employed.

Table 6.1: The range of perfused flow rates, expressed in U^* , for the four samples. The flow rate was measured in the parent branch.

Sample	$U^* (\text{s}^{-1})$
Healthy - PBS	74 - 106
GA 0.08% - PBS	72 - 142
Healthy - Dextran	99 - 145
GA 0.08% - Dextran	89 - 132

As expected from the previous findings of Chapter 3, healthy samples suspended in PBS produce higher values of B_H than hardened samples. This means that healthy RBC samples produce haematocrit profiles with less sharp distribution compared to hardened samples (Figure 6.2).

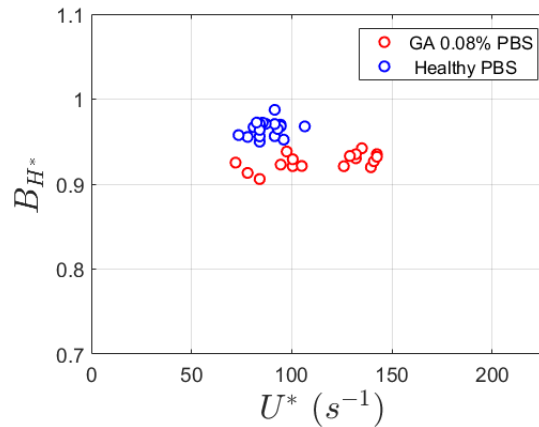


Figure 6.2: Haematocrit bluntness index comparison in the parent branch between samples suspended in PBS healthy against hardened (GA 0.08%).

Figure 6.3 shows comparisons of typical haematocrit profiles measured in the outlet and daughter branches at low, medium and high flow ratios Q^* for healthy RBCs (Figure 6.3a,b) and GA 0.08% hardened RBCs (Figure 6.3c,d) suspended in PBS. The haematocrit distributions of both healthy and hardened cells in the outlet branch, Figure 6.3 a and c, are strongly skewed towards the wall that faces the daughter branch ($y^* = -0.5$) and this effect is more pronounced at low and medium flow ratios. Similarly to the outlet branch, the daughter branch haematocrit profiles exhibit a strong skewness towards the wall that faces the outlet branch ($x^* = 0.5$) which is also more pronounced at low and medium flow ratios (Figure 6.3b,d). The healthy RBC suspensions exhibit a bimodal haematocrit distribution in both daughter and outlet branches, which is more pronounced at high flow ratios (Figure 6.3a,b). The bimodal behaviour of healthy RBC suspensions has also been observed by Sherwood *et al.* (2014).

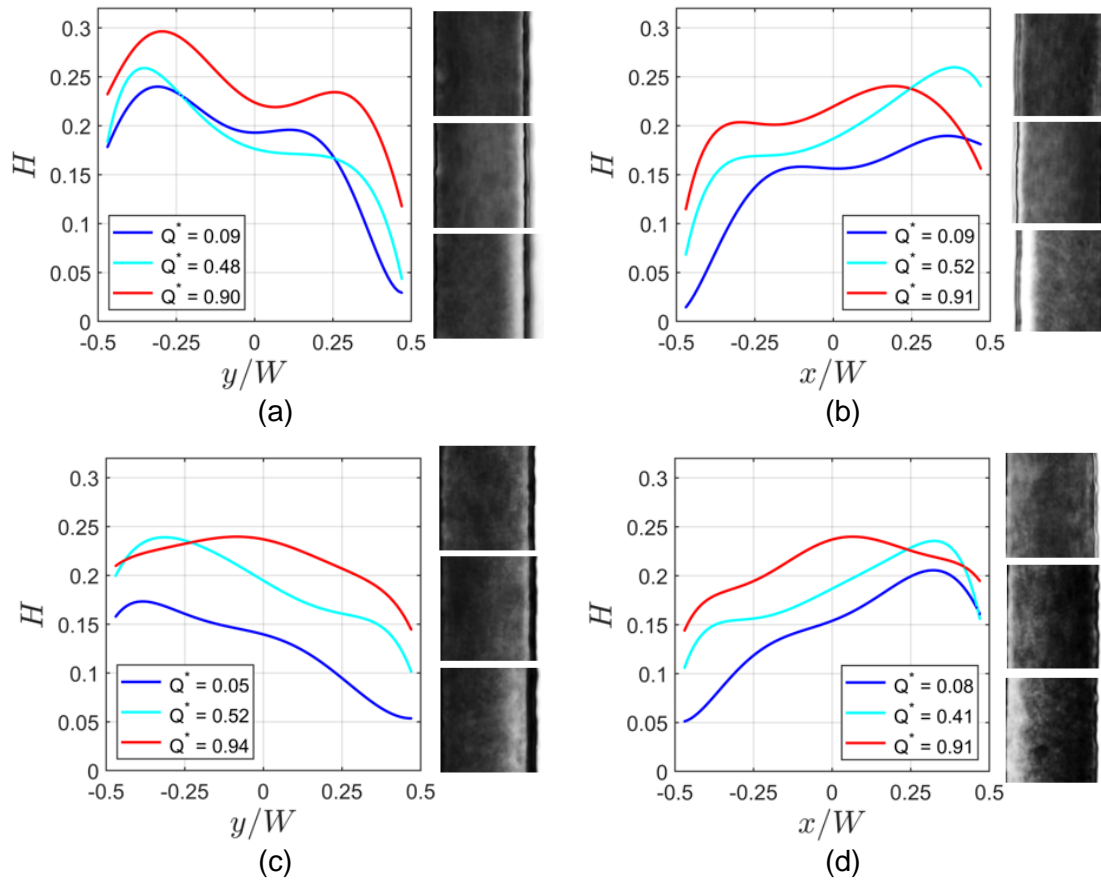


Figure 6.3: Haematocrit profiles of healthy and GA 0.08% RBC samples at low medium and high flow ratios with the time averaged images from which the profiles were extracted from; outlet branch on the left side (a,c) and daughter branch on the right side (b,d). (a,b) Healthy sample suspended in PBS (c,d) GA 0.08% hardened sample suspended in PBS. The contrast of the time averaged images was enhanced for clarity.

Moreover, healthy RBC suspensions, exhibit in general steeper haematocrit gradients, compared to the hardened RBC samples which show a smoother transition (Figure 6.3c,d) and this effect is more pronounced at lower flow ratios. In particular, the haematocrit of GA 0.08% hardened sample, at low flow ratios, does not reach to almost zero as in healthy samples meaning that the frequency of RBCs penetrating the cell depleted layer is higher than that of the healthy samples. This steep decrease of haematocrit of healthy RBCs near the wall with the lower concentration, i.e. $y^* = 0.5$ and $x^* = -0.5$ for the daughter and outlet

branch respectively, might translate to a wider cell depleted layer of the healthy RBC sample compared to the hardened one. The cell depleted layers of each distribution, which will be analysed later in the chapter, can be seen in the time averaged images of Figure 6.3.

The extent of asymmetry in the measured haematocrit distributions was investigated utilizing the haematocrit skewness index (S_H) as described by equation (2.10) in Chapter 2. In Figure 6.4, the haematocrit skewness is plotted against flow ratio Q^* for the samples shown in Figure 6.3. The skewness indices do not show any statistically significant differences between the healthy and hardened RBC samples in outlet and daughter branches. It would be expected that the haematocrit profile differences between healthy and hardened RBCs in the parent branch would produce haematocrit distributions with different skewness in the outlet and daughter branches but this is not the case in the comparisons shown in Figure 6.4. However, the individual haematocrit profiles in Figure 6.3 clearly show differences between hardened and healthy RBCs which are not captured by the skewness index.

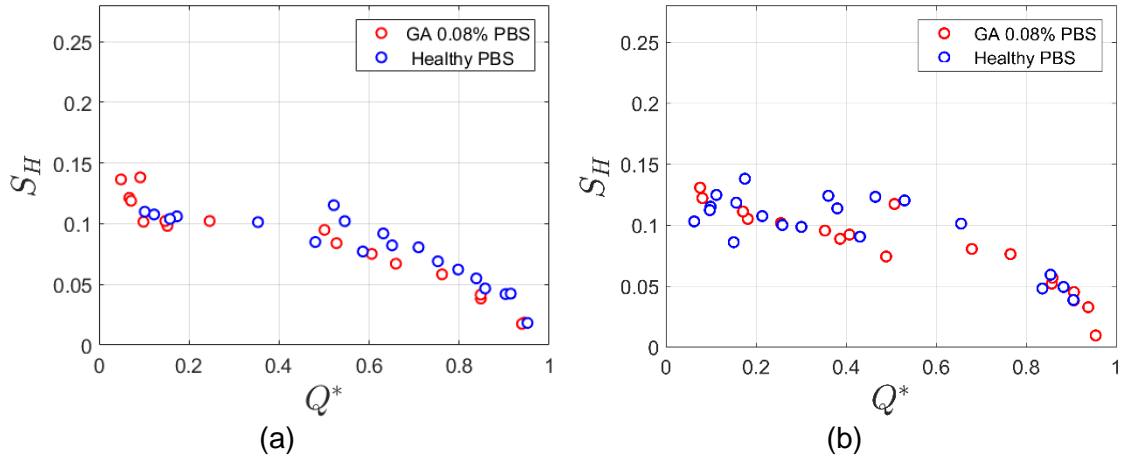


Figure 6.4: Haematocrit profile skewness, against flow ratio; comparison of healthy samples against GA 0.08% hardened sample both suspended in PBS, (a) outlet branch and (b) daughter branch.

6.2.2 Flow partitioning and plasma skimming

In the previous section the local haematocrit distributions in each branch were described. The haematocrit profiles showed skewed distributions at low flow ratios for both outlet and daughter branches. In this section, the ratio of haematocrit between the branches is analysed in order to investigate the extent of plasma skimming for the various flow ratios investigated.

Figure 6.5 shows the ratio between branch haematocrit and parent haematocrit, H/H_P , as a function of the flow ratio, Q^* . It can be seen that the haematocrit ratio is decreased ($H/H_P < 1$) at low flow ratios ($Q^* < 0.5$) and increased ($H/H_P > 1$) at higher flow ratios ($Q^* > 0.5$). When the flow ratio approaches unity ($Q^* \approx 1$), the haematocrit also approaches one, since all the parent branch RBCs will enter one branch of the bifurcation. Even though the differences between healthy and

hardened RBCs are not statistically significant, the plasma skimming phenomenon is evident.

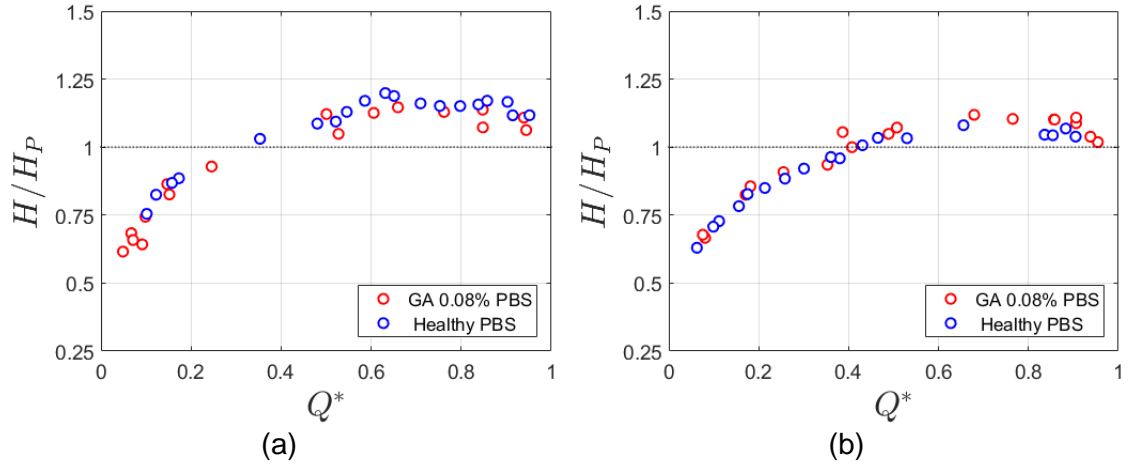


Figure 6.5: Haematocrit ratio H/H_P against flow ratio; comparison of healthy against GA 0.08% hardened RBC samples in PBS in (a) outlet branch and (b) daughter branch.

In order to investigate further the plasma skimming phenomenon the RBC flux ratio (F^*) was calculated by equation (6.1). A single-phase fluid exhibits no ‘plasma skimming’ and $F^* = Q^*$. The fitting curves in Figure 6.6, were produced based on Pries *et al.* (1989) according to equation (6.2):

$$F^* = \frac{H_{o,d}}{H_P} \frac{Q_{o,d}}{Q_P} = H^* Q^* \quad (6.1)$$

$$\text{logit}(F^*) = A + B \text{logit}(Q^*) \quad (6.2)$$

with

$$\text{logit}(x) = \ln \frac{x}{1-x} \quad (6.3)$$

and

$$F^* = \frac{e^{A+B \logit(Q^*)}}{1 + e^{A+B \logit(Q^*)}} \quad (6.4)$$

where B expresses the non-linearity of the relation between haematocrit and flow ratio and A describes the asymmetry of that relation. In case that there is no plasma skimming A should be zero and B equal to 1; when B is greater than 1, the extent of plasma skimming increases.

Figure 6.6 shows that plasma skimming occurs in both healthy and hardened RBC samples as the curves deviate from the $F^* = Q^*$ line. The comparison between healthy-PBS and GA 0.08%-PBS samples in the outlet branch, shows no significant difference in the extent of plasma skimming, with B-values of 1.38 ± 0.16 and 1.36 ± 0.19 for the healthy and hardened samples respectively. In the daughter branch the GA 0.08% RBC samples have higher B-value than healthy-PBS samples, 1.29 ± 0.12 to 1.19 ± 0.21 respectively. However, it should be mentioned that the differences are not statistically significant as in both cases comparisons fall within the range of uncertainty.

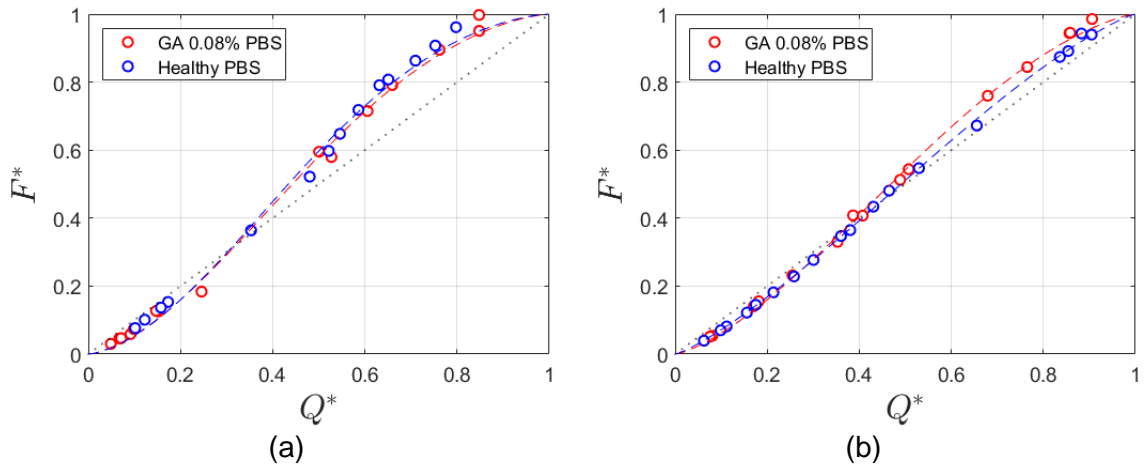


Figure 6.6: Flux-flow ratio curves; Comparison of healthy samples against GA 0.08% hardened sample both suspended in PBS in the (a) outlet branch and in (b) daughter branch. Fitting curves according to Equation (6.4), dotted line corresponds to $F^* = Q^*$.

Table 6.2: Fitting coefficients A and B for the fitting for the samples in outlet and daughter branches of Figure 6.6 with 95% confidence intervals.

	Outlet		Daughter	
	A	B	A	B
Healthy PBS	0.39 ± 0.06	1.38 ± 0.16	0.04 ± 0.04	1.19 ± 0.21
GA 0.08% PBS	0.33 ± 0.05	1.36 ± 0.19	0.16 ± 0.06	1.29 ± 0.12

6.2.3 Cell depletion layer

In this section the effect of flow ratio on the cell depleted layer (CDL) will be analysed. The CDL was estimated from the time averaged images from each set of measurements. Figure 6.8a shows a sample image of healthy RBC flows in the daughter branch for a 0.09 flow ratio. It can be clearly seen that RBCs produce a depleted layer near the wall. Figure 6.8b shows the time averaged image corresponding to this set of measurements; the red line corresponds to the distribution of image intensity across the channel and the blue line the derivative

of image intensity across the channel, dl/dx and dl/dy , for the daughter and outlet branch respectively. The width of the CDL, δ , was calculated as the average distance between the two local minima and maxima of dl/dx and dl/dy that correspond to the channel wall and the CDL boundary respectively, along the ROI. Figure 6.8c shows the binarized time averaged image. The error bars in the graphs of Figure 6.8 show one standard deviation of the measured CDL thickness along the ROI.

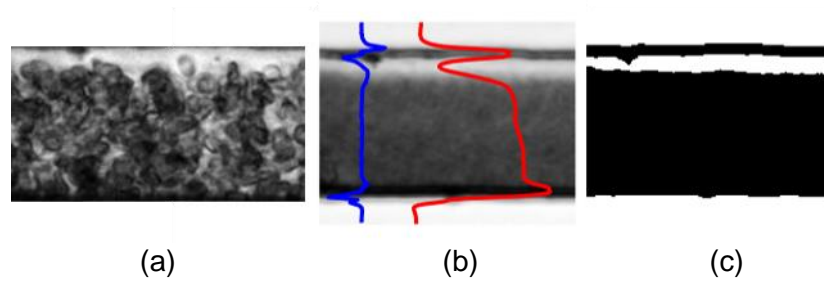


Figure 6.7: (a) Sample image of healthy RBCs in the daughter branch, $Q^* = 0.09$. (b) Time averaged image out of 60 pairs of images; the red line shows the image intensity distribution and blue line the derivative of image intensity across the channel width. (c) Binarised time averaged image.

Studies in straight vessels with similar dimensions have shown that a typical CDL thickness (δ) is in the order of 2-3 μm for healthy non-aggregating blood (Pries *et al.*, 1983; Kim *et al.*, 2007) while downstream of bifurcations the thickness of CDL increases; it is also affected by the presence of aggregation and varies with flow ratio (Sherwood *et al.*, 2012). Figure 6.8, shows the effect of flow ratio on the CDL thickness normalised with the channel width, $\delta^* = \delta/W$, in both outlet and daughter branches for healthy and hardened RBC samples. In all cases, the CDL thickness is inversely proportional to the flow ratio as its thickness increases at low flow ratios and gradually decreases at higher flow ratios. The effect of flow ratio on

CDL width is less pronounced in hardened RBCs compared to the healthy ones. The decreasing flow ratio has a larger impact on the healthy samples as δ^* increases at flow ratios close to 0.6 while in the hardened case, δ^* increases at lower flow ratios ($Q^* \approx 0.4$). Hardened RBCs would be expected to produce wider CDL than the healthy ones, since it has been shown in the previous chapters that hardened RBCs tend to concentrate towards the centre line. However, it should be noted that in the findings of the previous chapters, the flow was imaged 160 channels widths downstream of the inlet of the channel, meaning that the flow was fully developed. In contrast, in the present case, the flow was imaged only two channel widths downstream of the bifurcation, a length that cannot be considered sufficient for the cell interactions and migration phenomena to reach equilibrium. In addition, the decreased haematocrit that is exhibited in low flow ratios, as shown earlier, combined with the lower flow rates, i.e. local shear distributions, might produce less frequent RBC collisions with lower intensity, leading to weaker migration phenomena.

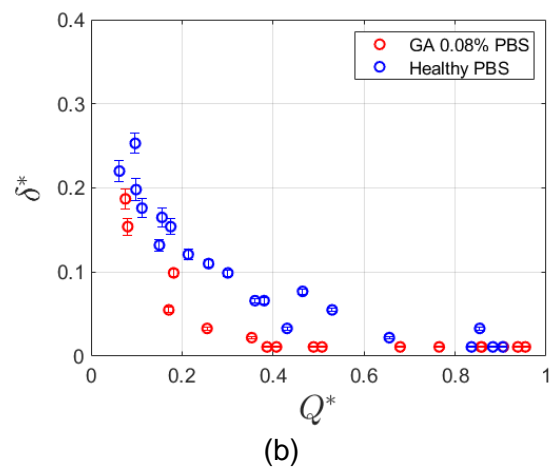
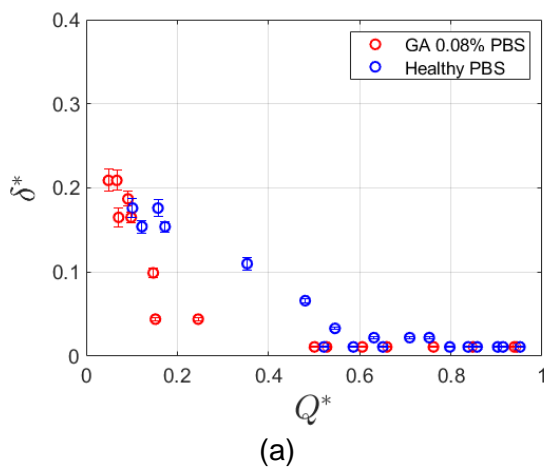


Figure 6.8: Normalised cell depleted layer with channel width, δ^* , as a function of flow ratio, Q^* . Comparison between healthy and hardened (GA 0.08%) RBC samples in PBS (a) in the outlet branch and (b) in the daughter branch.

6.2.4 Velocity distributions

The heterogeneous haematocrit distribution downstream of the bifurcation is expected to affect the velocity profiles. In the parent branch the velocity profiles are symmetrical and their shape can be characterised in terms of the bluntness using equation (2.3) from Chapter 2. Figure 6.9 compares the bluntness index (B_{U^*}) values obtained as a function of the normalised velocities, U^* , for healthy and hardened RBCs suspended in PBS. The range of normalised velocities was adjusted within a narrow region as explained in Figure 6.2. The profiles of the healthy RBC samples exhibit B_U values within 0.19 and 0.28 while the GA 0.08% hardened samples have B_U values ranging from 0.10 to 0.21, i.e. the hardened RBCs produce velocity profiles with lower bluntness compared to healthy RBCs in agreement with the findings of Chapter 3.

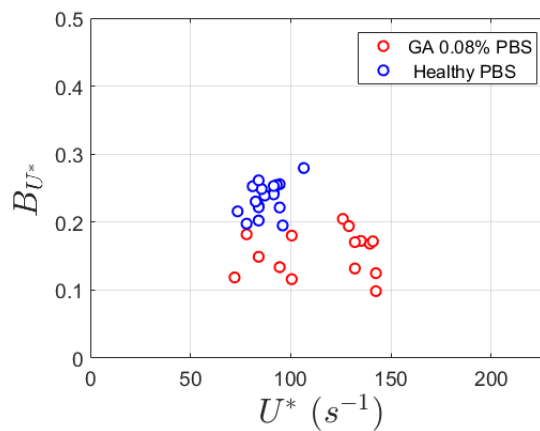
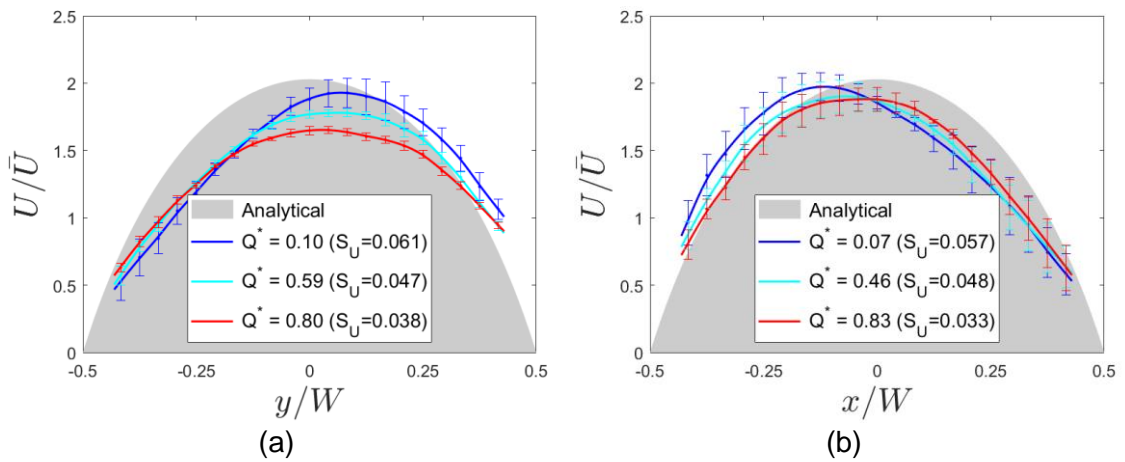


Figure 6.9: Velocity profile bluntness index against normalised velocity, U^* , in the parent branch. Comparison between healthy samples and hardened RBCs (GA 0.08%) suspended in PBS.

Figure 6.10 shows normalised velocity distributions in outlet and daughter branches for each sample at selected flow ratios. In order to analyse the velocity skewness for all measurements, the skewness index equation (2.9) was utilised. The velocity profile skewness index, S_U , determined for each profile is also indicated in the figure. In all cases, the velocity profiles were skewed in the opposite direction compared to the haematocrit profiles. The healthy RBC samples show more intense skewness (Figure 6.10a,b) in both outlet and daughter branches, compared to the GA 0.08% hardened RBC samples (Figure 6.10c,d).



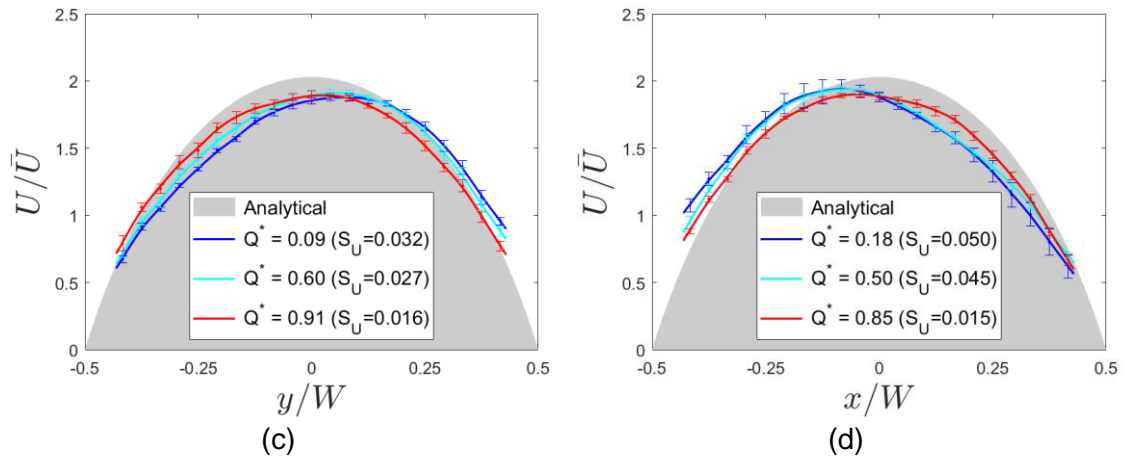


Figure 6.10: Normalised velocity profiles of the samples at different flow ratios. The velocity skewness index, S_U , is also indicated. Healthy RBC sample suspended in PBS in the (a) outlet and (b) in the daughter branch. GA 0.08% hardened RBC samples suspended in PBS (c) in the outlet and (d) in the daughter branch. The grey area indicates the analytical velocity profile for a Newtonian fluid in a square channel.

Figure 6.11 shows the skewness index of the velocity profiles in the outlet and daughter branches plotted against the flow ratio for the cases examined. In both branches, outlet (Figure 6.11a) and daughter (Figure 6.11b) healthy RBCs have S_U values ranging from 0.02 to 0.06 that vary little with flow ratio. The GA 0.08% hardened samples have lower S_U values ($p < 0.05$) than healthy ones in the outlet branch (Figure 6.11a) but this is not the case in the daughter branch (Figure 6.11b) as both GA 0.08% and healthy samples exhibit similar values of S_U . In both cases there is no strong correlation of S_U to flow ratio.

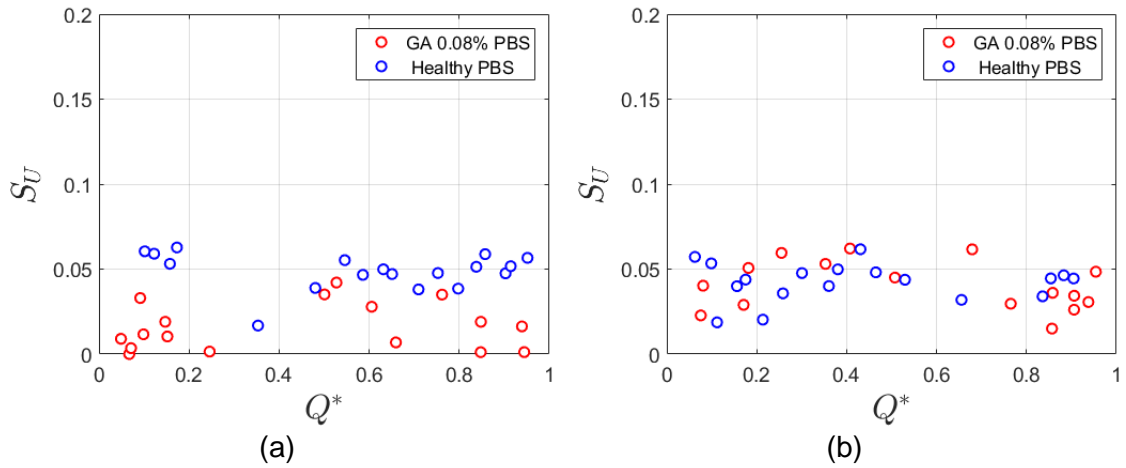


Figure 6.11: Velocity profile skewness plotted against flow ratio. Comparison between healthy sample against GA 0.08% hardened sample suspended in PBS in the (a) outlet and (b) daughter branches respectively.

As has been demonstrated in Chapter 3 (Figure 3.9) and in Passos *et al.* (2019), the velocity and haematocrit profile bluntness are correlated. In particular, a negative correlation was found for the healthy samples and a positive for the hardened ones. The skewness of the haematocrit and velocity profiles downstream of the bifurcation would be expected to be correlated as well. In Figure 6.12, the velocity profile skewness is plotted against the haematocrit skewness for the examined samples. The correlation between S_U and S_H was tested with Pearson showing a positive correlation, however no statistically significant correlation was indicated ($p > 0.05$).

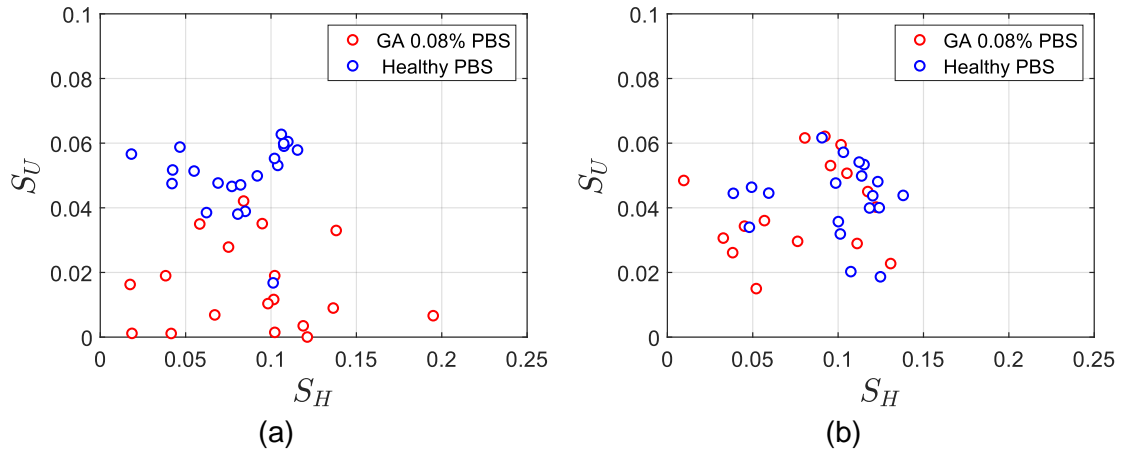


Figure 6.12: Velocity profile skewness S_U , against haematocrit skewness S_H ; comparison of healthy sample against GA 0.08% hardened sample suspended in PBS in the (a) outlet and (b) daughter branch.

6.3 The effect of parent branch flow rate on velocity and haematocrit distributions

In the previous section the parent branch flow rates were kept within a narrow range as seen in Figure 6.2. while the flow ratios between the outlet and daughter branch were varied between 0.05 to 0.95 ($Q_{o,d}/Q_p = 0.05 - 0.95$). On the contrary, in this section, the flow between the outlet branches was adjusted in order to have equal flow ratio between the outlet/daughter and parent branch i.e. $Q_{o,d}/Q_p \approx 0.5$, while the parent branch flow rates - expressed in terms of U^* - varied from 1 to 250 s^{-1} . The purpose of this set of experiments was to investigate the effect of parent branch flow rate on haematocrit and velocity distribution downstream of the T-junction.

6.3.1 Local haematocrit distributions

Figure 6.13 compares the haematocrit bluntness indices between the healthy and hardened (GA 0.08%) RBC samples in the parent branch, for the range of measured normalised velocities. The results agree with the findings of Chapter 3. GA 0.08% hardened RBCs exhibit a sharper haematocrit distribution than the healthy sample at the whole range of measured flow rates as analysed in Chapter 3.

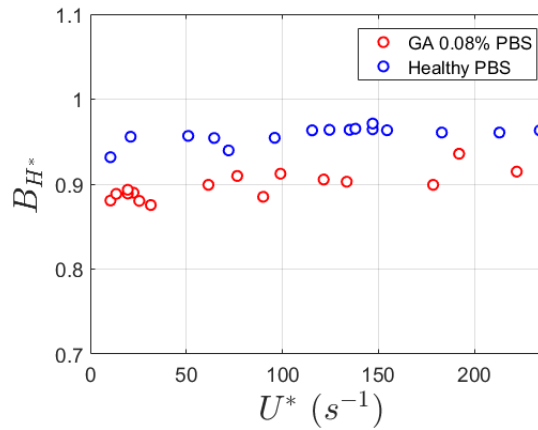


Figure 6.13: Haematocrit bluntness index comparison in the parent branch of (a) healthy and hardened (GA 0.08%) RBC suspensions in PBS.

Figure 6.14 shows typical haematocrit profiles in the outlet and daughter branches for the cases examined at low, medium and high parent branch normalised velocities. In all cases the haematocrit distribution is skewed towards one wall. In the outlet branch (Figure 6.14a,c) the haematocrit profile is skewed towards $y^* = -0.5$ while in the daughter branch (Figure 6.14b,d) towards $x^* = 0.5$. Similar differences between healthy and hardened samples were observed in Figure 6.3, for flow ratio around to 0.5, i.e. equal split. The effect of parent branch

6.3 The effect of parent branch flow rate on velocity and haematocrit distributions

flow rate on the shape of the haematocrit profiles is evident; the haematocrit skewness is more pronounced at lower parent branch flow rates and this is more clear for the healthy RBC samples. Due to the equal split, as seen in the previous section, for $Q^* = 0.5$, the $H/H_P \approx 1$ (Figure 6.5) meaning that the haematocrit levels are similar as seen in Figure 6.14.

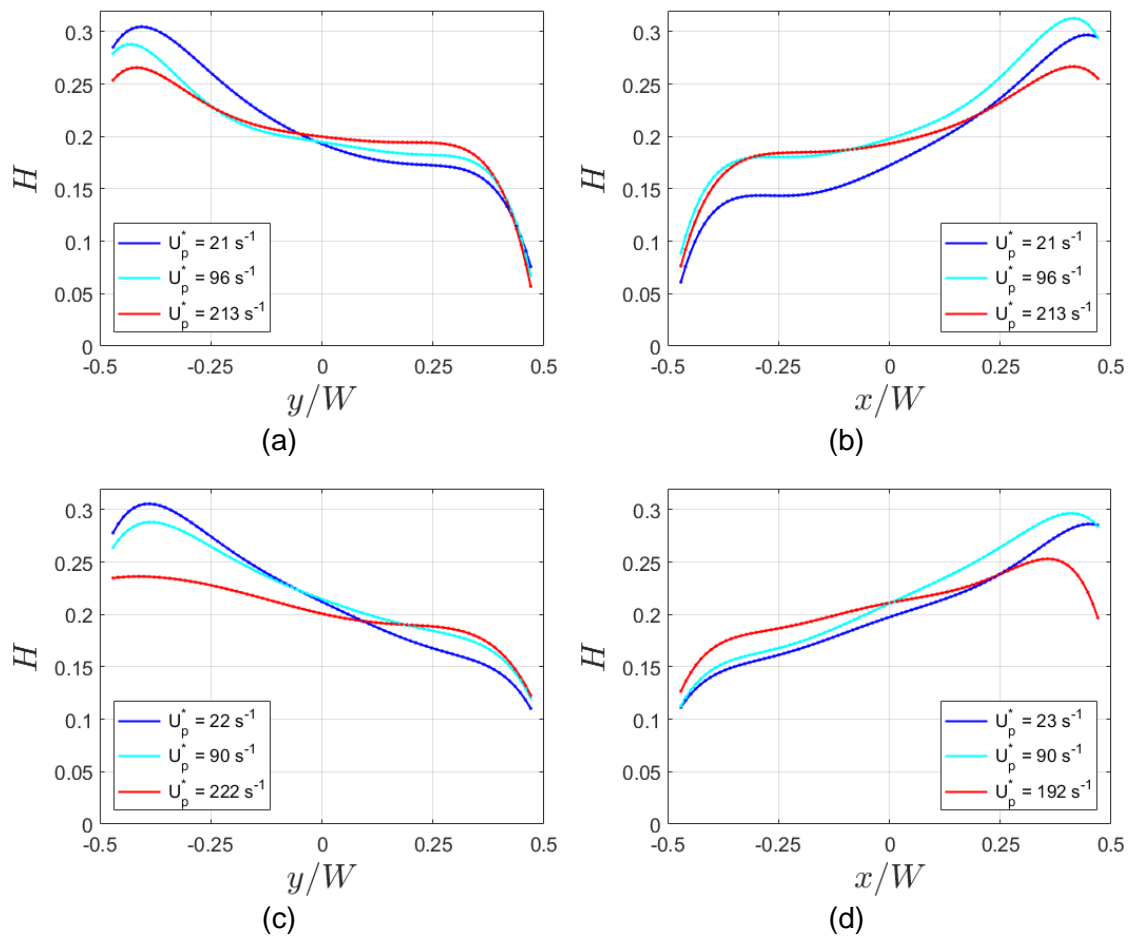


Figure 6.14: Haematocrit profiles in the outlet and daughter branches at low, medium and high normalised parent branch velocities for $Q^* \approx 0.5$; Healthy sample suspended in PBS (a) outlet and (b) daughter branches. GA 0.08% hardened sample suspended in PBS (c) outlet and (d) daughter branches.

The haematocrit profile skewness is plotted in Figure 6.15 as a function of the parent branch U^* , comparing the healthy and hardened RBC samples in the outlet

and daughter branches. Both the healthy and hardened RBC samples in the outlet (Figure 6.16a,c) and daughter branches (Figure 6.15b,d) show a gradual decrease in skewness with flow rate. Since, $Re \ll 1$ and inertial forces are negligible in the whole range of U^* , the haematocrit skewness variations can be attributed to the shear induced migration and cell-cell interactions. The two mechanisms have a competitive role as the mechanism of migration concentrates the RBCs towards the area with minimum shear, i.e. towards the centre of the flow and cell collisions induce random lateral motion of the RBCs, with the net effect producing a motion away from the concentration gradient, i.e. toward the wall. The decrease of haematocrit skewness with flow rate results in more uniform haematocrit distribution, thus, it can be assumed that with the increasing flow rate the cell-cell interactions dominate the shear induced mechanism for the current conditions.

The haematocrit skewness exhibits a negative correlation with the parent branch flow rate for equal flow split. The significance of the trend was tested with the Pearson correlation test and all the cases showed statistically significance apart from the healthy sample in the daughter branch with $p=0.067$. The Pearson correlation coefficients and p-values are shown in Table 6.3.

Table 6.3: Pearson correlation coefficients for haematocrit skewness as a function of parent branch flow rate in outlet and daughter branches. RBCs suspended in PBS (no aggregation).

RBC samples	Outlet		Daughter	
	r	p	r	p
Healthy in PBS	-0.88	$<10^{-4}$	-0.48	<0.07
GA 0.08% in PBS	-0.80	$<10^{-3}$	-0.88	$<10^{-5}$

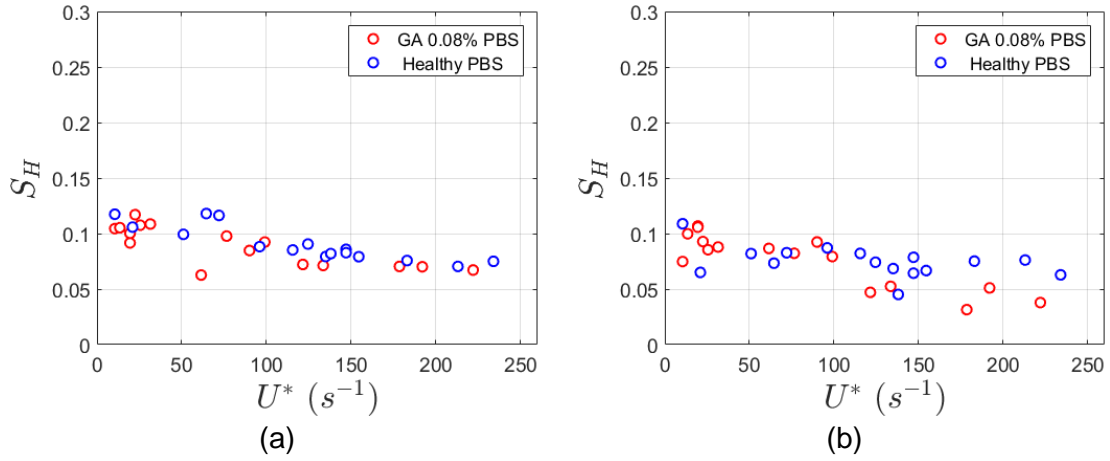


Figure 6.15: Haematocrit profile skewness against parent branch normalised velocity; comparison of healthy against GA 0.08% hardened RBC samples both suspended in PBS: (a) outlet and (b) daughter branch.

6.3.2 Cell depleted layer

As discussed previously, the thickness of the cell depletion layer is expected to increase with haematocrit skewness. Figure 6.16 plots the normalised cell depleted layer thickness, δ^* , downstream of the bifurcation for healthy and hardened cells. The findings in the previous set of experiments showed that δ^* was minimal for flow ratios, Q^* , above 0.5 for the healthy sample, while for the hardened samples, δ^* was minimal for flow ratios larger than 0.4 (Figure 6.8). In this set of experiments the flow ratio between the branches is constant and close to 0.5 ($Q^* \approx 0.5$), so a minimum δ^* would be expected.

The values of CDL thickness of the healthy RBC samples in Figure 6.16 a and b correspond to a range from 1 to 3 μm and is independent of parent branch flow rate for the whole range of measurements. The GA 0.08% sample in PBS also

exhibits low values of CDL thickness in the whole range of measurements regardless of the flow rate in the parent branch, in agreement with the previous experiments (Figure 6.8). In both outlet and daughter branches, the hardened RBC samples produce a narrower CDL than the healthy sample as was also shown in the previous section.

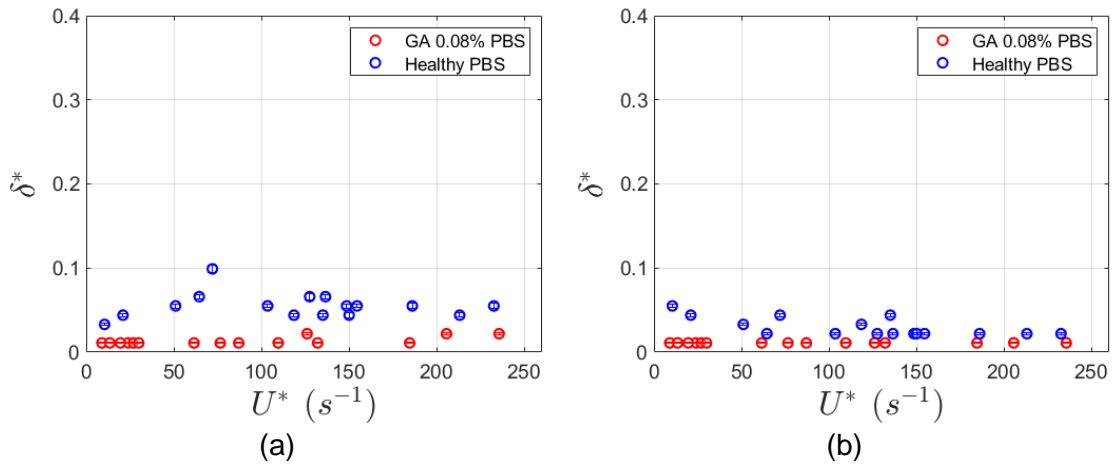


Figure 6.16: Normalised cell depleted layer width as a function of parent branch flow rate; comparison of healthy against GA 0.08% hardened RBC samples both suspended in PBS in (a) the outlet and (b) daughter branches.

6.3.3 Velocity distributions

The bluntness index, B_u , of the symmetric velocity profiles upstream of the bifurcation (parent branch), is analysed in Figure 6.17. The comparison between healthy and hardened RBC samples shows that healthy RBCs produce blunter velocity profiles than the hardened RBCs in the whole range of U^* ($p < 0.05$) (Figure 6.17a). The decrease of velocity profile bluntness with hardening, agrees with the findings of Chapter 3.

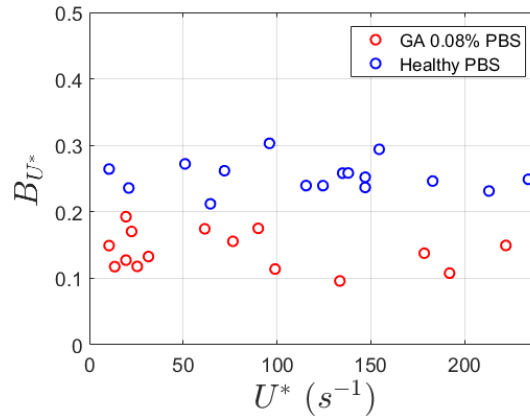


Figure 6.17: Velocity bluntness index against normalised velocity in the parent branch. Comparison between healthy and GA 0.08% hardened RBC samples suspended in PBS.

The velocity profiles downstream of the bifurcation are expected to develop a non-symmetric shape, that is skewed towards the opposite side of the haematocrit skewness as explained earlier in the chapter. Figure 6.18 shows typical velocity profiles at low, medium and high parent branch U^* , for each sample in the outlet and daughter branches at equal flow split between the branches ($Q^* \approx 0.5$). The differences in skewness of the velocity profiles between the parent branch U^* seems to be less pronounced compared to the differences that exhibited at different flow ratios, illustrated in Figure 6.10. Moreover, it can be observed that in the outlet branch the velocity profiles of healthy samples (Figure 6.18 a), apart from the skewed shape they also exhibit blunter shape compared to hardened samples (Figure 6.18 c) as shown and discussed in Chapter 3; however, this is effect less pronounced in the daughter branch. It should be noted that the T-junction in these experiments is such that the outlet branch is a continuation of the parent branch, while the daughter branch is perpendicular, hence some flow characteristics observed in the parent branch

are more likely to be continued in the outlet branch rather than the daughter branch.

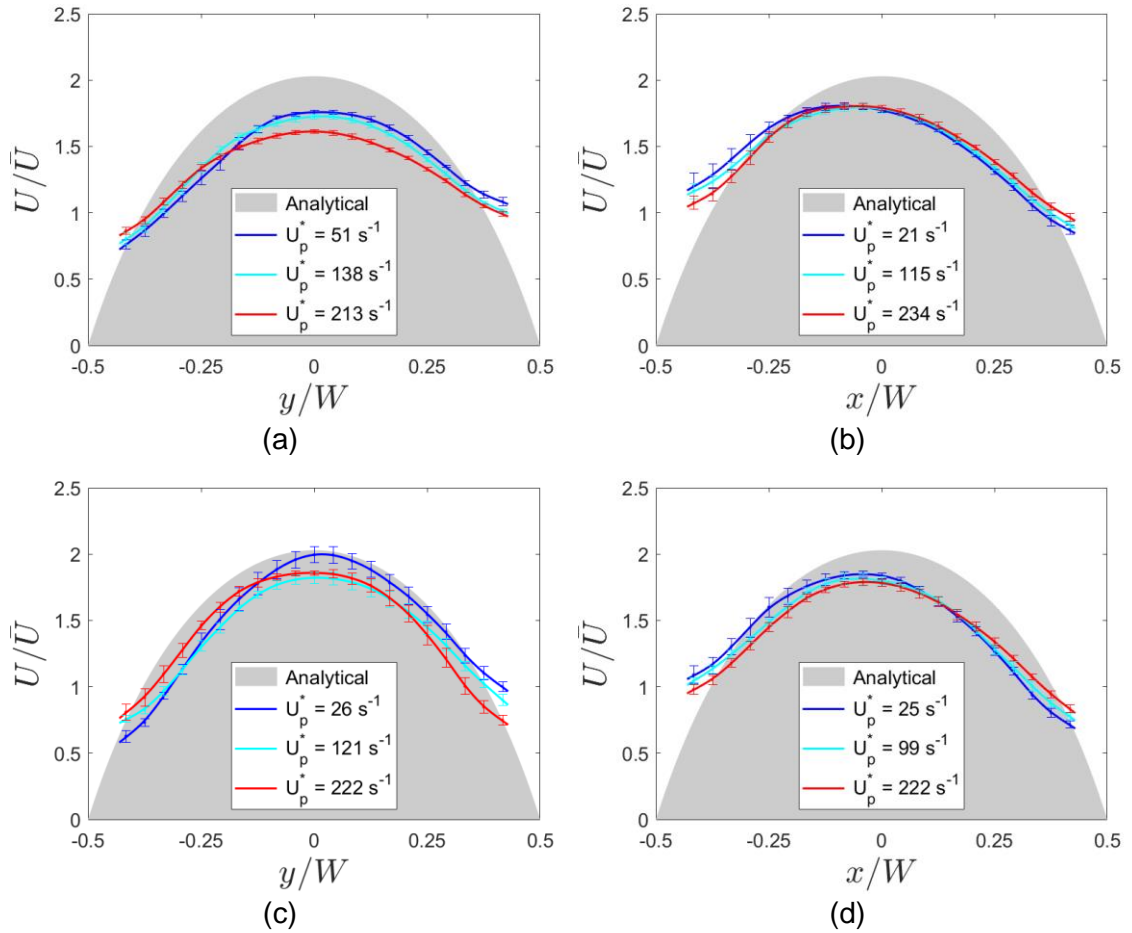


Figure 6.18: Normalised velocity profiles for different parent branch flow rates, U_p^* . Comparison of healthy RBC samples suspended in PBS in the (a) outlet and (b) daughter branches. GA 0.08% hardened RBC samples in PBS in the (c) outlet and (d) daughter branches.

The velocity profiles were characterised in terms of skewness using the velocity skewness index, S_U (2.9). Figure 6.19 shows the velocity skewness indices downstream of the bifurcation as a function of parent branch flow rate, expressed in normalised velocity, U^* . Both, the healthy and GA 0.08% hardened RBC samples exhibit S_U values that are independent of the parent branch flow rate.

Moreover, the S_U values of both samples do not exhibit statistically significant differences in the outlet (Figure 6.18a) and daughter (Figure 6.18b) branches.

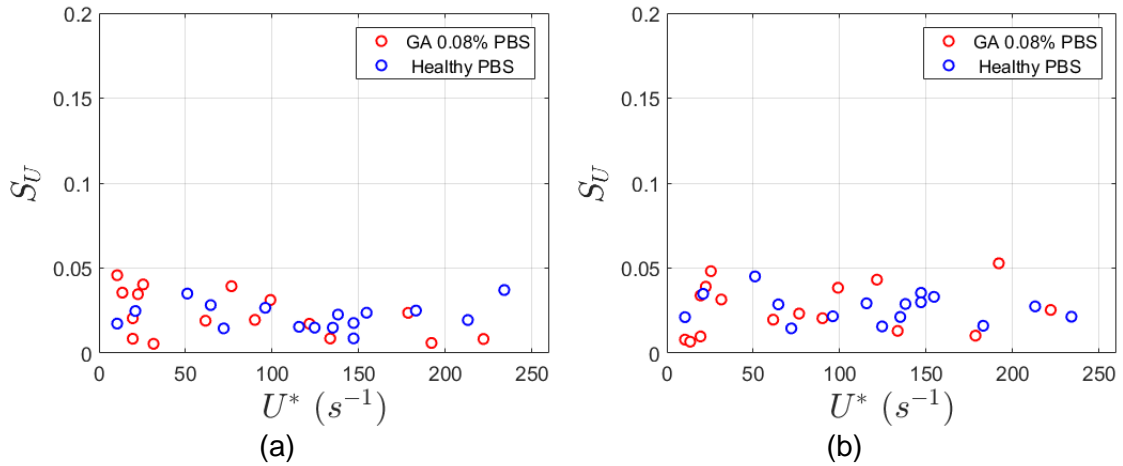


Figure 6.19: Velocity profile skewness, against parent branch U^* . Comparison of healthy and GA 0.08% hardened RBC samples in the (a) outlet and (b) daughter branches.

6.4 The effect of aggregation

In this section, the effect of aggregated RBC samples, both healthy and hardened, on haematocrit and velocity distributions downstream of the bifurcation is investigated. Aggregation was induced by adding Dextran in the PBS solution as explained in Chapter 2. Two different conditions of sample perfusion through the T-junction were examined similarly to the previous sections: (i) varying flow ratio between the branches downstream of the bifurcation under a constant parent branch flow rate and (ii) a varying parent branch flow rate at an equal flow split between the outlet and daughter branches. Healthy and hardened RBC samples suspended in Dextran will be compared in order to examine the effect of aggregation on the bifurcating flows in conjunction with RBC deformability.

6.4.1 Haematocrit distributions

Figure 6.20 compares the S_H values for varying flow ratios between the branches; the healthy and hardened RBC samples suspended in Dextran were compared respectively in both outlet and daughter branches.

The healthy-Dextran sample shows higher haematocrit skewness at low flow ratios in comparison with the GA 0.08%-Dextran sample both in outlet and daughter branches as seen in Figure 6.20a and b respectively. This can be attributed to the presence of aggregation, which is apparent for the healthy RBCs, in contrast to the hardened samples which show no evidence of aggregation, in agreement with the findings of Chapter 5. The shear forces increase with flow ratio and for $Q^* > 0.5$ the RBC aggregates tend to disaggregate resulting in both healthy and hardened RBC samples to exhibit similar S_H values in both branches (Figure 6.20a,b).

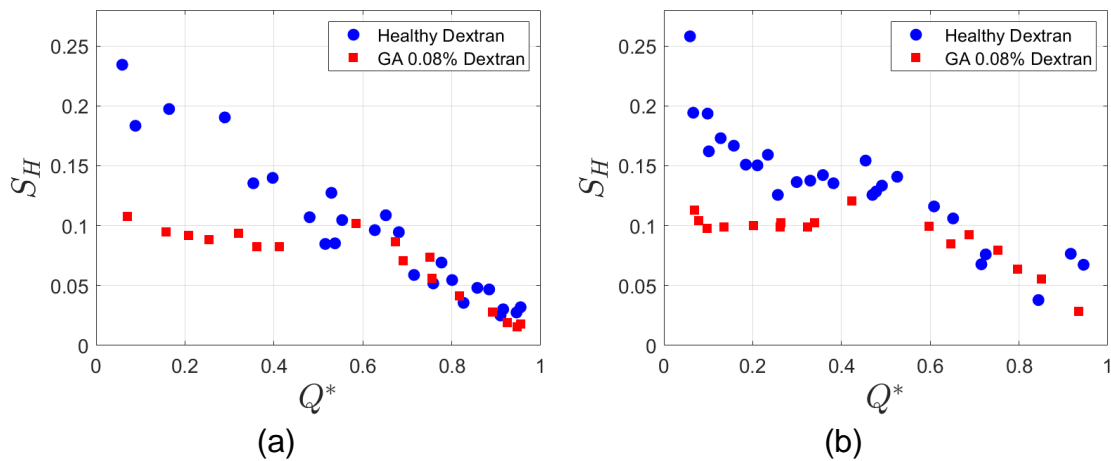


Figure 6.20: Haematocrit profile skewness S_H as a function of flow ratio Q^* . Comparison between healthy and GA 0.08% hardened RBC samples suspended in PBS-Dextran solution in the (a) outlet and (b) daughter branches respectively of a T-junction bifurcation.

In Chapter 5, it was shown that the bluntness of the haematocrit profiles for the healthy-Dextran samples in a straight channel, i.e. in the parent branch for the present case, is inversely proportional to the flow rate; at low flow rates, aggregation is pronounced and the RBCs concentrate towards the centre of the flow producing sharper haematocrit profiles compared to higher flow rates where the aggregates disaggregate. On the other hand, the hardened GA 0.08% samples showed no evidence of aggregation in the whole range of investigated flow rates. Figure 6.21 shows haematocrit skewness index comparisons between healthy and hardened RBCs in Dextran for equal flow ratio between the two branches and varying parent branch flow rate. Downstream of the bifurcation the apparent differences in parent branch haematocrit profile bluntness between healthy and hardened RBC samples is translated into haematocrit skewness differences. In particular, at parent branch flow rates lower than 100 s^{-1} , the healthy RBC samples exhibit higher haematocrit skewness than the hardened RBC samples in both branches. At higher flow rates ($U^* > 100 \text{ s}^{-1}$), aggregation is less apparent and the haematocrit skewness values of the two RBC samples exhibit similar levels. Moreover, in both cases, the haematocrit skewness exhibits a negative correlation with the parent branch flow rate as was showed previously; the Pearson correlation coefficients and p-values are shown in Table 6.4.

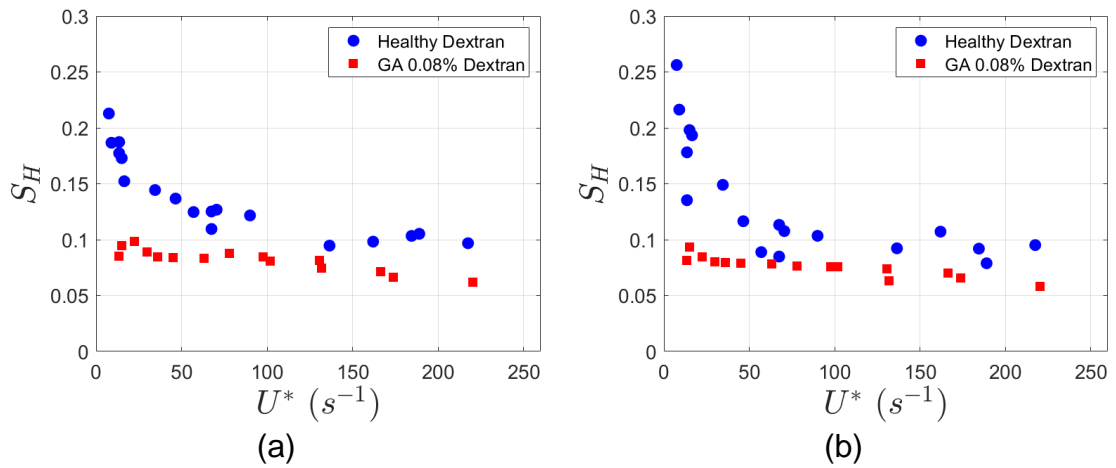


Figure 6.21: Haematocrit profile skewness S_H as a function of parent branch normalised velocity U^* . Comparison between healthy and GA 0.08% hardened RBC samples suspended in PBS-Dextran solution in (a) the outlet and (b) daughter branches respectively of a T-junction bifurcation.

Table 6.4: Pearson correlation coefficients for haematocrit skewness in the outlet and daughter branches as a function of parent branch flow rate.

Sample	Outlet		Daughter	
	r	p	r	p
Healthy in Dextran	-0.84	$<10^{-4}$	-0.70	$<10^{-3}$
GA 0.08% in Dextran	-0.91	$<10^{-5}$	-0.90	$<10^{-5}$

6.4.2 Cell depletion layer

The cell depletion layer downstream of the bifurcation was measured for the healthy-Dextran and GA 0.08%-Dextran samples and plotted as a function of flow ratio and parent branch flow rate in Figure 6.22 and Figure 6.23 respectively.

The CDL of the healthy-Dextran RBC in both outlet and daughter branches sample exhibits higher δ^* (Figure 6.22a,b) compared to GA 0.08%-Dextran RBC samples at $Q^* < 0.5$, i.e. when aggregation is pronounced. In particular, at $Q^* < 0.1$, $\delta^* \approx 0.3$ corresponding to $\delta \approx 15 \mu\text{m}$ thickness. With a flow rate increase, the

CDL thickness gradually decreases to its minimum levels. It should be noted that the hardened RBC samples exhibit minimum CDL thickness for $Q^* > 0.4$ and $Q^* > 0.3$, for the outlet and daughter branch respectively, while the healthy RBC samples for $Q^* > 0.5$ in both branches. Moreover, in the outlet branch the minimum CDL of the healthy sample is slightly wider than that of the daughter branch.

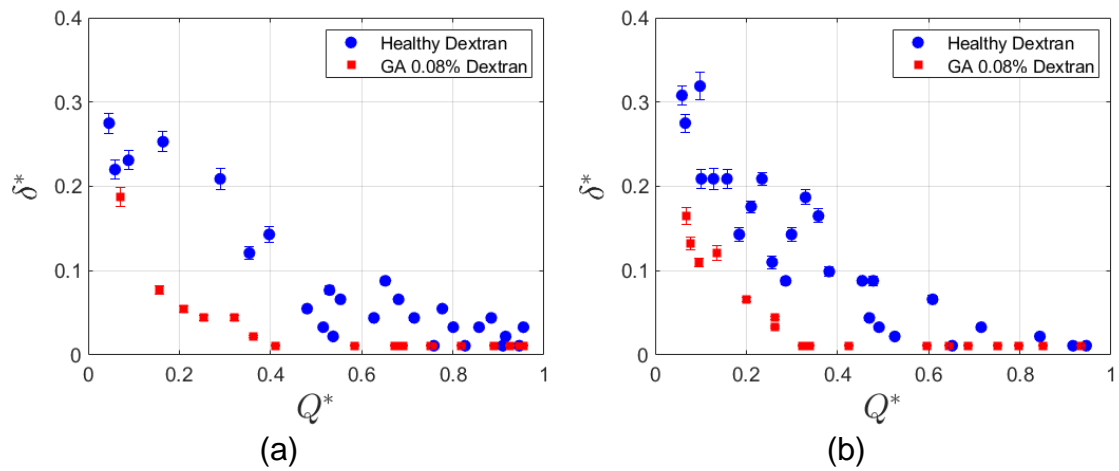


Figure 6.22: Normalised cell depleted layer width, δ^* , as a function of flow ratio Q^* . Comparison of healthy and GA 0.08% hardened RBC samples suspended Dextran in the (a) outlet and (b) daughter branches.

Figure 6.23 shows the normalised CDL thickness, δ^* , for the equal flow split case, i.e. $Q^* \approx 0.5$, examining the effect of parent branch flow rate for U^* ranging from 1 to 250 s^{-1} . The CDL thickness of the healthy-Dextran sample increases in both the outlet and daughter branches for parent branch U^* lower than 100 s^{-1} , reaching a maximum value of $\delta^* \approx 0.35$ corresponding to 17 μm , in agreement with the increased S_H which occurs in the same flow rates shown in Figure 6.21 a and b. Above 100 s^{-1} , the CDL thickness of the healthy-Dextran RBC samples decreases and reaches low values similar to the healthy-PBS ones while being

independent of the parent branch flow rate. In contrast, the effect of aggregation on GA 0.08% hardened RBC samples is not evident as the CDL width in the outlet and daughter branches remains minimum for the whole range of parent branch flow rates. The findings are in agreement with the results of the previous section, indicating minimum CDL width for $Q^* = 0.5$ and for constant parent branch flow rate around 100 s^{-1} (Figure 6.16).

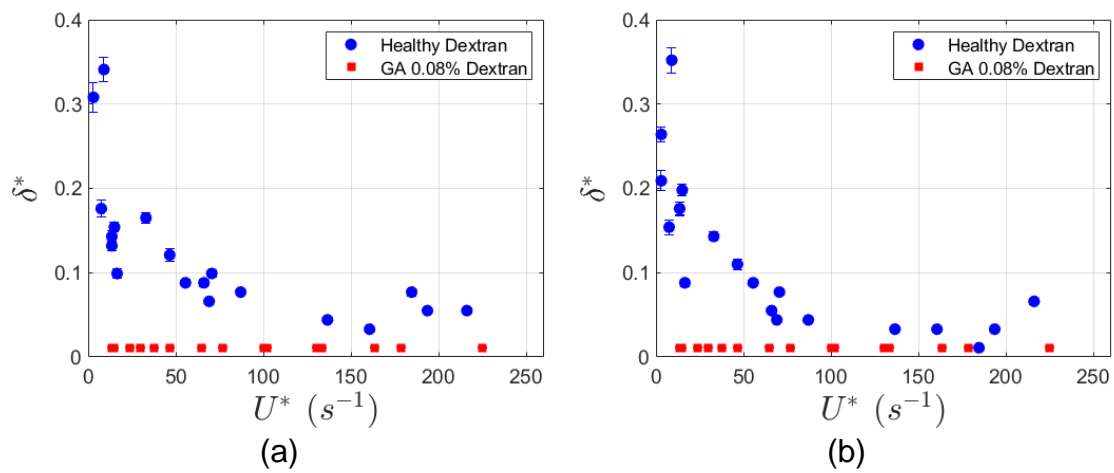


Figure 6.23: Normalised cell depleted layer width, δ^* , as a function of parent branch U^* . Comparison of healthy and GA 0.08% hardened RBC samples suspended Dextran in the (a) outlet and (b) daughter branches.

6.4.3 The effect of aggregation on plasma skimming

In this section, the effect of aggregation on plasma skimming is investigated as a function of flow ratio, Q^* . Figure 6.24 a and b, compares the healthy and GA 0.08% hardened RBC samples suspended in Dextran in the outlet and daughter branches. Plasma skimming is apparent in both branches as the data deviate from the $F^* = Q^*$ and follow the empirical expression of Pries *et al.* (1989). The plasma skimming effect seems to be more intense for the healthy-Dextran RBC samples compared to the GA 0.08%-Dextran ones. This is also indicated by the

fitting parameters A and B. However, as mentioned earlier, the observed differences fall within the uncertainty of fitting coefficients, A and B, as demonstrated in Table 6.5

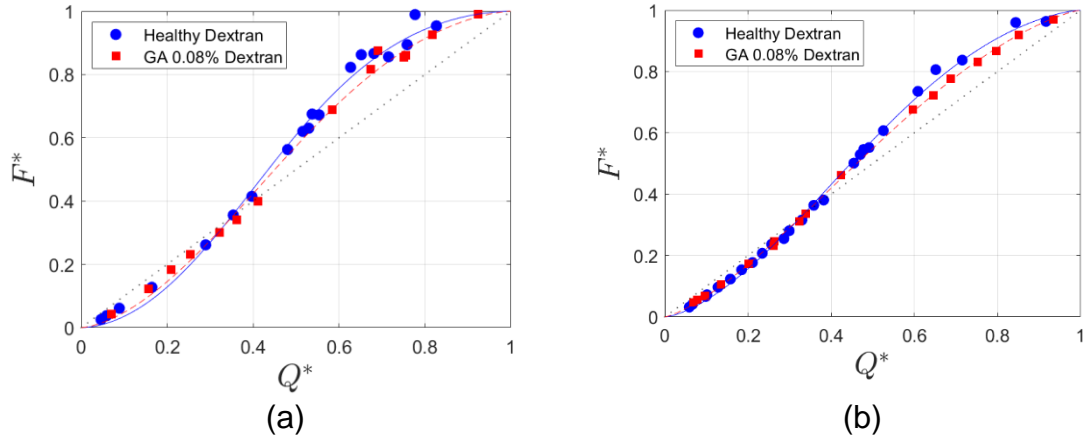


Figure 6.24: Flux-flow ratio curves; outlet branch on the left side (a,c), daughter branch on the right side (b,d). Fitting curves according to equation (6.9). (a,b) Comparison of healthy samples suspended in PBS against Dextran ones (c,d) Comparison of GA 0.08% hardened sample suspended in PBS against Dextran. Dotted line corresponds to $F^* = Q^*$.

Table 6.5: Fitting coefficients A and B for the fitting for the samples in outlet and daughter branches of Figure 6.24 with 95% confidence intervals.

	Outlet		Daughter	
	A	B	A	B
Healthy Dextran	0.44 ± 0.07	1.45 ± 0.18	0.24 ± 0.05	1.32 ± 0.20
GA 0.08% Dextran	0.29 ± 0.06	1.35 ± 0.20	0.19 ± 0.05	1.26 ± 0.13

6.4.4 Velocity distributions

Figure 6.25 shows some typical normalised velocity profiles in the outlet and daughter branches for the healthy and hardened RBC samples suspended in

Dextran at different flow ratios; the skewness index, calculated using equation (2.9) is also indicated. In all cases, the velocity profiles were skewed in the opposite direction compared to the haematocrit profiles. The healthy RBC samples show more intense skewness (Figure 6.25a,b) in both outlet and daughter branches, compared to the GA 0.08% hardened RBC samples (Figure 6.25c,d).

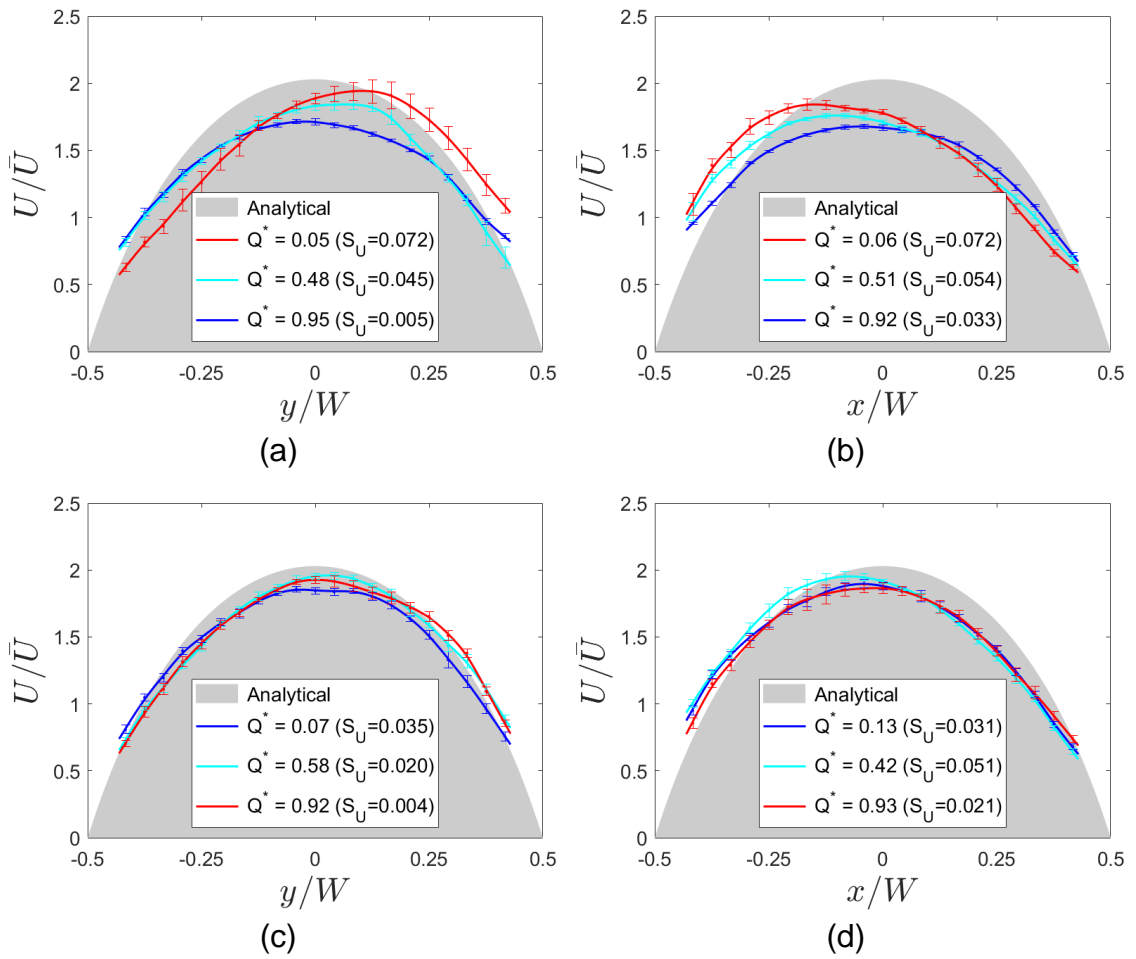


Figure 6.25: Normalised velocity profiles of aggregated RBC samples at different flow ratios. The velocity skewness index, S_U , is also indicated. Healthy RBC sample suspended in Dextran in the (a) outlet and (b) in the daughter branch. GA 0.08% hardened RBC samples suspended in Dextran (c) in the outlet and (d) in the daughter branch. The grey area indicates the analytical velocity profile for a Newtonian fluid in a square channel.

Figure 6.26a,b show a comparison of velocity profile skewness against flow ratio between the healthy-Dextran and GA 0.08%-Dextran RBC samples. The skewness index of the healthy-Dextran sample exhibits an inversely proportional correlation with flow ratio as S_U gradually decreases with flow ratio. The Pearson statistical test indicated strong correlation of healthy-Dextran S_U and flow ratio with $r = -0.65$ ($p < 0.001$) and $r = -0.55$ ($p < 0.002$) for the outlet and daughter branch respectively. On the other hand, the hardened GA 0.08% RBC samples suspended in Dextran showed to be independent of the flow ratio Q^* ($p > 0.05$).

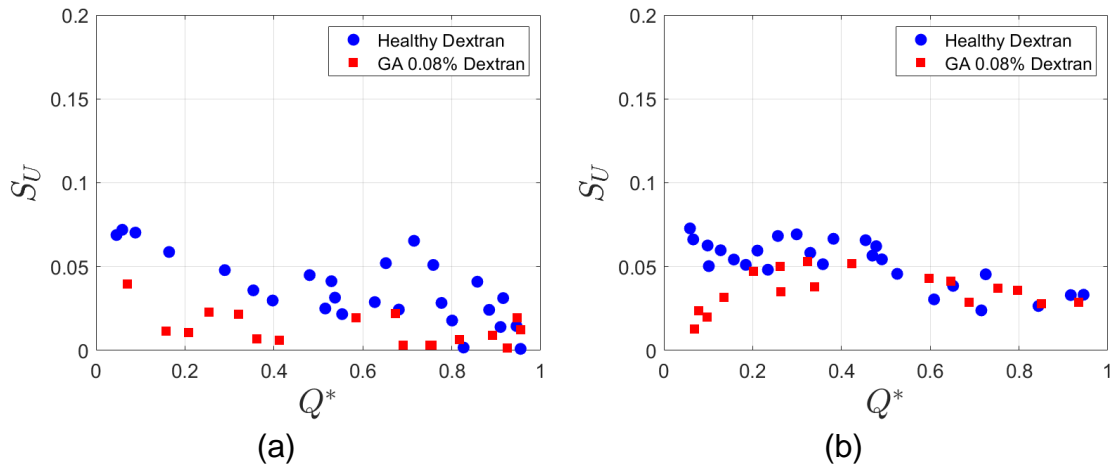


Figure 6.26: Velocity profile skewness S_U , as a function of flow ratio Q^* . Comparison of healthy and GA 0.08% hardened RBC samples suspended in Dextran in the (a) outlet and (b) daughter branches.

At this point it would be interesting to examine the correlation between the S_U and S_H as examined in the previous section. It should be noted that in $S_U - S_H$ correlation in the previous section showed no statistically significant correlations of S_U and S_H for the healthy and hardened RBC samples suspended in PBS. The healthy-Dextran RBC samples show a positive correlation between $S_U - S_H$ using Pearson's correlation test with $r = 0.65$ ($p < 10^{-3}$) and $r = 0.55$ ($p < 0.002$) for the

daughter and outlet branches respectively (Figure 6.27a,b), while the $S_U - S_H$ correlation of the GA 0.08% hardened RBC samples is not statistically significant.

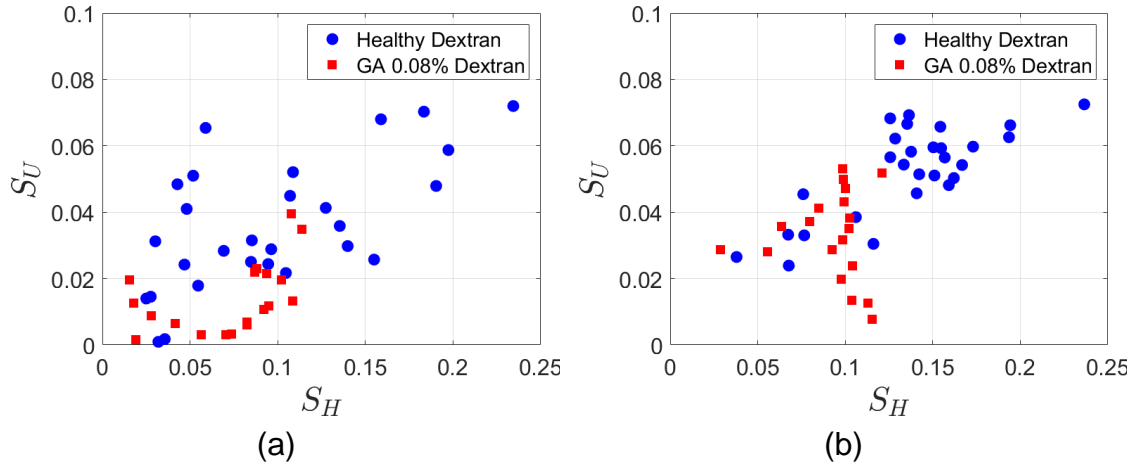


Figure 6.27: Velocity profile skewness S_U , against haematocrit skewness S_H ; Comparison of healthy sample against GA 0.08% hardened sample suspended in Dextran in the (a) outlet and (b) daughter branch.

Figure 6.28 shows the velocity skewness indices downstream of the bifurcation as a function of the parent branch flow rate for equal split flow between the daughter and outlet branches. Both the healthy-Dextran and GA 0.08% RBC samples in both outlet and daughter branch are independent with parent branch flow rate U^* . Furthermore, the hardened RBC samples in the outlet branch exhibit lower S_U values for range of parent branch flow rates (t-test, $p < 10^{-3}$) (Figure 6.28a).

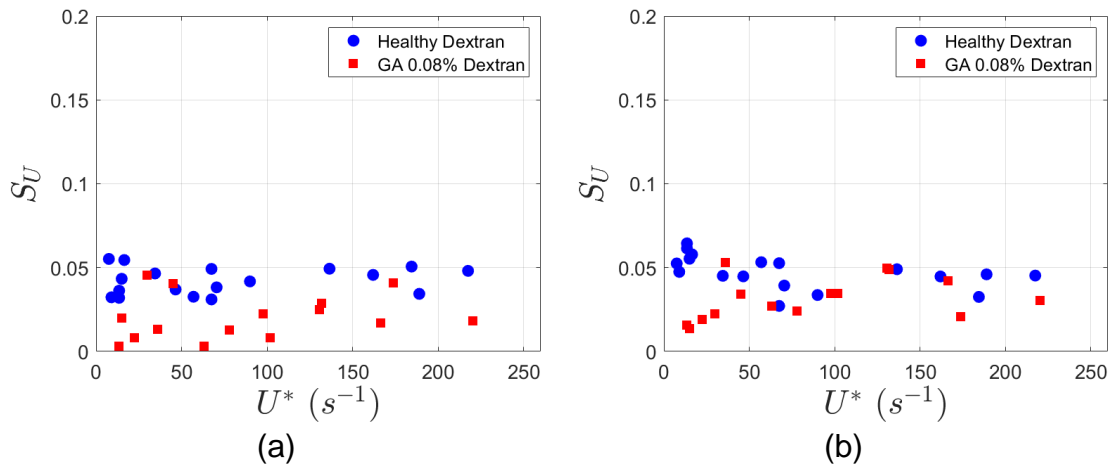


Figure 6.28: Velocity profile skewness S_U , as a function of parent branch flow rate U^* . Comparison of healthy and GA 0.08% hardened RBC samples suspended in Dextran in the (a) outlet and (b) daughter branches.

6.5 Discussion

The goal of this chapter was to investigate the evolution of the trends, that were found in straight microchannels in the Chapters 3 and 5, downstream of a T-junction with different flow ratios between the outlet branches and for different parent branch flow rates. In Chapter 3, it was found that the GA 0.08% hardened samples of 25% haematocrit, were found to exhibit sharper haematocrit distributions than the healthy ones in flow rates ranging from 1 to 150 s^{-1} in straight microchannels ($50 \times 50 \mu m^2$), while the velocity profiles showed decreased bluntness compared to the healthy samples. In chapter 5, it was shown that the RBC distribution of the aggregated healthy samples was more concentrated towards the centre of the channel at low flow rates when aggregation was apparent, resulting in blunter velocity profiles. In contrast, the

GA 0.08% hardened RBC samples did not exhibit evidence of aggregation within the studied flow rates (1 to 200 s⁻¹). The experiments in this chapter investigated the effect of deformability in the presence and absence of aggregation downstream of the T-junction bifurcation (i) with variable flow ratio ($Q^* = 0.05 - 0.95$) between the daughter and outlet branches and constant parent branch flow rate (Q^* around 100 s⁻¹) and (ii) equal split flow ($Q^* = 0.5$) between the daughter and outlet branches and varying parent branch flow rate (1 to 250 s⁻¹).

It has been reported that the RBC distribution in microvascular networks and bifurcations is affected by the vessel geometry and size (Fenton *et al.*, 1985), the haematocrit in the feeding vessel, the asymmetry of haematocrit profile in the feeding vessels (Pries *et al.*, 1989; Pries and Secomb, 2003) as well as the presence of aggregation (Sherwood *et al.*, 2014a; Kaliviotis *et al.*, 2017; Reinhart *et al.*, 2017). The present experiments investigated the effect of RBC hardening on the haematocrit and velocity profiles downstream of the bifurcation, the plasma skimming effect, the thickness of the cell depleted layer as well as the combined effect of hardening and aggregation downstream of the T-junction.

The discussion will be separated into three sections, based on the structure of the chapter. Firstly, the effect of flow ratio, between the daughter and outlet branches, on velocity and haematocrit distributions of hardened RBCs will be discussed. Subsequently, a discussion regarding the effect of parent branch flow rate on velocity and haematocrit distributions downstream of the bifurcation, will be provided and finally the effect of RBC hardening on aggregation downstream of the bifurcation will be analysed.

6.5.1 Velocity/haematocrit distributions and flow ratio

The haematocrit distribution in the parent branch showed that the hardened RBC samples in PBS, produced haematocrit profiles with lower bluntness (B_u^*) compared to the healthy-PBS samples in the parent branch (Figure 6.2). However, the haematocrit profile differences in bluntness upstream of the bifurcation, exhibited no significant impact on the haematocrit skewness downstream of the bifurcation, as seen in Figure 6.4a,b. The main differences were observed in the individual haematocrit profiles; the healthy-PBS RBC samples produce a bimodal distribution which is pronounced at higher flow ratios, compared to the GA 0.08%-PBS RBC samples which exhibit a more uniform distribution in both outlet and daughter branches (Figure 6.3). Moreover, the different haematocrit distributions downstream of the bifurcation for GA 0.08%-PBS and healthy-PBS were also captured by the thickness of the CDL, δ^* : the GA 0.08%-PBS sample exhibits lower δ^* values than the healthy-PBS sample at flow ratio lower than 0.5 (Figure 6.8a,b). It would be expected that the sharper haematocrit distributions of GA 0.08%-PBS samples in the parent branch would produce haematocrit distributions with higher skewness compared to healthy-PBS downstream the bifurcation, however, the results showed similar values of haematocrit skewness despite the differences in the corresponding haematocrit profiles and cell depleted layer thickness. This implies that maybe the skewness index might have not been sensitive enough to distinguish the difference between these measurements; in many cases the area under the haematocrit profile in each half of the channel ($\int_0^{0.5} H(y^*) dy^*$, $\int_{-0.5}^0 H(y^*) dy^*$) has similar values, even

if the profile shape is different. The results have also been tested using an additional skewness index indicating the deviation of the maximum haematocrit value from the centreline position; however, the results were subject to uncertainty due to the non-monotonic nature of the distributions.

The effect of haematocrit distribution on the velocity profiles downstream of the bifurcation was also analysed. The skewed haematocrit distribution produced velocity profiles that were skewed in the opposite side of the channel as was also shown by Sherwood et al. (2014b). However, the increase of haematocrit skewness S_H at low flow ratios, did not affect velocity skewness S_U remarkably (Figure 6.12). Moreover, the velocity skewness downstream of the bifurcation was found not to be as sensitive as the haematocrit skewness to the flow ratio (Figure 6.11).

The plasma skimming effect in the current experiments was reported in Figure 6.5. The haematocrit ratio, H/H_P , was found to decrease proportionally to the flow ratio in the branches downstream of the bifurcation. In particular, at flow ratios lower than 0.5 the perfused samples showed an overall decrease of haematocrit, while at flow ratios higher than 0.5 the haematocrit was increased. In agreement with these findings, Sherwood et al. (2014b), reported no discernible differences between aggregated and non-aggregated samples regarding the extent of plasma skimming in a T-shaped bifurcation. Yamamoto *et al.* (2019), also investigated the partitioning of healthy RBCs in a T-junction with varying flow ratios and showed a similar decrease of haematocrit ratio at flow ratios lower than 0.5; at flow ratios higher than 0.5 the haematocrit ratios were almost equal to one,

while in our case, H^* reached close to 1.2, similarly to Pries *et al.* (1989). However, it should be noted that the sample haematocrit in Yamamoto's experiments was 0.5%, much lower than the 25% haematocrit concentration in the current experiments. Figure 6.5 shows that the plasma skimming intensity is not affected by the RBC hardening as both healthy-PBS and GA 0.08%-PBS samples exhibit similar haematocrit partitioning with flow ratio in both branches. The plasma skimming effect was further investigated, by utilising the flux-flow curves as described by Pries *et al.* (1989). The comparison of healthy-PBS and GA 0.08%-PBS samples showed some differences that were pronounced in the daughter branch, with $B_{GA-PBS} = 1.29 \pm 0.12$ against $B_{h-PBS} = 1.19 \pm 0.21$ (Figure 6.6).

6.5.2 Velocity/haematocrit distributions and parent branch flow rate

The second set of experiments investigated the impact of parent branch flow rate downstream of the bifurcation when the flow partition between the branches was equal, i.e. Q^* was around 0.5. The haematocrit distribution in the parent branch was in agreement with the analysis of Chapter 3, capturing the sharper haematocrit profiles of hardened RBCs for the whole range of measurements (Figure 6.13). Similarly to the *in vivo* microcirculation flows, the Reynolds number in the current experiments is less than 0.1 and the red blood cell based Re is much less than 1 ($Re_{rbc} \approx 10^{-4}$) indicating the negligible effect of inertia. At low haematocrit levels ($H \approx 0.5\%$), where interactions between RBC are not significant, the RBC trajectories would be expected to follow the streamlines of the suspended medium as shown by Yamamoto *et al.* (2019) where the

experimental RBC trajectories almost agreed with the fluid streamlines predicted by the simulation. In the current experiments the haematocrit concentration was higher ($H \approx 25\%$), and cell-cell and cell-wall interactions are considerable. In Figure 6.15, the haematocrit skewness is gradually decreased as the flow rate increased indicating the role of cell-cell interactions in the haematocrit distributions. Considering the negligible impact of inertial forces, the frequency and intensity of cell-cell interactions might also increase with the increasing flow rate. Thus, a shear induced dispersion motion of the cells away from the areas of high haematocrit gradient might occur, producing a more uniform haematocrit distributions with parent branch flow rate increase, downstream of the bifurcation. Moreover, the skewed velocity profiles exhibited in the daughter and outlet branches, affect the shear induced inward migration which might be more intense due to the skewness of the profiles and hence the sharper shear gradients. Healthy RBC samples which produce velocity profiles with higher skewness also exhibit thicker cell depleted layer in comparison with the hardened RBC samples (Figure 6.16).

6.5.3 RBC deformability and aggregation

The bluntness of the haematocrit profile (B_H^*) in the parent branch was in agreement with the findings of Chapter 5 (data not shown for brevity) i.e. the B_U^* of the healthy-Dextran sample was quite similar with the healthy-PBS in the range of perfused flow rates, as for $U^* > 100 \text{ s}^{-1}$ aggregation is not expected to be apparent (Figure 6.2). Likewise, the GA 0.08%-PBS and GA 0.08%-Dextran bluntness indices were quite similar as also shown in Chapter 5. In Figure 6.20

the haematocrit skewness S_H of GA 0.08%-Dextran RBC samples exhibits lower values compared to the S_H of the healthy-Dextran ones in the low flow ratios ($Q^* < 0.5$) indicating the decreased effect of aggregation for hardened RBCs. In addition, in higher flow ratios ($Q^* > 0.5$) in which the effect of aggregation is expected to decrease, the GA 0.08%-Dextran RBC samples, exhibit similar S_H values with the healthy-Dextran samples as it would be expected. Similarly, in Figure 6.21 the healthy-Dextran and GA 0.08%-Dextran RBC samples exhibit high differences in haematocrit skewness S_H in the low range of parent branch flow rates while in the higher range of U^* , the S_H differences between the two samples diminish. The behaviour of the cell depleted layer thickness δ^* follows the same pattern as the haematocrit skewness. The CDL differences between the healthy-Dextran and GA 0.08%-Dextran RBC samples are enhanced in low flow ratios and parent branch flow rates as seen in Figure 6.22 and Figure 6.23 respectively, while in the higher range of flow ratio and parent branch flow rates the differences decrease.

The plasma skimming of the healthy-Dextran RBC sample was measured to be higher than the GA 0.08%-Dextran in both branches, with fitting parameters $B_{h-Dex} = 1.45 \pm 0.18$, $B_{GA-Dex} = 1.35 \pm 0.20$ and $B_{h-Dex} = 1.32 \pm 0.20$, $B_{GA-Dex} = 1.26 \pm 0.13$ for the outlet and daughter branches respectively (Figure 6.24). This implies that the decreased deformability of RBCs inhibits plasma skimming compared to the healthy RBCs in the presence of aggregation. In literature no studies have been found investigating the effect of RBC deformability on plasma skimming; however, Sherwood *et al.* (2014b), analysed the flux-flow curves between a healthy-PBS and healthy-Dextran RBCs for sequential bifurcations and indicated

that plasma skimming was pronounced in the second bifurcation for the Dextran sample.

Finally, the velocity skewness S_u was found to be higher for the healthy-Dextran RBC samples compared to the GA 0.08% ones and this was pronounced in the outlet branch (Figure 6.26 and Figure 6.27). In general, the differences that were observed between the daughter and outlet branches might occur due to the non-symmetrical shape of the bifurcation; the outlet branch extends the flow direction of the parent branch (in the x-axis), while the daughter branch is perpendicular (y-axis) to the flow of the parent branch. Downstream of the bifurcation the RBCs flowing towards the daughter branch need to change direction (y-direction) and have to be redistributed more compared to the population of RBCs that continue flowing towards the outlet branch (x-direction). The increased redistribution of RBCs that flow towards the daughter branch might affect the shear induced migration, the collision intensity and frequency between the RBCs and the mechanism of aggregation compared to the flows towards the outlet branch which might be less disturbed. This asymmetry might be the reason that in some cases the outlet and daughter branches do not exhibit similar results regarding the haematocrit and velocity skewness and cell depleted layer thickness.

6.6 Closure

In this chapter, the impact of RBC membrane stiffening and aggregation was examined on a T-shaped bifurcation with varying flow ratio between the daughter

and outlet branches in a range of parent branch flow rates. The haematocrit and velocity profiles downstream of the bifurcation were analysed utilising skewness indices and were correlated with the flow ratio between the branches and flow rate of the parent branch. Plasma skimming was also investigated. RBC hardening was found to affect the shape of the individual haematocrit and velocity profiles in the range of flow ratios that were studied; however, no significant differences were observed in the haematocrit and velocity skewness indices as well as in the extent of plasma skimming. The parent branch flow rate affected the redistribution of both healthy and hardened RBC samples downstream of the bifurcation which produced less skewed distributions as flow rate increased. The velocity skewness did not show a strong correlation with haematocrit skewness. Aggregation was found to be affected by deformability as the velocity and haematocrit skewness and cell depleted layer thickness were decreased. Moreover, the extent of plasma skimming for hardened RBC was decreased compared to healthy ones in the presence of aggregation. The next chapter summarises the main findings of the thesis and provides recommendations for future work.

Chapter 7

Conclusions and recommendations for future work

In diseases such as malaria, sickle cell anaemia, diabetes and others, RBC stiffness plays a major role in microvascular angiopathies and occlusions. The aim of the present work was to study the role of red blood cell mechanical properties on haemodynamics in order to improve understanding of impaired RBCs in microvascular flow. Multiple studies have investigated the flow of hardened RBCs individually or at low haematocrit, however, limited information

is available in the literature relative to the flow of hardened RBC at high concentrations where cell interactions play a significant role. The *in vitro* experiments conducted in this thesis employed physiological haematocrit levels, flow rates and dimensions in order to investigate microscale blood flows and identify potential physical biomarkers for diagnostic purposes. This research can form the basis for the development of a low-cost medical diagnostic tool which can provide a rapid screening test for diseases in which the mechanical properties of RBCs play a key role.

7.1 Main contributions

The main contributions of this study can be summarised as follows:

- High resolution description of the velocity and haematocrit distribution of healthy and hardened RBCs flowing in straight microchannels at physiological haematocrit levels and flow rates in the presence and absence of aggregation.
- Elucidated the role of cell concentration (haematocrit) on the flow behaviour of stiffened RBCs.
- Correlations between the velocity and haematocrit distributions between healthy and hardened RBCs in flow.
- *In vitro* characterization of hardened RBC margination while flowing in a high concentrated suspension of healthy RBCs.

- Elucidated the role of confinement on RBC flow properties and cell distributions as a function of membrane deformability.
- Velocity and cell distribution measurements for aggregated and hardened RBCs, highlighting the combined effects of aggregation and RBC hardening downstream of a T-shaped bifurcation. Plasma skimming effect and cell depleted layer were quantified and compared between healthy and hardened RBCs in a range of flow ratios among the branches.

7.2 Summary of main findings

The main findings of this study elucidated the role of RBC deformability on physical haemodynamic properties such as velocity and haematocrit distributions, the aggregation intensity, the margination during flow and RBC flow partitioning at a bifurcation.

In particular, Chapter 3, demonstrated that hardened RBCs exhibited sharper haematocrit profiles than the healthy RBCs meaning that their distribution was more focused in the centre of the channel. In addition, the velocity profiles of the hardened RBCs were sharper than the healthy ones. This trend was haematocrit dependent as it was mostly apparent in the denser RBC suspensions, i.e. 25%, while at the most dilute suspensions (5%) the differences were negligible. The flowrates examined seemed that have no statistically significant effect on the haematocrit and velocity profiles of the perfused samples.

The margination of hardened RBCs while flowing within healthy RBC suspensions was examined in Chapter 4. It was found that hardened RBCs get

pushed towards the walls by the dominant in concentration healthy RBCs. The margination of hardened RBCs was found to occur near the outlet of the channel, 300 channel widths downstream the inlet where radial migration and margination forces were in an equilibrium. In contrast, margination of hardened RBCs was not apparent near the inlet (10 channel widths downstream the inlet). The control sample consisting of hardened labelled RBCs within hardened RBC suspensions exhibited no margination as expected.

In Chapter 4, the effect of channel aspect ratio on haematocrit and velocity distributions of healthy and hardened RBC suspensions was also investigated. In microchannels with higher aspect ratio ($100 \times 25 \mu\text{m}^2$, $\text{AR} = 4$) the haematocrit and velocity distributions of the samples were wider than the profiles in Chapter 3, where microchannels of aspect ratio equal to one were used. The hardened samples in the $100 \times 25 \mu\text{m}^2$ channels exhibited less uniform haematocrit distribution than the healthy ones. Moreover, the velocity profiles of hardened RBCs were closer to the analytical velocity profile of Newtonian fluids as expected from the findings of Chapter 3.

The impact of RBC membrane hardening on aggregation properties was investigated in Chapter 5. The extent of aggregation was found to be significantly reduced with membrane hardening. The RBCs samples with mild hardening (GA 0.04%) showed less pronounced aggregation while the effect of aggregation on moderately hardened samples (GA 0.08%) was negligible.

Finally, the impact of RBC membrane hardening and aggregation was examined in a T-shaped bifurcation with various flow ratios between the branches and in a

range of parent branch flow rates. Reduced RBC deformability was found to affect the shape of haematocrit distributions as well as the thickness of the cell depleted layer downstream of the bifurcation. In addition, the effect of aggregation on hardened RBCs was not evident in the velocity and haematocrit distributions and it was shown that the extent of plasma skimming was reduced with hardening in the presence of aggregation.

7.3 Future work

The present work investigated the impact of RBC deformability on haemodynamic properties mimicking blood flow in disease. The same set of experiments can be conducted using more physiological approach in terms of fluids and suspensions. For example, PBS and Dextran can be replaced by plasma of the blood and patient blood with decreased deformability can be used instead of the artificially hardened RBCs. In addition, endothelial cells can be cultured in the interior channel walls in order to mimic the main properties of physiological microvessels.

Moreover, the study can be extended in a range of parameters such as haematocrit concentration (higher levels corresponding to inflammatory cases), higher flow rates (arterial flow – inertial effects), channel dimensions and aspect ratios (20 x 20 μm or single file flows) and geometries (circular cross section, sequential bifurcations etc).

In terms of experimental set up, the experiments could be conducted in a temperature-controlled environment, using physiological temperatures (37 °C).

Moreover, high speed imaging would minimise the time of acquisition and could provide the option for determining the trajectories of individual RBCs during flow. Different types of perfused flow rates could be provided, such as pulsatile, accelerating and periodic flows.

Furthermore, the findings on hardened RBC margination can be the base of separation experiments between healthy and diseased (hardened) RBCs, in a similar way to the techniques that are currently used for separating platelets and leukocytes from RBCs.

Finally, the results of the present experiments provide a useful set of data for the optimization and verification of computational approaches related to multi-phase hydrodynamic modelling of microvascular blood flow and in general multi-phase particulate flows.

References

- Abay, A., Recktenwald, S. M., et al. (2019a) 'Cross-sectional focusing of red blood cells in a constricted microfluidic channel', *Soft Matter*.16:534-543.
- Abay, A., Simionato, G., et al. (2019b) 'Glutaraldehyde - A Subtle Tool in the Investigation of Healthy and Pathologic Red Blood Cells.', *Frontiers in physiology*. Frontiers Media SA, 10, p. 514.
- Abkarian, M. et al. (2008) 'Cellular-scale hydrodynamics', *Biomedical Materials*. Institute of Physics Publishing, 3(3) 034011.
- Abkarian, M., Faivre, M. and Viallat, A. (2007) 'Swinging of Red Blood Cells under Shear Flow', *Physical Review Letters*. American Physical Society, 98(18), p. 188302.
- Adar, T. et al. (2008) 'Increased red blood cell aggregation in patients with Gaucher disease is non-inflammatory', *Clinical Hemorheology and Microcirculation*. IOS Press, 40(2), pp. 113–118.
- Agrawal, R. et al. (2016) 'Assessment of red blood cell deformability in type 2 diabetes mellitus and diabetic retinopathy by dual optical tweezers stretching technique', *Scientific Reports*. Nature Publishing Group, 6, p. 15873.
- Alonso, C. et al. (1995) 'Transient rheological behavior of blood in low-shear tube flow: velocity profiles and effective viscosity.', *The American journal of physiology*, 268(1 Pt 2), pp. H25-32.
- Alonso, C., Pries, A. R. and Gaehtgens, P. (1993) 'Time-Dependent Rheological Behavior of Blood at Low Shear in Narrow Vertical Tubes - Journals - NCBI', *American Journal of Physiology - Heart and Circulatory Physiology*, 265(2), pp. H553–H561.
- Van Amersfoort, E. S. and Van Strijp, J. A. G. (1994) 'Evaluation of a flow cytometric fluorescence quenching assay of phagocytosis of sensitized sheep erythrocytes by polymorphonuclear leukocytes', *Cytometry*, 17(4), pp. 294–301.
- Amirouche, A. et al. (2020) 'Dual shape recovery of red blood cells flowing out of a microfluidic constriction', *Biomicrofluidics*. AIP Publishing LLC, 14(2), p. 024116.
- Artmann, G. M. (1995) 'Microscopic photometric quantification of stiffness and relaxation time of red blood cells in a flow chamber.', *Biorheology*, 32(5), pp. 553–70..
- Baar, S. and Arrowsmith, D. J. (1970) 'Thermal damage to red cells', *J. clin. Path*, 23, pp. 572–576.
- Babu, N. and Singh, M. (2004) 'Influence of hyperglycemia on aggregation, deformability and shape parameters of erythrocytes', *Clinical Hemorheology and Microcirculation*, 31, pp. 273–280.
- Bagchi, P. (2007) 'Mesoscale simulation of blood flow in small vessels.', *Biophysical journal*. The Biophysical Society, 92(6), pp. 1858–77.

- Barabino, G. A., Platt, M. O. and Kaul, D. K. (2010) 'Sickle Cell Biomechanics', *Annual Review of Biomedical Engineering*, 12(1), pp. 345–367.
- Barber, J. O. et al. (2008) 'Simulated two-dimensional red blood cell motion, deformation, and partitioning in microvessel bifurcations', *Annals of Biomedical Engineering*, 36(10), pp. 1690–1698.
- Baskurt, O. K. et al. (2009) 'Comparison of three commercially available ektacytometers with different shearing geometries.', *Biorheology*. IOS Press, 46(3), pp. 251–64.
- Baskurt, O. K., Bor-Küçükatay, M. and Yalçın, Ö. (1999) 'The effect of red blood cell aggregation on blood flow resistance', *Biorheology*, 36, pp. 447–452.
- Baskurt, O. K., Yalcin, O. and Meiselman, H. J. (2004) 'Hemorheology and vascular control mechanisms.', *Clinical hemorheology and microcirculation*, 30(3–4), pp. 169–78.
- Bellelli, A. et al. (1988) 'Human erythrocytes cross-linked with glutaraldehyde general properties and significance as a blood substitute', *Biochemical and Biophysical Research Communications*. Academic Press, 156(2), pp. 970–977.
- Ben-Ami, R. et al. (2003) 'A synergistic effect of albumin and fibrinogen on immunoglobulin-induced red blood cell aggregation', *American Journal of Physiology - Heart and Circulatory Physiology*. American Physiological Society, 285(6 54-6), pp. H2663–H2669.
- Bishop, Jeffrey J., Nance, P. R., et al. (2001a) 'Effect of erythrocyte aggregation on velocity profiles in venules', *American Journal of Physiology-Heart and Circulatory Physiology*. American Physiological Society Bethesda, MD , 280(1), pp. H222–H236.
- Bishop, Jeffrey J., Popel, A. S., et al. (2001b) 'Effects of erythrocyte aggregation and venous network geometry on red blood cell axial migration', *American Journal of Physiology-Heart and Circulatory Physiology*. American Physiological Society Bethesda, MD , 281(2), pp. H939–H950.
- Boynard, M., Razavian, M. and Beuzard, Y. (1988) 'Evaluation of sickle cell aggregation by ultrasound backscattering', *Clinical Hemorheology*. IOS Press, 8(5), pp. 687–694.
- Bremmell, K. E., Evans, A. and Prestidge, C. A. (2006) 'Deformation and nano-rheology of red blood cells: An AFM investigation', *Colloids and Surfaces B: Biointerfaces*, 50(1), pp. 43–48.
- Bronkhorst, P.J. H. et al. (1997) 'The mechanism of red cell (dis)aggregation investigated by means of direct cell manipulation using multiple optical trapping', *British Journal of Haematology*. Blackwell Science Ltd, 96(2), pp. 256–258.
- Brown, C. D. et al. (2005) 'Association of reduced red blood cell deformability and diabetic nephropathy', *Kidney International*. Blackwell Publishing Inc., 67(1), pp. 295–300.
- Brust, M. et al. (2013) 'Rheology of human blood plasma: Viscoelastic versus Newtonian behavior', *Physical Review Letters*. American Physical Society, 110(7), p. 078305.
- Brust, M. et al. (2015) 'The plasma protein fibrinogen stabilizes clusters of red blood cells

in microcapillary flows', *Scientific Reports*. Nature Publishing Group, 4(1), p. 4348.

Bruus, H. (2008) *Theoretical Microfluidics*. USA.

Bucherer, C. et al. (1992) 'Effect of deoxygenation on rheological behavior of density separated sickle cell suspensions', *Clinical Hemorheology and Microcirculation*. IOS Press, 12(3), pp. 415–425.

Burstain, J. M. et al. (1994) 'Blood volume determination as a function of hematocrit and mass in three preservative solutions and saline', *American Journal of Clinical Pathology*, 102(6), pp. 812–815.

Buys, A. V et al. (2013) 'Changes in red blood cell membrane structure in type 2 diabetes: a scanning electron and atomic force microscopy study', *Cardiovascular Diabetology*. BioMed Central, 12, p. 25.

Cabrales, P. (2007) 'Effects of erythrocyte flexibility on microvascular perfusion and oxygenation during acute anemia', *American Journal of Physiology - Heart and Circulatory Physiology*, 293(2).

Carboni, E. J. et al. (2016) 'Direct Tracking of Particles and Quantification of Margination in Blood Flow', *Biophysical Journal*, 111(7), pp. 1487–1495.

Caro, C. G. (Colin G. (2012) *The mechanics of the circulation*. Cambridge University Press.

Celle, P. L. (1969) 'Alteration of Deformability of the Erythrocyte Membrane in Stored Blood', *Transfusion*. Blackwell Publishing Ltd, 9(5), pp. 238–245.

Chang, H. Y., Li, X. and Karniadakis, G. E. (2017) 'Modeling of Biomechanics and Biorheology of Red Blood Cells in Type 2 Diabetes Mellitus', *Biophysical Journal*. Biophysical Society, 113(2), pp. 481–490.

Charansonney, O. et al. (1993) 'Red blood cell aggregation and blood viscosity in an isolated heart preparation.', *Biorheology*, 30(1), pp. 75–84.

Chen, Y. et al. (2017) 'Margination of Stiffened Red Blood Cells Regulated By Vessel Geometry', *Scientific Reports*. Nature Publishing Group, 7(1), p. 15253.

Chien, S. et al. (1967) 'Blood Viscosity: Influence of Erythrocyte Deformation', *Science*, 157(3790), p. 827.

Chien, S. (1970) 'Shear dependence of effective cell volume as a determinant of blood viscosity.', *Science (New York, N.Y.)*, 168(3934), pp. 977–9.

Chien, S. (1975) 'Biophysical Behavior of Red Cells in Suspensions', in *The Red Blood Cell* vol. 2, pp. 1031–1133.

Chien, S. et al. (1985) 'Model studies on distributions of blood cells at microvascular bifurcations.', *The American journal of physiology*. American Physiological Society Bethesda, MD , 248(4 Pt 2), pp. H568-76.

Chien, S. (1987) 'Red cell deformability and its relevance to blood flow.', *Annual review*

of physiology, 49(1), pp. 177–192..

Chien, S. and Jan, K.-M. (1973) 'Ultrastructural Basis of the Mechanism of Rouleaux Formation', *Microvascular Research*, 5(2), pp. 155–166.

Chu, F. and Ng, K. M. (1989) 'Flow in Packed Tubes with a Small Tube to Particle Diameter Ratio', *AIChE Journal*, 35(1), pp. 148–158.

Cokelet, G. R. (1999) 'Poiseuille Award Lecture. Viscometric, in vitro and in vivo blood viscosity relationships: how are they related?', *Biorheology*, 36(5–6), pp. 343–58.

Cokelet, G. R. and Goldsmith, H. L. (1991) 'Decreased hydrodynamic resistance in the two-phase flow of blood through small vertical tubes at low flow rates.', *Circulation Research*, 68(1), pp. 1–17.

Condon, M. R. et al. (2003) 'Appearance of an erythrocyte population with decreased deformability and hemoglobin content following sepsis', *American Journal of Physiology-Heart and Circulatory Physiology*. American Physiological Society Bethesda, MD , 284(6), pp. H2177–H2184.

Connes, P. et al. (2018) 'Blood rheological abnormalities in sickle cell anemia', *Clinical hemorheology and microcirculation*, 68(2–3), pp. 165–172.

Czaja, B. et al. (2020) 'The influence of red blood cell deformability on hematocrit profiles and platelet margination', *PLOS Computational Biology*. Edited by J. M. Haugh. Public Library of Science, 16(3), p. e1007716.

D'Apolito, R. et al. (2015) 'Red blood cells affect the margination of microparticles in synthetic microcapillaries and intravital microcirculation as a function of their size and shape', *Journal of Controlled Release*. Elsevier, 217, pp. 263–272.

Das, B., Enden, G. and S, A. (1997) 'Stratified Multiphase Model for Blood Flow in a Venular Bifurcation', *Annals of Biomedical Engineering*, 25, pp. 135–153.

Das, B., Johnson, P. C. and Popel, A. S. (1998) 'Effect of nonaxisymmetric hematocrit distribution on non-Newtonian blood flow in small tubes', *Biorheology*, 35(1), pp. 69–87.

Demiroğlu, H. et al. (1998) 'Increased erythrocyte aggregation as an indicator for an aggressive clinical course in Behçet's disease: a prospective study.', *Annals of the rheumatic diseases*. BMJ Publishing Group Ltd, 57(11), pp. 694–6.

Dondorp, A. M. et al. (2000) 'Abnormal blood flow and red blood cell deformability in severe malaria.', *Parasitology today (Personal ed.)*, 16(6), pp. 228–32.

Dondorp, A. M. et al. (2002) 'The role of reduced red cell deformability in the pathogenesis of severe falciparum malaria and its restoration by blood transfusion', *Transactions of the Royal Society of Tropical Medicine and Hygiene*. Narnia, 96(3), pp. 282–286.

Doyeux, V. et al. (2011) 'Spheres in the vicinity of a bifurcation: Elucidating the Zweifach-Fung effect', *Journal of Fluid Mechanics*. Cambridge University Press, 674, pp. 359–388.

Dulińska, I. et al. (2006) 'Stiffness of normal and pathological erythrocytes studied by

means of atomic force microscopy.’, *Journal of biochemical and biophysical methods*, 66(1–3), pp. 1–11.

Dupire, J., Socol, M. and Viallat, A. (2012) ‘Full dynamics of a red blood cell in shear flow.’, *Proceedings of the National Academy of Sciences of the United States of America*. National Academy of Sciences, 109(51), pp. 20808–13.

Ellsworth, M. L. and Pittman, R. N. (1986) ‘Evaluation of photometric methods for quantifying convective mass transport in microvessels.’, *The American journal of physiology*, 251(4 Pt 2), pp. H869-79.

Evans, E. A. (1973) ‘New membrane concept applied to the analysis of fluid shear and micropipette deformed red blood cells’, *Biophysical Journal*, 13(9), pp. 941–954.

Fahraeus, R. (1958) ‘The influence of the rouleau formation of the erythrocytes on the rheology of the blood.’, *Acta medica Scandinavica*, 161(2), pp. 151–65.

Fåhraeus, R. (1929) ‘The Suspension Stability of the Blood’, *Physiological Reviews*, 9(2), pp. 241–274.

Fåhraeus, R. and Lindqvist, T. (1931) ‘The viscosity of the blood in narrow capillary tubes’, *Am. J. Physiol*, 96, pp. 562–68.

Faivre, M. et al. (2006) ‘Geometrical focusing of cells in a microfluidic device: An approach to separate blood plasma’, *Biorheology*. IOS Press, 43(2), pp. 147–159.

Falcó, C. et al. (2005) ‘Influence of fibrinogen levels on erythrocyte aggregation determined with the Myrenne aggregometer and the Sefam erythro-aggregometer.’, *Clinical hemorheology and microcirculation*, 33(2), pp. 145–51.

Fedosov, D. A. et al. (2010) ‘Blood Flow and Cell-Free Layer in Microvessels’, *Microcirculation*. NIH Public Access, 17(8), pp. 615–628.

Fenton, B. M., Carr, R. T. and Cokelet, G. R. (1985) ‘Nonuniform red cell distribution in 20 to 100 μm bifurcations’, *Microvascular Research*. Academic Press, 29(1), pp. 103–126.

Fiebig, E., Ley, K. and Arfors, K. E. (1991) ‘Rapid leukocyte accumulation by spontaneous rolling and adhesion in the exteriorized rabbit mesentery.’, *International journal of microcirculation, clinical and experimental*, 10(2), pp. 127–44.

Fischer, T. M. and Korzeniewski, R. (2013) ‘Threshold shear stress for the transition between tumbling and tank-treading of red blood cells in shear flow: dependence on the viscosity of the suspending medium’, *Journal of Fluid Mechanics*. Cambridge University Press, 736, pp. 351–365.

Fitzgibbon, S. et al. (2015) ‘In vitro measurement of particle margination in the microchannel flow: effect of varying hematocrit.’, *Biophysical journal*. The Biophysical Society, 108(10), pp. 2601–2608.

Fornal, M. et al. (2006) Erythrocyte stiffness in diabetes mellitus studied with atomic force microscope, *Clinical Hemorheology and Microcirculation*. IOS Press.

- Forsyth, A. M. et al. (2010) 'The dynamic behavior of chemically "stiffened" red blood cells in microchannel flows.', *Microvascular Research*, 80(1), pp. 37–43.
- Forsyth, A. M. et al. (2011) 'Multiscale approach to link red blood cell dynamics, shear viscosity, and ATP release.', *Proceedings of the National Academy of Sciences of the United States of America*. National Academy of Sciences, 108(27), pp. 10986–91.
- Freund, J. B. (2007) 'Leukocyte margination in a model microvessel', *Physics of Fluids*. American Institute of Physics Inc., 19(2), p. 023301.
- Fujiwara, H. et al. (2009) 'Red blood cell motions in high-hematocrit blood flowing through a stenosed microchannel.', *Journal of biomechanics*, 42(7), pp. 838–43.
- Fung, Y. C. (1973) 'Stochastic flow in capillary blood vessels', *Microvascular Research*. Academic Press, 5(1), pp. 34–48.
- Gaehtgens, P. (1980) 'Flow of blood through narrow capillaries: rheological mechanisms determining capillary hematocrit and apparent viscosity.', *Biorheology*, 17(1–2), pp. 183–9.
- Gaehtgens, P., Albrecht, K. H. and Kreutz, F. (1978) 'Fahraeus effect and cell screening during tube flow of human blood. II. Effect of dextran-induced cell aggregation', *Biorheology*. IOS Press, 15(3–4), pp. 155–161.
- Gaehtgens, P., Duehrssen, C. and Albrecht, K. H. (1980) 'Motion, deformation, and interaction of blood cells and plasma during flow through narrow capillary tubes', *Blood Cells*, 6(4), pp. 799–812.
- Geislinger, T. M. and Franke, T. (2014) 'Hydrodynamic lift of vesicles and red blood cells in flow — from Fåhræus & Lindqvist to microfluidic cell sorting', *Advances in Colloid and Interface Science*, 208, pp. 161–176.
- Girasole, M. et al. (2007) 'Roughness of the plasma membrane as an independent morphological parameter to study RBCs: A quantitative atomic force microscopy investigation', *Biochimica et Biophysica Acta (BBA) - Biomembranes*, 1768(5), pp. 1268–1276.
- Go, T. et al. (2017) 'Focusing and alignment of erythrocytes in a viscoelastic medium', *Scientific Reports*. Nature Publishing Group, 7, p. 41162.
- Goldsmith, H. L. (1968) 'The microrheology of red blood cell suspensions.', *The Journal of general physiology*. The Rockefeller University Press, 52(1), pp. 5–28.
- Goldsmith, H. L. (1971) 'Red cell motions and wall interactions in tube flow.', *Federation proceedings*, 30(5), pp. 1578–90.
- Goldsmith, H. L. and Marlow, J. (1972) 'Flow Behaviour of Erythrocytes. I. Rotation and Deformation in Dilute Suspensions', *Proceedings of the Royal Society of London B: Biological Sciences*, 182(1068).
- Grandchamp, X. et al. (2013) 'Lift and Down-Gradient Shear-Induced Diffusion in Red Blood Cell Suspensions', *Physical Review Letters*, 110(10), pp. 101–108.

- Guo, Q. et al. (2014) 'Microfluidic analysis of red blood cell deformability.', *Journal of biomechanics*, 47(8), pp. 1767–76.
- Gustafsson, L., Appelgren, L. and Myrvold, H. E. (1981) 'Effects of increased plasma viscosity and red blood cell aggregation on blood viscosity in vivo.', *The American journal of physiology*, 241(4), pp. H513-8.
- de Haan, M. et al. (2018) 'Numerical Investigation of the Effects of Red Blood Cell Cytoplasmic Viscosity Contrasts on Single Cell and Bulk Transport Behaviour', *Applied Sciences. Multidisciplinary Digital Publishing Institute*, 8(9), p. 1616.
- Halpern, D. and Secomb, T. W. (1992) 'The squeezing of red blood cells through parallel-sided channels with near-minimal widths', *Journal of Fluid Mechanics. Cambridge University Press*, 244, pp. 307–322.
- Haradin, A. R., Weed, R. I. and Reed, C. F. (1969) 'Changes in Physical Properties of Stored Erythrocytes', *Transfusion. John Wiley & Sons, Ltd* (10.1111), 9(5), pp. 229–237.
- Haubert, K. et al. (2006) 'PDMS bonding by means of a portable, low-cost corona system', *Lab on a Chip. The Royal Society of Chemistry*, 6(12), p. 1548.
- Hénon, S. et al. (1999) 'A new determination of the shear modulus of the human erythrocyte membrane using optical tweezers', *Biophysical Journal*, 76(2), pp. 1145–1151.
- Hochmuth, R. M., Worthy, P. R. and Evans, E. A. (1979) 'Red cell extensional recovery and the determination of membrane viscosity', *Biophysical Journal*, 26(1), pp. 101–114.
- Hou, H. W. et al. (2010) 'Deformability based cell margination—A simple microfluidic design for malaria-infected erythrocyte separation', *Lab on a Chip. The Royal Society of Chemistry*, 10(19), p. 2605.
- Iss, C. et al. (2019) 'Self-organization of red blood cell suspensions under confined 2D flows', *Soft Matter. Royal Society of Chemistry*, 15(14), pp. 2971–2980.
- Jan, K., Usami, S. and Smith, J. A. (1981) 'Influence of oxygen tension and hematocrit reading on ESRs of sickle cells. Role of RBC aggregation', *Archives of Internal Medicine*, 141(13), pp. 1815–1818.
- Jayavanth, S., Jagadeesan, K. and Singh, M. (2004) 'Influence of *P. vivax* malaria on erythrocyte aggregation and deformability.', *Clinical hemorheology and microcirculation*, 31(4), pp. 257–66.
- Jeffery, G. B. (1922) 'The Motion of Ellipsoidal Particles Immersed in a Viscous Fluid', *Proceedings of the Royal Society A: Mathematical, Physical and Engineering Sciences. The Royal Society*, 102(715), pp. 161–179.
- Jovtchev, S. et al. (2000) 'Role of electrical and mechanical properties of red blood cells for their aggregation', *Colloids and Surfaces A: Physicochemical and Engineering Aspects*, 164(2–3), pp. 95–104.
- Jovtchev, S. et al. (2009) 'Investigations on the Polymer Induced Aggregation of Red Blood Cells', *Biotechnology & Biotechnological Equipment. Taylor & Francis*, 23(sup1),

pp. 581–584.

Kaliviotis, E. et al. (2016) 'Quantifying local characteristics of velocity, aggregation and hematocrit of human erythrocytes in a microchannel flow', *Clinical Hemorheology and Microcirculation*. IOS Press, 63(2), pp. 123–148.

Kaliviotis, E., Sherwood, J. M. and Balabani, S. (2017) 'Partitioning of red blood cell aggregates in bifurcating microscale flows', *Scientific Reports*. Nature Publishing Group, 7(1), p. 44563.

Kaliviotis, E. and Yianneskis, M. (2008) 'Fast response characteristics of red blood cell aggregation', *Biorheology*. IOS Press, 45(6), pp. 639–649.

Kaoui, B. et al. (2008) 'Lateral migration of a two-dimensional vesicle in unbounded Poiseuille flow', *Physical Review E - Statistical, Nonlinear, and Soft Matter Physics*. American Physical Society, 77(2), p. 021903.

Kaoui, B., Biro, G. and Misbah, C. (2009) 'Why Do Red Blood Cells Have Asymmetric Shapes Even in a Symmetric Flow?', *Physical Review Letters*. American Physical Society, 103(18), p. 188101.

Kaoui, B., Krüger, T. and Harting, J. (2012) 'How does confinement affect the dynamics of viscous vesicles and red blood cells?', *Soft Matter*, 8(35).

Katsumoto, Y. et al. (2010) 'Electrical classification of single red blood cell deformability in high-shear microchannel flows', *International Journal of Heat and Fluid Flow*, 31(6), pp. 985–995.

Kaul, D. K. and Nagel, R. L. (1993) 'Sickle cell vasoocclusion: Many issues and some answers', *Experientia*. Birkhäuser-Verlag, 49(1), pp. 5–15.

Kawahara, J. et al. (1997) 'Chemical Cross-Linking by Glutaraldehyde between Amino Groups: Its Mechanism and Effects', in Swift Graham, and Carraher, C. E., and Bowman Christopher N (eds) *Polymer Modification*. Boston, MA: Springer US, pp. 119–131.

Kihm, A. et al. (2018) 'Classification of red blood cell shapes in flow using outlier tolerant machine learning', *PLOS Computational Biology*. Edited by I. V. Pivkin. Public Library of Science, 14(6), p. e1006278.

Kim et al. (2007) 'Contributions of collision rate and collision efficiency to erythrocyte aggregation in post capillary venules at low flow rates', pp. 1947–1954.

Kim, S. et al. (2007) 'Temporal and spatial variations of cell-free layer width in arterioles', *American Journal of Physiology-Heart and Circulatory Physiology*. American Physiological Society, 293(3), pp. H1526–H1535.

Kim, S. et al. (2009) 'The cell-free layer in microvascular blood flow', *Biorheology*. IOS Press, 46(3), pp. 181–189.

Kim, S., Ong, P. K. and Johnson, P. C. (2009) 'Effect of dextran 500 on radial migration of erythrocytes in postcapillary venules at low flow rates.', *Molecular & cellular biomechanics : MCB*, 6(2), pp. 83–91.

- Krüger, T. et al. (2013) 'Crossover from tumbling to tank-treading-like motion in dense simulated suspensions of red blood cells'.
- Kumar, A. and Graham, M. D. (2011) 'Segregation by membrane rigidity in flowing binary suspensions of elastic capsules', *Physical Review E. American Physical Society*, 84(6), p. 066316.
- Kumar, A. and Graham, M. D. (2012a) 'Margination and segregation in confined flows of blood and other multicomponent suspensions', *Soft Matter. The Royal Society of Chemistry*, 8(41), p. 10536.
- Kumar, A. and Graham, M. D. (2012b) 'Mechanism of Margination in Confined Flows of Blood and Other Multicomponent Suspensions', *Physical Review Letters. American Physical Society*, 109(10), p. 108102.
- Lanotte, L. et al. (2016) 'Red cells' dynamic morphologies govern blood shear thinning under microcirculatory flow conditions', *Proceedings of the National Academy of Sciences. National Academy of Sciences*, 113(47), pp. 13289–13294.
- Leighton, D. and Acrivos, D. A. (1987) 'The shear-induced migration of particles in concentrated suspensions', *J. Fluid Mech*, 181, pp. 415–439.
- Lemonne, N. et al. (2012) 'Increased blood viscosity and red blood cell aggregation in a patient with sickle cell anemia and smoldering myeloma', *American Journal of Hematology. John Wiley & Sons, Ltd*, pp. E129–E129.
- Lenormand, G. et al. (2001) 'Direct measurement of the area expansion and shear moduli of the human red blood cell membrane skeleton.', *Biophysical Journal*, 81(1), pp. 43–56.
- Li, X. et al. (2016) 'Patient-specific blood rheology in sickle-cell anaemia', *Interface Focus. Royal Society of London*, 6(1), p. 20150065.
- Li, X., Popel, A. S. and Karniadakis, G. E. (2012) 'Blood-plasma separation in Y-shaped bifurcating microfluidic channels: a dissipative particle dynamics simulation study.', *Physical biology. NIH Public Access*, 9(2), p. 026010.
- Linderkamp, O. et al. (1986) 'Deformability and Intrinsic Material Properties of Neonatal Red Blood Cells', *Blood*, 67(5), pp. 1244–1250.
- Linderkamp, O. and Meiselman, H. J. (1982) 'Geometric, osmotic, and membrane mechanical properties of density- separated human red cells', *Blood*, 59(6), p. 1121.
- Lipowsky, H. H. and Zweifach, B. W. (1974) 'Network analysis of microcirculation of cat mesentery', *Microvascular Research*, 7(1), pp. 73–83.
- Long, D. S. et al. (2004) 'Microviscometry reveals reduced blood viscosity and altered shear rate and shear stress profiles in microvessels after hemodilution.', *Proceedings of the National Academy of Sciences of the United States of America. National Academy of Sciences*, 101(27), pp. 10060–5.
- Losserand, S., Coupier, G. and Podgorski, T. (2019) 'Migration velocity of red blood cells in microchannels', *Microvascular Research. Academic Press*, 124, pp. 30–36.

- Lowe, G. D. O. (1988) Clinical blood rheology. CRC Press.
- Maeda, N. et al. (1983) 'Alteration of rheological properties of human erythrocytes by crosslinking of membrane proteins', *Biochimica et Biophysica Acta (BBA) - Biomembranes*, 735(1), pp. 104–112.
- Maeda, N. and Shiga, T. (1985) 'Inhibition and acceleration of erythrocyte aggregation induced by small macromolecules', *Biochimica et Biophysica Acta*, 843, pp. 128–136.
- Mchedlishvili, G. (2007) 'Hemorheological changes in microcirculation: Their mechanism and measurement technique', *Indian Journal of Experimental Biology*, 45, pp. 32–40.
- Meiselman, H. J. (2009) 'Red blood cell aggregation: 45 years being curious', *Biorheology*. IOS Press, 46(1), pp. 1–19.
- Meiselman, H. J., Evans, E. A. and Hochmuth, R. M. (1978) 'Membrane mechanical properties of ATP-depleted human erythrocytes', *Blood*, 52(3), p. 499.
- Meng, Q. and Higdon, J. J. L. (2008) 'Large scale dynamic simulation of plate-like particle suspensions. Part II: Brownian simulation', *Journal of Rheology. The Society of Rheology*, 52(1), pp. 37–65.
- Mohandas, N. and Gallagher, P. G. (2008) 'Red cell membrane: past, present, and future.', *Blood*. American Society of Hematology, 112(10), pp. 3939–48.
- Moia, M. et al. (1985) 'An improved method for measuring red blood cell filterability', *La Ricerca in Clinica e in Laboratorio*, 15(2), pp. 127–131.
- Moon, J. S. et al. (2016) 'Impaired RBC deformability is associated with diabetic retinopathy in patients with type 2 diabetes', *Diabetes and Metabolism*. Elsevier Masson SAS, 42(6), pp. 448–452.
- Morel, F. M., Baker, R. F. and Wayland, H. (1971) 'Quantitation of human red blood cell fixation by glutaraldehyde.', *The Journal of cell biology*. The Rockefeller University Press, 48(1), pp. 91–100.
- Munn, L. L. and Dupin, M. M. (2008) 'Blood cell interactions and segregation in flow', *Annals of Biomedical Engineering*. NIH Public Access, 36(4), pp. 534–544.
- Nakano, A. et al. (2003) 'Measurement of red cell velocity in microvessels using particle image velocimetry (PIV)', *Clinical Hemorheology and Microcirculation*, 29, pp. 445–455.
- Namgung, B. et al. (2016) 'Biomimetic Precapillary Flow Patterns for Enhancing Blood Plasma Separation: A Preliminary Study', *Sensors*. Multidisciplinary Digital Publishing Institute, 16(9), p. 1543.
- Namgung, B. et al. (2017a) 'Near-Wall Migration Dynamics of Erythrocytes in Vivo: Effects of Cell Deformability and Arteriolar Bifurcation.', *Frontiers in Physiology*. Frontiers Media SA, 8, p. 963.
- Namgung, B. et al. (2017b) 'Near-Wall Migration Dynamics of Erythrocytes in Vivo: Effects of Cell Deformability and Arteriolar Bifurcation', *Frontiers in Physiology*. Frontiers, 8, p. 963.

- Neu, B. and Meiselman, H. J. (2002) 'Depletion-mediated red blood cell aggregation in polymer solutions', *Biophysical Journal*. Biophysical Society, 83(5), pp. 2482–2490.
- Noguchi, H. and Gompper, G. (2005) 'Shape transitions of fluid vesicles and red blood cells in capillary flows', *Proceedings of the National Academy of Sciences*. National Academy of Sciences, 102(40), pp. 14159–14164.
- Olsen, M. & Adrian, R. (2000) 'Out-of-focus effects on particle image visibility and correlation in microscopic particle image velocimetry', *Experiments in fluids*, Suppl., S166–S174
- Park, H. et al. (2016) 'Measuring cell surface area and deformability of individual human red blood cells over blood storage using quantitative phase imaging', *Scientific Reports*. Nature Publishing Group, 6(1), p. 34257.
- Parrow NL, Violet PC, Tu H, et al. (2018) 'Measuring Deformability and Red Cell Heterogeneity in Blood by Ektacytometry.' *J Vis Exp*;(131):56910.
- Passos, A. et al. (2019) 'The effect of deformability on the microscale flow behavior of red blood cell suspensions', *Physics of Fluids*. AIP Publishing LLC, 31(9), p. 091903.
- Popel, Aleksander S and Johnson, P. C. (2005) 'Microcirculation and Hemorheology.', *Annual review of fluid mechanics*. NIH Public Access, 37, pp. 43–69.
- Popel, Aleksander S. and Johnson, P. C. (2005) 'Microcirculation and Hemorheology', *Annual Review of Fluid Mechanics*. Annual Reviews, 37(1), pp. 43–69.
- Pozrikidis, C. (2005) 'Numerical simulation of cell motion in tube flow', *Annals of Biomedical Engineering*. Springer, 33(2), pp. 165–178.
- Pribush, A., Zilberman-Kravits, D. and Meyerstein, N. (2007) 'The mechanism of the dextran-induced red blood cell aggregation', *European Biophysics Journal*, 36(2), pp. 85–94.
- Pries, A. R. et al. (1989) 'Red cell distribution at microvascular bifurcations', *Microvascular Research*. Academic Press, 38(1), pp. 81–101.
- Pries, A. R. et al. (1990) 'Blood flow in microvascular networks. Experiments and simulation.', *Circulation research*, 67(4), pp. 826–34.
- Pries, A. R. et al. (1994) 'Resistance to blood flow in microvessels in vivo.', *Circulation research*, 75(5), pp. 904–15.
- Pries, A. R., Kanzow, G. and Gaehtgens, P. (1983) 'Microphotometric determination of hematocrit in small vessels.', *The American journal of physiology*. American Physiological Society Bethesda, MD , 245(1), pp. H167-77.
- Pries, A. R., Neuhaus, D. and Gaehtgens, P. (1992) 'Blood viscosity in tube flow: dependence on diameter and hematocrit.', *The American journal of physiology*, 263(6 Pt 2), pp. H1770-8.
- Pries, A. R. and Secomb, T. W. (2003) 'Rheology of the microcirculation', in *Clinical Hemorheology and Microcirculation*, pp. 143–148.

- Raj, K. M. et al. (2018) 'Collective dynamics of red blood cells on an in vitro microfluidic platform', *Lab on a Chip. The Royal Society of Chemistry*, 18(24), pp. 3939–3948.
- Reinhart, W. H., Piety, N. Z. and Shevkoplyas, S. S. (2017) 'Influence of red blood cell aggregation on perfusion of an artificial microvascular network', *Microcirculation*. Wiley Blackwell, 24(5).
- Reinke, W., Gaehtgens, P. and Johnson, P. C. (1987) 'Blood viscosity in small tubes: effect of shear rate, aggregation, and sedimentation.', *The American journal of physiology*, 253(3 Pt 2), pp. H540-7.
- Rodrigues R et al. (2013) 'Red Blood Cells Deformability Index Assessment In A Hyperbolic Microchannel: The Diamide And Glutaraldehyde Effect', *Webmed Central plus Biomedical Engineering* 1970, 4(8), p. WMC004375.
- Schmid-Schönbein, G. W. (1999) 'Biomechanics of Microcirculatory Blood Perfusion', *Annual Review of Biomedical Engineering*. Annual Reviews, 1(1), pp. 73–102.
- Schmid-Schönbein, H. and Gaehtgens, P. (1981) 'What is red cell deformability?', *Scandinavian journal of clinical and laboratory investigation. Supplementum*, 156, pp. 13–26.
- Schmid-Schönbein, H. and Heidtmann, H. (1982) 'Nonspecific rheological abnormalities in sickle cell disease.', *Blood cells*, 8(1), pp. 89–101.
- Schmid-Schönbein, H., Volger, E. and Klose, H. J. (1972) 'Microrheology and light transmission of blood. II. The photometric quantification of red cell aggregate formation and dispersion in flow.', *Pflugers Archiv: European journal of physiology*, 333(2), pp. 140–55.
- Schmid-Schönbein, H. and Wells, R. (1969) 'Fluid drop-like transition of erythrocytes under shear', *Science. American Association for the Advancement of Science*, 165(3890), pp. 288–291.
- Schultze (1865) 'Max Schultze (1865), G. Bizzozzero (1882) and the discovery of the platelet', *British Journal of Haematology*, 133(3), pp. 251–258.
- Seaman, G. V. F. (1975) 'Electrokinetic Behavior of Red Cells', in *The Red Blood Cell*. Elsevier, pp. 1135–1229. doi: 10.1016/b978-0-12-677202-9.50020-4.
- Secomb, T. W. (2017) 'Blood Flow in the Microcirculation', *Annu. Rev. Fluid Mech*, 49, pp. 443–61.
- Shen, Z. et al. (2016) 'Inversion of hematocrit partition at microfluidic bifurcations.', *Microvascular research*, 105, pp. 40–6.
- Sherwood, J. M. et al. (2012) 'The effect of red blood cell aggregation on velocity and cell-depleted layer characteristics of blood in a bifurcating microchannel', *Biomicrofluidics*. American Institute of Physics, 6(2), p. 024119.
- Sherwood, J. M. (2013) *Blood velocity and viscosity in bifurcating microchannels*. UCL.
- Sherwood, J. M., Kaliviotis, E., et al. (2014a) 'Hematocrit, viscosity and velocity

- distributions of aggregating and non-aggregating blood in a bifurcating microchannel', *Biomechanics and Modeling in Mechanobiology*. Springer Berlin Heidelberg, 13(2), pp. 259–273.
- Sherwood, J. M., Holmes, D., et al. (2014b) 'Spatial distributions of red blood cells significantly alter local haemodynamics.', *PloS one*. Public Library of Science, 9(6), p. e100473.
- Shevkoplyas, S. S. et al. (2006) 'Direct measurement of the impact of impaired erythrocyte deformability on microvascular network perfusion in a microfluidic device', *Lab on a Chip*, 6(7), p. 914.
- Shin, S. et al. (2007) 'Erythrocyte deformability and its variation in diabetes mellitus', *Indian Journal of Experimental Biology*, 45(1), pp. 121–128.
- Simchon, S., Jan, K. M. and Chien, S. (1987) 'Influence of reduced red cell deformability on regional blood flow.', *The American journal of physiology*. American Physiological Society, 253(4 Pt 2), pp. H898-903.
- Skalak, R. and Branemark, P. I. (1969) 'Deformation of red blood cells in capillaries.', *Science (New York, N.Y.)*, 164(3880), pp. 717–9.
- Skotheim, J. M. and Secomb, T. W. (2007) 'Red blood cells and other nonspherical capsules in shear flow: Oscillatory dynamics and the tank-treading-to-tumbling transition', *Physical Review Letters*. American Physical Society, 98(7), p. 078301.
- Smith, B. L. and Neal, D. R. (2016) *Handbook of Fluid Dynamics*, Second Edition. CRC PR Inc., 2nd ed.
- Sosa, J. M., Nielsen, N. D., Vignes, S. M., Chen, T. G., Shevkoplyas, S. S., et al. (2014) 'The relationship between red blood cell deformability metrics and perfusion of an artificial microvascular network.', *Clinical hemorheology and microcirculation*. IOS Press, 57(3), pp. 275–89.
- Sosa, J. M., Nielsen, N. D., Vignes, S. M., Chen, T. G. and Shevkoplyas, S. S. (2014) 'The relationship between red blood cell deformability metrics and perfusion of an artificial microvascular network.', *Clinical hemorheology and microcirculation*. NIH Public Access, 57(3), pp. 275–89.
- Squier, C. A., Hart, J. S. and Churchland, A. (1976) 'Changes in red blood cell volume on fixation in glutaraldehyde solutions', *Histochemistry*. Springer-Verlag, 48(1), pp. 7–16.
- Stone, H. A. et al. (2009) 'Viewpoint Slipping through blood flow A Viewpoint on: Why Do Red Blood Cells Have Asymmetric Shapes Even in a Symmetric Flow?', *Physics Phys. Rev. Lett*, 2(103).
- Stuart, J. and Nash, G. B. (1990) 'Red cell deformability and haematological disorders', *Blood Reviews*. Churchill Livingstone, 4(3), pp. 141–147.
- Svanes, K. and Zweifach, B. W. (1968) 'Variations in small blood vessel hematocrits produced in hypothermic rats by micro-occlusion', *Microvascular Research*. Academic Press, 1(2), pp. 210–220.

- Szwarocka, A. et al. (2001) 'The combined effect of IDA and glutaraldehyde on the properties of human erythrocytes', *International Journal of Pharmaceutics*. Elsevier, 220(1–2), pp. 43–51.
- Tangelder, G. J. et al. (1985) 'Distribution of blood platelets flowing in arterioles.', *The American journal of physiology*. American Physiological Society Bethesda, MD , 248(3 Pt 2), pp. H318-23.
- Tangelder, G. J. et al. (1986) 'Velocity profiles of blood platelets and red blood cells flowing in arterioles of the rabbit mesentery.', *Circulation Research*, 59(5), pp. 505–14.
- Tario, J. D. et al. (2012) 'Optimized Staining and Proliferation Modeling Methods for Cell Division Monitoring using Cell Tracking Dyes', *Journal of Visualized Experiments*, (70), p. e4287.
- Tatsumi, K. et al. (2019) 'Particle and rigidized red blood cell concentration distributions in microchannel flows', *Physics of Fluids*. AIP Publishing LLC, 31(8), p. 082006.
- Tomaiuolo, G. et al. (2016) 'Microconfined flow behavior of red blood cells', *Medical Engineering & Physics*. Elsevier, 38(1), pp. 11–16.
- Tong, X. and Caldwell, K. D. (1995) 'Separation and characterization of red blood cells with different membrane deformability using steric field-flow fractionation', *Journal of Chromatography B: Biomedical Applications*, 674(1), pp. 39–47.
- Tortora, G. J. and Grabowski, S. R. (2001) *Introduction to the human body*, 5th edition. John Wiley & Sons Inc.
- Tsai, C.-H. D., Kaneko, M. and Arai, F. (2014) 'Improving the evaluation of cell deformability by different channel width in a microfluidic device', in 2014 11th International Conference on Ubiquitous Robots and Ambient Intelligence (URAI). IEEE, pp. 522–524.
- Tsukada, K. et al. (2001) 'Direct measurement of erythrocyte deformability in diabetes mellitus with a transparent microchannel capillary model and high-speed video camera system.', *Microvascular research*. Academic Press, 61(3), pp. 231–9.
- Usami, S. et al. (1975) 'Effect of deoxygenation on blood rheology in sickle cell disease', *Microvascular Research*. Academic Press, 9(3), pp. 324–334.
- Varchanis, S. et al. (2018) 'How viscoelastic is human blood plasma?', *Soft Matter*. Royal Society of Chemistry, 14(21), pp. 4238–4251.
- Vassar, P S et al. (1972) 'Physicochemical effects of aldehydes on the human erythrocyte.', *The Journal of cell biology*. The Rockefeller University Press, 53(3), pp. 809–18.
- Vassar, P. S. et al. (1972) 'Physicochemical effects of aldehydes on the human erythrocyte', *Journal of Cell Biology*. The Rockefeller University Press, 53(3), pp. 809–818.
- Vennemann, P. et al. (2006) 'In vivo micro particle image velocimetry measurements of blood-plasma in the embryonic avian heart', *Journal of Biomechanics*, 39, pp. 1191–

1200.

Viallat, A. and Abkarian, M. (2014) 'Red blood cell: From its mechanics to its motion in shear flow', *International Journal of Laboratory Hematology*. Blackwell Publishing Ltd, pp. 237–243.

Walter, H. and Krob, E. J. (1989) 'Fixation with even small quantities of glutaraldehyde affects red blood cell surface properties in a cell- and species-dependent manner. Studies by cell partitioning', *Bioscience Reports*.

Westerweel, J. and Scarano, F. (2005) 'Universal outlier detection for PIV data', *Experiments in Fluids*. Springer, 39(6), pp. 1096–1100. doi: 10.1007/s00348-005-0016-6.

Woods, S. L. (1995) *Cardiac nursing*. Lippincott.

Wu, Y. et al. (2009) 'Time-dependent surface adhesive force and morphology of RBC measured by AFM', *Micron*, 40(3), pp. 359–364.

Yamamoto, K. et al. (2019) 'Study of the Partitioning of Red Blood Cells Through Asymmetric Bifurcating Microchannels', *Journal of Medical and Biological Engineering*. Springer Berlin Heidelberg, pp. 1–9.

Yeom, E., Kang, Y. J. and Lee, S.-J. (2014) 'Changes in velocity profile according to blood viscosity in a microchannel', *Biomicrofluidics*. American Institute of Physics, 8(3), p. 034110.

Yoon, Y.-Z. et al. (2009) 'Flickering analysis of erythrocyte mechanical properties: dependence on oxygenation level, cell shape, and hydration level.', *Biophysical journal*, 97(6), pp. 1606–15.

Zhang, J., Johnson, P. C. and Popel, A. S. (2009) 'Effects of erythrocyte deformability and aggregation on the cell free layer and apparent viscosity of microscopic blood flows.', *Microvascular research*. Elsevier Inc., 77(3), pp. 265–72.

Zheng, Y. et al. (2013) 'Electrical measurement of red blood cell deformability on a microfluidic device.', *Lab on a chip*, 13(16), pp. 3275–83.

